



Terms and Conditions of Use of Digitised Theses from Trinity College Library Dublin

Copyright statement

All material supplied by Trinity College Library is protected by copyright (under the Copyright and Related Rights Act, 2000 as amended) and other relevant Intellectual Property Rights. By accessing and using a Digitised Thesis from Trinity College Library you acknowledge that all Intellectual Property Rights in any Works supplied are the sole and exclusive property of the copyright and/or other IPR holder. Specific copyright holders may not be explicitly identified. Use of materials from other sources within a thesis should not be construed as a claim over them.

A non-exclusive, non-transferable licence is hereby granted to those using or reproducing, in whole or in part, the material for valid purposes, providing the copyright owners are acknowledged using the normal conventions. Where specific permission to use material is required, this is identified and such permission must be sought from the copyright holder or agency cited.

Liability statement

By using a Digitised Thesis, I accept that Trinity College Dublin bears no legal responsibility for the accuracy, legality or comprehensiveness of materials contained within the thesis, and that Trinity College Dublin accepts no liability for indirect, consequential, or incidental, damages or losses arising from use of the thesis for whatever reason. Information located in a thesis may be subject to specific use constraints, details of which may not be explicitly described. It is the responsibility of potential and actual users to be aware of such constraints and to abide by them. By making use of material from a digitised thesis, you accept these copyright and disclaimer provisions. Where it is brought to the attention of Trinity College Library that there may be a breach of copyright or other restraint, it is the policy to withdraw or take down access to a thesis while the issue is being resolved.

Access Agreement

By using a Digitised Thesis from Trinity College Library you are bound by the following Terms & Conditions. Please read them carefully.

I have read and I understand the following statement: All material supplied via a Digitised Thesis from Trinity College Library is protected by copyright and other intellectual property rights, and duplication or sale of all or part of any of a thesis is not permitted, except that material may be duplicated by you for your research use or for educational purposes in electronic or print form providing the copyright owners are acknowledged using the normal conventions. You must obtain permission for any other use. Electronic or print copies may not be offered, whether for sale or otherwise to anyone. This copy has been supplied on the understanding that it is copyright material and that no quotation from the thesis may be published without proper acknowledgement.

EXFOLIATION AND DISPERSION OF
LAYERED MATERIALS THROUGH LIQUID
PHASE PROCESSING

MUSTAFA LOTYA



A thesis submitted for the degree of
Doctor of Philosophy

Supervised by Prof. Jonathan Coleman
Chemical Physics of Low Dimensional Nanostructures Group

School of Physics
Trinity College Dublin

2012



Thesis 9565
—

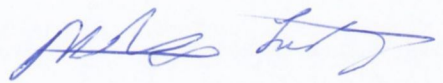
To my family and friends...

DECLARATION

I declare that this thesis has not been submitted as an exercise for a degree at this or any other university and it is entirely my own work.

I agree to deposit this thesis in the University's open access institutional repository or allow the library to do so on my behalf, subject to Irish Copyright Legislation and Trinity College Library conditions of use and acknowledgement.

Elements of this work that have been carried out jointly with others or by collaborators have been duly acknowledged in the text wherever included.



Mustafa Lotya

ABSTRACT

Graphene is a nanomaterial that has been the focus of intense research efforts in recent times. Production methods that yield high quality graphene without the need for detrimental chemical processing are needed in order to exploit this novel material in real-world applications.

Our group makes use of ultrasound-assisted exfoliation in a liquid-phase production process that can meet this challenge. In this work, the energetics governing the dispersion of graphene in a wide range of solvents has been studied. 40 solvents were tested to show that good graphene solvents are characterised by surface tensions close to 40 mJ/m² and Hildebrand parameter close to 23 MPa^{1/2}. Hansen solubility parameters for graphene itself have been derived as $\langle\delta_D\rangle = 18.0\text{ MPa}^{1/2}$, $\langle\delta_P\rangle = 9.3\text{ MPa}^{1/2}$ and $\langle\delta_H\rangle = 7.6\text{ MPa}^{1/2}$. The resultant calculation of the Flory-Huggins parameter has shown that the energetic cost of exfoliation is a key parameter in governing the dispersibility of pristine graphene in solvents.

Graphene dispersions in aqueous media have also been prepared with the aid of surfactant stabilisers. The dispersions were composed of largely few-layer graphene with significant quantities of mono and bilayer material observed. The dispersions were analysed using colloidal theory and the graphene flakes shown to be stabilised against re-aggregation by an electrostatic potential barrier. The graphene flakes were shown to be of extremely high quality by chemical analyses, demonstrating that oxidative treatments or other functionalisation routines are not required to produce graphene in water-based systems.

In order to facilitate the use of surfactant-stabilised graphene in applications, the processing was enhanced using prolonged mild sonication to yield concentrations exceeding 1 mg/ml. High-concentration aqueous few-layer graphene dispersions were prepared with up to 20% monolayer number fractions. TEM and Raman evidence showed that the flake dimensions and defect levels were unchanged under continuous

sonication conditions over a time frame of 18 days. It was also shown that tuning the centrifugation rate allowed a degree of flake size selection. These dispersions were used to create free-standing conductive films of randomly stacked graphene flakes, demonstrating the utility of the method.

In addition to graphene, there exists a diverse set of compound materials composed of layers of atomic planes. Liquid-phase dispersions of MoS_2 and WS_2 in selected solvents were examined and shown to contain graphene-like nanosheets. It was shown that the crystal structure of bulk MoS_2 was retained on exfoliation. Hybrid materials of these inorganic materials were prepared by blending with liquid dispersions of other nanomaterials. As an example an MoS_2 /carbon nanotube hybrid was tested for use as a cathode in lithium ion batteries showing improved capacity and cycling performance compared to pure MoS_2 . In addition, the exfoliation of a class of layered compounds with thermoelectric properties was examined, offering a potential route to enhance energy conversion devices.

PUBLICATIONS

Aspects of the work presented in this thesis have appeared previously in the following publications.

Publications containing major contributions from material in this thesis are marked with *.

1. Smith, R. J.; King, P. J.; Lotya, M.; Wirtz, C.; Khan, U.; De, S.; O'Neill, A.; Duesberg, G. S.; Grunlan, J. C.; Moriarty, G.; Chen, J.; Wang, J.; Minett, A. I.; Nicolosi, V.; Coleman, J. N., Large-Scale Exfoliation of Inorganic Layered Compounds in Aqueous Surfactant Solutions. *Advanced Materials* 2011, 23 (34), 3944-3948.

2. Lee, K.; Kim, H.-Y.; Lotya, M.; Coleman, J. N.; Kim, G.-T.; Duesberg, G. S., Electrical Characteristics of Molybdenum Disulfide Flakes Produced by Liquid Exfoliation. *Advanced Materials* 2011.

3.* Coleman, J. N.; Lotya, M.; O'Neill, A.; Bergin, S. D.; King, P. J.; Khan, U.; Young, K.; Gaucher, A.; De, S.; Smith, R. J.; Shvets, I. V.; Arora, S. K.; Stanton, G.; Kim, H.-Y.; Lee, K.; Kim, G. T.; Duesberg, G. S.; Hallam, T.; Boland, J. J.; Wang, J. J.; Donegan, J. F.; Grunlan, J. C.; Moriarty, G.; Shmeliov, A.; Nicholls, R. J.; Perkins, J. M.; Grievson, E. M.; Theuwissen, K.; McComb, D. W.; Nellist, P. D.; Nicolosi, V., Two-Dimensional Nanosheets Produced by Liquid Exfoliation of Layered Materials. *Science* 2011, 331 (6017), 568-571.

4. De, S.; Boland, C. S.; King, P. J.; Sorel, S.; Lotya, M.; Patel, U.; Xiao, Z. L.; Coleman, J. N., Transparent conducting films from NbSe₃ nanowires. *Nanotechnology* 2011, 22 (28), 285202.

5. Smith, R. J.; Lotya, M.; Coleman, J. N., The importance of repulsive potential barriers for the dispersion of graphene using surfactants. *New Journal of Physics* 2010, 12.

6. De, S.; King, P. J.; Lotya, M.; O'Neill, A.; Doherty, E. M.; Hernandez, Y.; Duesberg, G. S.; Coleman, J. N., Flexible, Transparent, Conducting Films of Randomly Stacked

Graphene from Surfactant-Stabilized, Oxide-Free Graphene Dispersions. *SMALL* 2010, 6 (3), 458-464.

7. Khan, U.; O'Neill, A.; Lotya, M.; De, S.; Coleman, J. N., High-Concentration Solvent Exfoliation of Graphene. *SMALL* 2010, 6 (7), 864-871.

8.* Hernandez, Y.; Lotya, M.; Rickard, D.; Bergin, S. D.; Coleman, J. N., Measurement of Multicomponent Solubility Parameters for Graphene Facilitates Solvent Discovery. *Langmuir* 2010, 26, (5) 3208-3213.

9.* Lotya, M.; King, P. J.; Khan, U.; De, S.; Coleman, J. N., High-Concentration, Surfactant-Stabilized Graphene Dispersions. *Acs Nano* 2010, 4 (6), 3155-3162.

10. King, P. J.; Khan, U.; Lotya, M.; De, S.; Coleman, J. N., Improvement of Transparent Conducting Nanotube Films by Addition of Small Quantities of Graphene. *Acs Nano* 2010, 4 (7), 4238-4246.

11.* Lotya, M.; Hernandez, Y.; King, P. J.; Smith, R. J.; Nicolosi, V.; Karlsson, L. S.; Blighe, F. M.; De, S.; Wang, Z.; McGovern, I. T.; Duesberg, G. S.; Coleman, J. N., Liquid Phase Production of Graphene by Exfoliation of Graphite in Surfactant/Water Solutions. *Journal of the American Chemical Society* 2009, 131 (10), 3611-3620.

12. Proctor, J. E.; Gregoryanz, E.; Novoselov, K. S.; Lotya, M.; Coleman, J. N.; Halsall, M. P., High-pressure Raman spectroscopy of graphene. *Physical Review B* 2009, 80 (7).

13. Wang, J.; Hernandez, Y.; Lotya, M.; Coleman, J. N.; Blau, W. J., Broadband Nonlinear Optical Response of Graphene Dispersions. *Advanced Materials* 2009, 21 (23), 2430-2435.

14. Bergin, S. D.; Nicolosi, V.; Cathcart, H.; Lotya, M.; Rickard, D.; Sun, Z. Y.; Blau, W. J.; Coleman, J. N., Large populations of individual nanotubes in surfactant-based dispersions without the need for ultracentrifugation. *Journal of Physical Chemistry C* 2008, 112 (4), 972-977.

15. Hernandez, Y.; Nicolosi, V.; Lotya, M.; Blighe, F. M.; Sun, Z.; De, S.; McGovern, I. T.; Holland, B.; Byrne, M.; Gun'Ko, Y. K.; Boland, J. J.; Niraj, P.; Duesberg, G.; Krishnamurthy, S.; Goodhue, R.; Hutchison, J.; Scardaci, V.; Ferrari, A. C.; Coleman, J. N., High-yield production of graphene by liquid-phase exfoliation of graphite. *Nature Nanotechnology* 2008, 3 (9), 563-568.

If you thought that science was certain - well, that is just an error on your part

(Richard P. Feynman)

Fatigue is not an option

(Pavel Tsatsouline)

Ask not what your country can do for you, ask what you can do for yourself

(M.L.)

ACKNOWLEDGMENTS

First and foremost I must thank Prof. Johnny Coleman for his valued efforts in supervising this work. Put simply, this work would not have been possible without his enduring support, inspiration and guidance. I also thank IRCSET and their Embark Initiative for providing the financial support to conduct this research.

Through the last four years I have been fortunate to work with a fantastic collection of people. To begin I'd like to thank Dr. Valeria Nicolosi who was there on my first day with the Coleman group as a final year undergrad student, she introduced me to the wonderful world of carbon nanomaterials and ignited my interest in the field. I also thank her for her valuable help over the last few years with all things TEM-related and especially for arranging a highly enjoyable TEM training trip over in Oxford last year. The journey of this research was taken with the group CoCo+Bu family stationed in 22 Westland Row over the years. I salute the former members Shane, Yenny, Helen, Denise, Niall, Brian, "Rickard", Paula and Fiona. Hats off to the current team Umar, Sukante, Phil, Karen, Marguerite, Evelyn, Arlene, Paul, Pete, Ronan, Sophie, Tom and Graeme. I especially thank Yenny, Paul, Arlene and Ronan with whom I've worked closely over the past few years in the study of these layered nano-things. Also, best of luck to the "newbies" Conor and Sebastian. Thanks to the MI folks Eddie, Trevor and Anna; Anna deserving a special mention for keeping the labs and us crazy experimentalists safe

and sound. And of course General Lee, thank you for the regular daleenews updates, gossip and techno support! To all of these colleagues and friends I say a big thank you for the great times and adventures we have shared. I've had the greatest pleasure working with you all and I look forward to celebrating many viva nights and PhD graduations with you in the future!

The folks down at the CMA deserve a mention for their help in acquiring the wealth of TEM images shown here, with thanks to Neal, Heath and Amanda. Thanks also to Markus and Cathal at the CRANN AML for HR-TEM and SEM support and training. I also thank the administrative and technical staff in the School of Physics - Robbie, Marie, Ciara and Samantha who look after the department coffers; the handy-men down in the workshop; Safety Joe and Gillian; IT gurus Ken and Alan; Jeanette, Una and Rebecca; and of course the ever provocative and playful John Kelly and accomplice Gemmer. I also thank the various academic staff in the Schools of Physics and Chemistry from whom I've learned a great deal in years gone by and with whom I've worked over the course of this PhD. Special thanks are due to Arlene, Paul, Pete, Ronan, Graeme and Niall for your help proof-reading this thesis.

I also want to thank two special friends, Gary and Sasha, for some really fun times and for your support over many many years. Finally I wish to express deepest thanks to my family, parents Juzer and Nafisa and sister Alifya. Without your love, encouragement, support (and cups of tea!) this work could not have happened.

Enjoy!

CONTENTS

1	MOTIVATION AND THESIS OUTLINE	1
2	MATERIALS AND BACKGROUND	5
2.1	Introduction	5
2.2	Carbon Nanomaterials and Carbon Nanotubes	5
2.2.1	Structure and Properties of Carbon Nanotubes	7
2.2.2	Synthesis and Applications of Carbon Nanotubes	7
2.3	Graphene	9
2.3.1	Properties and Applications of Graphene	10
2.3.2	Graphene Production Methods and Challenges	11
2.4	Inorganic Layered Compounds	15
2.4.1	Transition Metal Dichalcogenides - MoS ₂ , WS ₂	15
2.4.2	Thermoelectric Materials	18
2.5	Background - Liquid Phase Exfoliation of Carbon Nanomaterials	21
2.5.1	Carbon Nanotube and Graphene Exfoliation in Solvents	21
2.5.2	Carbon Nanotube Exfoliation using Surfactants	26
3	THEORY	29
3.1	Introduction	29
3.2	Solubility Theory	29
3.2.1	Solution Thermodynamics and Surface Energetics	30
3.2.2	Solubility Parameters	31
3.3	Surfactant Stabilisation Theory	33
3.3.1	Charged Colloidal Particles & Zeta Potential	35
3.3.2	DLVO Theory	36
4	CHARACTERISATION AND METHODS	41
4.1	Introduction	41

4.2	Optical Spectroscopy	41
4.2.1	Beer-Lambert Law & UV-vis Spectroscopy	43
4.2.2	Infrared Spectroscopy	45
4.2.3	Raman Spectroscopy	47
4.3	Ultrasonication	51
4.4	Centrifugation and Sedimentation	52
4.5	Zeta Potential	53
4.6	Atomic Force Microscopy	55
4.7	Transmission Electron Microscopy	57
4.8	Scanning Electron Microscopy	61
5	MULTICOMPONENT SOLUBILITY PARAMETERS FOR GRAPHENE	65
5.1	Introduction	65
5.2	Experimental Procedure	65
5.3	Results and Discussion	67
5.3.1	Graphene Dispersibility and Stability	67
5.3.2	Degree of Exfoliation in Various Solvents - TEM Analysis	70
5.3.3	Surface Tension as a Graphene Solubility Parameter	73
5.3.4	Graphene Dispersibility Through Hansen Solubility Parameters	75
5.3.5	Estimating the Hansen Solubility Parameters of Graphene	78
5.4	Conclusions	82
6	GRAPHENE PRODUCTION IN AQUEOUS SURFACTANT SOLUTIONS	85
6.1	Introduction	85
6.2	Experimental Procedure	86
6.3	Results and Discussion	88
6.3.1	Dispersion Preparation and Optimisation	88
6.3.2	Evidence of Exfoliation	91
6.3.3	Dispersion Stability	96
6.3.4	Stabilisation Mechanism	99
6.3.5	Graphene Films - Characterisation	102
6.3.6	Deposition on Surfaces - AFM Characterisation	110

6.4	Conclusions	113
7	HIGH-CONCENTRATION SURFACTANT STABILISED GRAPHENE DISPERSIONS	115
7.1	Introduction	115
7.2	Experimental Procedure	115
7.3	Results and Discussion	117
7.3.1	Production of High-Concentration Graphene Dispersions	117
7.3.2	Exfoliation Quality - TEM Analysis	125
7.3.3	Graphene Quality - Raman Analysis	130
7.3.4	Film Formation	135
7.4	Conclusions	137
8	LIQUID-PHASE EXFOLIATION OF INORGANIC LAYERED COMPOUNDS	139
8.1	Introduction	139
8.2	Experimental Procedure	140
8.3	Results and Discussion: MoS ₂ and WS ₂	142
8.3.1	Dispersion Preparation and Optical Characterisation	142
8.3.2	Exfoliation Quality - TEM Analysis	145
8.3.3	MoS ₂ Deposition on Surfaces - AFM, SEM and Raman	149
8.3.4	TMD Films and Hybrid Materials	152
8.4	Results and Discussion: Bi ₂ Te ₃ and Related Compounds	157
8.5	Conclusions	168
9	CONCLUSIONS AND FUTURE WORK	171
9.1	Conclusions	171
9.2	Future Work	174
9.2.1	Investigation of the mechanics/kinetics of ultrasound-assisted liquid-phase exfoliation of 2D materials	174
9.2.2	Investigation of the improvement of thermoelectric devices using liquid-exfoliated 2D nanomaterials	175
10	APPENDIX	179
10.1	Graphene dispersibility in solvents	179

10.2 High Concentration Graphene/SC Dispersions - TEM Statistics 183

10.3 Inorganic Layered Compounds - MoS₂ AFM Data 185

BIBLIOGRAPHY 187

LIST OF FIGURES

Figure 2.1	Illustrations of some allotropes of carbon	6
Figure 2.2	Sample molecular structure and electronic characters for common layered transition metal dichalcogenides	16
Figure 2.3	Illustration of the crystal structure of Bi_2Te_3	20
Figure 2.4	Optical characterisation of dispersions of graphite exfoliated by mild sonication in amide solvents	23
Figure 2.5	TEM images of graphene flakes produced by exfoliation in <i>N</i> -methyl-2-pyrrolidone	23
Figure 2.6	Molecular sketches of common surfactants used in the dispersion of carbon nanotubes	27
Figure 3.1	Sketch of a typical surfactant micelle and illustration of zeta potential	34
Figure 3.2	Sketch of atom-sheet and sheet-sheet van der Waals interaction	37
Figure 4.1	Optical phenomena as light propagates through a medium.	43
Figure 4.2	Representation of the Beer-Lambert law.	43
Figure 4.3	Schematic of ATR-FTIR measurement	46
Figure 4.4	Diagram of spectroscopic transitions underlying vibrational and Raman spectroscopy	48
Figure 4.5	Typical Raman spectra of graphite and graphene	49
Figure 4.6	Capillary cell used for zeta potential measurements	54
Figure 4.7	Atomic force microscope layout and tip-sample force curve	55
Figure 4.8	Optical system schematics of common transmission electron microscopes	58
Figure 4.9	Illustration of methodology used to assess graphene flake size from bright-field TEM images	62

Figure 4.10	Schematic of lens system in Zeiss Ultra Plus scanning electron microscope	63
Figure 5.1	SEM micrograph of starting graphite material	66
Figure 5.2	Sedimentation data for graphene in selected solvents	69
Figure 5.3	Selected monolayer and multi-layer graphene flakes from six solvents	71
Figure 5.4	Histograms for numbers of layers per flake from TEM analysis of six solvents	72
Figure 5.5	Graphene dispersibility, C_g , for all solvents tested as a function of solvent surface tension and surface energy.	74
Figure 5.6	Graphene dispersibility, C_g , for all solvents tested as a function of Hildebrand solubility parameter.	75
Figure 5.7	Graphene dispersibility as a function of solvent Hansen solubility parameters	77
Figure 5.8	Graphene dispersibility as a function of the Flory-Huggins parameter, χ	81
Figure 6.1	Photos of aqueous graphitic dispersions and optical absorbance spectra	89
Figure 6.2	Absorbance per unit length as a function of aqueous graphitic dispersion concentration	90
Figure 6.3	Selected TEM images of flakes produced by surfactant-assisted processing of graphite	92
Figure 6.4	Close-up TEM images of graphene flake edges showing visible layered structure	92
Figure 6.5	Histogram of number of layers per flake for a standard dispersion from surfactant-assisted processing of graphite	93
Figure 6.6	High-resolution TEM images of surfactant exfoliated graphene flakes	94
Figure 6.7	Sedimentation curve for a standard graphene/SDBS dispersion .	96
Figure 6.8	Zeta potential spectra for a freshly prepared graphene dispersion, aged graphene dispersion and surfactant solution	97

Figure 6.9	Plot of total interaction potential energy per unit area as a function of separation for two charged parallel sheets	101
Figure 6.10	SEM and optical images of a typical graphene film made by vacuum filtration	102
Figure 6.11	Raman spectra for a graphene film (~ 300 nm thick) deposited on an alumina membrane	104
Figure 6.12	ATR-FTIR spectra of graphene films	105
Figure 6.13	XPS spectrum for a thin graphene film produced by vacuum filtration and dried under vacuum	106
Figure 6.14	AFM images of spray deposited graphene	109
Figure 6.15	Statistics derived from AFM analysis of 182 graphene flakes	111
Figure 7.1	Absorbance per unit cell length as a function of sodium cholate concentration	118
Figure 7.2	Photos of surfactant stabilised dispersions	119
Figure 7.3	Differentiated TGA curves for graphene films made using a range of centrifugation rates	120
Figure 7.4	Extinction coefficient as a function of centrifugation rate for graphene/SC dispersions	120
Figure 7.5	Dispersed graphene concentration as a function of centrifugation rate	123
Figure 7.6	Dispersed graphene concentration as a function of sonication time	123
Figure 7.7	Sedimentation behaviour for a typical high concentration graphene dispersion	124
Figure 7.8	Selected TEM images from high concentration aqueous graphene/SC dispersions	126
Figure 7.9	Flake size data derived from TEM analysis as a function of centrifugation rate and sonication time	129
Figure 7.10	Raman spectra for thin films made with high concentration graphene dispersions	131
Figure 7.11	Mean Raman D:G band intensity ratios as a function of sonication time and centrifugation rate	132

Figure 7.12	Mean Raman D:G band intensity ratio as a function of mean graphene flake length	133
Figure 7.13	Free-standing graphene films from aqueous graphene/SC dispersions	136
Figure 8.1	Images of starting material and typical MoS ₂ and WS ₂ liquid phase dispersions	143
Figure 8.2	Optical absorption spectra for MoS ₂ and WS ₂ dispersions	144
Figure 8.3	Sedimentation behaviour for typical MoS ₂ and WS ₂ dispersions	145
Figure 8.4	TEM and STEM images of MoS ₂ and WS ₂ from exfoliation in NMP	146
Figure 8.5	Statistical TEM analysis of flake size for MoS ₂ and WS ₂	148
Figure 8.6	AFM, SEM and scanning Raman analysis of a fixed area of MoS ₂ flakes deposited on silicon	150
Figure 8.7	Images of MoS ₂ and WS ₂ nanosheet films and hybrid materials	153
Figure 8.8	Comparison of battery capacity for MoS ₂ and MoS ₂ /SWNT cathode materials	155
Figure 8.9	Extended battery capacity and efficiency testing of MoS ₂ /SWNT cathode material	155
Figure 8.10	Optical absorption spectra for Bi ₂ Te ₃ , Bi ₂ Se ₃ and Sb ₂ Se ₃ dispersed in CHP	158
Figure 8.11	Sedimentation behaviour of Bi ₂ Te ₃ , Bi ₂ Se ₃ and Sb ₂ Se ₃ dispersions in CHP	158
Figure 8.12	Final Bi ₂ Te ₃ dispersion concentration as a function of initial concentration and sonication time	159
Figure 8.13	TEM and STEM images of material found in Bi ₂ Te ₃ and Bi ₂ Se ₃ dispersions prepared in CHP	161
Figure 8.14	SEM images of Bi ₂ Te ₃ , Bi ₂ Se ₃ and Sb ₂ Se ₃ flakes and thin films	162
Figure 8.15	SEM/EDX analysis of Bi ₂ Te ₃ film deposited on a PVDF membrane	163
Figure 8.16	Raman spectra for a film of Bi ₂ Te ₃ flakes deposited on an alumina membrane	164
Figure 8.17	AFM/SEM analysis of Bi ₂ Te ₃ flakes deposited on silicon by spray casting	167

Figure 10.1	Graphene dispersibility, C_g , as a function of the sum of polar and hydrogen bonding HSPs	182
Figure 10.2	Histograms of TEM data as a function of centrifuge rotation rate.	183
Figure 10.3	Histograms of TEM data as a function of sonication time	184
Figure 10.4	Flake height from AFM analysis vs Raman peak position for solvent exfoliated MoS ₂	185

LIST OF TABLES

Table 2.1	Relative merits of graphene production techniques	24
Table 5.1	Graphene concentration after centrifugation (dispersibility, C_g) in 40 solvents	68
Table 5.2	Layer number statistics from TEM analysis of six solvents	73
Table 8.1	EDX elemental analysis for exfoliated Bi ₂ Te ₃ deposited on a PVDF membrane	164
Table 10.1	Graphene dispersibilities, Hansen solubility parameters and Hildebrand parameters for all 40 solvents studied	179

MOTIVATION AND THESIS OUTLINE

Throughout history humankind has sought to understand and manipulate the materials that make up the world around us. Stone and a succession of metals were the defining materials of ancient times. Today, in the era of technology, we now exploit a myriad of materials. In particular, a wealth of knowledge has been gained through the study of materials at the nano scale. Nanotechnology plays a crucial role in our modern world and encompasses many scientific fields including physics, chemistry, engineering and biology. Indeed, what can be classed as a new field of nanotechnology was opened with the discovery of fullerenes [1] and carbon nanotubes [2]. A great deal of research interest and investment over the last two decades has focused on the production and characterisation of carbon nanotubes due to their superlative properties and potential for use in novel applications [3–5]. The isolation of graphene in 2004 revealed yet another low dimensional carbon nanomaterial with unique properties [6, 7]. Since then, 2D graphene has become one of the major “hot topics” in nanoscience, culminating with the awarding of the Nobel Prize in Physics 2010 to Andre Geim and Konstantin Novoselov [8].

However, the primary challenge in studying and exploiting graphene, as for carbon nanotubes, has centred on production. For realistic applications, a facile, low-cost, non-destructive and scalable production method is required. To this end, our research group examined liquid-phase processing strategies that built on previous experience with carbon nanotubes [9]. It was shown that organic solvents such as *N*-methylpyrrolidone successfully produced high quality graphene using simple processing techniques, without the need for aggressive and detrimental chemical treatments [10]. This breakthrough in liquid-phase graphene production motivated the work presented in this thesis.

To begin, my work aims to characterise the interaction of graphene with a broad range of solvents through the use of solubility parameters. It is envisaged that determining the solubility parameters of graphene itself will promote future advances in dispersion preparation and composite formation. Following this, a method is shown to exfoliate graphite to yield surfactant-stabilised graphene suspended in water, with the aim of assessing the quality of the nanomaterials produced and understanding the stabilisation mechanism. This work is then extended to explore higher concentration graphene dispersions prepared in aqueous media using improved processing conditions. In addition to graphene, many other layered compounds exist offering a diverse range of physical and chemical properties. The large-scale liquid-phase exfoliation of other layered materials has the potential to provide a valuable source of two-dimensional crystals for use in a wide range of applications from electronics to energy storage and energy conversion. This prospect motivated my study of liquid-phase dispersions of other layered compounds for the final part of this thesis. Dispersions of two transition metal dichalcogenides and a class of materials with novel thermoelectric properties are examined. It is hoped that the body of work presented in thesis will facilitate the development of advanced functional materials based on two-dimensional nanostructures with enhanced properties and performance.

THESIS OUTLINE

Chapter 2: Materials and Background

An overview of carbon nanomaterials is given, including a brief discussion of carbon nanotubes. History, properties and potential applications of graphene are reviewed. Various graphene production methods that have been developed over recent years are outlined, with due attention to alternative liquid-phase processing methods. General properties of transition metal dichalcogenides are reviewed, along with a summary of literature studies on molybdenum disulphide and tungsten disulphide. A class of

layered compounds that includes bismuth telluride are discussed. Finally, a review of past work into carbon nanotube exfoliation and dispersion is given.

Chapter 3: Theory

Theory relating to graphene exfoliation in solvent and aqueous-surfactant systems is discussed. Solution thermodynamics is considered along with solubility parameters. Hansen solubility parameters are defined and related to solute-solvent interactions. Surfactant stabilisation theory is discussed and the concept behind zeta potentials outlined. A DLVO model to be applied to graphene/surfactant systems is developed.

Chapter 4: Characterisation and Methods

The main characterisation methods and experimental techniques used in this thesis are discussed.

Chapter 5: Multicomponent Solubility Parameters for Graphene

Graphene dispersibility in 40 solvents is tested and exfoliation quality in a set of solvents characterised. Solvent surface tensions and solubility parameters are related to graphene dispersibility. Hansen solubility parameters for graphene are determined.

Chapter 6: Graphene Production in Aqueous Surfactant Solutions

Graphene dispersions are prepared in aqueous/surfactant media. Dispersions are optically characterised and their stability assessed. Flakes extracted from dispersions are analysed by TEM to demonstrate exfoliation. A DLVO model is applied to explain the stabilisation mechanism. Films of graphene deposited from the dispersions are shown and analysed by Raman spectroscopy, FTIR spectroscopy and XPS. Individual graphene flakes are deposited for AFM analysis.

Chapter 7: High-Concentration Surfactant Stabilised Graphene Dispersions

High-concentration graphene dispersions are demonstrated in water using prolonged bath ultrasonication. Key dispersion parameters including sonication time and centrifugation rate are assessed. Thick graphene-based films are shown, characterised and used to accurately determine extinction coefficients for the dispersions. Exfoliation quality is assessed by TEM and Raman spectroscopy and data from the two analyses correlated.

Chapter 8: Liquid-phase Exfoliation of Inorganic Layered Compounds

Dispersions of MoS_2 and WS_2 are shown in solvent-based systems and characterised optically. Exfoliation quality is assessed by TEM. MoS_2 flakes are deposited on substrates and characterised by Raman spectroscopy, AFM and SEM. Hybrid MoS_2/CNT films are demonstrated as proof of concept and tested for use in lithium ion batteries. Dispersions and films of Bi_2Te_3 , Bi_2Se_3 and Sb_2Se_3 are prepared. Bi_2Te_3 flakes are characterised by TEM, AFM, SEM/EDX and Raman spectroscopy.

MATERIALS AND BACKGROUND

2.1 INTRODUCTION

This chapter will discuss the core materials used in this work. The structure, synthesis and properties of the materials will be discussed, along with existing and potential future applications. Current production techniques will be outlined with due attention to the advantages and drawbacks of the various methods. The first section will deal with carbon nanomaterials and carbon nanotubes (CNTs). Following this will be a discussion of graphene. The next section will discuss inorganic layered compounds, with emphasis on the specific transition metal dichalcogenides examined in this thesis. In addition, a selection of layered compounds with useful thermoelectric properties will be discussed. Finally, there will be a review of past work into the liquid phase exfoliation of carbon nanomaterials that has formed a basis for this work. Due to the wide range of materials covered in this chapter, an all-inclusive review of literature cannot be given. My discussion will focus on key points of interest that are pertinent to the work presented in this thesis.

2.2 CARBON NANOMATERIALS AND CARBON NANOTUBES

Carbon is a special element; it is pivotal to all life on Earth. Carbon is one of the most versatile elements in the periodic table. Having a valency of four it has the ability to attain a stable electronic configuration by covalently binding to other carbon atoms or to a wide range of other elements, forming a myriad of compounds. Carbon is commonly found in its two naturally occurring polymorphs of diamond and graphite [11]. In diamond, a network of tetragonally arranged sp^3 hybridised σ bonds forms a rigid

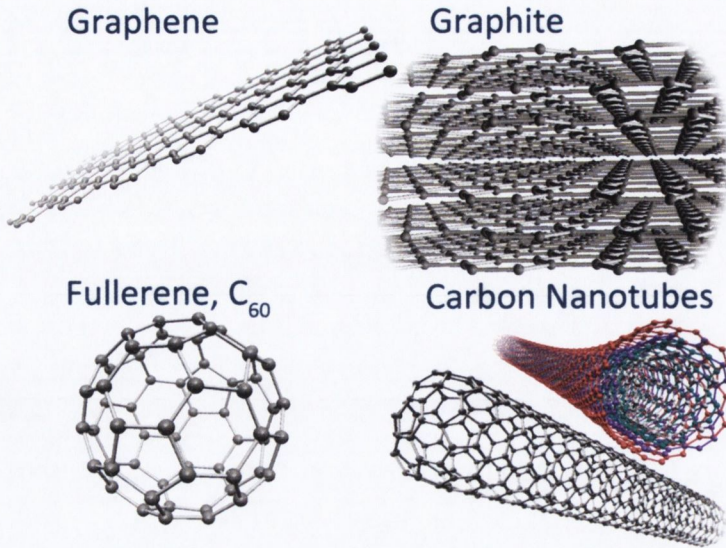


Figure 2.1: Illustrations of some allotropes of carbon

three dimensional network yielding one of the strongest materials known. Graphite is composed of strata of sp^2 hybridised carbon atoms bound in a trigonal planar atomic arrangement giving a hexagonal lattice; the individual planes are graphene layers. The graphene planes stack on top of each other, held together by weak van der Waals forces acting on the delocalised π orbital system.

In 1985 a new allotrope of carbon was discovered in the form of the C_{60} molecule (fullerene, buckyball) by Harry Kroto and co-workers [1]. The C_{60} molecule was found to be composed of carbon atoms in the shape of a geodesic spheroid made up of hexagons and pentagons; the atoms are hybridized in a mixed character of sp^2 and sp^3 molecular orbitals [11]. This discovery paved the way for a research drive into carbon nanomaterials that led to the discovery of “Helical microtubules of graphitic carbon” by Sumio Iijima and co-workers in 1991 [2]. These structures would later come to be known as CNTs. Fullerenes and CNTs can be visualised as rolled-up sheets of graphene; the various related allotropes of carbon are shown in Figure 2.1. Until relatively recently graphene, the final 2D allotrope of carbon, was not thought to exist freely and was treated as a purely academic platform for condensed matter physics [12]. In 2004, Andre Geim and co-workers reported the first identification of graphene layers isolated from bulk graphite [6]. This stimulated a great deal of research interest

that ultimately led to the work presented in this thesis. CNTs will now be discussed in further detail.

2.2.1 *Structure and Properties of Carbon Nanotubes*

CNTs can be visualized as rolled-up sheets of graphene, or linear elongations of the C_{60} molecule, capped at each end by a pentagonal network of carbon atoms. There are two distinct types of CNTs, single walled carbon nanotubes (SWNTs) and multi-walled carbon nanotubes (MWNTs). SWNTs are formed from a single rolled-up graphene sheet with diameter upwards of 0.4 nm and lengths up to several centimetres. MWNTs are formed of concentric graphene cylinders, with separation between layers of around 0.35 nm [2].

Research interest in CNTs has been motivated by their unique physical and electrical properties. Charge carriers can move without scattering in a pristine CNT due to the effective 1D geometry, resulting in ballistic transport with minimal resistive heating and the support of very large current densities (up to 100 MA/cm² has been reported [13]). Also of note is that CNTs can have different electronic characteristics depending on the way the graphene basal plane is rolled to form the tube. The process of rolling disrupts the symmetry of planar graphene, confining electrons around the circumference of the tube leading to metallic, semi-metallic or semiconducting character. In addition, CNTs can be extremely strong withstanding tensile strain of up to 12% with ultimate tensile strength up to 60 GPa and Young's modulus up to 1 TPa (this makes them approx two orders of magnitude stronger than steel) [14]. Also of note are the low densities of CNTs with values around 1.3 g/cm³ [5]. The combination of all these properties makes CNTs ideal for a range of applications.

2.2.2 *Synthesis and Applications of Carbon Nanotubes*

Early CNT production techniques used modified Fullerene arc discharge reactors [2, 5, 15]. Modern methods commonly use either laser ablation or chemical vapour

deposition (CVD) [5]. In the case of CVD, the thermal decomposition of carbon monoxide is widely used. However, all production methods result in a mixture of CNT electronic types, diameters and lengths with contaminants of residual metal catalyst (typically iron nano-particles) and amorphous carbon. The HiPco process can yield SWNTs of narrow diameter distribution that can, to a limited extent, be purged of metal catalyst and residual amorphous carbon [16]. A typical batch of SWNTs will contain a mixture of tube types, with a ratio of 2 : 1 metallic to semiconducting being common in the case of SWNTs [17].

CNTs have been in use since long before their relatively recent discovery. Around 400 years ago swordsmiths in Damascus were inadvertently reinforcing their curved sabre blades with MWNTs; these were formed during thermal cycling and forging of a unique blend of specific woods and iron ores [18]. In a more modern application, CNTs are found in commercially available tips for scanning probe microscopy [19]; the narrow radius of a SWNT enables high spatial resolution. They have been proposed for uses in field emission displays, hydrogen storage media, transparent conductive films, sensors and microelectronic interconnects [3]. They can also be found in conductive plastics for electronic packaging and automotive fuel delivery systems [20]. This latter application illustrates one of the main focal points for CNT usage, as a reinforcing and/or conductive filler in a composite matrix.

One of the primary challenges in using CNTs for these applications is dispersion. Van der Waals forces between individual CNTs promote bundling and entanglement in as-produced tubes. CNT bundles lose the superlative properties of isolated tubes. For instance, in effective polymer reinforcement applications, stress must be uniformly transferred to the CNT with polymer molecules coating individual CNTs. The presence of CNT bundles will hinder performance as CNTs slip over each other under stress or create stress concentration centres [5]. In energy storage applications, bundles will have reduced accessible surface area thereby reducing capacity. Liquid-phase processing has enabled efficient debundling of CNTs as a route to realising these applications. CNT dispersions have been prepared in a range of systems using aqueous surfactant [21–27], polymeric dispersion aids [28–33], biological aids (including DNA and protein) [34, 35] and direct dispersion/exfoliation in organic solvents [36–40].

SWNTs are used to a limited extent in the work of this thesis as a reinforcing and electrically conductive component in hybrid systems - inorganic layered compounds will serve as the primary material of the hybrids. However, the liquid-phase processing of CNTs in solvent and aqueous surfactant systems provides a foundation which is built upon and extended to layered materials in this thesis. This will be discussed further in Section 2.5 on page 21.

2.3 GRAPHENE

Definition - GRAPHENE [41]

noun - *a form of carbon consisting of planar sheets which are one atom thick, with the atoms arranged in a honeycomb-shaped lattice*

The term graphene was first coined in the 1980s to describe the electronically decoupled layers within graphite intercalation compounds [42, 43]. Work on splitting apart graphite can be traced back to the 1840s with an exfoliation process using sulphuric and nitric acids developed by the German chemist Schafhaeutl [43, 44]. Since then, many forms of graphite oxidation and intercalation have been explored [45]; all either using covalent attachment of carbon-oxygen functional groups or the insertion of small ions such as alkali metals to widen the natural graphitic inter-layer spacing. All of these graphitic products are chemically distinct from the starting material. The ideal sp^2 hybridised hexagonal network of carbon atoms is disrupted by these chemical functionalities as functional groups are attached to local sp^3 hybridised sites. This process alters the physical and chemical properties of the original graphite. Thinning of *pristine* graphite was shown in 1999 when islands of highly oriented pyrolytic graphite (HOPG) were thinned down a thickness of a few hundred graphene layers by mechanical dragging using the probe of an atomic force microscope [46]. The idea of mechanical exfoliation of graphite was extended using adhesive tape to repeatedly peel slices of HOPG. This “Scotch-tape” method ultimately led to the isolation and observation of monolayer graphene by Geim and co-workers [6]. This work sparked a

great deal of scientific interest that has made graphene one of the most exciting and fast-moving research topics in nanoscience of late.

2.3.1 *Properties and Applications of Graphene*

Since its popularisation in 2004, graphene has demonstrated a range of interesting physical properties. These include an ambipolar electric field effect where room temperature electron or hole concentrations can be tuned by changing the sign and amplitude of an applied gate bias [7]. More importantly, mobilities up to $200,000 \text{ cm}^2 \text{ V}^{-1} \text{ s}^{-1}$ have been demonstrated [47]. In a defect-free sample of graphene the charge carriers can maintain high mobilities at high carrier concentrations ($>10^{12} \text{ cm}^{-2}$), giving ballistic transport over length scales of a few hundred nanometres [7]. In principle such electrical properties could lead to ultra-fast integrated circuits, with single-device speeds up to 100 GHz already demonstrated [48].

Graphene's high electrical conductivity has fuelled interest in using it as a transparent conductor film capable of replacing indium tin oxide (ITO) in devices such as flat panel displays and touch screens. ITO is a brittle material whose cost is rising rapidly as global supplies of indium dwindle. Suggested minimum industry requirements for such films are visible light transmittance $T > 90\%$ and sheet resistance $R_s < 100 \Omega/\square$; where $R_s = (\sigma_{DC}t)^{-1}$, given by DC conductivity σ_{DC} and thickness t [49]. Graphene films could feature in photovoltaic devices and organic light emitting diodes, as transparent conductor windows, charge transport channels or catalytic surfaces [50]. It is noteworthy that graphene features a visible light absorption of 2.3% per monolayer [51–53]. Indeed, viewing graphene on top of silicon bearing a 300 nm thick oxide coating gives a constructive interference that yields enhanced contrast of around 12% and enables optical identification of monolayer graphene [51]. This presents a challenge for deploying graphene in transparent conductor applications as devices built using only a few graphene layers will exhibit significant light attenuation.

Another key property of graphene is its mechanical strength. Nano-indentation measurements on suspended graphene showed a Young's modulus of 1 TPa with an

intrinsic strength of 130 GPa; this made graphene the strongest material measured to date [54]. Such mechanical robustness, comparable to that of CNTs, opens the prospect of using graphene as a reinforcing filler in composite matrices. Graphene also has a very high specific surface area, with a theoretical maximum of $2630 \text{ m}^2/\text{g}$ for non-overlapping sheets [55]. Applications requiring high surface area coupled to high electrical conductivity include electrochemical supercapacitors and lithium ion batteries. In addition, the high specific surface area of graphene makes it an ideal candidate for thin film gas sensors.

2.3.2 *Graphene Production Methods and Challenges*

The key problem with graphene, as was the case in the early days of CNT research, centres on mass-production. Micromechanical cleavage of graphite can yield a range of monolayer graphene flake sizes ranging up to millimetre length scales. However, micromechanical cleavage of graphite is a labour-intensive, slow and very inefficient process with an extremely low yield. The monolayer, bi-layer or few-layer graphene sheets make up a small fraction of the total ensemble of particles, the bulk of the material produced is ordinary graphite. This makes searching for the desired material very difficult, even with sufficient image contrast under an optical microscope. Furthermore, micromechanical cleavage cannot be scaled up for any realistic applications. What is needed is a new approach to producing graphene.

This thesis considers one of the potential routes to bulk production of graphene, but it is worth noting the various other methods that have been reported. Several groups have tried epitaxial growth of graphene by annealing silicon carbide surfaces, but in general the results are a non-uniform array of graphitic domains [56–58]. The major drawback of the technique, as with micromechanical cleavage, is that monolayer graphene makes up a tiny fraction of the material on the surface. Also, it is noteworthy that epitaxial graphene growth requires rigid processing conditions, with atomically clean highly polished growth surfaces and ultra-high vacuum required [59]. In addition, the processing requires the use of high substrate temperatures typically of the order of

1300 °C, along with subsequent high temperature annealing to improve graphitisation [59, 60]. These intense processing conditions mean a limited range of substrates can be used. For example, flexible substrates based on plastics or polymers are incompatible with direct epitaxial growth due to their relatively low melting temperatures.

Recent work with bottom-up production of graphene using CVD has yielded more promising results. By using a flow gas mixture of methane, hydrogen and argon at 1000 °C over a thin (300 nm) layer of nickel on a SiO₂/Si substrate, Kim et. al. produced a coating of mostly mono and bi-layer graphene [61]. They were able to transfer their graphene films to a variety of substrates using commonly used poly-dimethyl siloxane (PDMS) stamping methods - this transfer procedure overcomes the substrate limitations inherent in epitaxial graphene growth. The best patches of their films showed sheet resistances as low as 280 Ω/□ at 80% optical transparency. Reina et. al. produced similar results using slightly different growth conditions [62]. Iijima's group built on these results, reporting R_s values as low as 30 Ω/□ at 90% transparency for a four layer graphene film transferred to polyethylene terephthalate (PET) [63]; this compares favourably to indium tin oxide (ITO) used in devices [49]. CVD growth approaches to graphene production will undoubtedly suit some electronic applications and will likely be used for creating graphene layers to integrate into existing lithographic manufacturing processes.

However, the total mass of graphene that can be produced by both epitaxial and CVD methods is severely limited as the processable substrate size dictates the graphene yield. In addition, thermally grown films of graphene are simply not suited to a wide variety of applications such as spray-cast anti-static coatings, device components from free-standing graphene films or composite materials. An alternative bottom-up route to graphene has been suggested through the chemical assembly of polycyclic aromatic hydrocarbons [60, 64]. This method has been shown to produce tiny graphene-like nanoribbons up to around 12 nm in length [64]. Beyond this size the flakes collapse from suspension and the chemical reactions needed to fuse the precursors cannot take place. Given the small length scales of these objects it remains to be seen if they exhibit the electronic properties of large-area graphene. Thus, it may be more appropriate to

classify the product as carbon macromolecules. If the method can be improved to yield large-area defect-free graphene then it may in the future become a viable technique.

Liquid phase-exfoliation of graphene from graphite can potentially produce large quantities of graphene and open routes to applications that bottom-up growth techniques cannot provide. A liquid-phase dispersion of graphene is not easily made. For a liquid-phase dispersion to be successful, the graphene must be exfoliated from a parent graphite stack and then stabilised against its natural tendency to re-aggregate.

Early work into producing small graphite particles used graphite intercalation compounds [65], resulting in small graphite fragments and needle-like structures. Similar methods involving acid treatment, combined with thermal shock, also yielded small and disordered graphite as opposed to graphene [66]. The majority of research into the production of graphene using liquid-phases has revolved around some form of chemical modification of graphite, usually involving aggressive oxidation to form graphite oxide. The oxidation of graphite is not new, according to literature graphite oxide was first prepared using aggressive oxidisers and highly concentrated acids in 1859 [67], following on from earlier work on producing expanded graphite using acids [44]. In 1957 W. Hummers and R. Offeman developed a somewhat safer method using potassium permanganate, sodium nitrate and sulphuric acid [68]. This process converts hydrophobic graphite to hydrophilic graphite oxide that easily forms a colloidal dispersion* in water. This is due to the attachment of hydroxyl (-OH), carboxyl (-COOH) and epoxy (C-O-C) groups to the graphite [69–71]. Improvements to the Hummers method in 2006 led to the production of aqueous dispersions of mono-layer and few-layer graphene oxide (GO) [72, 73]. Some groups have tried using graphite intercalation compounds as pre-cursors to the oxidation process [74] – the presence of molecules lodged between graphene layers in the starting graphite assists the exfoliation and oxidation process. The GO from these types of dispersions was deposited on substrates [75, 76] and analysed with techniques such as atomic force microscopy (AFM), Fourier transform infrared (FTIR) spectroscopy and X-ray photoelectron spectroscopy (XPS).

* A colloid is a homogeneous non-crystalline substance consisting of large molecules or ultramicroscopic particles of one substance uniformly dispersed through a second substance [41].

The data indicated a good level of exfoliation but, critically, highlighted that the each GO flake was covered in an extensive array of functional groups.

Subsequent work by a number of groups tried to convert GO back to graphene by aggressive reduction, to give reduced graphene oxide (r-GO). This is commonly done using chemicals such as hydrazine [77] and by using high temperature annealing conditions, often in excess of 800 °C [76]. Many papers have reported limited success in removing the chemical functional groups from the graphene basal plane, thus giving a partial restoration of expected graphene properties [74, 77–86].

All these reported results share one common problem. The process of chemically oxidising the graphene, to date, has not been completely reversible. The functional groups attached to the graphene basal plane severely disrupt the electronic structure of graphene. Each functionalised carbon site represents an sp^3 hybridised carbon atom as opposed to the sp^2 hybridised form that would normally contribute an electron to the delocalised π system of pristine graphene. The presence of these functionalised sites in graphene turn an excellent electrical conductor into an insulator or semiconductor [79, 87]. The various aggressive chemical reduction and thermal annealing processes reported in the literature (often up to 1000 °C in inert atmosphere) remove some of the functional groups but not all of them. XPS shows that even after these harsh treatments there is still a substantial population of oxygen functionalities [74, 76, 79, 80, 82, 85, 88–90] – these are often carboxyl and epoxide species that are extremely difficult to remove once formed. FTIR spectra, where reported [74, 80, 81, 85], also show peaks characteristic of persistent carbon-oxygen functional groups. Whilst the presence of residual functional groups in r-GO may be advantageous for some polymer reinforcement applications [88], the persisting structural and electronic damage to the graphene flakes degrades the quality of the end product and limits the potential of this technique. In addition, the processing conditions can pose hazards as the prolonged use of concentrated acids is required as well as combustible gases such as hydrazine for GO reduction. The high temperature annealing steps needed to partially remove residual functional groups and defects also limits the usefulness of this method.

From the above survey it is clear that non-covalent liquid-phase exfoliation methods for graphene need to be developed and understood. Such methods are explored in

this thesis. Sonication-induced exfoliation of graphene from graphite in solvent and aqueous surfactant systems will be discussed in Chapters 5, 6 and 7.

2.4 INORGANIC LAYERED COMPOUNDS

Graphite is the most well-known layered material, but other layered systems in the form of transition metal dichalcogenides (TMDs), transition metal oxides (TMOs) and compounds such as hexagonal boron nitride (BN) are also very important. These classes of layered materials offer a diverse range of chemical, electrical and physical characteristics. Obtaining these materials in a 2D structure yields high specific surface areas, potentially making these materials useful in catalysis, sensing, energy storage and energy conversion applications. However, as has been the case with graphene, the development and exploitation of these 2D materials has been hampered by the lack of a simple and scalable production process to yield mono or few-layer flakes. The work shown in this thesis characterises the liquid phase exfoliation of TMDs, with particular attention given to molybdenum disulphide (MoS_2) and tungsten disulphide (WS_2). In addition, a set of layered materials (Bi_2Te_3 , Bi_2Se_3 and Sb_2Se_3) with interesting thermoelectric properties will be examined.

2.4.1 *Transition Metal Dichalcogenides - MoS_2 , WS_2*

The TMDs form a well-defined structural family, with all members having the general molecular formula MX_2 , where M is a transition metal and X is a chalcogen. They occur in around 60 different types [91]. MoS_2 is the most common of the TMDs and is found as a naturally occurring molybdenite ore; the other TMDs are usually chemically synthesised [91]. Depending on the metal and chalcogen combination the TMDs span a wide spectrum of electrical characteristics, from insulating (e.g. HfS_2) to semiconducting (e.g. MoS_2 , WS_2) to semi-metallic (e.g. WTe_2 , TeS_2), metallic (e.g. NbSe_2 , TaS_2 , PtTe_2) and superconducting (e.g. TaS_2) [91, 92]. Within the TMDs, around two thirds are composed of a layered structure via the stacking of hexagonally packed

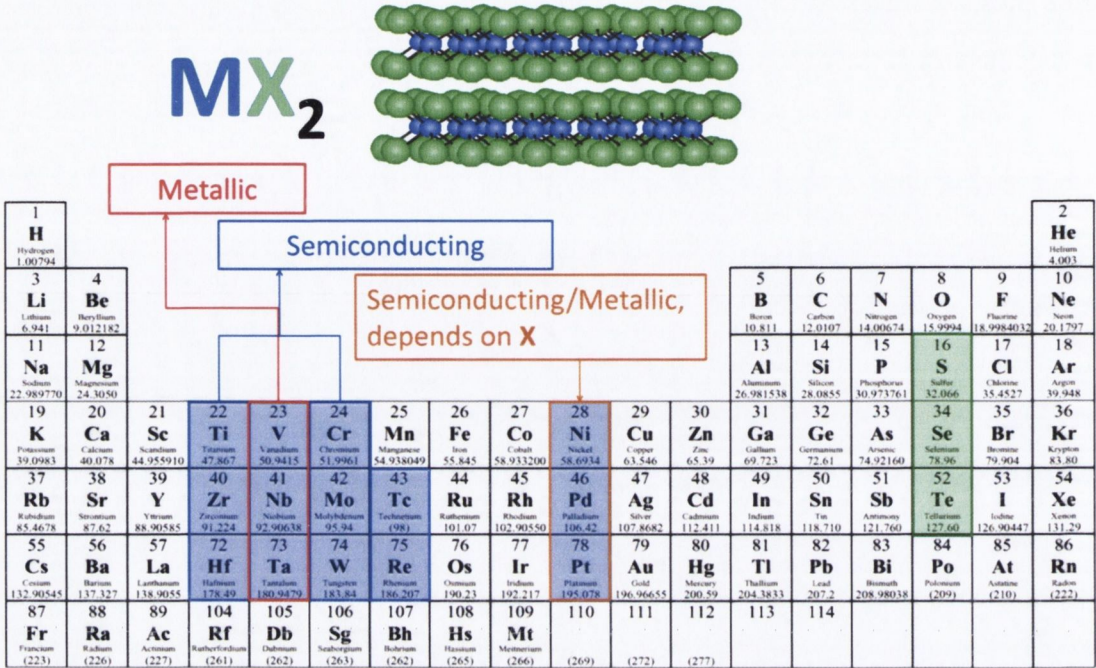


Figure 2.2: Sample molecular structure and electronic characters for common layered transition metal dichalcogenides. The electronic characteristics have been assigned by Wilson and Yoffe [91].

planes [91]; the metal atoms M are sandwiched between chalcogen atoms X giving a monolayer unit structure of X-M-X. The molecular planes in these crystals are weakly held together by van der Waals forces, with extreme anisotropy observed in mechanical and electrical properties [91]. Common configurations around the metal atoms are trigonal prismatic or octahedral. A sketch of the trigonal prismatic structure (found in naturally occurring MoS₂ and WS₂) and a periodic table with overlay of electronic character for common layered TMDs is shown in Figure 2.2.

The study of low-dimensional MoS₂ and WS₂ has largely focused on 0D and quasi-1D structures. In 1992 closed polyhedral and cylindrical tubes of WS₂ were synthesised by annealing WS₂ films deposited on quartz at 1000 °C [93], with similar processing yielding MoS₂ closed polyhedra [94]. These hollow closed structures are similar to carbon-based fullerenes, with literature referring to these species as inorganic fullerene-like (IF) nanoparticles [95]. IF-WS₂ and IF-MoS₂ were found to exhibit excellent tribological properties, with 0.5 mass % mixtures in oils enabling a twofold reduction

in wear and friction tests [96]. Since their discovery, the production of IF-MoS₂, IF-WS₂ and their nanotube variants [95, 97] has been scaled up sufficiently to enable use in commercial products, primarily as lubricant enhancers. Nanotubes of other TMDs including HfS₂, NbS₂, ZrS₂ and TaS₂ have also been synthesised [98].

Experimental studies of thin layered MoS₂ can be traced back to 1965. Frindt used adhesive tape to micromechanically cleave bulk MoS₂ and performed optical absorption measurements on the resulting thinned crystals [99]. Frindt reported crystals as thin as 3 nm. The method was similar to that used by Geim, Novoselov and co-workers to produce monolayer graphene and single layer 2D MoS₂ almost 40 years later [6, 100]. Such mechanically cleaved 2D MoS₂ has not yet found practical use in any applications with studies primarily focussed on the electrical characterisation of single flakes. Transistor measurements have been made on single-layer MoS₂ with current on-off ratios $I_{\text{on}}/I_{\text{off}}$ up to 10^8 and room temperature mobility up to $200 \text{ cm}^2\text{V}^{-1}\text{s}^{-1}$ [92, 101]; these values are comparable to modern silicon devices, though large scale processing remains a challenge.

Liquid-phase processing methods for layered MoS₂ and WS₂ have centred on chemical exfoliation in water [102, 103]. The first reported liquid exfoliation of layered MoS₂ was by Joensen, Frindt and Morisson in 1986 via a lithium ion intercalation method. The procedure involved immersion of bulk MoS₂ in n-butyllithium (n-BuLi - C₄H₉Li) in hexane for 48 hrs, under inert atmosphere, to give an intercalation compound of the form Li_x-MoS₂ [104] (typically $0.1 < x < 1$ [105]). This was followed by immersion in water to give a violent evolution of H₂ gas that forced the separation of the layers, leaving exfoliated MoS₂ suspended in water for up to a few days. However, the MoS₂ produced in this way was structurally different from the starting material. Raman spectra and X-ray diffraction (XRD) studies showed that the lithiation process had changed the atomic arrangement from the original trigonal prismatic structure (as shown in Figure 2.2), corresponding to 2H-MoS₂, to a distorted octahedral configuration (distorted 1T-MoS₂) [105–108]. The distorted 1T-MoS₂ dispersions and thin films displayed metallic behaviour, having lost the optical absorption features of the original material in the visible range [105–107]. Raman spectra of the exfoliated flakes were also consistent with an octahedral coordination [105, 107]. This phase was found to be

metastable, reverting back to 2H-MoS₂ after prolonged ageing over a period of months or after annealing deposited material [107, 109].

A similar n-BuLi exfoliation procedure was applied to WS₂, but again the exfoliated material had octahedral atomic coordination and a metallic band structure, as shown by XRD analysis and UV-vis absorption spectra respectively [109, 110]. This structural distortion due to lithiation was also observed in MoSe₂ [108]. It is clear there are problems with liquid-phase methods that rely on ion intercalation. The processing conditions are complex, requiring the use of highly reactive agents which are unstable under normal ambient conditions. The processing is carried out over a protracted period to yield a meta-stable exfoliated material with structural and electronic properties dramatically different from the parent crystal configuration. The liquid-phase processing to be discussed in this thesis (Chapter 8) will examine a simple liquid-phase exfoliation process that leads on to functional hybrid materials.

2.4.2 *Thermoelectric Materials*

In modern times the need for improved energy conversion, recovery and conservation has focused research interest. Thermoelectric materials function as solid-state heat engines, enabling a direct conversion between electrical and thermal energy using the electron gas as the working fluid [111]. They can be used to drive cooling or heating in devices without the need for moving parts. More importantly, they can be used to recover waste heat, potentially generating electricity from a range of currently inefficient energy systems such as automotive engines or power plants. Thus, thermoelectric materials can play a major role in addressing the global energy challenges of the future.

While solid-state energy conversion is appealing, thermoelectric materials are currently far too inefficient to be cost-effective for everyday applications. The effectiveness of thermoelectric materials is commonly gauged by a dimensionless figure of merit defined as

$$ZT = \frac{S^2 \sigma T}{\kappa} \quad (2.1)$$

where σ is electrical conductivity, T is absolute temperature, and κ is thermal conductivity [112–114]. S in this equation is the Seebeck coefficient, a measure of the electric current induced by a given temperature gradient. For viable devices, an average figure of merit > 1 within the operating temperature range of device is required [115, 116].

To improve ZT values, the power factor given by $S^2\sigma$ must be increased and the thermal conductivity κ decreased. These properties are intimately linked, creating a problem. The Seebeck coefficient is inversely related to the carrier concentration in the material, thus the effect of raising σ by conventional methods such as doping are negated by the fall-off in S [117]. Raising the carrier concentration also increases the contribution of electron/hole transport to the thermal conductivity, further reducing ZT . Thus, the use of alloys and nano-structured materials has been suggested as a means to decouple these parameters, enabling reduced thermal conductivity through enhanced phonon scattering at crystal interfaces whilst maintaining electrical pathways through the material [112, 117].

All current state-of-the-art thermoelectric materials have been made using some form of nano-structuring applied to a range of semiconducting materials such as Bi_2Te_3 , Bi_2Se_3 , Sb_2Se_3 , PbTe , SiGe and many other variants and alloys of these [112, 116, 118, 119]. Some examples from literature for making nano-structured thermoelectric materials include the use of planetary ball-milling and alloying [115, 120], electrodeposition of films and quasi 1D nanowires from solution [121–125], co-sputtering of elemental precursors [126, 127] and precipitation from solution-based reagents [128, 129]. All of these methods have their own advantages and disadvantages regarding scalability, reproducibility and production hazards.

These materials have a layered structure built from weakly bound planes, each plane composed of five hexagonally packed monatomic sheets along the crystal's c axis. The planes are referred to as quintuple layers (QLs). Taking Bi_2Te_3 as an example, QLs have the sequence $-\text{Te-Bi-Te-Bi-Te}-$. Each QL has thickness ~ 1 nm with the overall crystal structure of Bi_2Te_3 having a unit cell which is three QLs thick (~ 3 nm) [130, 131]. A schematic of this rhombohedral Bi_2Te_3 crystal structure is given in Figure 2.3. Small-scale micromechanical cleavage of Bi_2Te_3 and Bi_2Se_3 , analogous to that

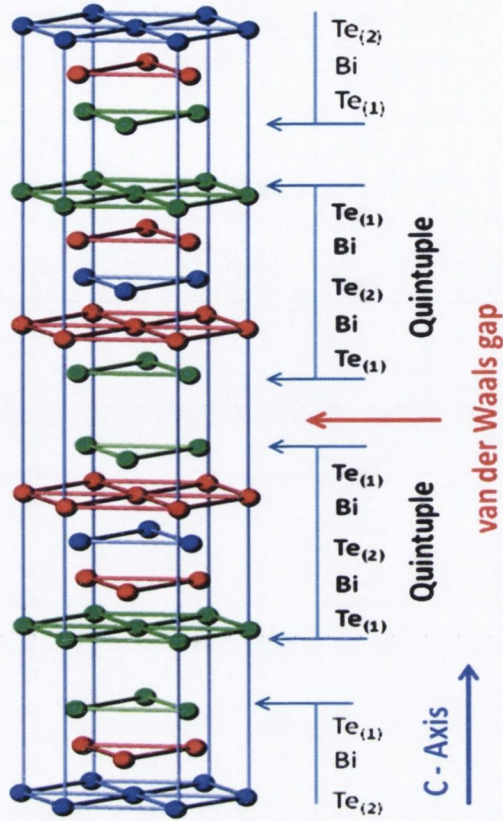


Figure 2.3: Illustration of the crystal structure of Bi_2Te_3 . Image from Teweldebrhan et al. [130]

used for graphene, has been shown [130, 132–135] as well as exfoliation using Li-ion intercalation procedures similar to those used for graphite and MoS_2 exfoliation [136].

Each different process produces thermoelectric materials of a particular composition and morphology with unique electronic and thermal properties. Liquid-phase processing of the type discussed in this thesis can complement these methods, potentially allowing facile exfoliation and dispersion of layered thermoelectric materials. The formation of such dispersions could allow homogeneous hybrid materials to be readily formed using simple mixing and deposition techniques. Thermoelectric materials such as Bi_2Te_3 and Bi_2Se_3 are also of interest due to their topological insulator behaviour [137]. Topological insulators are materials that exhibit an insulating bulk band gap whilst having metallic surface or edge states - the behaviour of these surface states is changed in exfoliated topological insulator material as the surface to volume ratio is increased [138, 139]. The properties of the surface states are useful

for fundamental research, and potentially in applications such as spintronics [139]. Liquid-phase exfoliated material could potentially contribute to this field.

2.5 BACKGROUND - LIQUID PHASE EXFOLIATION OF CARBON NANOMATERIALS

The work of this thesis focuses on the exfoliation of graphite and, by extension, layered inorganic materials in solvents and aqueous surfactant-based systems. The methodology used in this work builds on knowledge gained from previous studies of CNT liquid-phase dispersions. The procedures used in the historical work, and in this thesis, do not invoke the use of chemical modification or functionalisation but rather aim to use favourable solution energetics and electrostatic stabilisation to yield stable dispersions of pristine well exfoliated nanomaterials.

2.5.1 Carbon Nanotube and Graphene Exfoliation in Solvents

During early research into CNTs it was clear that dispersions of nanotubes in liquid phases would be useful. Given the agglomerated nature of as-produced CNTs, exfoliation using solvents potentially offered a route to separating nanotubes from one another. It was originally thought that dissolution in solvents would be impossible due to the rigid nature and size of CNTs and their agglomerates [9]. Thus, liquid-phase processing of CNTs was initially approached using colloidal stabilisation methods, as will be discussed in Section 2.5.2.

CNT debundling in amide solvents was eventually shown in 1999 with the deposition of individual SWNTs from *N,N*-dimethylformamide (DMF) dispersions [140]. Following this, SWNT dispersion was shown, assisted by mild ultrasonication, in other solvents such as *N*-methyl-2-pyrrolidone (NMP), *N,N*-dimethylacetamide (DMA) and cyclopentanone (CPO) [141–143]. It was shown that some of the SWNTs could be completely separated from one another [144]. Subsequent work showed that SWNTs could be exfoliated and stably dispersed in NMP, γ -butyrolactone (GBL) and cyclohexylpyrrolidone (CHP) using mild sonication, with mild centrifugation allowing the

removal of large aggregates [38, 39, 145, 146]. The dispersions were found to consist of up to 70% (by number) isolated SWNTs with the majority of the remaining material consisting of small bundles [38–40]. Further work explored the energetics involved in forming CNT dispersions and explored the use of solubility parameters to determine optimum solvents [146–149].

This work prompted the investigation of graphite exfoliation using amide solvents by our research group [10] and others [53]. It was shown that mild sonication of graphite in NMP, GBL, Dimethylacetamide (DMA) and 1,3-dimethyl-2-imidazolidinone (DMEU) yielded grey dispersions along with large numbers of visible macroscopic aggregates [10]. Mild centrifugation was sufficient to remove these aggregates. The dispersions showed linear scaling of optical absorbance with concentration (Beer-Lambert behaviour), this is illustrated in Figure 2.4 along with molecular sketches of the solvents used. Transmission electron microscopy (TEM) examination of the supernatant revealed the presence of monolayer graphene, as verified by electron diffraction studies and Raman spectroscopy. Images of typical graphene flakes produced by exfoliation in NMP are shown in Figure 2.5. Further systematic TEM analysis showed that the dispersions in NMP consisted of mainly few-layer graphenes (<5 layers) with a yield of up to 28% monolayer graphene by number fraction. In addition, Raman, FTIR and XPS spectroscopies showed that graphene produced in this manner is of high quality and is, crucially, free of the functional groups and structural defects that have hindered previous attempts to produce liquid-phase graphene dispersions. This initial solvent-based exfoliation work was continued as part of this thesis. In Chapter 5 a systematic study of solvent efficacy through Hansen solubility parameters will be given, with the aim of facilitating the future discovery of good graphene solvents or solvent blends.

In light of this discussion of solvent-mediated graphene exfoliation, it is instructive to compare the merits of this production technique with those discussed earlier in Subsection 2.3.2. Table 2.1 gives a summary of the merits of the various graphene production methods discussed so far.

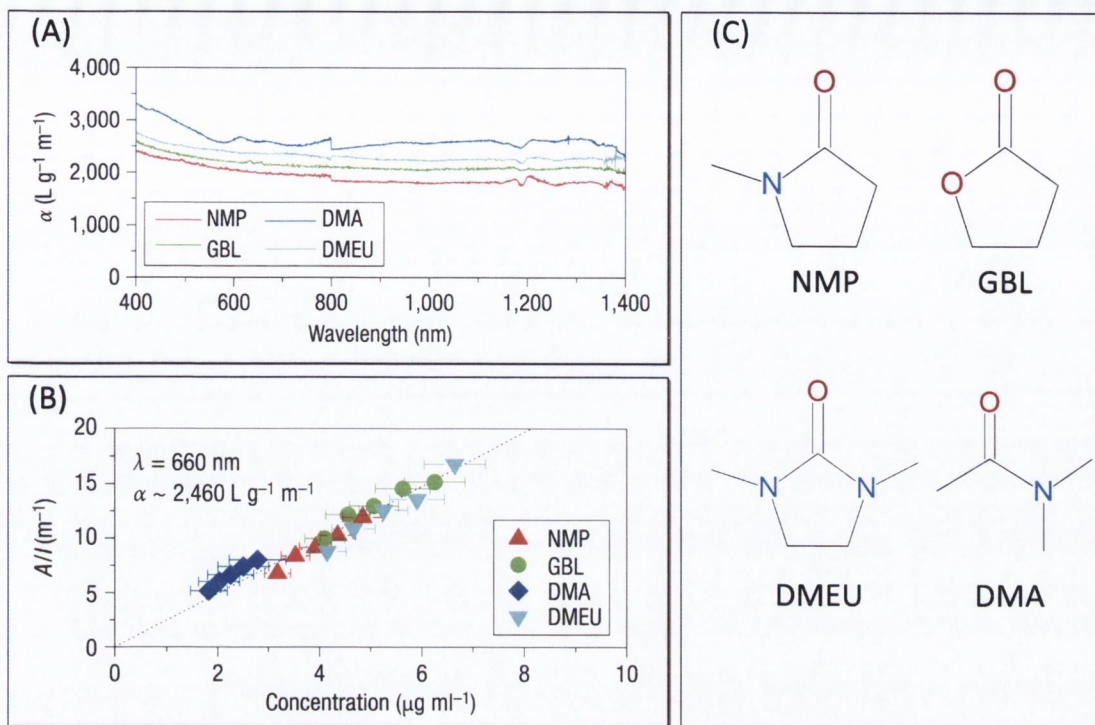


Figure 2.4: Optical characterisation of dispersions of graphite exfoliated by mild sonication in solvents. (A) UV-vis NIR absorption spectra of typical dispersions in *N*-methylpyrrolidone (NMP), γ -Butyrolactone (GBL), Dimethylacetamide (DMA) and 1,3-Dimethyl-2-imidazolidinone (DMEU) [10]. (B) Beer-Lambert behaviour of dispersions allowing measurement of extinction coefficient [10]. (C) Molecular sketches of the amide solvents used.

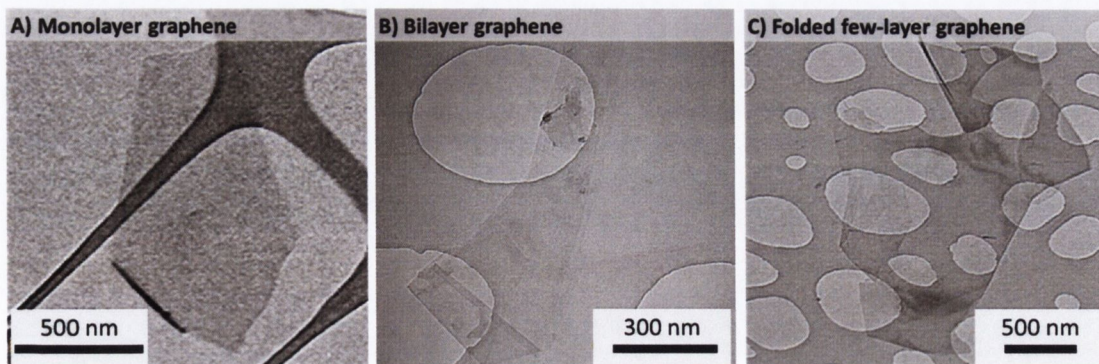


Figure 2.5: TEM images of graphene flakes produced by exfoliation in *N*-methyl-2-pyrrolidone. (A), (C) from Hernandez et al. [10], (B) from own image archive.

Table 2.1: Relative merits of graphene production techniques

	Advantages	Disadvantages
<i>Mechanical exfoliation</i>	<p>Low cost, no special equipment required</p> <p>High quality, no functional groups, defect-free basal plane</p> <p>Large area flakes (~ mm size [150])</p>	<p>Slow process, extremely low yield</p> <p>Not suitable for high volume production, limited to single-flake experiments</p>
<i>Epitaxial growth</i>	<p>Compatible with CMOS processing</p>	<p>Largely multi-layer graphitic domains formed</p> <p>Intensive surface preparation required, strong influence on graphene quality</p> <p>High temperature processing required, limited substrate choice</p> <p>Limited production volumes</p>
<i>CVD growth</i>	<p>Large area graphene coatings now possible</p> <p>Compatible with CMOS processing</p> <p>High quality graphene produced, high monolayer yield</p> <p>Product is transferable to other substrates</p>	<p>Limited scalability potential, dictated by furnace and growth substrate sizes</p> <p>Not suitable for formation of composites</p> <p>High temperature processing</p> <p>Transfer process damages graphene - cracks, increased electrical resistance [63]</p>

	Advantages	Disadvantages
	Graphene produced is candidate for use in thin film electronics applications	Requires the use of metal substrates, e.g. copper - cost issues if scale-up required
<i>Polycyclic aromatic hydrocarbon assembly</i>	Bottom-up process Uses liquid phase processing	Tiny flakes produced - limited usefulness Max graphene flake size limited by synthesis - solubility Complex chemical synthesis Questionable flake quality - further spectroscopic investigations required
<i>Graphite intercalation/Graphene Oxide</i>	Scalable liquid phase route High monolayer yield possible Water-processable graphene oxide intermediate High concentration dispersions possible (up to 4 mg/ml [45]) Useful for composite formation	Persistent chemical function groups - extremely difficult to fully remove Electronically altered product - due to residual defects Safety issues - Graphene oxide production requires use of concentrated acids Non-trivial reduction step required - uses dangerous reducing agents such as hydrazine and/or high temperature annealing

	Advantages	Disadvantages
<i>Direct liquid phase exfoliation in amide solvents</i>	<p>Fully scalable facile process - suited to bulk production</p> <p>Non-covalent processing, no chemical modification of graphene basal plane required - high quality product</p> <p>Useful for composite formation</p>	<p>Cost and hazards with use of amide solvents</p> <p>Largely few-layer graphene produced by default, though monolayer yield can be increased with additional processing</p> <p>Limited flake sizes - max lateral dimensions of a few μm</p> <p>Not suited to transparent conductor applications - high sheet resistances due to inter-flake junctions</p>

2.5.2 Carbon Nanotube Exfoliation using Surfactants

Dispersion of carbon nanomaterials in solvents has drawbacks including cost of solvents, high boiling points of good CNT solvents and incompatibility with biological systems. The use of an aqueous medium would be convenient, but carbon nanomaterials in a chemically unaltered state are highly hydrophobic and will not stably exfoliate in water.

Early work on CNT dispersion in aqueous media used colloidal stabilisation. The most common method uses amphiphilic surface active molecules where non-polar tail groups interact with the hydrophobic CNTs allowing the polar, hydrophilic, head groups to interact with the water solvent medium; in this way the surfactant acts as an interfacial stabiliser [151]. Early work in the late 1990s demonstrated the formation of stable dispersions of small bundles of CNTs via surfactant coating [140, 152–155]. Subsequent work revealed the fluorescence of surfactant-based CNT dispersions; such an

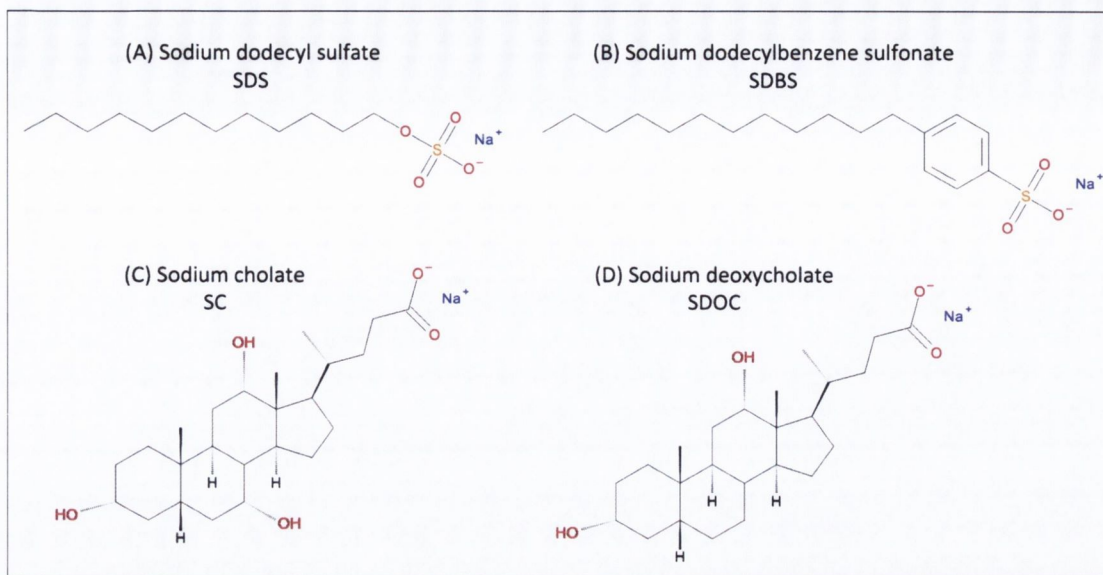


Figure 2.6: Molecular sketches of common surfactants used in the dispersion of carbon nanotubes.

effect can only be expected from the presence of well exfoliated CNTs with significant proportions of individual nanotubes in the dispersion [21, 22, 156]. Surfactant-assisted CNT exfoliation is well-documented [9, 157] with optimum dispersion parameters [27, 158] and surfactant efficiencies [159–161] having been studied. Molecular sketches of common surfactants used in CNT dispersion work are shown in Figure 2.6.

This body of research into CNT exfoliation served as stimulus for the work shown in Chapter 6 where graphite exfoliation in aqueous surfactant systems was attempted for the first time [162]. This work was then extended to scale-up the production process and produce much higher concentrations of graphene to feed into future applications [163], as discussed in Chapter 7.

THEORY

3.1 INTRODUCTION

This chapter discusses key theory relevant to this thesis. Specific aspects of solvent solution theory are used in Chapter 5 for studying the behaviour of graphene in a wide range of solvents. In Chapters 6 and 7 concepts from colloid theory are used in the characterisation of aqueous suspensions of graphene. Key background ideas, terminology and derivations for these chapters are covered.

3.2 SOLUBILITY THEORY

Solvent-based dispersion of graphene is the simplest method of liquid-phase processing. In general terms, the process involves direct interactions between two phases. From experience with CNT dispersions, it is clear that large molecular solutes cannot be stably dispersed in all solvents [9]. Forced dispersion of CNTs in unsuitable solvents using ultrasound forms unstable dispersions, resulting in rapid flocculation and precipitation. The energetics of the solute-solvent interactions are key to understanding CNT or graphene dispersibility in solvents. In the following subsection, the thermodynamics of the graphene-solvent interaction will be discussed in the context of surface energies. A more versatile treatment is given using energy components in the form of Hansen solubility parameters; these parameters are used in the solvent assessment work of this thesis and will also be discussed in this section.

3.2.1 Solution Thermodynamics and Surface Energetics

The mixing of two chemical compounds, be they simple small molecules or macromolecules, leads to changes in the entropy (S) and enthalpy (H) of the overall system. In general, solubility of a material in a given solvent is thermodynamically favourable if the free energy of mixing (ΔG_{mix}) is negative [164]. Under isothermal conditions this is given by

$$\Delta G_{mix} = \Delta H_{mix} - T\Delta S_{mix} \quad (3.1)$$

where ΔH_{mix} and ΔS_{mix} are the enthalpy and entropy of mixing respectively. ΔS_{mix} is the change in disorder of the system due to the mixing process and thus is always positive. From Equation 3.1 positive values of ΔS_{mix} are beneficial to the formation of solutions. However, in the case of large rigid molecules such as CNTs or graphene ΔS_{mix} is very small and so ΔH_{mix} is the dominant term [9, 165]. Stable exfoliation of graphite to graphene in solvents can only occur if the net energy cost, given by the enthalpy change ΔH_{mix} , is very small. The enthalpy of mixing for graphene has been derived in previous work by our group using surface energy* parameters for solute and solvent [10]. The derivation calculated the energy input required to separate all solvent molecules and all individual graphene flakes from one another, subtracting the energy regained by forming a graphene/solvent dispersion consisting of re-stacked flakes of a given thickness. This gave an approximate energy cost of exfoliation per unit volume of mixture V_{mix} as

$$\frac{\Delta H_{mix}}{V_{mix}} \approx \frac{2}{T_{flake}} (\partial_{graphene} - \partial_{solvent})^2 \phi \quad (3.2)$$

where T_{flake} is the graphene thickness, $\partial_i = \sqrt{E_{sur}^i}$ is the square root of the surface energy of phase i and $\phi = V_{graphene}/V_{mix}$ is the graphene volume fraction [9]. For the

* Surface energy arises from surface atoms or molecules of a material not interacting with the maximum number of nearest neighbours. The surface atoms or molecules are in a higher energy state than atoms at interior locations, giving a surface energy expressed in units of J/m² [166].

solvent phase, the surface energy $E_{sur}^{solvent}$ is linked to the measurable surface tension γ via

$$\gamma = E_{sur}^{solvent} - TS_{sur}^{solvent} \quad (3.3)$$

where $S_{sur}^{solvent}$ is the solvent surface entropy (which is a generic value close to $0.1 \text{ mJ m}^{-2} \text{ K}^{-1}$ for common CNT and graphene amide solvents) [9, 167]. The graphene surface energy is the energy required to peel two flakes apart and completely overcome the van der Waals binding force. The merit of Equation 3.2 is that it shows how the enthalpy of mixing is dictated by the difference between graphene and solvent surface energies (or equivalently surface tensions). Dispersions prepared with solvents having surface energy closest to that of graphene will have been formed with minimal energy cost; from a surface energy perspective these solvents are expected to perform the best.

3.2.2 Solubility Parameters

Solubility theory can be largely summed up by the phrase “like seeks like”. Solubility parameters allow for a quantitative assessment of solvents and are used to predict which solute-solvent systems are likely to behave favourably. They are commonly used in polymer physics. Solvent solubility parameters are derived from vaporisation energy, i.e. the energy required to break all the van der Waals bonds holding the liquid’s molecules together. Therefore, solubility parameters are related to the total cohesive energy of the solvent [165].

The Hildebrand solubility parameter is the most common solubility parameter and is defined as the square root of the solvent’s cohesive energy density

$$\delta_T = \sqrt{\frac{E_{C,T}}{V}} \quad (3.4)$$

where V is the solvent molar volume. Using this parameter, the Hildebrand-Scratchard expression can be derived for small molecular solutes, giving an approximation of the enthalpy of mixing as

$$\Delta\bar{H}_{mix} \approx \phi(1-\phi)(\delta_{T,a} - \delta_{T,b})^2 \quad (3.5)$$

where ϕ is the solute volume fraction, $\Delta\bar{H}_{mix}$ is the enthalpy of mixing per unit volume of mixture and $\delta_{T,a}$ and $\delta_{T,b}$ are the Hildebrand parameters of the a solute and b solvent species respectively [9, 146]. It should be noted that the form of this equation precludes negative values of $\Delta\bar{H}_{mix}$; this is due to geometric mean approximations made in the derivation [9, 146].

An alternative form of Equation 3.5 is the Flory-Huggins equation given as

$$\Delta\bar{H}_{mix} = \frac{\chi kT\phi(1-\phi)}{v_0} \quad (3.6)$$

where $\Delta\bar{H}_{mix}$ is again the enthalpy of mixing per unit volume of mixture, k is the Boltzmann constant, T is absolute temperature and v_0 is the solvent molecular volume [9, 146, 168]. The term χ in this equation is the Flory-Huggins parameter, a dimensionless term that measures the pairwise interaction energies between species in the mixture. If $\chi < 0$ then solute-solvent interactions dominate and a true solution is possible. If $\chi > 0$ solute molecules have a net attraction to each other resulting in a thermodynamically unfavourable system. Comparing Equations 3.5 and 3.6 gives the following approximation in terms of Hildebrand parameters:

$$\chi \approx \frac{v_0}{kT} (\delta_{T,a} - \delta_{T,b})^2 \quad (3.7)$$

Strictly speaking this form of the Flory-Huggins parameter is approximate as it does not allow negative values. This form of the equation works reasonably well for species with non-polar interactions, when only van der Waals forces act between species [168]. However, it still captures the key physical logic of solubility theory, i.e. dispersion is favoured with small values of χ when solute and solvent solubility parameters are matched.

Hansen Solubility Parameters

Charles Hansen recognised that the use of the Hildebrand solubility parameter in the form of Equation 3.4 is limited as it is based on the total vaporisation (cohesive) energy of a liquid. The interactions between solvent, or equally solvent and solute, molecules consist of several types. The strongest and most important of these for organic mo-

lecules are dispersion forces from atomic interactions (D), polar cohesive forces from permanent dipole-permanent dipole molecular interactions (P) and hydrogen bonding interactions from electron exchanges (H) [165]. Hansen suggested using these three components of the cohesive energy to form a new set of solubility parameters - the Hansen solubility parameters (HSPs) [165]. The basic rule governing these parameters involves splitting the cohesive energy density into D, P and H components as follows:

$$\frac{E_{C,T}}{V} = \frac{E_{C,D}}{V} + \frac{E_{C,P}}{V} + \frac{E_{C,H}}{V} \quad (3.8)$$

The HSPs are each defined as the square root of the above energy density components such that $\delta_i^2 = E_{C,i}/V$, ($i = D, P, H$) Hansen [165]. In this way, the Hildebrand solubility parameter can be defined using HSPs as

$$\delta_T^2 = \delta_D^2 + \delta_P^2 + \delta_H^2 \quad (3.9)$$

Using HSPs, Charles Hansen re-cast the Flory-Huggins parameter as

$$\chi \approx \frac{v_0}{kT} \left[(\delta_{D,a} - \delta_{D,b})^2 + (\delta_{P,a} - \delta_{P,b})^2 + (\delta_{H,a} - \delta_{H,b})^2 \right] \quad (3.10)$$

where the subscripts a and b represent the solute and solvent respectively. This functional form of the Flory-Huggins parameter enables solute-solvent interactions to be assessed using a set of well-documented HSPs and will be used in this thesis to study graphene exfoliated in a range of solvents.

3.3 SURFACTANT STABILISATION THEORY

In this thesis, aqueous surfactant-assisted dispersions of graphitic material are demonstrated. Such dispersions are described by colloidal theory. Surfactants are amphiphilic molecules, with a tendency to accumulate at interfaces between phases such that the polar part can immerse itself in the more polar phase (i.e. water) while the non-polar part can interact with the non-polar material (i.e. the dispersed phase).

Ionic surfactants, as used in this thesis, will dissociate in water to form a large molecular ion and a counterion. The surfactant molecules form solutions at low

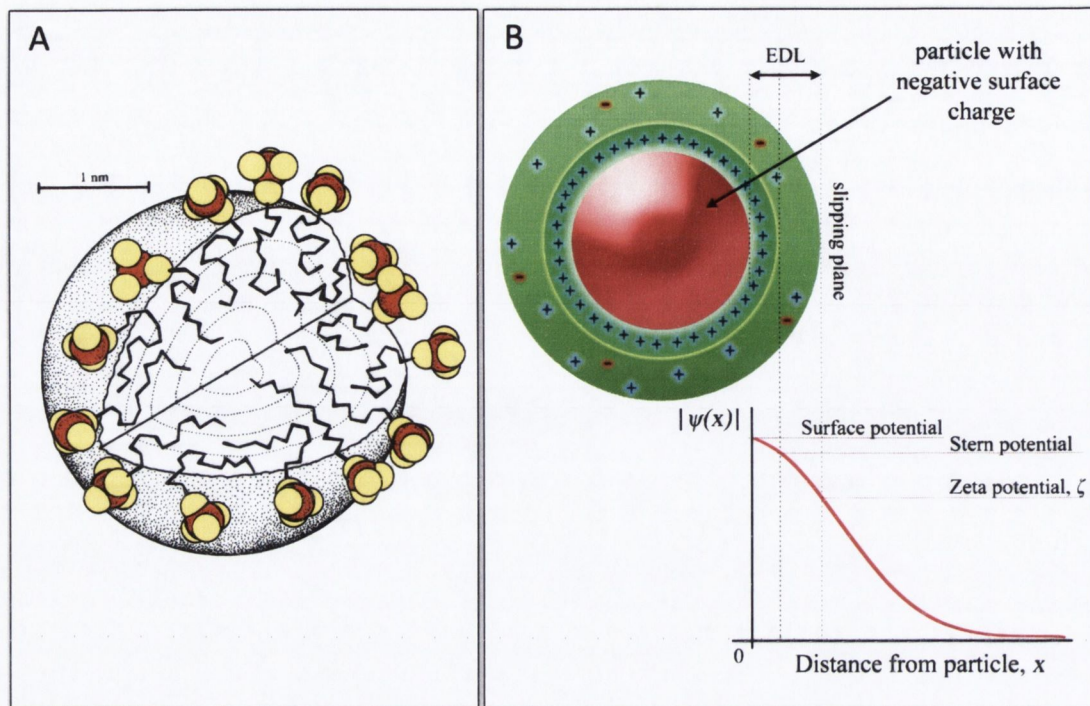


Figure 3.1: (A) Illustration of a sodium dodecyl sulfate micelle, counter-cations are not shown (adapted from Hunter [151]). (B) Electrostatic potential near a positively charged colloidal particle and the origin of zeta potential.

concentrations. Some molecules will accumulate at the air/solution interface or the container walls in order to find more stable conditions for the hydrophobic tail component [151]. With increasing surfactant concentration, the surfactant density at these interfaces increases until a monolayer of surfactant coats the surfaces [151]. A specific minimum concentration for each different ionic surfactant drives the interaction of surfactant molecules with themselves, bringing clustering of surfactant molecules into a micelle; this occurs at the critical micelle concentration (CMC). In a micelle the hydrophobic groups are directed towards the centre of the cluster to minimise contact with water, with the hydrophilic group directed towards the solvent. In this manner, the contact between hydrophobic groups and water is minimised thereby reducing the free energy of the system [169]. A sketch of a micelle is given in Figure 3.1A.

3.3.1 Charged Colloidal Particles & Zeta Potential

In the case of a surfactant-stabilised colloidal system, the adsorption of the molecular ions onto particles of the dispersed phase imparts a net charge. The interactions between the charged particles, and with the ionic solution surrounding them, govern key aspects of the system such as dispersion stability or flow behaviour.

The net charge of the colloid influences the distribution of ions in the surrounding dispersant medium, forming an ionic atmosphere around the particle. The region close to the particle has an increased concentration of counterions, this region is the electrical double layer (EDL) [170]. The EDL can be viewed as having two parts. The innermost region, known as the Stern Layer, consists of counterions that are tightly bound to the charged particle surface - the potential at the boundary of this region is the *Stern potential* [171, 172]. Adjacent to the Stern layer, the ions are more diffuse and less firmly attached. This outer region of the EDL which may also include water molecules, together with the Stern layer, is the major factor influencing the mobility of the charged particle [170]. The potential at a point a distance x away from the charged particle has the general form $\psi = \text{constant} \times e^{-\kappa x}$, where κ^{-1} is the Debye-Huckel parameter [151, 173]. κ^{-1} is also known as the Debye-length or Debye screening-length [151, 172]. It is sometimes referred to as the "thickness" of the EDL, this is technically incorrect as the full extent of the varying potential is closer to $4/\kappa$ (this gives $\psi_{x=4\kappa^{-1}} = 0.02\psi_{x=0}$) [151]. In the case of systems where the electrical energy is small compared with the thermal energy of the ions, ψ will be small with κ defined as

$$\kappa = \sqrt{\frac{e^2 \sum n_i z_i^2}{\epsilon_r \epsilon_0 k T}} \quad (3.11)$$

where e is electron charge, n_i is number of ions of type i per unit volume in the bulk of the solution, z_i is the charge of ions i , k is the Boltzmann constant, T is the absolute temperature, and $\epsilon_r \epsilon_0$ is the permittivity of the pure liquid (i.e. water) [151, 174]. From this equation it is clear that the size of the EDL depends only on temperature and the bulk electrolyte concentration.

The EDL plays a significant role in particle motion. When the charged particle moves (e.g. due to gravity, applied electric field, Brownian movement, convection) the ions

and water molecules within a specific boundary inside the EDL move with the particle while those species outside the boundary do not travel with the particle - this boundary is the *hydrodynamic shear plane* or *slipping plane* [170, 171, 175]. The electric potential at the slipping plane relative to the bulk solution is the *zeta potential*, ζ , and is used as measure of colloidal stability (typically stable dispersions are characterised by $|\zeta| > 25$ mV) [170, 171, 173]. Figure 3.1B illustrates the structure of the EDL and the origin of the zeta potential. The zeta potential can be measured by examining particle movement under an applied electric field; this electrophoresis method will be discussed further in Chapter 4, Section 4.5.

3.3.2 DLVO Theory

The balance between repulsive and attractive forces determines the overall stability of a colloidal system. The theory behind colloidal stability was named after DeJaguin, Landau, Verwey and Overbeek (DLVO) [173]. The zeta potential is a metric that deals exclusively with repulsive forces between charged colloidal particles. These forces are countered by attractive van der Waals interactions, primarily from dispersion forces. Van der Waals interactions are relatively short-range forces acting over length scales of up to 10 nm [151]. Unlike the EDL interaction, the van der Waals interaction potential is not influenced by changes in the electrolyte such as concentration or pH, thus it can be treated as invariant [173].

For this thesis, layered graphite is exfoliated in aqueous surfactant media. Therefore, it is appropriate to model interactions in the context of charged parallel two-dimensional sheets. Using the approach provided in DLVO theory, the overall potential energy (V_T) is given by the sum of the repulsive DLVO component (V_{DLVO}) and the attractive van der Waals energy (V_{vdW}) [173].

The van der Waals potential energy can be estimated using a pairwise additive summation over atoms in the sheets, similar to that used by Hamaker, based on the London interatomic potential [173, 174]. A circular 2D atomic sheet with radius R can be described as shown in Figure 3.2A. Consider a free atom interacting with atoms in

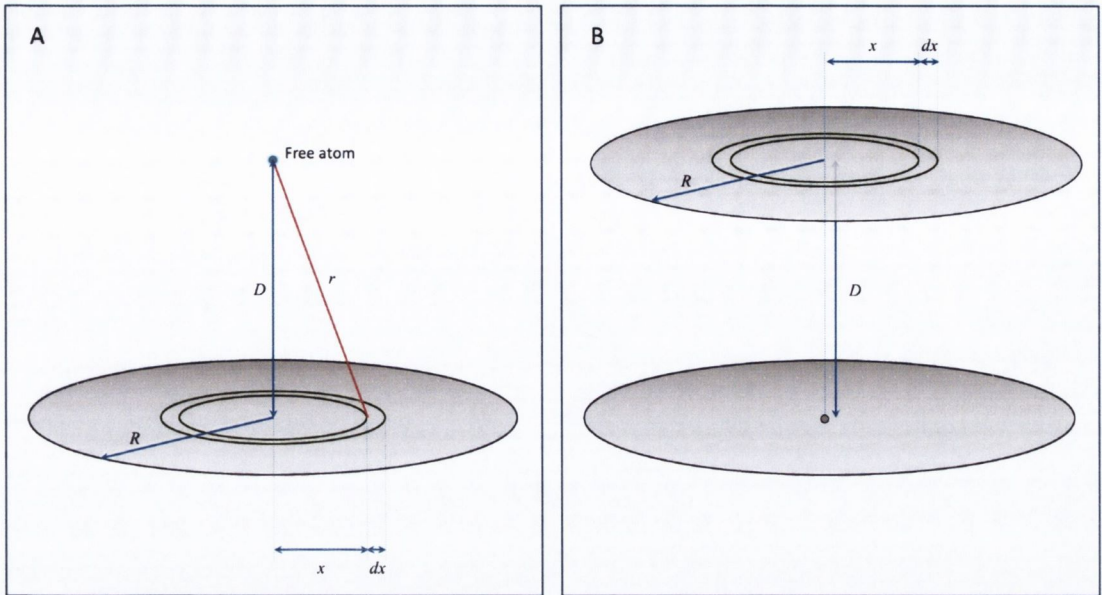


Figure 3.2: (A) Sketch of free atom interacting with planar sheet of atoms. (B) Sketch of interaction between two similar planar atomic sheets.

the sheet from a distance D , specifically looking at a ring of atoms in the sheet with radius x and width dx . The ring contains dN atoms such that

$$dN = 2\pi\rho x dx \quad (3.12)$$

where ρ is the atomic areal density of the sheet.

Van der Waals forces originate from quantum mechanical interactions between fluctuating dipole moments in atoms [172]. The van der Waals potential between two uncharged atoms can be approximated as a function of the inter-atomic separation r as

$$V(r) = -\frac{3}{4} \left(\frac{1}{4\pi\epsilon_0} \right)^2 \frac{\alpha^2}{r^6} E \quad (3.13)$$

where ϵ_0 is the permittivity of free space, α is the polarisability of the atom and E is an energy term that can be related to the first ionisation energy of the atom [172, 173, 176, 177]. Thus, the interaction energy between the free atom and any atom within the ring of the sheet is proportional to the inverse sixth power of distance [174] such that

$$V = -\frac{C}{r^6} = -\frac{C}{(x^2 + D^2)^3} \quad (3.14)$$

Combining Equations 3.12 and 3.14 gives the total van der Waals interaction energy between the free atom and all atoms in the ring:

$$dV_{atom-sheet} = -2\pi\rho C \frac{xdx}{(x^2 + D^2)^3} \quad (3.15)$$

This can be integrated over the extent of the sheet to give the total van der Waals interaction energy between free atom and sheet, $V_{atom-sheet}$, using an upper limit of ∞ rather than R due to the short range of the interaction [151]:

$$V_{atom-sheet} = -2\pi\rho C \int_0^{\infty} \frac{xdx}{(x^2 + D^2)^3} = -\frac{\pi\rho C}{2D^4} \quad (3.16)$$

This argument can be extended by replacing the free atom with a duplicate of the atomic sheet, as shown in Figure 3.2B. All atoms within the ring of the upper sheet interact with the lower sheet with an attractive potential energy of $V_{atom-sheet}$. The total interaction energy of all dN atoms in the ring of the upper sheet with the lower sheet, denoted dV_{vdW} , is given by the product of Equations 3.12 and 3.16 as

$$dV_{vdW} = -\frac{\pi^2\rho^2C}{D^4}xdx \quad (3.17)$$

The total van der Waals interaction, V_{vdW} , can then be found by integrating Equation 3.17 over the full size of the sheets, i.e. from $x = 0$ to $x = R$:

$$V_{vdW} = -\frac{\pi^2\rho^2C}{D^4} \int_0^R xdx = -\frac{\pi^2R^2\rho^2C}{2D^4} = \frac{A\pi\rho^2C}{2D^4} \quad (3.18)$$

where A is the area of the sheet.

V_{DLVO} is the repulsive potential energy between two charged planar surfaces in an electrolyte. This has been derived in literature by Israelachvili [173] to give

$$V_{DLVO} \approx 4A\varepsilon_r\varepsilon_0\kappa\zeta^2e^{-\kappa D} \quad (3.19)$$

where ε_r is the relative permittivity of the liquid, ζ is the zeta potential, κ the Debye length and A is the surface area. Strictly speaking Equation 3.19 is valid for low surface potentials below 25 mV [173], thus the equation should be treated as approximate any numerical data generated treated as rough values. This formulation also includes a multiplier of 2 to account for the presence of surface charges on both sides of

the interacting planes [173]. Thus, the overall potential of two idealised parallel 2D colloidal sheets can be written as

$$V_T \approx 4A\varepsilon_r\varepsilon_0\kappa\zeta^2e^{-\kappa D} - \frac{A\pi\rho^2C}{2D^4} \quad (3.20)$$

This theoretical model will be applied to assess the stability of colloidal graphene dispersions in Chapter 6.

CHARACTERISATION AND METHODS

4.1 INTRODUCTION

This chapter discusses the main characterisation methods and experimental techniques used in this thesis. In this work, liquid phase dispersions of layered materials were prepared using ultrasonication of bulk layered materials in specially selected solvent or surfactant/water media. The dispersions were then centrifuged to remove remnants of starting material and aggregates. Typical dispersions were initially characterised by absorption spectroscopy. This allowed derivation of sample concentration which can be used as a quality measure and as a comparative metric between samples. In addition, optical absorption was used to probe the temporal stability of the dispersions. The remaining characterisations were carried out on solid material deposited or extracted from the liquid dispersions. Infrared and Raman spectroscopies were used to probe the chemical nature and composition of the produced materials. Transmission electron microscopy was extensively used to examine lateral dimensions of exfoliated material and, where possible, flake thickness. Scanning electron microscopy was used to study macroscopic assemblies of flakes in the form of films and individual flakes deposited on silicon substrates. Scanning probe microscopy was also used to characterise the dimensions of flakes deposited on substrates. These various techniques will be now be discussed with reference to relevant literature as appropriate.

4.2 OPTICAL SPECTROSCOPY

Light interacts with matter in a multitude of ways leading to a wide range of useful effects for an experimentalist. Figure 4.1 gives a schematic of the fundamental processes

that occur as light propagates through a medium. A given medium can influence the speed of light propagating through it, with light travelling slower than in free space leading to the bending of light as governed by the laws of refraction. Scattering can also occur, whereby photons of light interact with the medium causing the photons to change direction. If the photon energy is unchanged, the process is elastic while if the photon exchanges energy with the medium inelastic scattering occurs. Absorption occurs when the frequency of the light matches an electronic transition of the material, only unabsorbed light will be transmitted. Light in the UV (200 - 400 nm), visible (400- 800 nm) and near-infrared (800 nm - 2500 nm) ranges of the electromagnetic spectrum can permit the excitation of valence electrons to excited states, and also promote vibrational and rotational transitions in molecules [178]. Thus, when probing individual molecules in the vapour phase, discrete absorption spectra with rotational and vibrational fine structure can be visible. In bulk materials, or materials dispersed in solvent phases, the atoms and molecules influence each other leading to the broadening of electronic energy levels, resulting in the loss of fine structure and the formation of continuous absorption bands. Luminescence can also occur when light interacts with matter; it is the general name given to the process of spontaneous emission of light by excited atoms in a solid state material and can accompany absorption. In some systems luminescence may be quenched as non-radiative relaxation processes can occur before radiative re-emission takes place. The optical processes mentioned so far concern the realm of linear optics, where the behaviour is independent of optical power. At high light intensity, as provided by powerful lasers, the non-linear dependence of the dielectric constant of the material on the incident electric field becomes evident . These non-linear effects are beyond the scope of this thesis but it is noted that graphene dispersions in solvents have displayed promising broadband non-linear optical limiting properties [179].

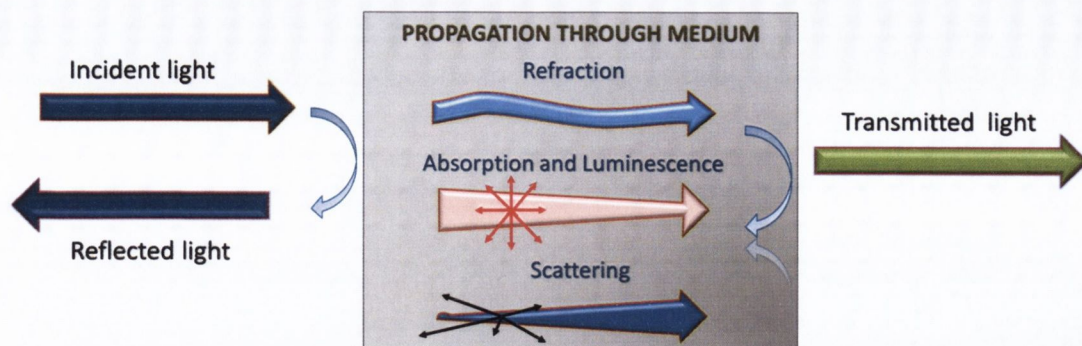


Figure 4.1: Optical phenomena as light propagates through a medium.

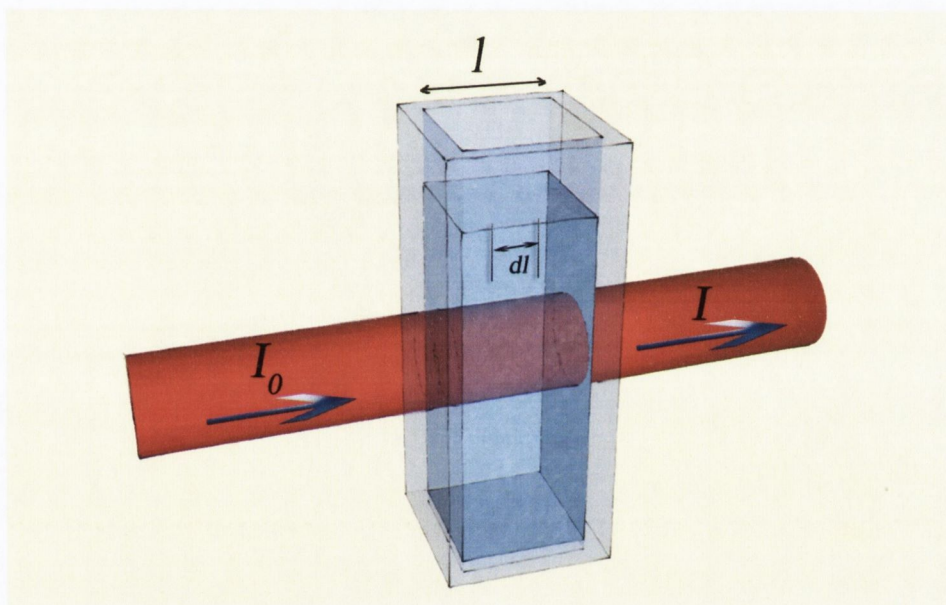


Figure 4.2: Representation of the Beer-Lambert law.

4.2.1 Beer-Lambert Law & UV-vis Spectroscopy

Light absorption by a sample can be easily quantified. A sketch illustrating the passage of light through a typical liquid sample is given in Figure 4.2. Consider a parallel beam of monochromatic light incident on a sample of total thickness l . Consider the passage of light through a portion of the sample with length dl . The intensity reduction dI is proportional to the light intensity I , sample concentration C and length. Thus one can write [170]

$$dI = -\beta ICdl \quad (4.1)$$

where β is a constant. This expression applies to each increment of the sample, so the emergent intensity can be found by integration over the full length of the sample, where the incident light intensity on the first face is I_0 :

$$\int_{I_0}^I \frac{dI}{I} = -\beta \int_0^l C dl \quad (4.2)$$

For a homogeneous system C is independent of position, this gives

$$\ln \left(\frac{I}{I_0} \right) = -\beta Cl \quad (4.3)$$

This can be re-written in terms of logarithmic base 10 by introducing a constant α such that $\beta = \alpha \ln 10$. This gives the Beer-Lambert law as follows:

$$\log_{10} \left(\frac{I}{I_0} \right) = -\alpha Cl$$

$$I = I_0 10^{-\alpha Cl} \quad (4.4)$$

α is the extinction coefficient (in units $L g^{-1} m^{-1}$, also known as the absorption coefficient). The transmittance T is defined by $T = I/I_0$ while the absorbance A is given by:

$$A = -\log_{10} T = -\log_{10} \frac{I}{I_0}$$

Thus, Equation 4.4 can be written as

$$A = \alpha Cl \quad (4.5)$$

which is the usual form of the Beer-Lambert law. For liquid samples, if the extinction coefficient is known then the sample concentration can be determined from the measured absorbance.

Equipment

UV-vis NIR absorption spectroscopy was used extensively in this research. For the majority of measurements a Varian Cary 6000i was used. This instrument is a dual-beam device, using broad-spectrum light sources of a tungsten halogen lamp (visible/NIR)

and a deuterium arc source (UV) [180]. A monochromator splits the light source into components using controllable slits and a movable diffraction grating. The resulting monochromatic beam is split in two with a half mirror. One of these beams passes through the sample while the other passes through a reference specimen. The reference consists of a matched cuvette filled with the same solvent as the sample or, in the case of solid samples, a matched substrate. The beams are collected and fed to an indium gallium-arsenide photodiode detector via a beam chopper that alternates in time which beam is collected. This gives values of I and I_0 , for sample and reference respectively, that are presented as values of absorbance A for each wavelength that is scanned. The instrument has a spectral resolution limited to 0.05 nm over a scanning range of 175 – 1800 nm [180]. For some measurements a Cary 50 was used, this spectrometer uses an internal reference collection without the use of a second sample. It features a lower spectral resolution of 1.5 nm with scanning range 190 – 1100 nm. Baseline spectra using the solvent or substrate in use were taken before sample scans.

4.2.2 *Infrared Spectroscopy*

Beyond the UV-vis near-infrared range of the electromagnetic spectrum lies the infrared (IR) region (> 2500 nm). The photons in this region have energy corresponding to molecular and crystal vibrations in materials. In IR spectroscopy, direct absorption of incident IR light by the material is probed. Fundamental transitions attributed to specific vibrations of a molecule, or molecular bonds within a crystal of a given material, will present as absorption events under IR illumination. The energy of a particular transition is dependent on the nature of the chemical bond. In this manner, IR spectroscopy can be used a fingerprint method to identify chemical species. IR spectra are often collected in transmission mode by using a wide-spectrum incident IR light source and applying a Fourier transform to the detected signal. In this manner, absorbance features at specific wavelengths are highlighted. Databases of FTIR spectra for a wealth of materials are available, making FTIR spectroscopy a useful identification technique. A key point of note is that vibrations are only IR active if the vibration

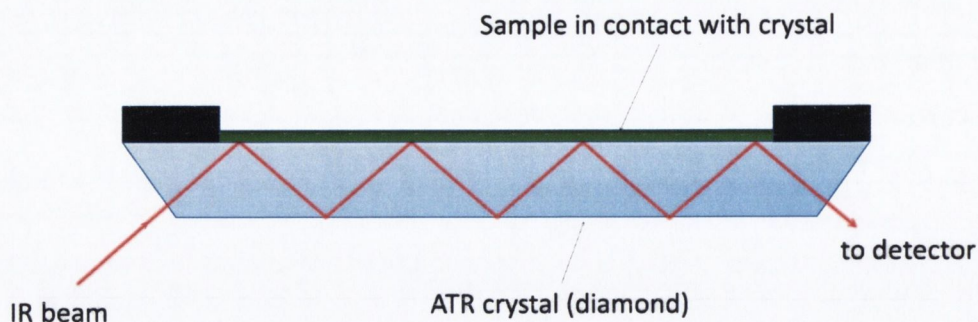


Figure 4.3: Schematic of ATR-FTIR measurement

induces a change in the permanent dipole moment of the molecule or molecular bond. This means that molecules such as N_2 or O_2 are IR-inactive, whereas dipolar molecules such as CO or H_2O are IR-active. Similarly, a chain of carbon atoms or a graphitic network do not possess IR-active vibrational modes. However, chemically bound functional groups such as C=O or C–OH are IR-active. Thus, FTIR spectroscopy can serve as an aid to assessing the quality of graphene and graphene derivatives, in particular for determining the large-scale presence of residual oxides.

Equipment

One of the most challenging aspects of FTIR analysis has been sample preparation. Traditionally, FTIR spectra of solids have been collected in transmission mode. This required crushing the material and dispersing in a matrix such as a liquid oil or a transparent solid. Potassium bromide (KBr) is the most widely used matrix. However of the order of a milligram of material in about 350 mg KBr is required to form a suitable disc sample. This method is destructive and is unsuitable for analysing thin film samples of low mass. The technique of Attenuated Total Reflectance FTIR (ATR-FTIR) removes these sample preparation limitations.

ATR-FTIR operates by monitoring the changes in an infrared beam that is totally internally reflected inside a crystal that is in direct contact with the sample. A sketch of the method is given in Figure 4.3. The refractive index of the sample must be significantly lower than the ATR crystal to permit total internal reflectance. In addition, this method requires good contact between sample and crystal, thus pressure is applied

to samples during measurements. The internal reflectance within the optically dense crystal generates an evanescent wave that extends beyond the crystal into the sample over a distance of $0.5 - 5 \mu\text{m}$ [181]. This evanescent wave is attenuated by IR absorption transitions in the material. The output IR beam is then fed to a detector and a Fourier Transform applied.

ATR-FTIR spectra in this thesis were taken on powders and thin film samples. Spectra were collected with a Perkin Elmer Spectrum 100 equipped with a diamond ATR crystal. An IR background was taken prior to sample scan acquisition. A minimum of 12 repeat acquisitions were taken per sample.

4.2.3 Raman Spectroscopy

Incident light can scatter from a material whilst interacting and exchanging energy with it; this scattering with a change in light frequency is called Raman scattering. This effect was first observed by C.V. Raman and K. S. Krishnan in 1928 while studying common liquids illuminated by focused sunlight [182]. As with IR spectroscopy, vibrational transitions are probed. IR absorption results from a one-photon annihilation event, i.e. the material is elevated in vibrational energy by the dissipated photon at the frequency of vibrational resonance. However, Raman spectroscopy exploits photon scattering processes. The vast majority of photons incident on molecules of a material are scattered elastically, this is known as Rayleigh scattering. A small proportion of the photons are scattered inelastically. This is a two-photon process and involves a change in the polarizability of the material with respect to the molecules' vibrational motion [183]. Incident monochromatic radiation (usually from a laser) interacts with the polarizability of the material to create an induced dipole moment. The radiation emitted by this induced dipole moment contains the observable Raman scattered photons. Due to energy conservation, the frequency shift of the Raman scattered light with respect to the incident beam corresponds to vibrational energy gained or lost by the material.

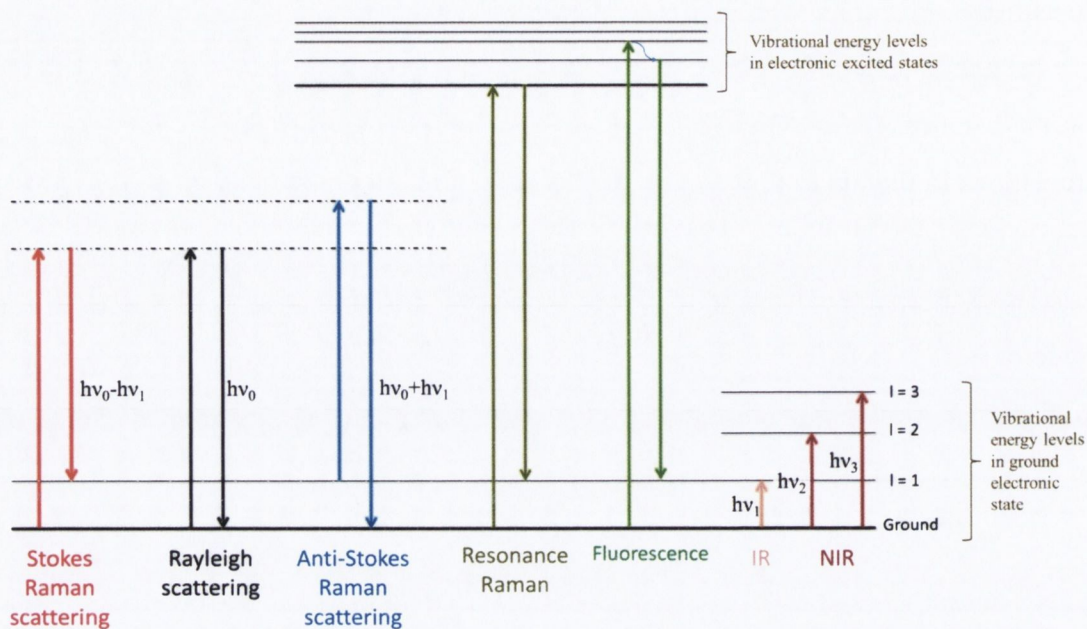


Figure 4.4: Diagram of spectroscopic transitions underlying vibrational and Raman spectroscopy. ν_0 indicates incident laser frequency, l_i ($i = 1, 2, 3, \dots$) denote vibrational levels with energy $h\nu_i$.

The transitions involved in Raman spectroscopy can be summarised diagrammatically as shown in Figure 4.4. Raman scattering events typically take place between electronic ground state energy levels and virtual excited states. These virtual states are short-lived distortions of the electron distribution by the incident electric field [184]. Stokes Raman scattering occurs when the material gains vibrational energy by terminating in an elevated vibrational state, with the scattered light reduced by the same energy. Anti-Stokes Raman scattering involves the scattered light gaining energy as the material transitions from an initial excited vibrational state to the ground state. Resonance Raman scattering can also occur whereby the frequency of incident light is close to an electronic transition of the material. In this case, Raman spectroscopy can become more sensitive with enhanced scattering of around 10^4 possible [185]. However, increased absorption by the material under resonance conditions can lead to more rapid sample decomposition [185]. Resonance Raman spectroscopy can also suffer from enhanced fluorescence, a process whereby inter-band relaxations in excited electronic states result in the emission of photons; this effect can drown out Raman spectral features.

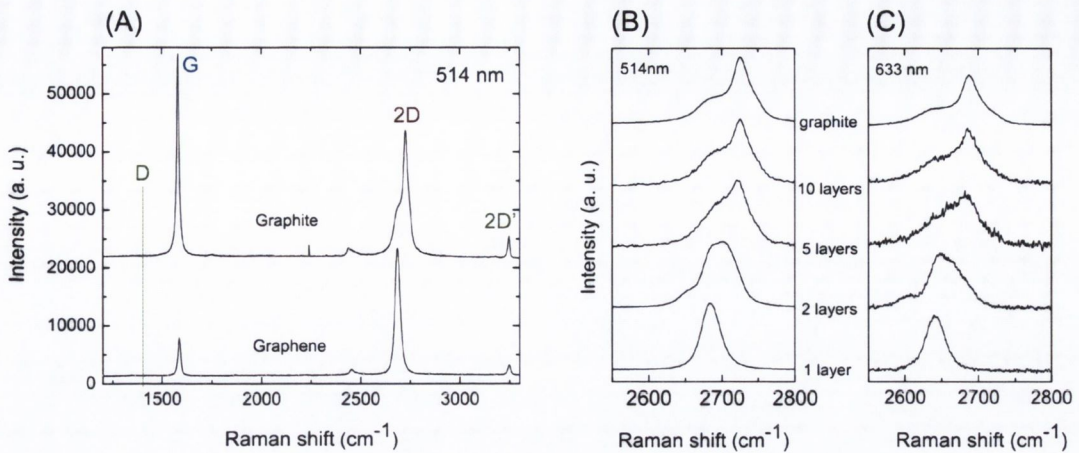


Figure 4.5: Typical Raman spectra of graphite and graphene. (A) Comparison of Raman spectra at 514 nm for bulk graphite and graphene. (B) and (C) Evolution of spectra of 2D peak shape with number of layers at 514 nm and 633 nm, respectively. Images adapted from [186].

Raman Spectroscopy of Graphene

Raman spectroscopy is a powerful tool for analysing carbon-based materials. It has been used over the past 40 years to study a range of graphitic materials including pyrolytic graphite, carbon fibres, graphitic foams, fullerenes, CNTs and now, most recently, graphene [187]. Graphene in particular yields a distinctive Raman spectrum whose features can reveal structural information about the material. In 2006, A.C. Ferrari and co-workers found that graphene ranging from one to five layers thick could be clearly identified using red (633 nm) or green (514 nm) laser excitation sources [186]. Figure 4.5A shows a typical Raman spectrum for a large-area monolayer graphene flake made by micromechanical cleavage in comparison to a spectrum for graphite. Three main peaks are commonly associated with graphene/graphite. A peak at $\sim 1580 \text{ cm}^{-1}$ labelled the G-band is characteristic of the sp^2 hybridised carbon structure, this peak is also found in CNTs [187]. The G-band originates in normal first order scattering processes; changes in graphene layer number can cause slight shifts in the shape and position of the G-band [188, 189]. The D-band, centred around $\sim 1350 \text{ cm}^{-1}$ is associated with breathing modes in sp^2 hybridised carbon rings and chains [190]; this is a second order process involving a phonon and a defect. Thus, observation of this

band requires that the ring be near a defect in the sp^2 structure; these defects can be atomic vacancies, functional groups bound to sp^3 hybridised sites or the edges of the sp^2 network. The D-band is absent from the spectra in Figure 4.5A as the areas of the materials sampled by the laser spot were defect-free. A third band, characteristic of graphene/graphite is centred around $\sim 2700\text{ cm}^{-1}$ and is now commonly denoted the 2D-band. This feature has been observed in the Raman spectra of graphite since 1981 [191] and is associated with a second order two-phonon scattering process. Ferrari et. al., and others, have showed that the shape of this band evolves with the numbers of graphene layers, in particular for flakes composed of 1 to 5 graphene layers [186, 189, 190, 192]. This evolution of the 2D peak with graphene layer number is shown in Figures 4.5B and C for two laser wavelengths. There are two more minor peaks that appear in the spectra of graphene/graphite. A D' -band around 1620 cm^{-1} can appear in defected graphitic structures, along its double-resonance $2D'$ -band around 3240 cm^{-1} [193].

Equipment

In this thesis, Raman spectroscopy was used to characterise films of deposited few-layer graphene. A Horiba Jobin Yvon LabRam HR confocal spectrometer was used, equipped with 532 nm and 633 nm laser excitation sources operating with power outputs up to 12 mW. Raman scattered light was isolated using notch filters. For all acquisitions a $100\times$ objective lens was used along with a diffraction grating having 600 lines per mm, this results in a manufacturer's rated spatial resolution of around $5\text{ }\mu\text{m}$ and spectral resolution of 0.3 cm^{-1} to 1 cm^{-1} . Grating calibration using a silicon dioxide/silicon standard and white-light spectrometer calibration were performed daily and before analysis of every batch of samples.

Exfoliated MoS_2 was also characterised by scanning Raman spectroscopy. For these samples a NT_MDT NTEGRA platform was used with a Renishaw Raman spectroscope equipped with a 1024×512 CCD camera. An Argon ion laser source at 488 nm was used with a $100\times$ objective and grating having 1200 lines per mm. Bi_2Te_3 flakes were examined with a Witec Alpha 300, with AFM option, equipped with edge filters and 532 nm laser using a $20\times$ lens.

4.3 ULTRASONICATION

In this research dispersions of layered materials are prepared by exfoliation of thin flakes from bulk materials via the application of ultrasonic energy. Ultrasound concerns sound waves with frequencies higher than those to which human ears can respond (i.e. > 16 kHz). Ultrasound is widely used in a range of applications including navigation, medicinal imaging, industrial scale chemical mixing and engineering (machining, cutting, drilling, welding).

In this work, ultrasonic energy is applied to layered materials immersed in liquid phases. The applied energy causes solvent molecules to oscillate about their mean positions, with the applied sound wave having compression and rarefaction cycles. During the rarefaction phase of the cycle the liquid molecules are drawn apart, if the average distance between the molecules exceeds the critical molecular distance to hold the liquid intact then void or cavities are created [194]. These cavitation bubbles can grow in size and subsequently collapse with the creation of shock waves [194]. These collapsing cavitation bubbles and shock waves result in the application of shear stresses to the material inside the liquid phase, these stresses result in the break-down of the material. In the case of weakly bound layered structures such applied stress can peel the layers from one another which then may be stabilised against re-aggregation by the given solvent environment.

Equipment

Laboratory grade ultrasonic equipment uses piezoelectric transducers to supply energy to the reaction vessel. Ultrasonic baths have one or more transducers attached to the base of a steel water-filled tank. In this case the ultrasonic waves penetrate the walls of reaction vessel(s) placed in the bath. Ultrasonic baths are often fixed frequency devices with fixed energy output. More intense and directed energy is provided by the use of horn or point probe sonicators directly immersed in the reaction vessel. With these devices the energy output at the tip of the horn/probe is controlled by the power intensity delivered to the transducer by a generator.

In this research a fixed ultrasonic frequency of 20 kHz is used with all apparatus. An ultrasonic bath (Branson 1510E-MT) and an ultrasonic horn/probe system (VibraCell CVX 750 W) are used for all samples. To ensure reproducibility when using the ultrasonic bath all samples for a given experiment are placed in identical viles/flasks using constant water levels. For horn/point probe tip sonication, sample temperature is controlled when necessary by the use of ice baths.

4.4 CENTRIFUGATION AND SEDIMENTATION

Dispersion assisted by ultrasonication yields a mixed suspension of exfoliated flakes, aggregated material and particles of raw starting material. These latter phases are unstably suspended and will settle out gradually over time. This settling process can be accelerated using centrifugation and the supernatant retained for further use.

In this work a Hettich Mikro 220R centrifuge is used, with rotation rate variable from 500 – 18000 rpm. The machine has a 6-way rotor (90 mm sample radius) for the range 500 – 6000 rpm and a 24-way rotor (87 mm sample radius) for the range 6000 – 18000 rpm. Literature sometimes quotes the centrifugation intensity in terms of relative centrifugal force (RCF), i.e. sample acceleration relative to gravitational acceleration, g . This can be derived from the centripetal acceleration, a , of the tubes inside a rotor of radius r from

$$a = r\omega^2 = r \left(\frac{2\pi\{\text{rpm}\}}{60} \right)^2 \quad (4.6)$$

where ω is the angular velocity of the rotor. The RCF is then given by

$$\text{RCF} = \frac{a}{g} = \frac{\pi^2 r \{\text{rpm}\}^2}{900g} = r (1.118 \times 10^{-3}) \times (\text{rpm})^2 \quad (4.7)$$

Particles can sediment out of a suspension after centrifugation. This can be due to incomplete removal of massive particles or re-aggregation of the particles in the dispersion. The temporal stability of dispersions can be probed by optical methods. In this research, the transmission intensity I through liquid-phase samples is monitored as function of time using an array of synchronised pulsed lasers (633 nm) and photodiodes. A blank sample with pure solvent gives the value of I_0 . Using the Beer-Lambert law

from Equations 4.4 and 4.5 gives the change in sample absorbance as function of time such that $A(t)/l = \alpha C(t)$. As the concentration of material in the dispersion falls over time due to sedimentation, the optical absorbance will fall in tandem. In a dispersion there may be more than one sedimenting phase, perhaps alongside a stable component. The total initial concentration of the dispersion can be written as

$$C_{Total,i} = C_0 + \sum_n C_n \quad (4.8)$$

where C_0 is the concentration of the stable phase and C_n represents the n sedimenting phases.

The concentration of the sedimenting phases can be shown to decay exponentially, with each sedimenting phase having its own time constant [195]. Thus, the local time dependent concentration of a given dispersion having n sedimenting phases and one stable phase can be written as

$$C(t) = C_0 + \sum_n C_n e^{-t/\tau_n} \quad (4.9)$$

where τ_n is the decay time constant of phase n [195]. In the context of the measured absorbance this can be written as

$$\frac{A(t)}{l} = \alpha_0 C_0 + \sum_n \alpha_n C_n e^{-t/\tau_n} \quad (4.10)$$

where α_0 and α_n denote the extinction coefficients of the stable and sedimenting phases respectively.

4.5 ZETA POTENTIAL

As mentioned in Chapter 3, the zeta potential is a key parameter of the EDL surrounding charged colloidal species. It is a useful parameter for evaluating the stability of surfactant-stabilised dispersions. In this thesis, the zeta potential of graphene exfoliated in aqueous surfactant media is assessed. Zeta potential measurements are made by examining the electrokinetic behaviour of charged colloidal particles. When an electric field is applied across the dispersion the charged particles are attracted towards the electrode of opposite sign, with the motion countered by viscous forces. This motion

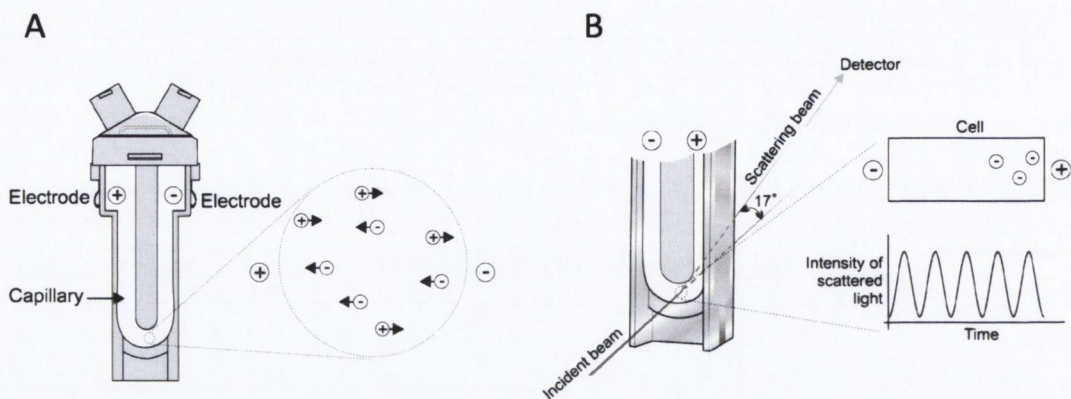


Figure 4.6: (A) Outline of capillary cell used for zeta potential measurements. (B) Illustration of laser doppler velocimetry technique. Images taken from Malvern Zetasizer Nano user manual [171].

under an applied electric field is known as electrophoresis [151]. At equilibrium the particles move with an overall drift velocity for the colloid denoted v . The electrophoretic mobility relates v to the applied electric field via $v = \mu E$. μ can be used to find the zeta potential, ζ , from the Henry equation for spherical particles

$$\mu = \frac{2\varepsilon_r\varepsilon_0\zeta}{3\eta} f(\kappa a) \quad (4.11)$$

where $\varepsilon_r\varepsilon_0$ is the permittivity of the medium, η is the liquid viscosity, a is the particle radius and κ is the inverse of the Debye-length (Equation 3.11) [196]. In the case of particles in a polar solvent like water, the size of the EDL, κ^{-1} , will be thin compared to the particle size and so $\kappa a \gg 1$. In this case $f(\kappa a)$ is defined as 1.5, which reduces Equation 4.11 to the Smoluchowski expression [196]. Note that this expression also holds for plate-like particles having a uniform surface charge, with negligible edge charges relative the surface charge and with radius much larger than the double layer thickness [175].

Equipment

In this research, zeta potential measurements were carried out with a Malvern Zetasizer Nano. Samples were injected into folded closed capillary cells with built in electrodes; a sketch of typical cell is shown in Figure 4.6A. The drift velocity of the particles under an applied potential, and hence the electrophoretic mobility, is essentially derived

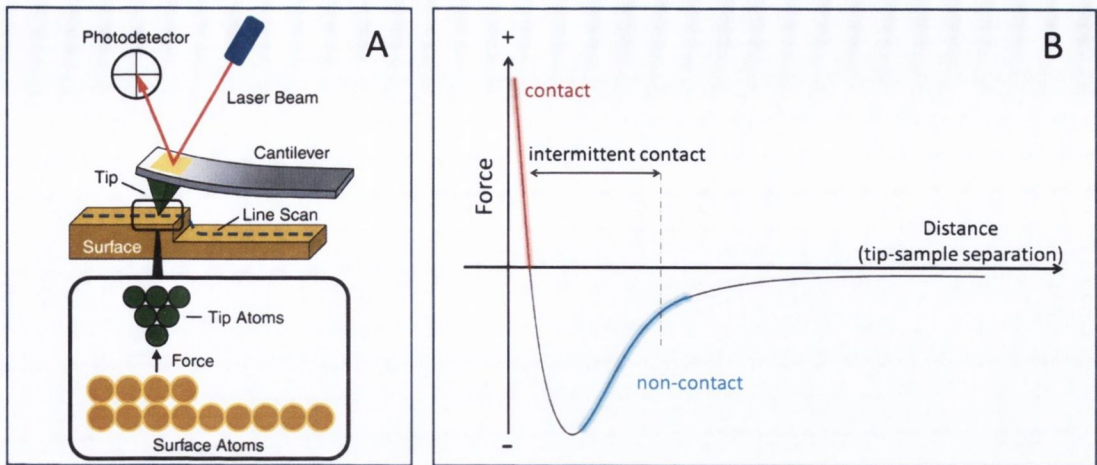


Figure 4.7: (A) Schematic representation of atomic force microscope [198]. (B) Sketch illustrating tip-sample force curve.

using a laser doppler velocimetry technique [171]. This method analyses the scattering of a 633 nm He-Ne laser incident on the capillary cell. Light scattered at a specific angle is re-combined with a reference beam to produce a signal with fluctuating intensity, the setup is illustrated in Figure 4.6B. The rate of fluctuation of this signal is proportional to the speed of the particles. This is the core technique underlying the measurement, it has been modified and enhanced by the device manufacturer to improve analytical results [171].

4.6 ATOMIC FORCE MICROSCOPY

Atomic force microscopy (AFM) is a scanning probe technique that maps surface topography. AFM images are obtained by measurement of the forces on a sharp tip generated by proximity to the surface of the sample [197]. These force interactions deflect the tip as it passes over the surface features of the sample, an AFM gauges these deflections to determine sample surface information. A schematic of a typical AFM is given in Figure 4.7A. The critical component of the AFM is the tip, attached to a cantilever that can deflect according to Hooke's law due to tip-sample interactions [199]. The degree of bending of the tip is monitored by a laser reflected off the cantilever and detected by a photodiode. The photodiode signal links into a feedback

circuit controlling the z-height of the sample relative the tip. AFM tips/cantilevers are commonly manufactured from silicon or silicon nitride. The radius of the end of the tip dictates the spatial scanning resolution. In most AFM devices the sample is rastered under the tip in the xy plane and along the z direction using piezoelectric motors.

Sample profile information with an AFM can be derived in three ways, probing different regimes of the tip-sample interaction, as illustrated in Figure 4.7B. In *contact mode* the tip tracks close to the sample surface probing the repulsive regime of the intermolecular force curve. This mode is only suitable for relatively smooth rigid surfaces as the feedback loop may not respond quickly enough to steep protrusions from the surface, causing the tip to crash.

In *non-contact mode* the tip oscillates just above its resonance frequency at a distance from the surface, interacting outside the repulsive regime. As the tip rasters the sample, surface features can alter the tip-surface distance thereby changing the van der Waals attractive force felt by the tip. This leads to a change in the oscillation frequency or amplitude, the AFM's feedback system responds by changing the sample height to maintain the original oscillation of the tip. However, non-contact mode suffers under ambient conditions due the presence of an adsorbed water layer on all samples. This dampens short-range interactions, requiring closer tip-samples distances. The water layer promotes a form of tip instability known as "jump-to-contact" whereby the attractive tip-sample forces can cause a sudden drop in tip height [200].

These problems were solved by use of an intermittent contact or *tapping mode*, the most widely used AFM mode. In this case the tip is oscillated at its resonance frequency, typically of the order of 100 kHz, with amplitude of the order of 10s of nanometres. The tip is positioned in such a way as to interact with the sample via short range repulsive forces for a brief portion of its oscillation cycle. In this way, tapping mode can be viewed as a hybrid of contact and non-contact mode, probing a range of interactions. The short contact time allows the tip to track rough surfaces with low lateral forces exerted on the sample, this makes tapping mode suitable for soft samples such as biological specimens.

The primary source of error in AFM imaging of nanoparticles concerns observed lateral dimensions. This arises when the nanoscale object or features of the sample

have lateral dimensions equal to or smaller than the tip radius. The path recorded by the tip will be distorted as the sides of the tip interact with the object before the apex. This results in observed overall lateral dimensions of such features being extended by a value roughly twice the tip radius.

In this thesis AFM analysis is carried out with a Digital Instruments Nanoscope IIIA from Veeco systems. All measurements are carried out under ambient atmosphere in tapping mode using monolithic silicon tips having resonance frequency ~ 300 kHz, force constant 40 N m^{-1} and tip radius $8 - 10 \text{ nm}$.

4.7 TRANSMISSION ELECTRON MICROSCOPY

Normal resolution TEM has been widely used in this research to study exfoliated layered materials. TEM works by directing an electron beam at samples under vacuum and examining the altered transmitted beam. Electrons can pass through unimpeded without interacting with the atoms in the sample or they can be scattered elastically or inelastically; the loss of electron beam intensity due to scattering by the sample is responsible for the contrast in a TEM image. The operating principles of a TEM are similar to those of a transmission light microscope with a source beam focused onto the sample by condensing electromagnetic lenses, and the transmitted beam gathered and focused onto a screen by objective and projector lenses. A schematic of a typical TEM system is shown in Figure 4.8.

The electrons are supplied at the top of the instrument column. The gun used depends on the instrument type, with thermionic LaB_6 or tungsten filaments in normal resolution microscopes and Shottky field emission or cold field emission guns in high resolution machines. The illumination system shown in Figure 4.8A regulates the shape of the incident beam, producing a parallel beam along the optic axis for normal TEM use. This coherent beam passes through the specimen and in doing so is disrupted. Some of the incident electrons pass straight through thin specimens unimpeded while others are scattered in the both the forward and back directions elastically and inelastically.

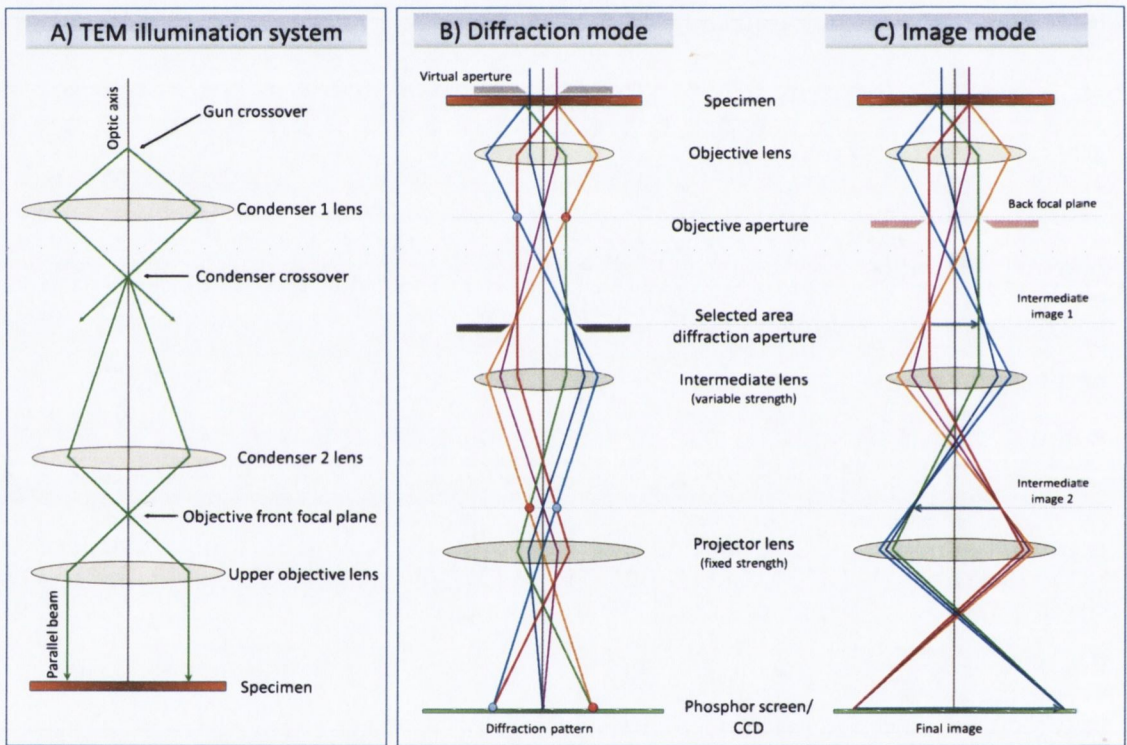


Figure 4.8: Optical system schematic of common transmission electron microscopes. (A) Illumination system layout. (B) Diffraction mode projecting diffraction pattern onto viewing screen. (C) Bright field mode projecting image of sample onto viewing screen. Schematic adapted from Williams and Carter [201].

The emergent beam passes through the objective lens to produce a diffraction pattern in the back focal plane, as shown by blue and red markers in Figure 4.8B. Use of a selected area aperture in the first image plane allows electron beams from a localised region of a specimen to be probed; this is equivalent to placing a virtual mask or aperture over the specimen. The intermediate and projector lenses focus the diffraction pattern onto the viewing screen, photographic plate or CCD. The diffractograms of single crystalline samples have spot patterns with spot positions governed by Bragg's law; the central bright spot comes from the transmitted beam [201]. Polycrystalline samples will exhibit ring patterns. Electron diffraction patterns can be calculated for many crystals. Electron diffraction has proved useful in the identification of monolayer graphene produced by micromechanical cleavage and liquid-exfoliation [10, 186, 202].

Under normal imaging conditions the selected area aperture is removed and an objective aperture is placed in the back focal plane as shown in Figure 4.8C. This objective aperture only allows electrons in the unscattered transmitted beam to contribute to the final image, cutting out the majority of diffracted beams and thereby boosting image contrast. The intermediate lens is adjusted to focus on the first intermediate image plane yielding an image of the sample on the screen. For high resolution TEM (HR-TEM), the objective aperture is set to the widest setting or removed altogether. In this case, the image is formed by the interference of many diffracted beams, giving a phase contrast that reflects the crystal's structure. The spatial resolution obtained in HR-TEM is limited by inherent aberrations in the microscope. These include the defocus setting, spherical aberrations (C_s , from imperfections in the focusing system) and chromatic aberrations (from non-identical electron energies incident on the specimen). Use of aberration corrected TEMs can correct spherical aberrations in the magnetic lenses via destructive interference, with some machines featuring chromatic aberration correctors as well. It is noted that, due to aberrations, atomic features in phase contrast images do not have a direct correspondence to the atomic scattering potentials of the crystal [201].

In this research normal TEM imaging was carried out with a Jeol 2100 operated at an accelerating voltage of 200 kV. This instrument has a LaB₆ filament electron gun. HR-TEM images were collected with a field-emission FEI-Titan operating at 300 kV.

Some HR-TEM was carried out by Dr. Valeria Nicolosi at the Department of Materials, University of Oxford using the Oxford-Jeol JEM2200MCO FEGTEM/STEM fitted with two CEOS C_s aberration correctors operating at 200 kV.

Quantitative TEM analysis

Previous TEM studies on graphene produced using sonication-induced liquid-phase processing revealed the presence of flake-like objects that were quite transparent to the incident electron beam (see Figure 2.5) [10]. Due to attenuation of the electron beam by the graphene crystalline lattice, a dark contrast was observed relative the vacuum background in bright-field images. With reference to Raman spectra and electron diffraction data it was shown that many of the observed flakes were monolayer graphene. In addition, few-layer graphene flakes were observed. It was observed that many of the multi-layered flakes showed visible straight line contrast features at one or more of their flake edges - these features corresponded to the individual graphene layers making up multi-layered flakes [10]. An example of this type of edge contrast is given in Figure 4.9A, with the individual layers highlighted. It is noted that the number of layers, N , counted for a given flake has a certain degree of uncertainty associated with it. Due to the limitations of the image contrast the gradation distinguishing one layer from the next may be difficult to see, thus for some flakes the count may only be determined to the nearest one or two layers. In order to balance the statistics obtained in layer counting for similar ranges of N an alternating bias was used: e.g. for a flake counted as either 4 or 5 layers, 4 would be selected, the next time a flake was counted as either 4 or 5, 5 would be used and so on. In this way the errors balance out and allow for an overall estimation for mean numbers of layers per flake, $\langle N \rangle$.

In addition to N the lateral dimensions of the flakes can also be quantified. As the flakes are of random shape, the values of length were taken across the longest axes of the flakes, with the width taken as the largest measurement perpendicular the longest axis. This is illustrated in Figures 4.9B and C. The uncertainty associated the length and width measurements was quite small, while the uncertainty in the estimation of N could be mitigated by using a large sample set. It is also worth noting the systematic errors in this type of quantitative TEM analysis. The first of these is attributable to the

method used to capture the graphene flakes from the liquid dispersions. For the work in this thesis the dispersions were dropped onto holey carbon grids. The holey carbon membrane acts as a mesh. As the dispersion passes through the grid some flakes are suspended by the carbon strands. The size of the holes in the carbon membrane can range from ~ 100 nm up to several microns in diameter, thus a significant proportion of the flakes incident on the membrane could pass through without being suspended. As the smallest flakes in the dispersion are more likely to pass through the holes it is possible that the statistics derived may be biased towards larger flakes. This would be especially true for low-concentration dispersions where only a few hundred flakes may be observable over an entire TEM grid. However, it will be shown from work on high concentration dispersions (Chapter 7, [163]) that small graphene flakes can be readily observed directly on top of the carbon membrane (these flakes are smaller than the strands of the membrane and so are not being suspended by the typical filtration action of the membrane). This is likely due to a strong affinity of the graphene flakes for the carbon-based membrane. By ensuring these flakes are included in any quantitative analysis the statistical error can be reduced. In addition, there can be a subjective bias in the collection of TEM images for analysis. It is reasonable to suggest that the larger flakes in a given sample will attract greater attention from the TEM operator and so lead to a bias in the collected image set. This subjective error was reduced in all the work shown in this thesis by attempting to randomise the data collection process. In particular, data was collected from across the entire TEM grid using random XY movements at low magnification to find individual flakes or clusters of flakes. Close-up images were acquired for all the observed flakes in each area sampled. This procedure also had the effect of compensating for bias due to localised hole size variations in the carbon grid that could have influenced the size of suspended flakes in a given area.

4.8 SCANNING ELECTRON MICROSCOPY

The scanning electron microscope (SEM) is a powerful analytical tool, widely used in scientific research and industry. In an SEM an electron beam is focused, by elec-

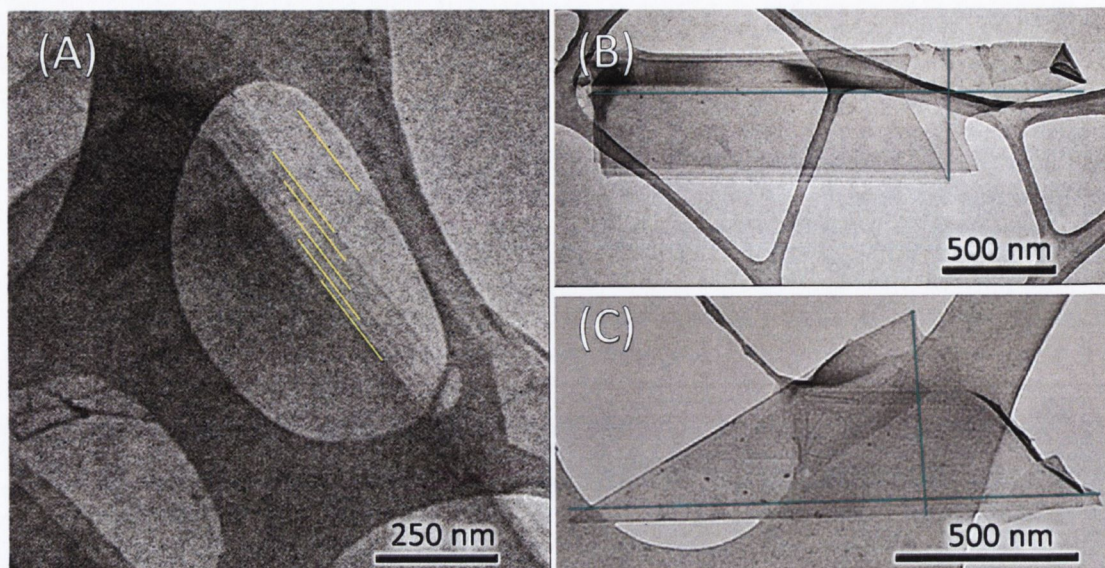


Figure 4.9: Illustration of methodology used to assess graphene flake size from bright-field TEM images. (A) Multi-layered graphene flake showing contrast due to individual graphene layers. (B) and (C) Illustrations of method used to determine length and width for a typical flake.

tromagnetic lenses, onto the sample under vacuum. When this primary beam strikes the sample several interactions occur within a teardrop-shaped volume of interaction depending on the beam energy and sample nature [122]. The most important effects of the bombardment are the formation of secondary and backscattered electrons [203]. Rastering of the beam across the sample and the collection of these electrons by various detection systems allows a digital image to be formed.

Secondary electrons are the result of ionisation of the sample by the primary electron beam. Secondary electrons have low energy, around 3 – 5 eV, resulting in a small escape depth of only a few nanometers [122, 204]. This allows secondary electrons to give good topographic information about the sample. Backscattered electrons are high energy inelastically scattered electrons that have undergone single or multiple scattering events, these electrons originate deeper in the sample [122]. Imaging using backscattered electrons yields chemical contrast as elements with higher atomic number will have a higher backscattered signal. However, as the backscattered electrons are of high energy they are not readily absorbed by the sample, meaning the sample region from which they are produced is much larger than it is for secondary electrons; this

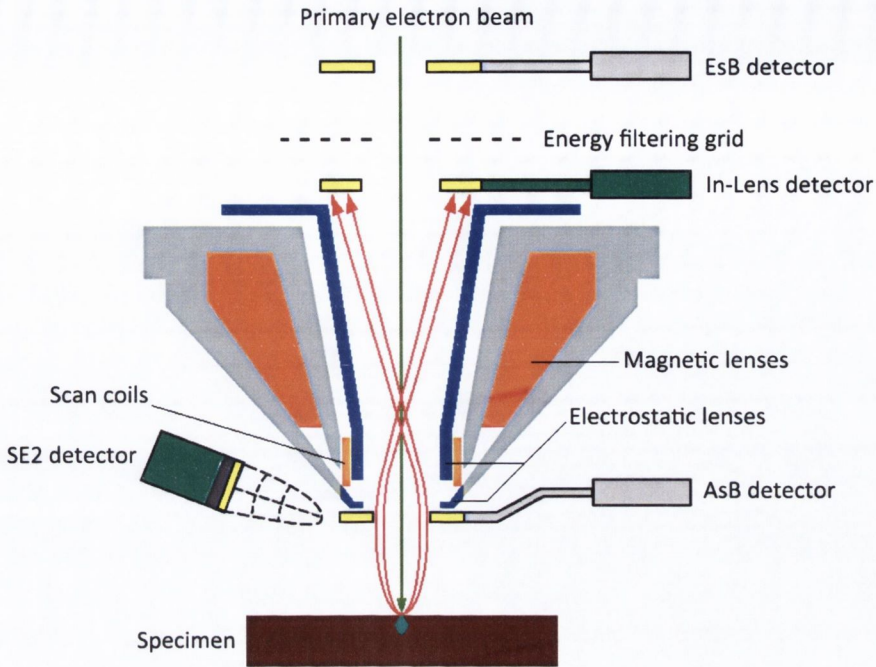


Figure 4.10: Schematic of lens system in Zeiss Ultra Plus scanning electron microscope. Adapted from Zeiss Ultra/Supra manual [204].

means lateral resolution is worse than when using secondary electrons ($\sim 1 \mu\text{m}$ vs $\sim 10 \text{ nm}$) [122].

In this thesis, a Zeiss Ultra Plus SEM with field emission electron gun is used. Some images were taken with an older Hitachi S-4300 field emission SEM. A schematic of the GEMINI® lens system in the Zeiss Ultra Plus SEM is given in Figure 4.10. The magnetic lenses and scan coils focus and move the sample beam. The secondary electron detector (SE2) is mounted inside the chamber to one side. The system features two backscattered electron detectors, one for low angle electrons (AsB detector) and one in-column for high angle electrons (EsB detector). In addition there is an In-Lens secondary electron detector inside the column; this probes secondary electrons having a very low penetration depth yielding images with very high surface sensitivity.

A final feature of modern SEMs is the incorporation of X-ray analysers. At sufficiently high electron accelerating voltages (typically 10 – 30 kV) core shell electrons can be knocked out by the primary beam, with the ions emitting characteristic X-rays when

they relax back to a lower energy state. These energy dispersive X-rays (EDX) can be analysed with reference to known atomic X-ray spectra. Care must be taken when using this technique as the use of an SEM column with limited electron output can yield low X-ray counts. In addition, X-rays produced in initial atom ionisation can create core level vacancies in other atoms of the sample, these will then re-emit X-rays of a lower energy in a process known as X-ray fluorescence [205]. Furthermore, information of sample tilt relative the X-ray analyser is passed to the analysis software, meaning samples should be level inside the SEM as far as possible. Low X-ray counts, fluorescence and sample tilt effects can be significant and bias the data manipulation performed by software [205]. This can lead to skewed quantitative elemental composition results. In general, use of SEM-based EDX gives excellent qualitative composition information, with care required when attempting to derive quantitative results.

PRODUCTION OF GRAPHENE IN SOLVENTS: INVESTIGATING THE ENERGETICS OF GRAPHITE EXFOLIATION THROUGH MULTICOMPONENT SOLUBILITY PARAMETERS

5.1 INTRODUCTION

This thesis examines the preparation of liquid phase dispersions of graphene and other layered materials in solvent and surfactant systems. This chapter specifically deals with the interaction of graphene with a wide range of solvents. Previous work has shown that graphene can be produced via mild sonication of bulk graphite platelets in selected amide solvents, with mild centrifugation used to remove large aggregates and graphite particles [10]. It was shown that high quality graphene, free from chemical functionalities, can be easily prepared in this manner. However, at that time only a small set of suitable solvents for graphene had been found. Furthermore, knowledge about the interactions between the solvents and the dispersed graphene was limited. In this chapter a study of the dispersibility of graphene in a wide range of solvents is presented. Hansen solubility parameters (HSPs) for graphene are identified. This in turn allows the energy cost of exfoliation to be probed for a given system through the estimation of the Flory-Huggins parameter. Finally, the quality of graphene produced in good and poor solvents is examined by TEM analysis.

5.2 EXPERIMENTAL PROCEDURE

The graphite powder used in all experiments was a natural flake graphite purchased from Sigma-Aldrich (product number 33246), having been sieved through a 0.5 mm mesh to remove the largest particles. All solvents were purchased from Sigma-Aldrich.

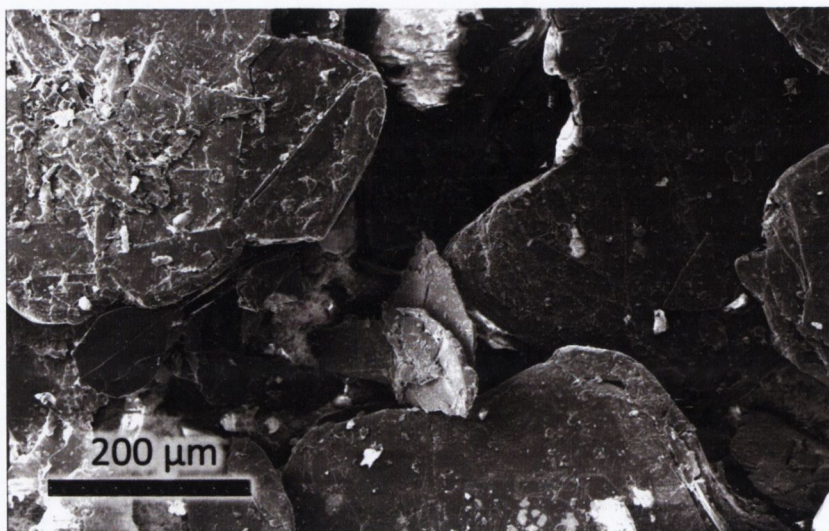


Figure 5.1: SEM micrograph of starting graphite material

The solvents were selected in a number of ways. Firstly, solvents that were known from literature as good CNT solvents were selected; these included *N*-methyl-pyrrolidone (NMP), cyclohexylpyrrolidone (CHP) and dimethylformamide (DMF) [142, 143, 206]. Other solvents were selected based on their structural similarity to NMP (see Figure 2.4C on page 23 for the structure of NMP). Some solvents were chosen as they had surface energy close to that experimentally estimated for graphene [10]. Finally, a few solvents were chosen during the course of the study based on preliminary estimations of the HSPs of graphene.

In all cases 0.1 mg/ml of starting graphite material was added to 10 ml of solvent in a 14 ml vial. An SEM micrograph of the starting material is given in Figure 5.1. The samples were sonicated in an ultrasonic bath for 30 min. After sonication, centrifugation was immediately carried out at 500 rpm (25g) for 90 min and the supernatant retained for analysis. Optical absorbance spectra were taken of the supernatant. In previous work graphene dispersions were found to follow Beer-Lambert behaviour and an extinction coefficient for graphene was determined ($\alpha = 2460 \text{ L}^{-1} \text{ g}^{-1} \text{ m}^{-1}$ at 660 nm wavelength) [10]. This figure was used to calculate the graphene concentration remaining after centrifugation, C_g . Each solvent was tested in this manner a minimum of three times, taking mean values of C_g and using the standard deviation as an estimate of experimental error.

Values for HSPs and solvent molecular values used for data analysis were taken HSPiP software (www.hansen-solubility.com). The software incorporates literature values [165] for the majority of solvents and has built-in algorithms to calculate values for some solvents with unknown HSPs.

Samples for TEM analysis were prepared by dropping approx 500 μl of the dispersions onto holey carbon grids (400 mesh), which allow the solvent to wick through whilst suspending graphene flakes. All images were taken in bright field mode at 200 kV.

5.3 RESULTS AND DISCUSSION

5.3.1 Graphene Dispersibility and Stability

In this study the value of C_g is used as a quantitative measure of the graphene dispersibility in each solvent. The measured values ranged from $0.16 \pm 0.05 \mu\text{g}/\text{ml}$ in the poorest solvent pentane to $8.5 \pm 1.2 \mu\text{g}/\text{ml}$ in cyclopentanone (CPO). The measured dispersibilities for all solvents tested are given in Table 5.1.

A full data set including estimated errors, HSPs and Hildebrand parameters for each solvent tested is given in Appendix Table 10.1, page 179. The values quoted are applicable to the specific set of experimental conditions used in this study (i.e. initial graphite concentration, sample volume, sonication method, sonication time and centrifugation settings). These conditions were held constant throughout the study allowing the data to be comparable.

While the data in Table 5.1 shows graphene is dispersible in a range of solvents, it is important to ensure that the dispersions are reasonably stable. This initial quality check was done by monitoring the optical absorbance at 650 nm of selected dispersions as a function of time using a dedicated sedimentation apparatus. Figure 5.2 shows the sedimentation data for the best solvent (CPO), a good solvent (NMP) and poor solvents (ethanol and toluene); these solvents are marked by * in Table 5.1. While some sedimentation was observed in all samples, the temporal stability was found to be very

Solvent	C_g ($\mu\text{g/ml}$)	Solvent	C_g ($\mu\text{g/ml}$)
Cyclopentanone (CPO) *^	8.5	1-octyl-2-pyrrolidone (N8P)	2.8
Cyclohexanone	7.3	1-3 dioxolane	2.8
N-formyl piperidine (NFP)	7.2	Ethyl acetate	2.6
N-vinyl pyrrolidone (NVP)	5.5	Quinoline	2.6
1,3-Dimethyl-2-imidazolidinone (DMEU) ^	5.4	Benzaldehyde	2.5
Bromobenzene	5.1	Ethanolamine	2.5
Benzonitrile	4.8	Diethyl phthalate	2.2
Benzyl benzoate	4.7	N-dodecyl-2-pyrrolidone (N12P) ^	2.1
N-methyl-pyrrolidone (NMP) *^	4.7	Pyridine	2.0
N,N-Dimethylpropylene urea (DMPU)	4.6	Dimethyl phthalate	1.8
γ -Butyrolactone (GBL)	4.1	Formamide	1.7
Dimethylformamide (DMF)	4.1	Ethanol *	1.6
N-ethyl-pyrrolidone (NEP) ^	4.0	Vinyl acetate	1.5
Dimethylacetamide (DMA)	3.9	Acetone ^	1.2
Cyclohexylpyrrolidone (CHP)	3.7	Water	1.1
Dimethyl sulfoxide (DMSO)	3.7	Ethylene glycol	1.0
Dibenzyl ether	3.5	Toluene *	0.8
Chloroform	3.4	Heptane	0.3
Isopropanol (IPA)	3.1	Hexane	0.2
Chlorobenzene	2.9	Pentane	0.2

Table 5.1: Graphene concentration after centrifugation (dispersibility, C_g) in 40 solvents. Temporal stability of the dispersions was tested for solvents marked with *. TEM analysis was carried out for solvents marked with ^.

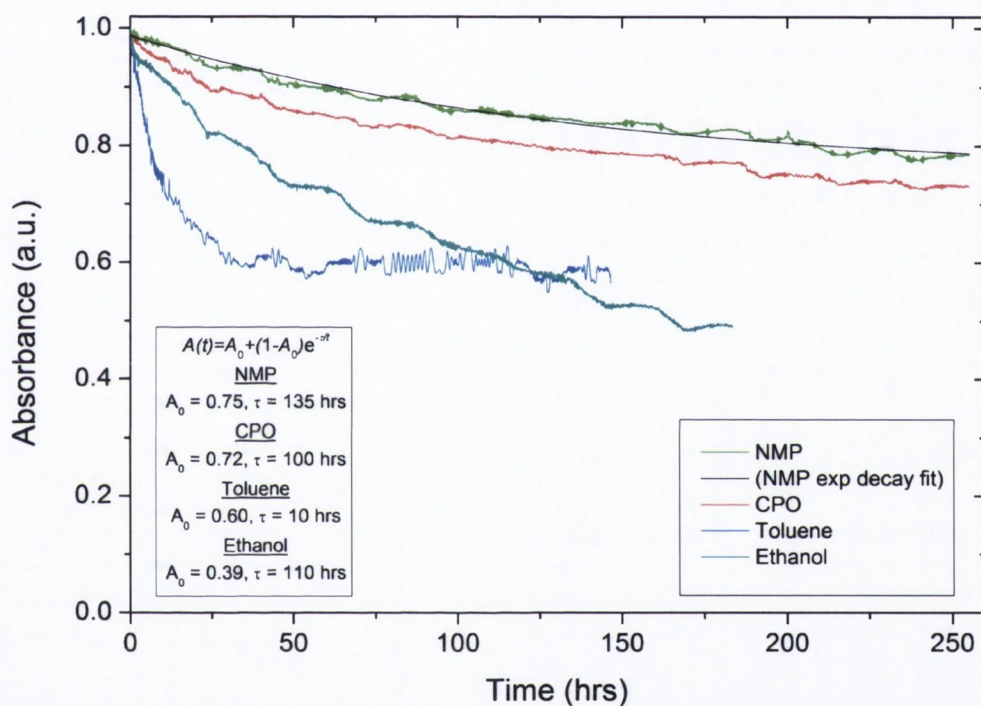


Figure 5.2: Sedimentation data for graphene in selected solvents. A single exponential decay fit for NMP is shown by the black dashed line with fit constants for the other dispersions shown in the graph table.

good in the case of CPO and NMP with > 70% of material remaining after over 10 days. Fitting of exponential decay functions to these curves as per Equation 4.10 showed stable phases of 75% and 72% of the graphene mass in NMP and CPO respectively. Toluene exhibited rapid sedimentation with a decay constant of only 10 hrs, whilst displaying an unexpectedly stable mass of 60% - the reason for the observed behaviour is unclear. Ethanol was significantly less stable with a stable phase of 39%. Overall, this data confirms that solvents with poorer ability to initially suspend graphene also have poorer retention properties.

5.3.2 Degree of Exfoliation in Various Solvents - TEM Analysis

Probing the graphene dispersibility through measurements of the optical absorbance does not confirm the presence of graphene in the dispersions. While previous work had demonstrated large-scale exfoliation of graphite in NMP to yield largely mono and bi-layer graphene [10], it could not be assumed that this would be the case in other solvents. Analysis of the degree of exfoliation is often carried out in literature by direct measurement of flake thickness via AFM. The use of AFM with solvent-exfoliated graphene and CNTs is challenging due to solvent drying effects [10, 38]. In a traditional drop-casting method onto a silicon wafer, the slowly evaporating solvent can increase the local concentration of dispersed material and lead to aggregation. These unpredictable aggregation effects are especially prevalent in high boiling point solvents, as often used in this work. In addition, folding of graphene flakes onto themselves is often observed in deposited samples making reliable thickness estimations from AFM analysis difficult.

In this chapter, TEM analysis is used to assess the degree of exfoliation in six solvents. The solvents were chosen to reflect high, intermediate and poor graphene dispersibility. These were compared to NMP which had been previously studied [10]. Figure 5.3 shows selected bright field TEM images for the six solvents tested, with folded monolayer and multilayer examples given for each. None of the samples showed evidence of the presence of large-scale defects. It is notable that all of the solvents

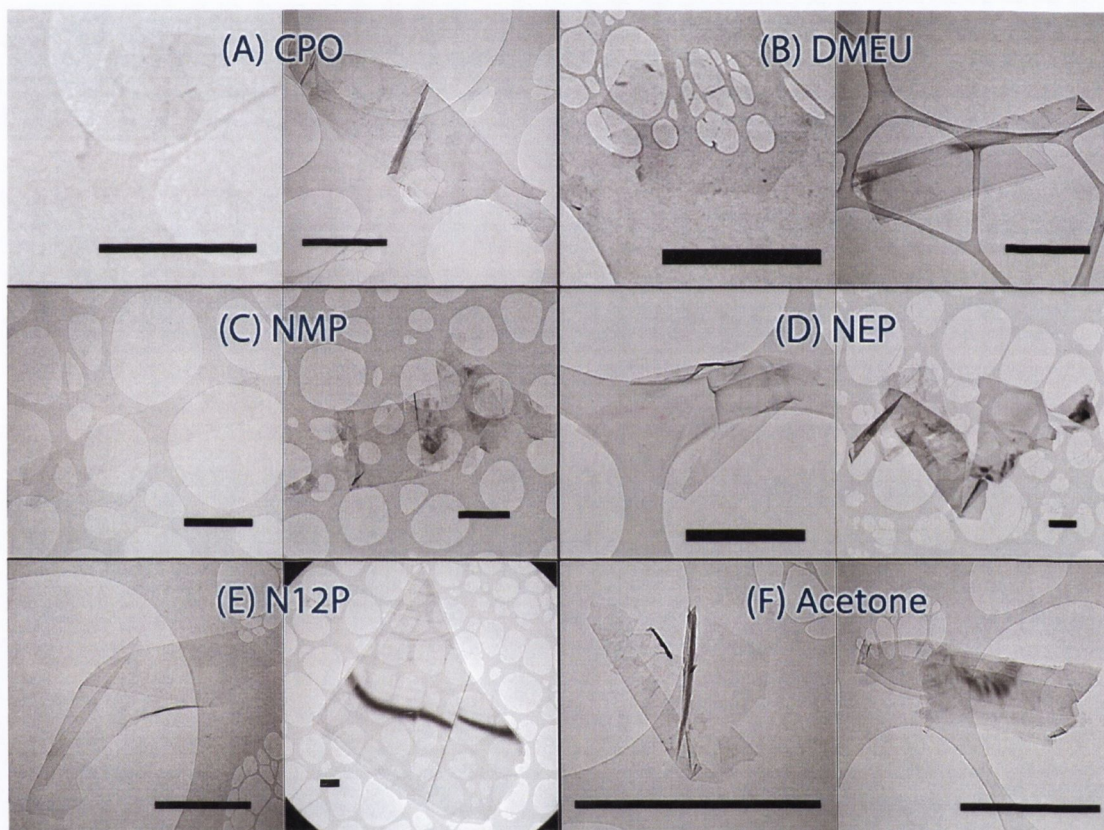


Figure 5.3: Selected monolayer and multi-layer graphene flakes from six solvents. All scale bars are 1 μm in length.

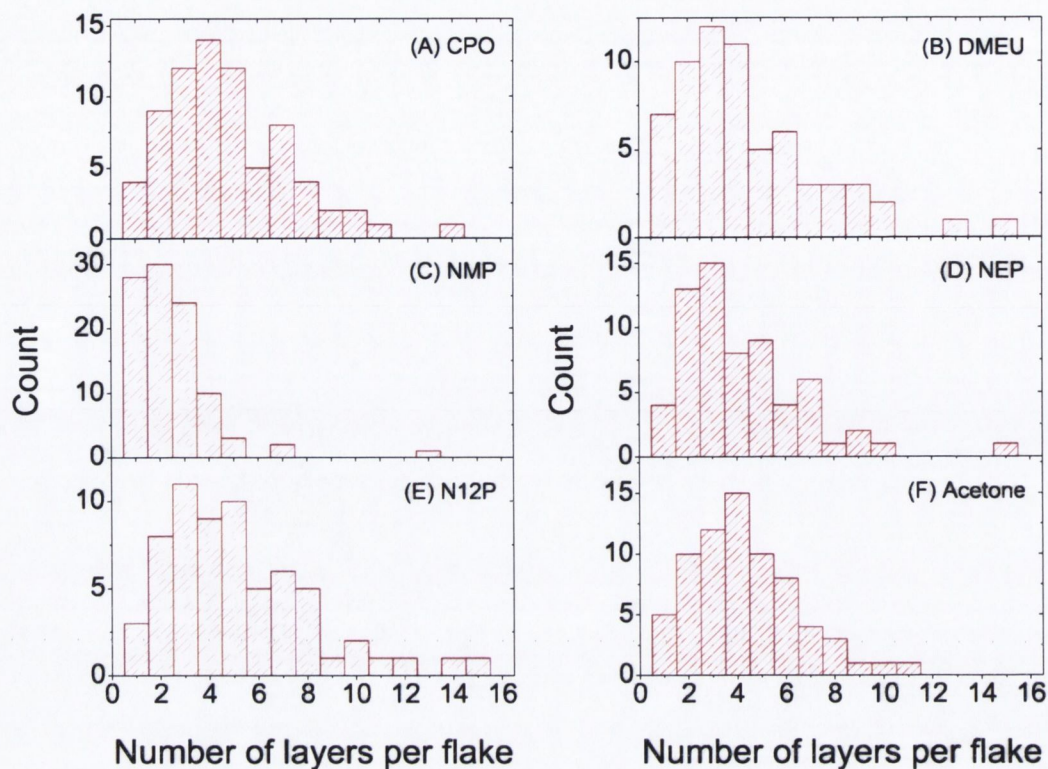


Figure 5.4: Histograms for numbers of layers per flake from TEM analysis of six solvents

examined produced some monolayer graphene, with many few-layer graphene flakes observed. In order to further study the quality of graphene produced, a detailed statistical TEM analysis was carried out over a large number of flakes for each solvent. Previous work had demonstrated that bright field TEM images yielded sufficient optical contrast to distinguish the edges of individual graphene layers within a flake [10]. By careful examination of flake edges the number of graphene layers per flake, N , has been estimated; this was done for a minimum of 64 flakes per solvent. It is acknowledged that for some multilayer flakes the exact counting of layers is difficult. Hence, only an estimate of N can be made, however it is expected that the random errors involved will cancel each other when statistically analysing the complete data set. Figure 5.4 charts the distribution of observed numbers of layers per flake for the six solvents tested. In all solvents the distributions are biased towards few-layer flakes. It is interesting to note that all solvents produced significant populations of mono and bi-layer material. The statistics are summarised in Table 5.2. The best performing solvent was NMP having a monolayer number fraction of 29%, with a mean number of

Solvent	$\langle N \rangle$	$\frac{N_1}{N_T}$ (%)	$\frac{N_{1-2}}{N_T}$ (%)	$\frac{N_{1-5}}{N_T}$ (%)
<i>N</i> -methyl-pyrrolidone (NMP)	2.5	29	59	97
1,3-Dimethyl-2-imidazolidinone (DMEU)	4.5	11	27	70
Cyclopentanone (CPO)	4.8	5	18	69
<i>N</i> -ethyl-pyrrolidone (NEP)	4.2	6	27	65
<i>N</i> -dodecyl-2-pyrrolidone (N12P)	5.2	5	17	64
Acetone	4.3	7	21	74

Table 5.2: Layer number statistics from TEM analysis of six solvents. Mean numbers of graphene layers per flake $\langle N \rangle$ and number fractions of monolayer graphene N_1/N_T , mono and bilayer graphene N_{1-2}/N_T and few-layer graphene N_{1-5}/N_T . Statistics for NMP taken from previous work by Hernandez et al. [10].

layers of 2.5. The most interesting point to note is that all the solvents have $> 63\%$ of flakes with 1 – 5 layers, even for the solvents with poorest C_g values such as acetone. This means that high quality graphene can be produced despite poor dispersibility in weak graphene solvents.

5.3.3 Surface Tension as a Graphene Solubility Parameter

The variation of C_g with solvent surface tension can be used as an initial assessment of graphene-solvent interactions. As mentioned previously with Equation 3.2 ($\Delta H_{mix}/V_{mix} \approx 2/T_{flake} (\partial_{graphene} - \partial_{solvent})^2 \phi$), the enthalpy of mixing, ΔH_{mix} , for graphene dispersed in a solvent is governed by the difference in surface energy of the two phases. A minimum enthalpy of mixing will maximise graphene dispersibility, this should be the case when solvent and graphene surface energies are closely matched. In this manner, the surface energy can be treated as a solubility parameter. The surface energy of the solvent is directly related to the solvent's measurable surface tension (Equation 3.3). As shown in Figure 5.5, the graphene dispersibility is maximised for solvents with surface tensions around 40 mJ/m^2 . This is in line with previous work that examined graphene

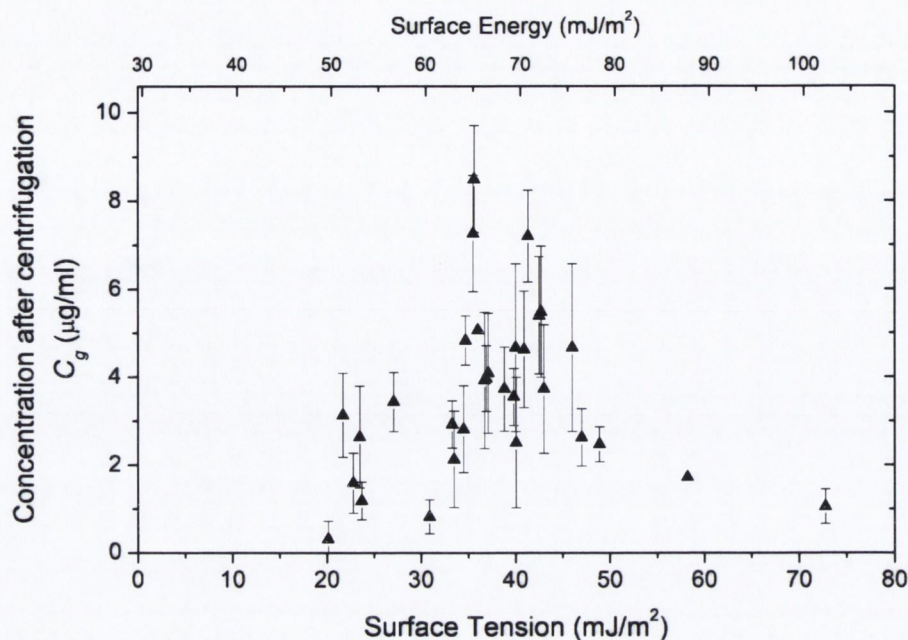


Figure 5.5: Graphene dispersibility, C_g , for all solvents tested as a function of solvent surface tension and surface energy.

dispersions in a small selection of solvents, primarily amide solvents [10]. This value also agrees with that observed for SWNTs [40]; this is not unexpected as graphene and CNTs share a common graphitic basal plane structure and should therefore have similar surface energies.

The graphene flakes are nanomaterials that interact with the solvents over a well-defined surface. Thus, it would seem plausible to expand this crude analysis by developing a set of solubility parameters for the solvents based on surface energies. The intermolecular interactions could be simplified into dispersive (D), polar (P) and hydrogen bonding (H) components [165]. This could then be used to probe the graphene-solvent interaction through surface energy components. In theory, an analogue of Equation 3.2 based on surface energy components could be developed. This methodology would lead directly to an understanding of the thermodynamics of the interactions via the enthalpy of mixing. However, this approach would be severely limited because surface energy components are only known for a limited array of solvents and for only a handful of the solvents tested in this study. In contrast, HSPs have been documented for over 1200 solvents as well as over 500 polymers [165]. This

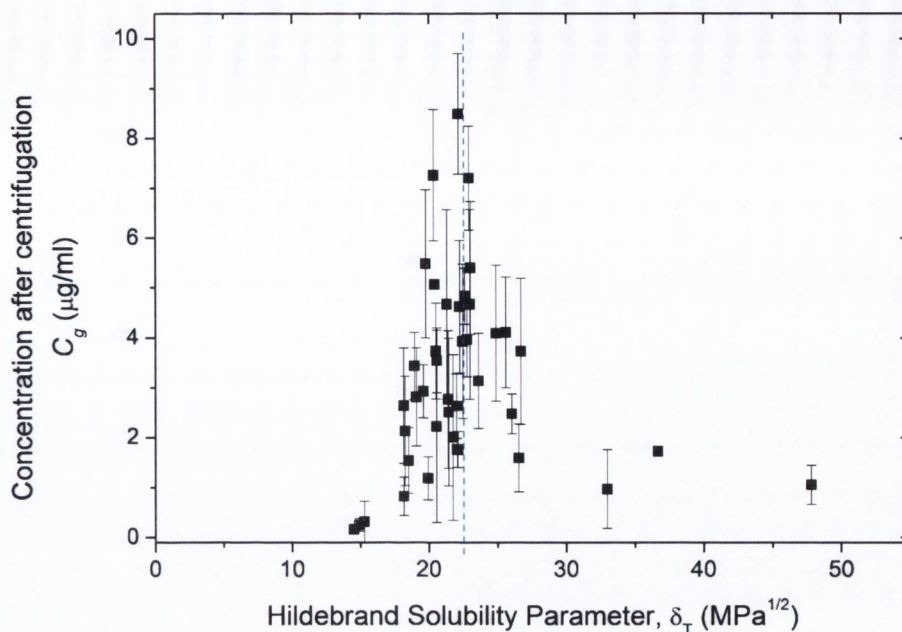


Figure 5.6: Graphene dispersibility, C_g , for all solvents tested as a function of Hildebrand solubility parameter.

makes HSPs far more useful, even though they are more commonly applied to systems involving molecular solutes.

5.3.4 Graphene Dispersibility Through Hansen Solubility Parameters

The Hildebrand parameter, δ_T , is the most common solubility parameter. It was previously defined in Equation 3.4 as the square root of the cohesive energy density of a given solvent, i.e. $\delta_T = \sqrt{E_{C,T}/V}$. The cohesive energy density is derived from the solvent vaporisation energy. When considering a solute interacting with the solvent, the Hildebrand-Scratchard equation, Equation 3.5, shows optimum dispersibility occurs by matching of the respective Hildebrand parameters. However, approximations in the formulation of the Hildebrand-Scratchard equation mean it only strictly applies to systems interacting solely through dispersion forces, i.e. for non-polar molecular solutes [146, 168].

The applicability of the Hildebrand parameter in the case of a nanomaterial like graphene can be tested with a plot as given in Figure 5.6. A well-defined peak in the

data centred at $22.5 \text{ MPa}^{1/2}$ is observed, this is marked by the dashed line in Figure 5.6. This is in good agreement with work on solvent dispersed SWNTs and MWNTs [146, 148]. However, some solvents with δ_T close to this peak show poor dispersibility. This means that the Hildebrand parameter alone is not sufficient to fully account for the behaviour of graphene in solvents. HSPs given by Equation 3.9 as components of the Hildebrand parameter ($\delta_T^2 = \delta_D^2 + \delta_P^2 + \delta_H^2$) allow for a more complete treatment of the solvent-graphene interaction. When considering HSPs, D, P and H interactions are accounted for. Good dispersibility should be achieved when all three parameters of graphene and solvent are similar.

Figure 5.7 plots the dispersibility as a function of the three Hansen components. In Figure 5.7A, a peak in C_g is observed at $\delta_D = 18 \text{ MPa}^{1/2}$, with good graphene solvents having dispersive components in the range $16 \text{ MPa}^{1/2} - 20 \text{ MPa}^{1/2}$. Figures 5.7B and C show very broad peaks in C_g in the polar and hydrogen bonding components around $11 \text{ MPa}^{1/2}$ and $7 \text{ MPa}^{1/2}$, respectively. These results are a little surprising as graphene should be a non-polar solute. Previous FTIR and XPS analysis showed that no oxygen-containing groups or other polar species were attached to graphene produced by graphite exfoliation in NMP [10]. Thus, one would expect that the Hildebrand parameter alone would be sufficient to determine dispersibility, as has been shown for the C_{60} molecule in literature [207]. The data in Figure 5.7 suggests that a certain fundamental degree of solvent polarity is required to successfully disperse graphene and that purely dispersive interactions are not sufficient. This agrees with a study by Park et. al. that examined the dilution of a stock dispersion of highly reduced graphene oxide in DMF/ H_2O with a set of other solvents [84]. They found that their reduced graphene oxide could be dispersed in solvents having $10 \text{ MPa}^{1/2} < (\delta_P + \delta_H) < 30 \text{ MPa}^{1/2}$. These values agree well with the data for defect-free graphene shown in this thesis, a plot of C_g vs $\delta_P + \delta_H$ is given in Appendix Figure 10.1, page 182. The need for non-zero solvent polarity is also found in solvent-assisted dispersions of SWNTs [146]. The reason why polar solvent interactions are important for the dispersibility of graphene and CNTs but not fullerenes is unclear at present.

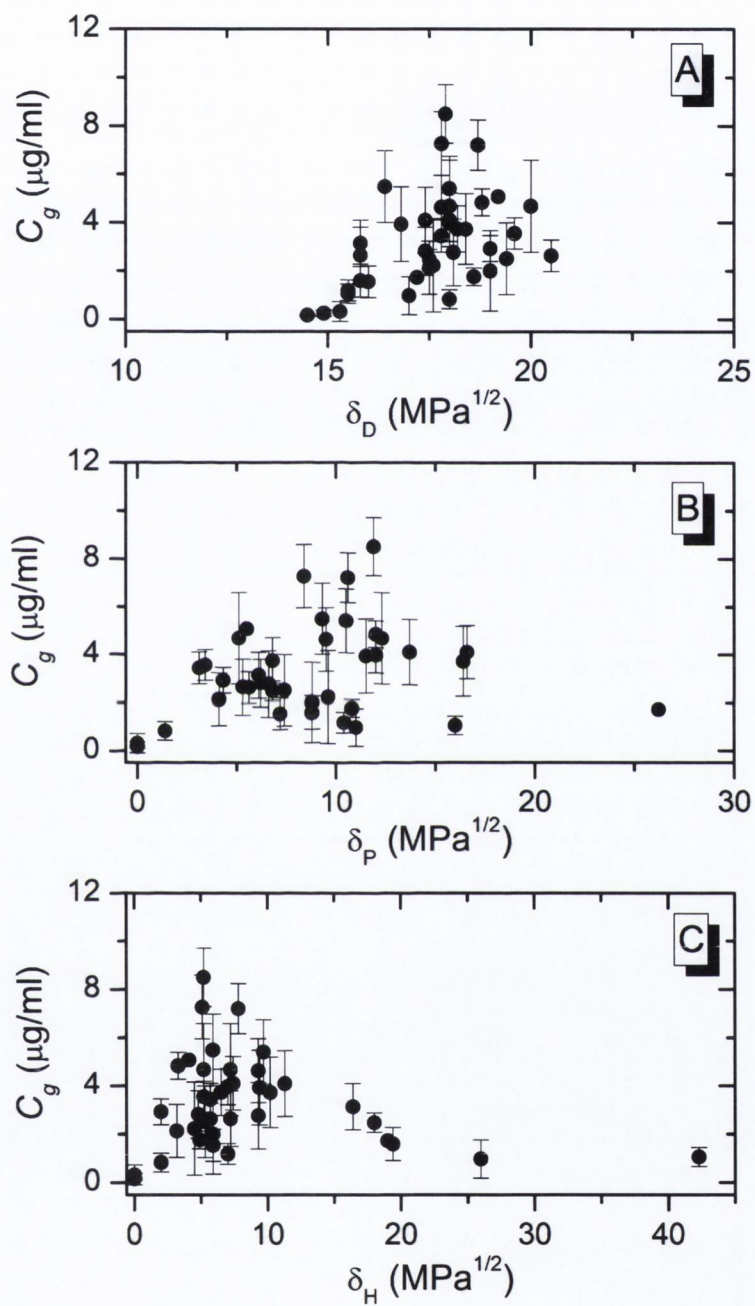


Figure 5.7: Graphene dispersibility, C_g , as a function of solvent HSPs. (A) dispersive HSP δ_D , (B) polar HSP δ_P and (C) hydrogen bonding HSP δ_H .

5.3.5 Estimating the Hansen Solubility Parameters of Graphene

The data shown in Figure 5.7 shows general trends in the scaling of graphene dispersibility with the three HSPs. However there is a large amount of scatter present. The parameters are treated individually in these plots. As a result, solvents having only one HSP matching graphene will appear under the envelope of the curves with a reduced C_g value. An alternative analysis that evaluates all three HSPs simultaneously can address this issue. This can be achieved by calculating the Flory-Huggins parameter, χ , for each solvent. This parameter is commonly used in polymer chemistry to quantify the energy cost of mixing of solute A in solvent B. χ is given in terms of HSPs by Equation 3.10 as

$$\chi \approx \frac{v_0}{kT} \left[(\delta_{D,a} - \delta_{D,b})^2 + (\delta_{P,a} - \delta_{P,b})^2 + (\delta_{H,a} - \delta_{H,b})^2 \right]$$

Solvent systems with all three HSPs close to the solute HSPs will have low values of χ . As χ is proportional to the enthalpy of mixing (Equation 3.6), solvents with low χ will have a low energetic cost of exfoliation and are expected to show good solute dispersibility. It is worth noting that negative values of χ are not permitted by this equation. Negative χ can occur when the solute-solvent interactions are very strong and can indicate true thermodynamic solubility; slightly negative χ has been suggested for SWNTs dispersed in NMP [9, 40]. Nevertheless, this expression retains the physical meaning of the Flory-Huggins parameter and links it to interaction components in the form of HSPs.

In order to determine values of χ for graphene dispersions the HSPs of graphene itself must be determined. One method to do this is to make the assumption that correct values of graphene HSPs will give a plot of χ vs C_g with the least scatter. A MATLAB program* was written to calculate χ using Equation 3.10 with user-selected values of δ_D , δ_P and δ_H for the solute (graphene). These input values were estimated crudely from solvents with the highest C_g . The program then fit a straight line to a plot of $\log(C_g)$ versus $\log(\chi)$ and calculated a parameter to gauge the fitting quality

* The MATLAB programs were written by Dr. David Rickard for analysing SWNT-solvent systems [146], and have been adapted for use in this thesis.

(this was the square root of the sum of the squared line fit residuals). The program repeated this procedure for a wide range of solute HSP values around the manually selected ones. The final output of the program was the set of δ_D , δ_P and δ_H that gave the best fit. As an additional calculation with a higher localised precision, the fitting was repeated using a constrained non-linear optimisation method using the “Fmincon” function within MATLAB’s optimisation toolbox. This resulted in best fit values of $\delta_D = 21.7 \text{ MPa}^{1/2}$, $\delta_P = 9.7 \text{ MPa}^{1/2}$ and $\delta_H = 8.5 \text{ MPa}^{1/2}$.

However, there is a slight weakness with this methodology. Equation 3.10 is normally written by Charles Hansen with a pre-factor of 0.25 before the second and third terms on the right-hand side [165], i.e.

$$\chi \approx \frac{v_0}{kT} \left[(\delta_{D,a} - \delta_{D,b})^2 + 0.25 (\delta_{P,a} - \delta_{P,b})^2 + 0.25 (\delta_{H,a} - \delta_{H,b})^2 \right]$$

This pre-factor is an empirical term that derives from solvent-selection routines. The pre-factors adjust the weighting of the polar and hydrogen bonding Hansen components, helping to account for “good” or “bad” solvents that would otherwise be excluded by calculations. Inclusion of the pre-factor is common in solubility research and is supported by notable quantities of empirical data [165], but its usage is not supported by a rigorous theoretical basis. In addition, Hansen notes that different values of the pre-factor are appropriate for some systems [165]. This is why it has been omitted from the above analysis and why a more intuitive form of χ has been retained in Equation 3.10. This presents a problem with the above analysis because a functional form of χ must be written into the MATLAB program. Repeating the computations including the pre-factor of 0.25, or some number close to it, significantly changes the values of the optimum HSPs. Given the requirement of some degree of polarity for successful graphene dispersion, shown in Figures 5.7B and C, it may be the case that some pre-factor value is needed to determine the correct expression for χ .

In order to avoid this problem, one can estimate the graphene HSPs using an alternative solvent screening method [146, 165]. This involves associating the graphene HSPs with those of the most successful solvents. This can be done by taking the weighted average of the Hansen parameters of the solvents; in this study C_g is the quantitative measure of solvent efficiency and is used as the weighting factor. This

approach has the benefit that solvents contribute to the final result in proportion to their quality and does not rely on the use of an explicit formulation of χ . The three HSPs can then be given by

$$\langle \delta_i \rangle = \frac{\sum_{all\ solvents} C_g \delta_{i,solvent}}{\sum_{all\ solvents} C_g} \quad (5.1)$$

where $i = D, P, H$ and $\delta_{i,solvent}$ is a Hansen component for each solvent. The summation is taken over all 40 solvents studied. This gives estimated HSPs for graphene of $\langle \delta_D \rangle = 18.0 \text{ MPa}^{1/2}$, $\langle \delta_P \rangle = 9.3 \text{ MPa}^{1/2}$ and $\langle \delta_H \rangle = 7.6 \text{ MPa}^{1/2}$. These values agree well with those measured for carbon nanotubes by our group ($\delta_{D,SWNT} = 17.8 \text{ MPa}^{1/2}$, $\delta_{P,SWNT} = 7.5 \text{ MPa}^{1/2}$ and $\delta_{H,SWNT} = 7.6 \text{ MPa}^{1/2}$) [146] and others [148]. It was expected that good graphene solvents would have HSPs close to those of graphene. Preliminary calculations of the graphene HSPs led to the selection of CPO and cyclohexanone from the HSPiP database, these solvents were measured as the best solvents. In addition, the worst solvents of heptane, hexane and pentane were discovered by looking for solvents with HSPs far from those estimated for graphene. This helps validate the methods used and the results obtained.

Using these computed values for the graphene HSPs allows the calculation of χ for each solvent. Figure 5.8 plots C_g as a function of χ using both sets of calculated graphene HSPs. Equation 3.10, excluding Hansen's 0.25 pre-factor, has been used. Inclusion of the pre-factor has been tested and has the effect of simply scaling the numerical values of χ ; this doesn't affect the observed trends or alter the interpretation of the results.

It is clear from Figure 5.8 that C_g rises with decreasing χ . This means that solvent and graphene solubility parameters converge as the graphene dispersibility improves; this further validates the use of HSPs in the study of graphene-solvent dispersions. It also confirms that the estimated values of graphene HSPs are close to the true values. These figures clearly demonstrate that the exfoliation of graphite in solvents to produce graphene is strongly influenced by the energetic cost of exfoliation.

It is noteworthy that all solvents tested with Hansen parameters close to those estimated for graphene (i.e. low χ) are shown to disperse graphene to some extent. This is in contrast to findings in literature for CNTs, where a significant number of

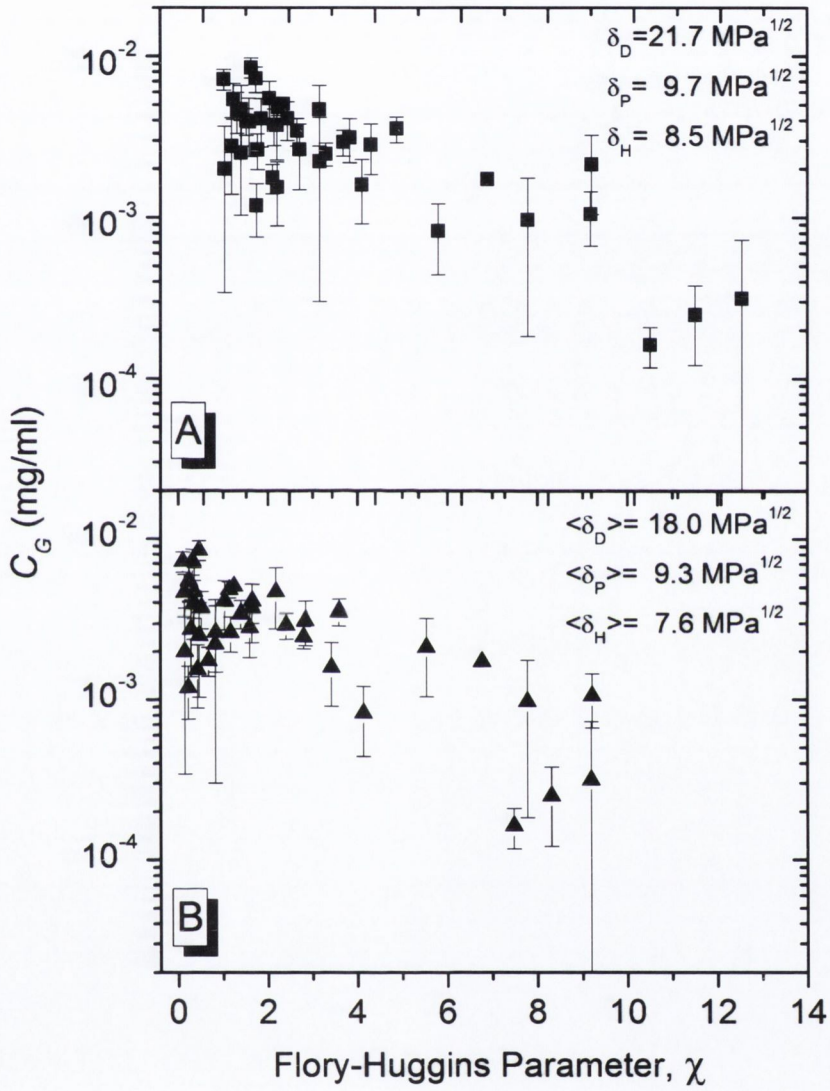


Figure 5.8: Graphene dispersibility, C_G , as a function of the Flory-Huggins parameter, χ . (A) Plotted using graphene HSPs from MATLAB fitting. (B) Plotted using graphene HSPs from solvent screening.

solvents with the correct HSPs failed to disperse SWNTs [146]. For SWNTs it was found that successful solvents were limited to amide solvents. It is thought that a solvent-specific interaction with the SWNTs, such as a charge-transfer process, is important in determining good dispersibility [146]. In the current graphene study the most successful solvent was a ketone (CPO) with no evidence that solvent-specific effects limit dispersibility. However, while raw dispersibility is highest for CPO, NMP as an intermediate solvent produces the best graphene flake thickness distributions and the most stable dispersions. Thus, the exact mechanism dictating graphene stabilisation by solvents remains unknown.

5.4 CONCLUSIONS

In conclusion, this work greatly enhances the field of liquid-phase graphene production. This work has demonstrated that graphene can be exfoliated from natural bulk graphite and dispersed in over 40 solvents, at the time this research was carried out 28 of these were new graphene solvents. TEM analysis confirms a high degree of exfoliation in even the poorest solvents, with significant populations of monolayer and bilayer graphene found regardless of the level of dispersibility. This is important as many of the new solvents have significant advantages over previously studied solvents such as NMP. For instance, use of NMP and similar solvents can be hindered by their high boiling points, often in excess of 200 °C, making the removal of solvent difficult; this applies for example in the case of depositing graphene flakes on surfaces by spray or drop casting. In addition, access to such a broad solvent set can facilitate the making of a diverse range of graphene-polymer composites.

The overall solvent-graphene interaction has been assessed through the use of surface tension data and Hildebrand solubility parameters. It has been confirmed, in line with previous work [10], that good graphene solvents are characterised by surface tensions close to 40 mJ/m² and by Hildebrand parameters around 23 MPa^{1/2}. This study has been extended by invoking the use of Hansen solubility parameters to examine the dispersive, polar and hydrogen-bonding components of the interaction. The Hansen

solubility parameters of graphene have been estimated as $\langle\delta_D\rangle = 18.0\text{ MPa}^{1/2}$, $\langle\delta_P\rangle = 9.3\text{ MPa}^{1/2}$ and $\langle\delta_H\rangle = 7.6\text{ MPa}^{1/2}$. This has allowed the use of the Flory-Huggins parameter to illustrate that the energetic cost of exfoliation is an important factor governing the level of graphene dispersibility in solvents. Surprisingly, non-zero values of the polar and hydrogen-bonding components are required for a solvent to successfully disperse graphene, a non-polar material. Knowledge of the graphene Hansen parameters may lead to the future discovery of better solvents or solvent blends. Use of graphene Hansen parameters will also aid polymer selection for composite formation.

LIQUID-PHASE PRODUCTION OF GRAPHENE DISPERSIONS BY EXFOLIATION OF GRAPHITE IN AQUEOUS SURFACTANT SOLUTIONS

6.1 INTRODUCTION

In Chapter 5, the production of graphene in a wide range solvents has been discussed. Such solvent-based processing produces high quality graphene but there are some drawbacks. When considering potential applications, some good graphene solvents such as NMP suffer problems associated with high boiling points. Some solvents like DMF require special handling if they are to be used in a safe manner. In addition, some solvents are relatively expensive compared to the negligible cost of the graphite starting material. Unfortunately, the safest, cheapest and most abundant solvent in the world, water, has far too high a surface tension to stably suspend useful quantities of graphene on its own. A lot of research has focused on chemically modifying naturally hydrophobic graphite to make a water-soluble graphene derivative, usually in the form of graphene oxide. In order to re-form graphene, additional reduction steps and high temperature annealing are required. However, the structural modifications of the graphene basal are impossible to completely reverse leaving a structurally damaged and electronically degraded end-product.

Thus, there is a need for an alternative, scalable, liquid-phase production technique to produce high quality graphene at a reasonable yield. The method should use non-oxidative processing conditions and should not require post-processing in the form of high temperature annealing or aggressive chemical treatments. In this chapter such a method is explored, using surfactants to stabilise graphene in an aqueous medium. The graphene is produced in a surfactant system similar to that previously applied to CNTs [27], using experimental conditions similar to those used in Chapter 5.

6.2 EXPERIMENTAL PROCEDURE

The graphite powder used in these experiments was as previously used in Chapter 5, purchased from Sigma Aldrich and sieved to remove the largest particles. Sodium dodecylbenzene sulfonate (SDBS) surfactant was purchased from Sigma Aldrich (lot no. 065K2511) and used as provided. Stock solutions of SDBS with concentrations between 5 and 10 mg/ml were prepared in Millipore water with overnight stirring. A typical sample was prepared by dispersing graphite in the desired SDBS solution in 25 ml cylindrical vials using 30 min of low power bath sonication. The resulting dispersions were left to stand for around 24 hrs to allow any unstable aggregates to form and then centrifuged at 500 rpm (25g) for 90 min. After centrifugation the top 15 ml was decanted by pipette and retained for use. For optical characterisation, a range of graphene concentrations were prepared. To maintain fixed surfactant concentration across samples, all dilutions were carried out by adding surfactant solution with SDBS concentration identical to the dispersion being diluted.

Zeta potential measurements were carried out with a Malvern Zetasizer Nano system (see Section 4.5), with the zeta potential determined by measuring the electrophoretic mobility and applying the Smoluchowski expression for plate-like particles (Equation 4.11). All measurements were carried out at 20 °C and at the natural pH of the dispersion unless otherwise stated.

Samples for AFM were prepared by spray-casting the dispersion onto freshly-cleaved mica. 1 ml of the dispersion was sprayed over the mica using an Evolution Airbrush spray gun (from www.graphics.co.uk). The mica surface was maintained at 120 °C using a hotplate. The spray gun was held approximately 20 cm from the mica surface and set to deliver a fine mist of the dispersion using a pressure of 1.5 bar. This method allowed the water to flash evaporate from the surface of the mica. After approximately 0.5 ml of dispersion had been dispensed, the sample was rinsed by immersion in a water bath for 30 seconds and gently dried with compressed air. The remaining 0.5 ml of dispersion was applied and the sample rinsed again.

Preparation of a typical graphene film was carried out immediately after centrifugation (CF) by vacuum filtration of the dispersion through nitrocellulose membranes (pore size 25 nm) or alumina membranes (pore size 20 nm, Whatman Anodisc) supported on a fritted glass holder. In some cases the resulting compact films were washed with water and dried overnight in a vacuum oven at room temperature at 10^{-3} mbar. The film thickness, t , was estimated from the known deposited mass per unit area, M/A using $t = M/A\rho$, where ρ is the film density. While the density was not precisely known, it was estimated as 2000 kg/m^3 , as these films were not expected to display significant porosity by analogy with graphene oxide films [75].

Electrical conductivity measurements were carried out with a four-probe method using a Keithley 2400 source meter. A linear array of four electrodes of length l were placed on the sample using silver paint. A DC current, I , was applied across the outer two electrodes with voltage, V , measured across the inner pair of electrodes. For voltage electrodes separated by width w on a film of thickness t , the resistance R was given by the inverse of the slope of the measured $I - V$ plot. R is related to the film resistivity ρ via

$$R = \frac{\rho w}{lt} = \frac{R_s w}{l} \quad (6.1)$$

where R_s is defined as the sheet resistance of the thin film (units of Ω/\square). The conductivity, σ , of the film was then given by $\sigma = 1/\rho$ such that $\sigma = 1/R_s t$.

XPS analysis was performed in a system equipped with a VG CLAM II electron analyzer and PSP twin anode source. Mg $K\alpha$ ($h\nu = 1253.6 \text{ eV}$) spectra were recorded at 10 eV pass energy and 2 mm slits, yielding an overall energy resolution of 0.85 eV. Samples were introduced via a loadlock and measurement base pressure was better than 10^{-9} mbar. Thermogravimetric analysis (TGA) was carried out using a Perkin Elmer Pyris 1 TGA in an oxygen atmosphere. The temperature was scanned from 25 to 900 °C at 10 °C/min. The optical transparency of deposited films, when required, was determined by comparing the transmitted intensity of a HeNe laser (632 nm) through the film to the transmitted intensity through the filter membrane alone. Mild annealing of some of these deposited films (on alumina membranes) was carried out in a GERO

Hochtemperaturöfen GmbH tube furnace. Electrical measurements to determine the sheet resistance of the films were made using a four probe technique with silver paint as electrodes and a Keithley 2400 source meter.

6.3 RESULTS AND DISCUSSION

6.3.1 Dispersion Preparation and Optimisation

The sonication procedure used in this study produced pale grey dispersions of graphitic material as shown in Figure 6.1A, with a decanted dispersion after CF shown in Figure 6.1B. The dispersions were analysed first with UV-vis spectroscopy. Figure 6.1C presents typical spectra for an SDBS solution and a dispersion with initial graphite concentration, $C_{g,i}$, of 0.1 mg/ml. The absorption spectrum of the graphitic dispersion was flat and featureless, as expected from calculations based on quasi two-dimensional graphene and bi-layer graphene and from results based on graphene dispersed in solvents [10, 208]. Below 280 nm a strong absorption band is observed, this feature is attributable to absorption by the surfactant as it scales linearly with SDBS concentration, C_{SDBS} , whilst being independent of the dispersion concentration. Graphite was also expected to have an optical absorption feature near this region [209, 210] but it appears that the peak was largely obscured by the surfactant's absorption peak.

To estimate the extinction coefficient, α , for these graphitic dispersions, a large stock (~ 400 ml) of decanted dispersion with $C_{g,i} = 0.1$ mg/ml and $C_{SDBS} = 0.5$ mg/ml was prepared. A precisely measured volume of this dispersion was filtered under high vacuum onto an alumina membrane of known mass. The resulting compact but relatively thick film ($\sim 5 \mu\text{m}$) was washed with 1 L of water and dried overnight at room temperature under vacuum. The mass of the deposited material was then determined using a micro-balance. From TGA analysis of the film (analysis by Dr. Fiona Blighe, not shown), it was determined that approximately 64% of the film was graphitic; the remainder was attributed to residual surfactant. The high level of residual surfactant was not surprising as the thickness of the film made it difficult

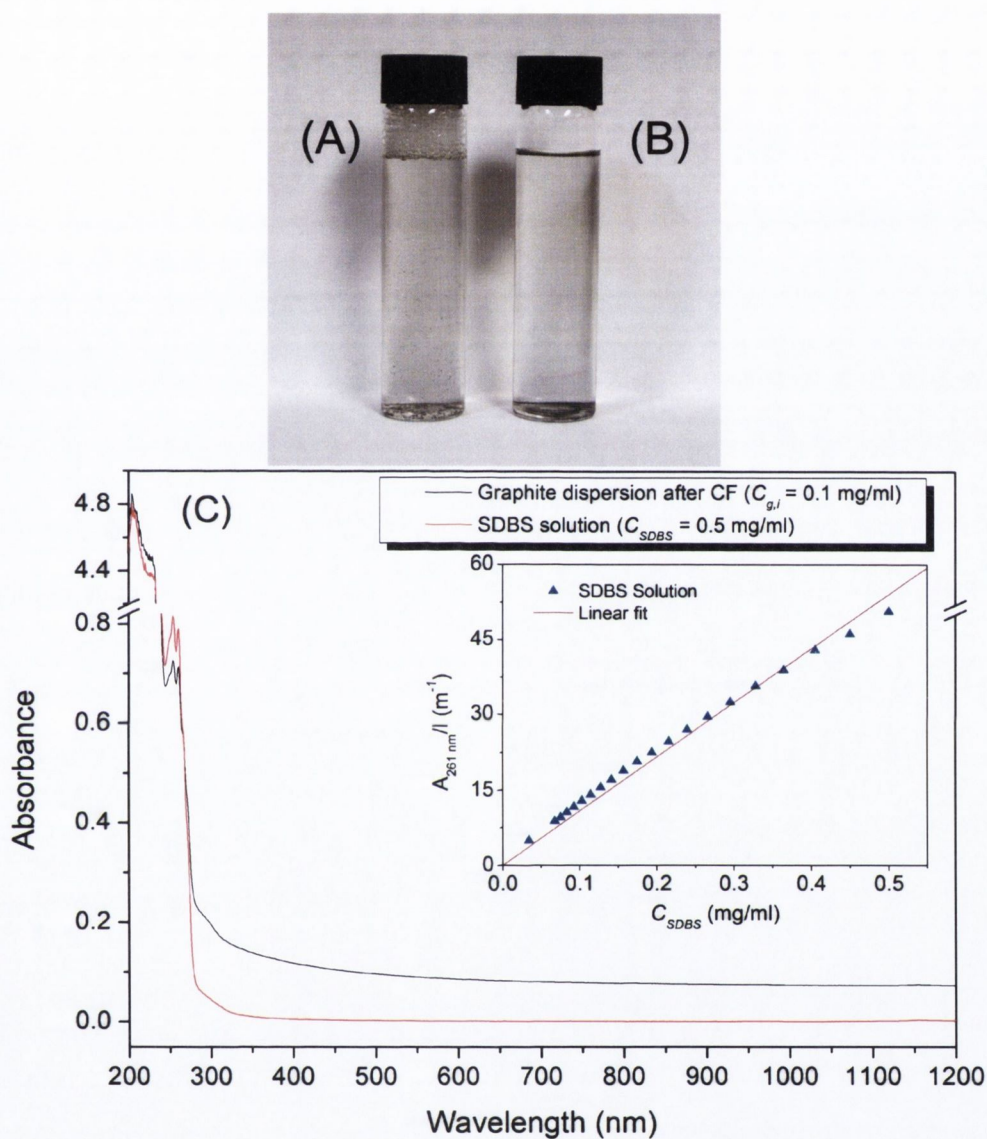


Figure 6.1: Photos of aqueous graphitic dispersions and optical absorbance spectra. (A) Graphitic dispersion after sonication. (B) Graphitic dispersion after centrifugation (CF). (C) Absorbance spectra of a typical graphitic dispersion after CF and a typical aqueous solution of SDBS. Inset: plot of absorbance of SDBS at 261 nm as a function of surfactant concentration, C_{SDBS} . C_{SDBS} was varied by serial dilution of a stock SDBS solution.

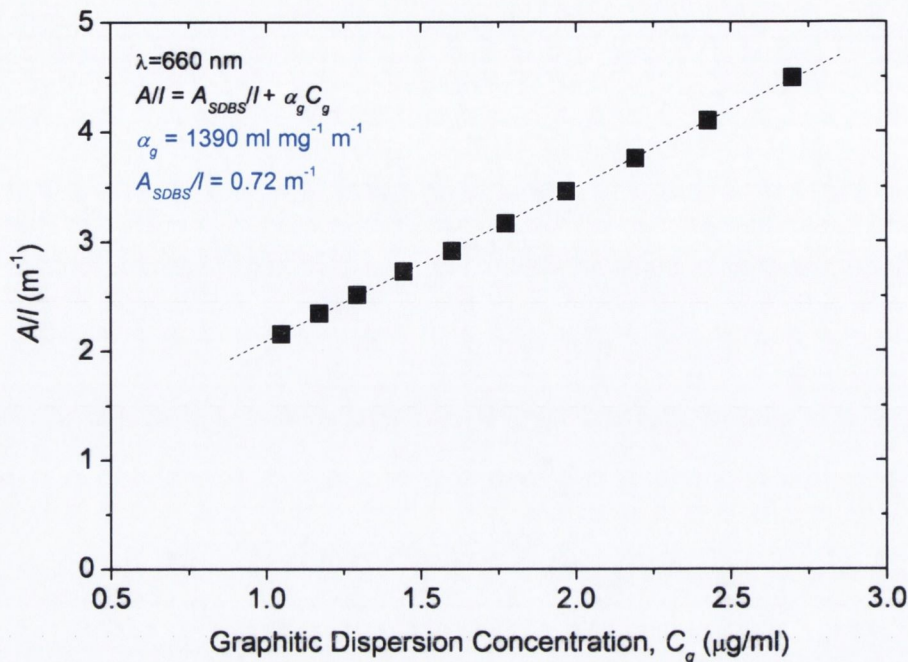


Figure 6.2: Absorbance per unit length ($\lambda = 660$ nm) as a function of dispersion concentration after centrifugation, C_g . Initial graphite concentration $C_{g,i} = 0.1$ mg/ml with $C_{SDBS} = 0.5$ mg/ml.

to remove the surfactant during film formation. Knowledge of the mass of graphitic material in the film allowed for the calculation of the dispersion concentration, C_g . A sample of the stock dispersion was then serially diluted allowing the measurement of absorbance per unit length (A/l) versus C_g , as shown in Figure 6.2. A straight line fit through these points gave the extinction coefficient at 660 nm, via Equation 4.5, as $\alpha_g = 1390 \text{ L g}^{-1} \text{ m}^{-1}$. This was in reasonable agreement with the value determined for graphene dispersed in solvents [10]. The non-zero intercept of 0.72 m^{-1} compared with the residual absorbance of SDBS at 660 nm of 0.5 m^{-1} for $C_{SDBS} = 0.5$ mg/ml.

Knowing α_g for these dispersions allowed the value of C_g to be determined for all future samples. In an early attempt to optimise the preparation conditions the weight percent ($100 \times C_g/C_{g,i}$) was used as a gauge of quality. The initial sample parameters of $C_{g,i}$ and C_{SDBS} were varied independently to find optimum values; this optimisation study was carried out by Dr. Yenny Hernandez. It was found that a maximum concentration after CF of $C_g = 0.05$ mg/ml could be achieved for $C_{g,i} = 14$ mg/ml when using a constant C_{SDBS} of 10 mg/ml, giving a fraction remaining

of 0.35 wt%. It was found that $C_{g,i} = 0.1$ mg/ml gave a yield of 3 wt%. Holding $C_{g,i}$ at this value, C_{SDBS} was then varied showing a maximum weight percent for C_{SDBS} between 0.5 and 1 mg/ml, with a fall-off in C_g below 0.5 mg/ml. The critical micelle concentration (CMC) of SDBS is known to be about 0.7 mg/ml [211, 212], and the observed fall-off in concentration was similar to the behaviour of CNT/SDBS systems below the CMC threshold [17, 27]. In this work, in order to keep the concentration of surfactant to a minimum, all subsequent experiments were performed on standard dispersions with surfactant concentration held close to the CMC ($C_{SDBS} = 0.5$ mg/ml, $C_{g,i} = 0.1$ mg/ml).

6.3.2 Evidence of Exfoliation

To further characterise the exact form of the nanocarbons in the dispersions, a detailed TEM analysis of a standard dispersion was conducted; this analysis was conducted jointly with Dr. Yenny Hernandez. TEM imaging revealed a large quantity of flakes of different types across a typical TEM grid, as shown in Figure 6.3. Some monolayer graphene flakes were observed as shown in 6.3A along with many monolayer protrusions from multilayered graphene stacks. A larger proportion of the flakes were few-layer graphenes including bilayer and trilayer material as shown in Figures 6.3B and C. Many of the objects exhibited folding of the graphene flake onto itself (Figure 6.3D) with a few instances of edge curling and scrolling (Figure 6.3E). A few very large and thick objects of the type shown in Figure 6.3F were also observed. It was found that these were graphite particles by the observation of protrusions of thin multilayer graphene. It is noteworthy that while these types of flakes were rare in number they contributed disproportionately by mass, e.g. in the measurements of extinction coefficient. It is likely that improved centrifugation and decanting procedures would remove such objects completely.

By carefully examining the edges of the flakes observed in TEM it was possible to count the number of graphene layers per flake for all but the largest multilayer particles. This is illustrated by the close-up TEM images of the edges of multilayered

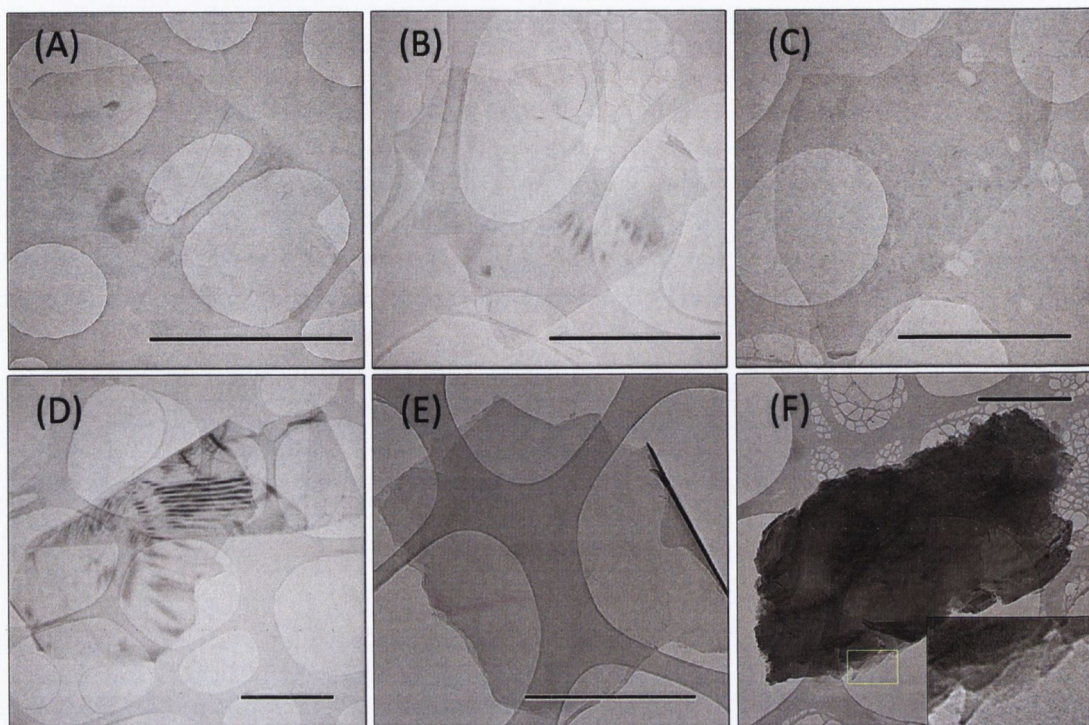


Figure 6.3: Selected TEM images of flakes produced by surfactant-assisted processing of graphite. (A) A monolayer graphene flake with a small patch of surface debris. (B) A bilayer graphene flake. (C) A trilayer graphene flake. (D) A folded multilayer flake. (E) A multilayer flake showing edge bending on right hand side. (F) A large and thick flake; inset showing magnification of marked edge with thin protruding graphene flakes. All scale bars are $1\ \mu\text{m}$ in length.

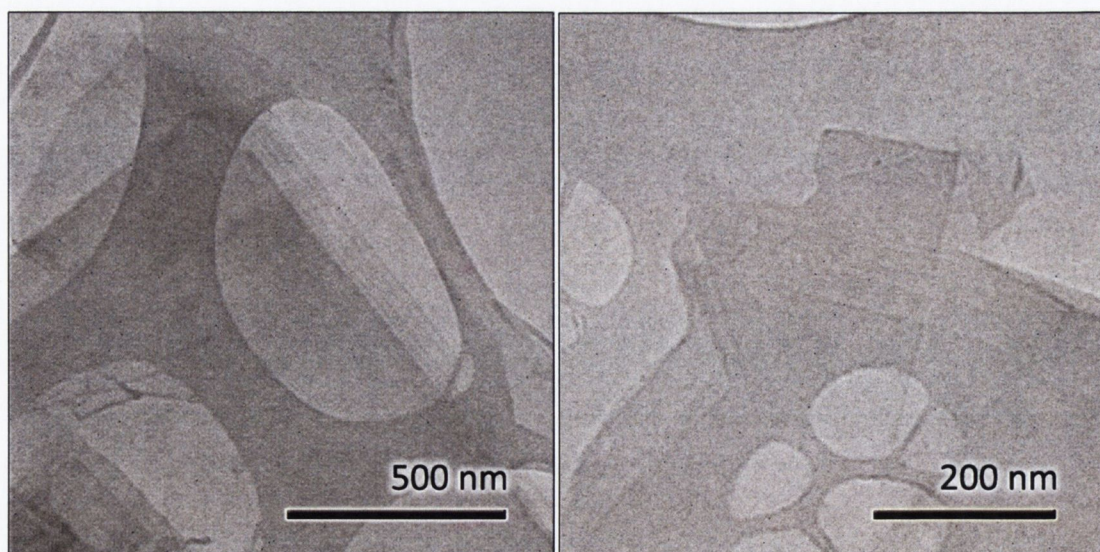


Figure 6.4: Close-up TEM images of graphene flake edges showing visible layered structure

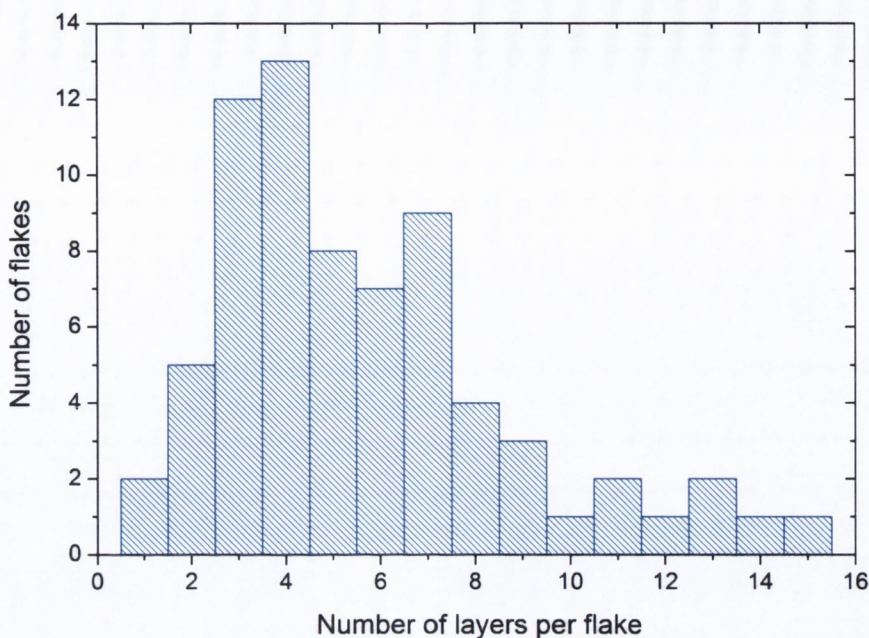


Figure 6.5: Histogram of number of layers per flake for a standard dispersion from surfactant-assisted processing of graphite, sample size of 71 flakes. The data does not include rare large objects of the type shown in Figure 6.3F.

flakes shown in Figure 6.4. A histogram of the data is presented in Figure 6.5. The data showed a good population of few-layer graphene with $\sim 43\%$ of the 71 flakes counted having < 5 layers. In general, the majority of these few-layer flakes had lateral dimensions ranging from 200 nm to $\sim 1\mu\text{m}$. Significantly, $\sim 3\%$ were monolayer graphene. While this is a relatively small percentage, it is broadly in line with the numbers observed in a range of solvents in the previous chapter, though not as good as NMP. Most importantly, the data confirms that monolayer graphene can be produced in aqueous media without the need for aggressive chemical treatment of the starting graphite material.

The TEM characterisation of these graphene flakes was extended further by the use of HR-TEM; this was carried out by Dr. Valeria Nicolosi at the University of Oxford. Shown in Figure 6.6A is a HR-TEM image of the edge of a trilayer graphene flake. In this image some non-uniformities are present which are likely due to contamination from residual surfactant on the graphene surface. The inset shows a fast Fourier transform (FFT) of the flake image, displaying hexagonal rings of spots characteristic of a graphitic structure. The information given by the FFT under the given imaging

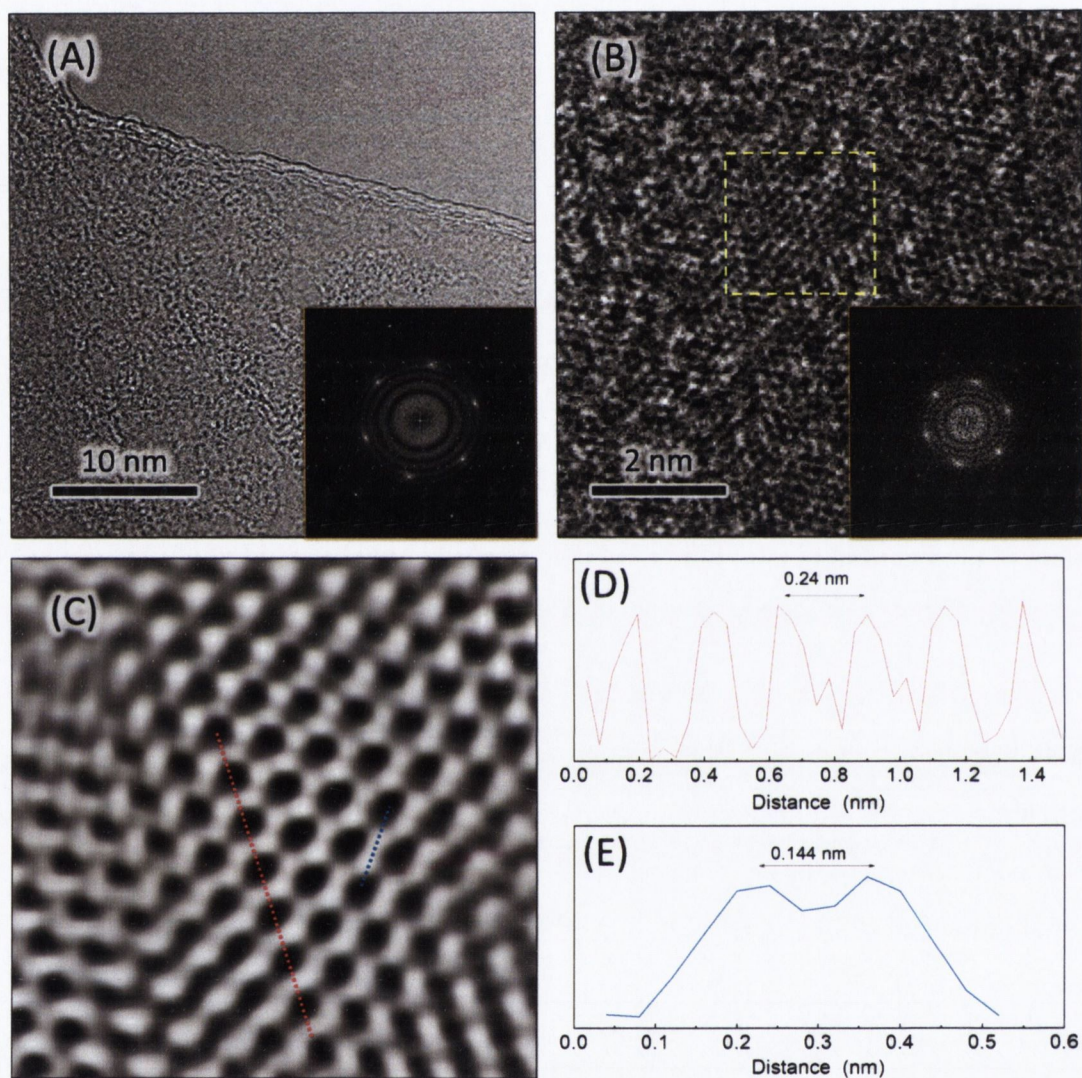


Figure 6.6: High-resolution TEM images of surfactant exfoliated graphene flakes. (A) HR-TEM image of a section of a trilayer graphene flake. Inset: fast Fourier transform of a portion of the image. (B) Aberration corrected HR-TEM image of a graphene monolayer. Inset: fast Fourier transform of the region enclosed by the yellow box. (C) Filtered image of marked region in image B. (D) Intensity cross-section along the red dotted line of image C showing graphene hexagon width of 2.4 \AA . (E) Intensity cross-section along the blue dotted line in image C showing C-C bond length of 1.44 \AA .

conditions is equivalent to an electron diffraction pattern [213]. The outer ring of {2110} spots are clearly brighter than the inner set of {1100} spots, thus confirming that the image is of a multilayer graphene flake [10]; the number of layers can be counted as three from the edge structure of the flake. Figure 6.6B is an image of a section of a graphene monolayer captured using an aberration corrected TEM; this machine compensated spherical C_s aberrations allowing spatial resolution up to 0.12 nm. In this case the FFT reveals {1100} spots that are more intense than the barely visible {2110} spots, confirming that this is an image of a graphene monolayer [10]. Again some non-uniformity is present in this image which can be attributed to either surface contaminants like residual surfactant or structural ripples along the graphene basal plane. The image in Figure 6.6B can be enhanced by using a low-pass filtering procedure (Fourier mask filtering using twin circular pattern masks and 5 pixel edge smoothing). This procedure has the effect of removing the artefacts and non-uniformity in a phase contrast HR-TEM image to reveal the underlying crystal structure. This has been done on the marked yellow box. The result, shown in Figure 6.6C, displays atomic resolution showing clearly the hexagonal atomic lattice of graphene. Examining the intensity of the image along the red dotted line, shown in Figure 6.6D, gives a hexagon width of 2.4 Å, very close to the expected value of 2.46 Å for graphene. Similar analysis along the blue dotted line gives the plot in Figure 6.6E, displaying a C-C bond length of 1.44 Å which is close to the expected value of 1.42 Å [214].

The TEM analysis clearly demonstrates that graphene can be produced in surfactant-based systems. It is important to note that at no stage of the analysis, using low-resolution and high-resolution imaging, was there any evidence of large-scale structural defects in the flakes. This strongly suggests that this exfoliation procedure is non-destructive. Further structural and chemical analysis of the flake quality will be given later in this chapter.

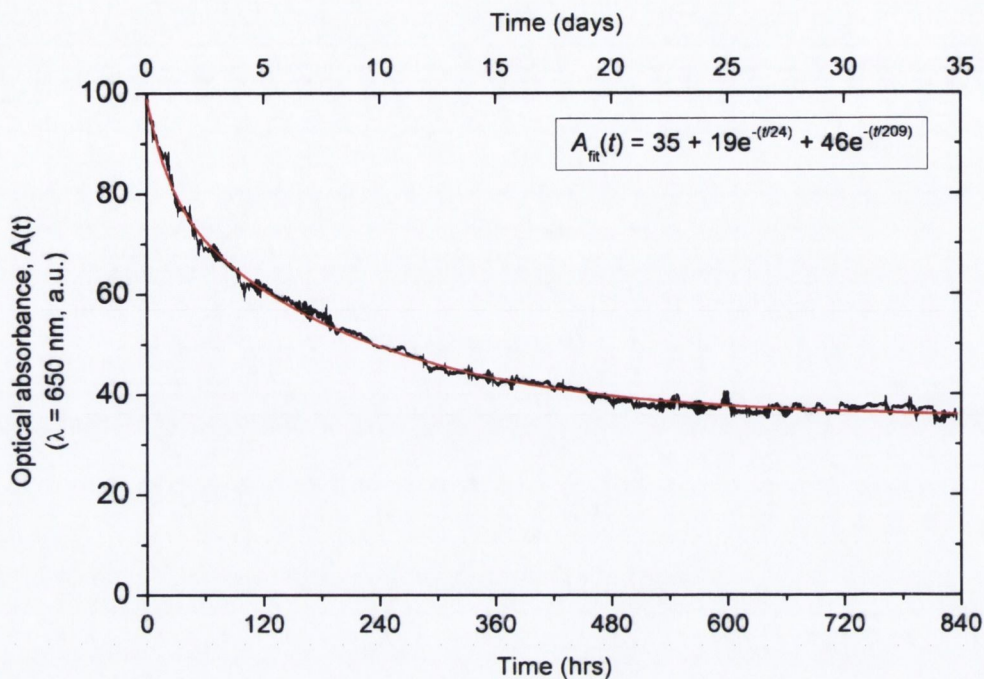


Figure 6.7: Sedimentation curve for a standard graphene/SDBS dispersion ($C_{SDBS} = 0.5 \text{ mg/ml}$, $C_g = 0.006 \text{ mg/ml}$). Optical absorbance at 650 nm as a function of time with bi-exponential decay fit.

6.3.3 Dispersion Stability

TEM analysis confirms the chosen method gives good exfoliation of graphite to produce graphene. The usefulness of the method in any potential application is heavily influenced by the temporal stability of the dispersions. After CF it was observed that these surfactant-stabilised graphene dispersions were quite stable, with only moderate sedimentation over time periods of months. This was also the case for systems with low surfactant concentrations, i.e. $C_{SDBS} = 0.1 \text{ mg/ml}$. As previously done for solvent-exfoliated graphene, the stability was quantified using sedimentation profiles for material retained after CF. The accumulated data over 5 weeks for a standard dispersion is shown in Figure 6.7. The measured absorbance fell steadily over an extended time frame. A bi-exponential decay curve was fitted to the data, indicating a stable phase of 35 wt%. The fit indicates that 19 wt% of the material fell out with a time constant of $\sim 24 \text{ hrs}$, with the 46 wt% slowly sedimenting over much a longer

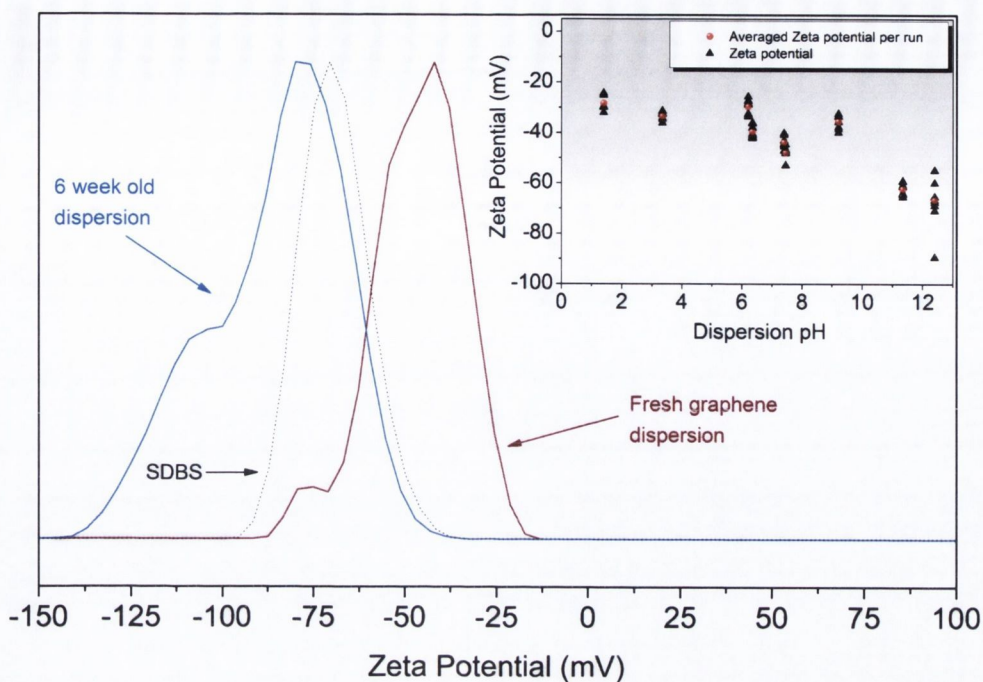


Figure 6.8: Zeta potential spectra for a fresh graphene/SDBS dispersion ($C_{SDBS} = 0.5 \text{ mg/ml}$, $C_g = 0.006 \text{ mg/ml}$), an SDBS solution ($C_{SDBS} = 0.5 \text{ mg/ml}$) and a six week old graphene/SDBS dispersion ($C_{SDBS} = 0.5 \text{ mg/ml}$, $C_g = 0.001 \text{ mg/ml}$). Inset: Zeta potential as a function of pH for the fresh graphene/SDBS dispersion.

time scale with a time constant of ~ 209 hrs. These results compare well with earlier data for solvent-based graphene dispersions.

In order to shed more light on the how the dispersions were stabilised the zeta potential was examined. In this system, graphene was prepared using the anionic surfactant SDBS. Thus, one would expect that the SDBS weakly attached onto the exfoliated graphene flakes (via physisorption) and imparted an effective charge. This mechanism has allowed the successful dispersion of CNTs in water using a range of surfactants. As discussed previously, the zeta potential is the potential at the interface between the tightly adsorbed surfactant molecular ions and the diffuse region of the electrolytic double layer (EDL). Thus, it directly quantifies the electrostatic repulsion between charged surfactant-coated flakes and gives a measure of stability. The zeta potential was determined using the Henry equation given in Equation 4.11 and applying Smoluchoski's approximation for spherical or plate-like particles such that

$\zeta = \eta\mu/\epsilon_r\epsilon_0$, where η is the solution viscosity and μ is the measurable electrophoretic mobility.

As shown in Figure 6.8, a peak zeta potential of -44 mV was observed in a fresh graphene/SDBS dispersion. This value is well beyond the -25 mV threshold for colloidal stability of negatively charged particles, indicating good dispersion stability with a minimal tendency towards re-aggregation of flakes. The small shoulder at -76 mV is likely due to free SDBS in the dispersion as this peak matches well with the peak for pure SDBS at $C_{SDBS} = 0.5$ mg/ml.

The pH of the fresh dispersion was also varied by addition of HCl and NaOH, with the data shown in the inset. The natural pH of the fresh graphene/SDBS dispersion was 7.4, this agrees well with literature data for CNT/SDBS dispersions [212]. As the pH was raised by increased $[\text{OH}^-]$, there was a trend towards more negative zeta potential values. This suggests that inter-particle repulsions were increased as more charges were added to the negatively biased flakes. For acidic dispersions at lower pH values a less negative zeta potential was observed, consistent with charge neutralisation and destabilisation of the system. This zeta potential versus pH trend is in line with trends reported for graphene oxide and reduced graphene oxide [78]. By lowering the pH, the zeta potential approached the limit of stability of the system but did not switch sign, i.e. the isoelectric point was never reached. This is may be due to very high surface coverage of the graphene flakes by SDBS ionic molecules or a buffer action by the free surfactant in the dispersion.

For comparison, the zeta spectrum of a six week old sample is also shown in Figure 6.8 with main peak at -78 mV and shoulder at -103 mV. In this case the peak can be attributed to the free surfactant while the shoulder represents the graphene flakes. The drop in intensity of the graphene peak relative the SDBS peak was likely due to the drop in C_g over the six week period. The observed shift of the graphene peak to a more negative zeta potential indicates that the electrophoretic mobility, μ , increased in magnitude. It is plausible to suggest that this was caused by a shift in the mean flake diameter towards smaller and hence more mobile flakes. To test this theory TEM analysis of the aged dispersion was carried out. This showed that only small flakes remained in the dispersion after six weeks. These were typically few-layer graphene

with flakes less than 500 nm in diameter. This can be linked to the sedimentation analysis suggesting the presence of a non-sedimenting phase. Taking the evidence from TEM, sedimentation and zeta potential data together one can suggest that the first sedimenting phase consists of large flakes (fragments of graphite) that inadvertently remained in the dispersion after CF, these are flakes of the type shown in Figure 6.3F. Medium sized flakes can be identified as those towards the right side of the distribution in Figure 6.5, which fall out of the dispersion over the 6 week period. This leaves small flakes remaining in the dispersion that display an increase in $|\mu|$ and hence an increase in $|\zeta|$ compared to the fresh dispersion.

6.3.4 Stabilisation Mechanism

Having examined the stability of these graphene/SDBS dispersions, one can now consider the underlying stabilisation mechanism. This can be achieved through the application of DLVO theory. This theory examines the interactions between charged species inside an electrolyte. In our case the SDBS molecular ions have adsorbed onto the graphene flakes imparting an effective charge with free surfactant ions and sodium counterions making up the surrounding electrolyte. The balance of repulsive and attractive forces between the charged colloidal particles will dictate whether a given dispersion will remain stable or collapse following aggregation of the particles.

The above zeta potential data quantifies the electrostatic repulsion between the graphene flakes. This can be used to derive the repulsive potential energy between two charged flakes of area A separated by a distance D via Equation 3.19

$$V_{DLVO} \approx 4A\epsilon_r\epsilon_0\kappa\zeta^2e^{-\kappa D}$$

The term κ is the inverse of the Debye screening length and relates back to the size of the EDL. This can easily be calculated using Equation 3.11:

$$\kappa = \sqrt{\frac{e^2 \sum n_i z_i^2}{\epsilon_r \epsilon_0 kT}}$$

Knowing that C_{SDBS} was 0.5 mg/ml (500 g/m³), with SDBS having a molar mass of 348.48 g/mol, gives the number density of surfactant molecules as $n_0 = 8.6 \times 10^{23} \text{ m}^{-3}$.

Each molecule dissociates to give two ions each having charge of magnitude 1. Thus, in our system the Debye length can be written as

$$\kappa^{-1} = \sqrt{\frac{\epsilon_r \epsilon_0 kT}{2e^2 n_0}} \quad (6.2)$$

Plugging in the dielectric constant of water $\epsilon_r = 80$ and absolute temperature taken as $T = 293$ K gives $\kappa^{-1} = 8.1$ nm for this graphene/SDBS system. Knowing κ and the experimental data for $\zeta \sim 50$ mV means V_{DLVO} can be calculated.

The attractive forces between the graphene flakes can be modelled via the idealised van der Waals interaction between two discs. To a first approximation the van der Waals interaction can be treated in isolation from the solvent. In this case, the total attractive potential, V_{vdW} , can be written as Equation 3.18

$$V_{vdW} = \frac{A\pi\rho^2C}{2D^4}$$

where ρ is the atomic areal density and C is a constant of proportionality. This equation can be reduced by relating the V_{vdW}/A to the energy required to separate two sheets in graphite from their van der Waals minimum at separation $d_0 = 0.35$ nm [11] to infinity; this is the surface energy γ . The graphene surface energy has been roughly estimated in Chapter 5, using Figure 5.5, as ~ 70 mJ/m². Setting $V_{vdW}/A = \gamma$ and $D = d_0$ gives

$$\rho^2 C \approx \frac{2\gamma d_0^4}{\pi} = 6.69 \times 10^{-40} \text{ J m}^2$$

Thus, using these estimated parameters, the overall interaction potential energy $V_T \approx V_{DLVO} - V_{vdW}$ can be plotted as a function of sheet separation D for a typical graphene/SDBS dispersion. This is shown as V_T/A in Figure 6.9. From this graph it can be seen that the surfactant-stabilised graphene flakes feel a potential barrier as they approach each other. This repulsive barrier peaks at $V_{T,Max}$ for a given zeta potential and resists aggregation effects. This barrier is responsible for the stabilisation of the surfactant-coated graphene flakes.

It is worth noting that the value of $V_{T,Max}$, as derived so far, is a lower limit. This is because the attractive V_{vdW} component has been over-estimated. The calculation used to derive V_{vdW} treated the interaction as between parallel sheets in vacuum. In reality, the presence of the solvent, i.e. water, between the graphene flakes will screen

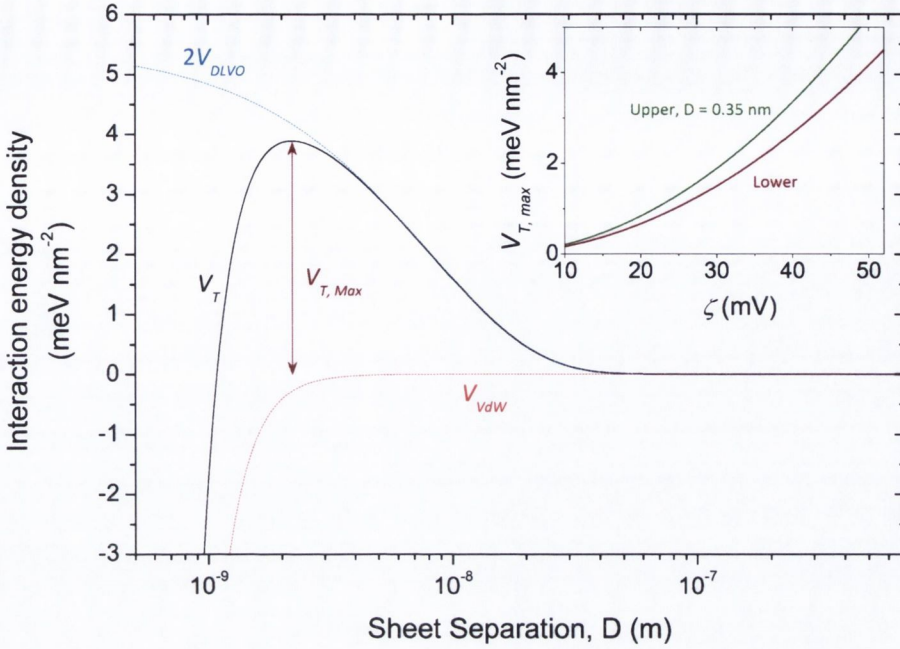


Figure 6.9: Plot of total interaction potential energy per unit area, V_T/A , as a function of separation D for two charged parallel sheets. Repulsive component V_{DLVO} and attractive component V_{vdW} also plotted. Inset: plot of lower and upper limits of the maximum net repulsive interaction energy $V_{T,Max}$ as a function of zeta potential.

the van der Waals interaction. The upper bound for $V_{T,Max}$ can be taken in the case of infinite solvent screening of the van der Waals interaction at the minimum possible sheet separation of 0.35 nm. This would mean treating V_{vdW} as negligible. This upper bound of $V_{T,Max}$ along with the lower bound are plotted in the inset of Figure 6.9. The curves are similar, with upper and lower bounds quite close together showing typical $V_{T,Max}$ values in the range 2 – 5 meV/nm² for ζ in the range 30 – 50 mV. These barrier values are quite large and would suggest a strong resistance to aggregation in the chosen sample.

As the derivation of V_T relied on several crude approximations, the numerical values derived can only reliably be used to compare similar graphene systems. This model serves to illustrate the physics underlying the stabilisation of graphene in aqueous surfactant-based systems. It shows that the observed stability can be related back to the electrostatic repulsion between charged colloidal particles and the fundamental attractive interactions between dispersed flakes.

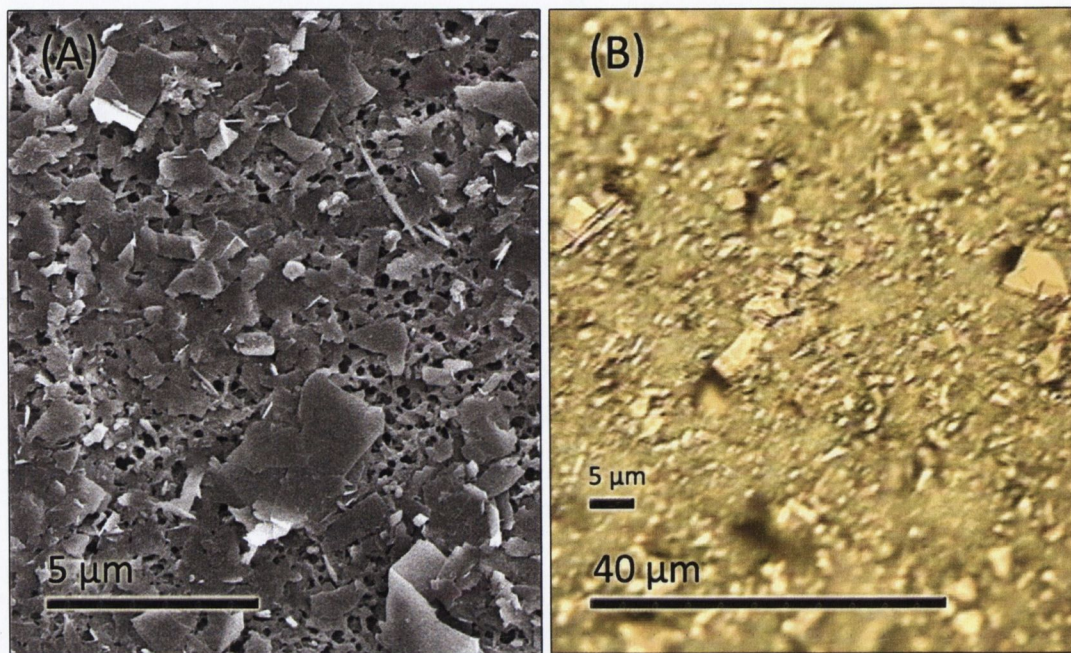


Figure 6.10: (A) SEM and (B) optical images of a typical graphene film made by vacuum filtration. Film thickness was estimated at 50 nm. In (A) thin regions of the film allow the porous nitrocellulose membrane to be visible.

6.3.5 Graphene Films - Characterisation

To examine the quality of the surfactant-assisted graphene dispersions and to explore potential uses thin films were cast by vacuum filtration of standard dispersions onto porous membranes. SEM and optical images of a typical film on a nitrocellulose membrane are shown in Figure 6.10. Similar films were also cast on alumina membranes.

The facile production of films of graphene as shown here enabled further characterisation of the flake quality. The novel electronic properties of graphene are highly sensitive to the presence of defects such as oxide functional groups. It was critical to determine whether the chosen exfoliation procedure damaged the physical or chemical make-up of the flakes. This was done by examining graphene films deposited on porous alumina membranes using Raman, FTIR and X-ray photoelectron spectroscopies.

Raman Spectroscopy

The deposited graphene films were initially characterised by Raman spectroscopy. Examples of typical spectra for a thin film deposited on an alumina membrane are shown in Figure 6.11. This film was similar to that shown in Figure 6.10 with large flakes embedded in a matrix of small flakes. All spectra were normalised to the intensity of the G-band. As per the starting graphite powder, the large flakes showed no D-band. This strongly supports the HR-TEM data that the processing used does not result in the formation of significant quantities of defects on the graphitic basal plane. The 2D-band of the large flake resembles that of graphite. This shows that the flake was > 5 layers [186, 190, 192]. This minimum thickness estimate and the large lateral dimensions means that such flakes are likely to be those that make up the rapidly sedimenting phase of the dispersions, as measured by Figure 6.7.

The spectrum for the small sub-micron sized flakes looked similar to that from films made using solvent-exfoliated graphene in NMP [10] (shown by the dashed black line in Figure 6.11). A small D-band was visible with intensity relative the G band similar to that seen in the solvent-exfoliated graphene. It is stressed that the spectral width and intensity of this D-band were far smaller than those seen in literature for graphene-oxide and reduced graphene-oxide [76, 79, 80, 215]. Also of note is the small size of the flakes relative the size of the laser spot and Raman spectroscopy resolution (estimated at $3\ \mu\text{m}$). Thus, while the presence of basal plane defects cannot be completely ruled out, it is reasonable to suggest that the observed D-band in the small flakes was largely due to edge contributions. The shape and intensity of this band, together with the absence of the D-band in large flakes, shows that the graphene films were composed of flakes with a low defect content.

The shape of the 2D-band for the small flakes can be examined with reference to literature (Figure 4.5). The shape is characteristic of thin flakes composed of less than five graphene layers. The 2D-band in Figure 6.11 was composed of a time-averaged value at a single laser spot location. To assess the uniformity of the film, a survey of the Raman spectra for the small flakes at over 30 random locations was carried out (by Ronan Smith). At every location the spectra were characteristic of flakes less than

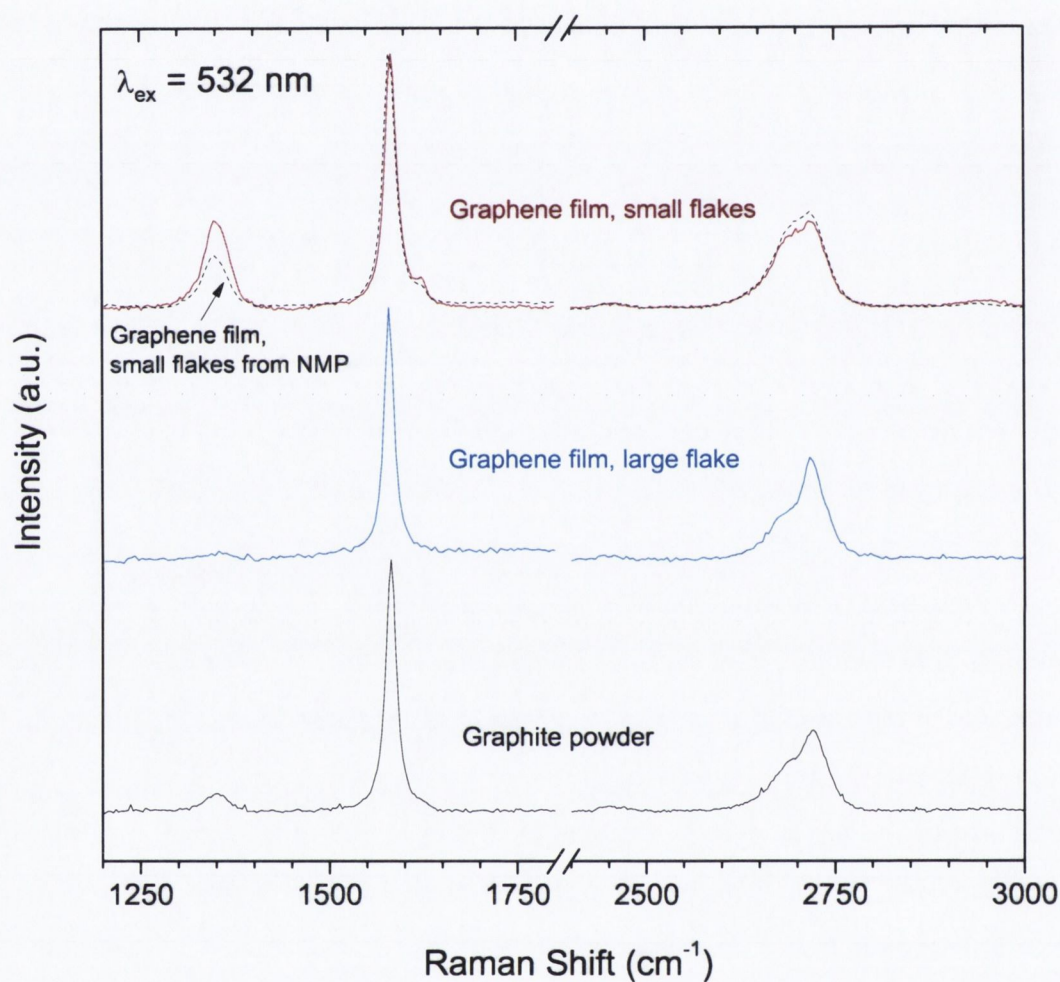


Figure 6.11: Raman spectra for a graphene film ($\sim 300 \text{ nm}$ thick) deposited on an alumina membrane and rinsed with 17.5 ml water. Spectra associated with small flakes ($\sim 1 \mu\text{m}$ or less) and a large flake ($> 5 \mu\text{m}$) are shown along with a reference spectrum for the starting graphite powder. The dashed line is a Raman spectrum from a comparable film of small flakes made using a graphene/NMP dispersion.

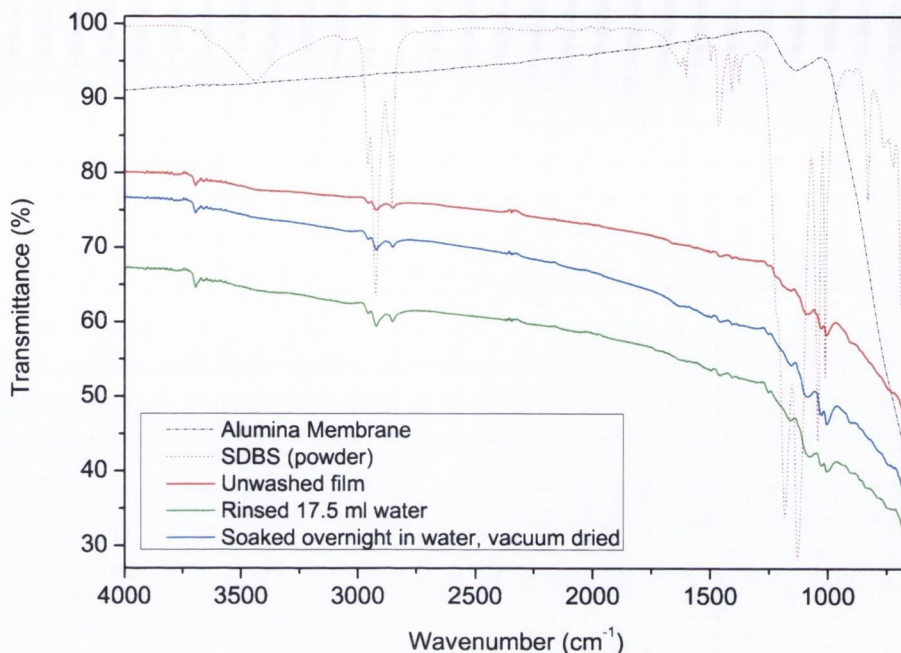


Figure 6.12: ATR-FTIR spectra of graphene films. Spectra for three graphene films having undergone three different washing regimes are shown. Films were ~ 300 nm thick and deposited on alumina. Reference spectra for the alumina membrane and SDBS are also shown.

five layers as shown in Figure 6.11. This shows that minimal aggregation occurred during film formation, with the small graphene flakes randomly assembling and not re-forming Bernal (AB) stacked graphite particles.

FTIR Spectroscopy

ATR-FTIR spectra were also acquired for ~ 300 nm thick graphene films. Figure 6.12 shows spectra for three films subjected to different washing regimes. These spectra show only very small features centred at 1100 cm^{-1} and 2900 cm^{-1} . By comparison to the reference spectra it is clear that these features are attributable to residual surfactant trapped in the film. While the observed peaks in FTIR spectra cannot be analysed quantitatively, it is clear that none of the various washing regimes succeeded in completely removing the surfactant. A key feature of the spectra in Figure 6.12 is the complete absence of peaks associated with C–OH (1340 cm^{-1}) and –COOH (1710 to 1720 cm^{-1}) groups [69, 71, 78, 81]. The spectra are in stark contrast to those provided

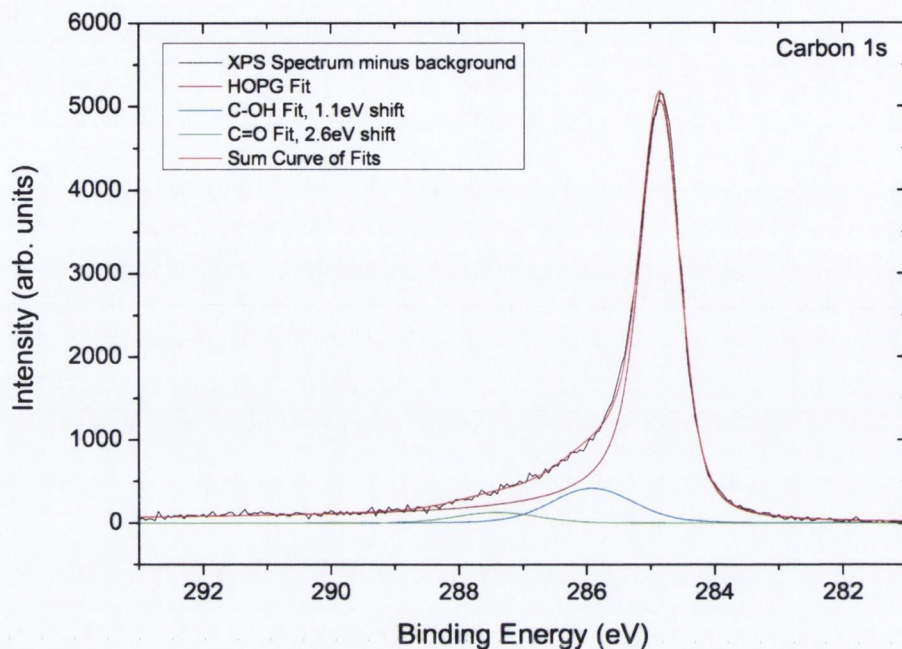


Figure 6.13: XPS spectrum for a thin graphene film produced by vacuum filtration and dried under vacuum. The Shirley background has been removed and empirical fits for C–OH and C=O have been added.

in literature for films made from reduced graphene oxide [69, 78] or chemically derived graphene [74, 80, 215]. This is further evidence that this surfactant-assisted exfoliation technique does not chemically functionalise the graphene/graphite and that the deposited films are composed of largely defect-free material.

X-Ray Photoelectron Spectroscopy

As a final test for the presence of functional groups, XPS spectra were taken for a very thin graphene film on alumina. This analysis was carried out by Zhiming Wang on a film of ~ 30 nm thickness, results are shown in Figure 6.13. The Shirley background has been removed to correct for asymmetry in the spectrum from inelastically scattered photoelectrons [216]. The spectrum was dominated by a feature near 285 eV that corresponded to the Carbon 1s core level - this was associated with the graphitic carbon from the film. There was no evidence of sulphur in the spectra, suggesting that the top few nanometres of the film were relatively free of surfactant.

In order to fully explain the observed spectra a manual fitting procedure was carried out. A spectrum for HOPG was recorded and additional small fitting components for C–OH and C=O were included, at 286 eV and 287.5 eV respectively [90, 217]. This gave the fitted red line in Figure 6.13 that closely matched the graphene film spectrum. Requiring these fits indicates that low levels of oxidation have occurred during the processing. However, the levels of any oxidation are very small. The main C–C peak makes up 86% of the C 1s spectrum. This is similar to that found in reduced graphene oxide films that have been thermally annealed to around 1100 °C under vacuum [218]. Taking these results together with the Raman and FTIR data indicates that while a very low level of oxidation is induced by the processing, there is minimal structural damage to the graphene flakes.

Optical and Electrical Properties

To test the optical and electrical properties of such films, the optical transparency and sheet resistance were recorded for a number of thin films deposited on alumina membranes, with thickness ~ 30 nm. These films had transmittance of $\sim 62\%$, determined by comparing the transmitted intensity of a 632 nm HeNe laser through the deposited film and the bare membrane. Sheet resistance values of ~ 970 k Ω/\square were measured, giving a DC conductivity of ~ 35 S/m. This was quite a low value but it was believed to be largely due to the presence of residual surfactant; as mentioned previously thick films contained around 35 wt% residual surfactant after washing. In an attempt to remove surfactant and promote better inter-flake contacts, the film was annealed at 250 °C in Ar/N₂ for 2 hrs. After annealing the transmittance was unchanged but the sheet resistance had fallen to 22.5 k Ω/\square , corresponding to a DC conductivity of ~ 1500 S/m. This value is still significantly lower than the ~ 6500 S/m measured for similar films produced using graphene/NMP dispersions [10] or from reduced graphene oxide [78].

When considering the usefulness of such thin films in electronic applications, a figure of merit given by the ratio of electrical to optical conductivity (σ_{DC}/σ_{opt}) is usually used. This can be calculated from

$$\frac{\sigma_{DC}}{\sigma_{opt}} = \frac{z_0}{R_s \left(\frac{1}{\sqrt{T}} - 1 \right)} \quad (6.3)$$

where $z_0 = 377 \Omega$ is the impedance of free space and T is the film transmittance. This ratio needs to be > 35 to meet the bare minimum industry requirements for rivalling ITO in transparent conductor applications, requiring for example $R_s < 100 \Omega/\square$ with transmittance $T > 90\%$ [219]. More stringent requirements even specify a need for $\sigma_{DC}/\sigma_{opt} > 220$ [219]. While a detailed study of the potential uses of graphene as a transparent conductor are beyond the scope of this thesis, it is worth briefly considering the above data in the context of this figure of merit. The post-anneal sample had $R_s \sim 22.5 \text{ k}\Omega/\square$ at 62% transmittance, giving $\sigma_{DC}/\sigma_{opt} \sim 0.06$. Subsequent work by our group has shown that using improved graphene/surfactant dispersions and better film preparation conditions can lead to DC conductivities around $1.5 \times 10^4 \text{ S/m}$ [220]. This represented a significant improvement with optimum films having $\sigma_{DC}/\sigma_{opt} \sim 0.4$, in line with the best results from chemically-modified graphene [219, 220]. These results indicate that surfactant-processed graphene films are not good enough for transparent conductor applications. It has been subsequently shown that regardless of the processing method, a network of such small graphene flakes will be limited by fundamental constraints [219]. However, it is clear that film formation using surfactant-processed graphene has many advantages including lack of toxicity, cost, scalability and ease of transfer to surfaces. Using nitrocellulose membranes, the samples can be easily transferred from to a range of substrates including PET, glass and quartz using acetone vapour. Such conductive films could be easily used in applications where transparency is not critical such as sensors or in electrodes in thin film capacitors and batteries.

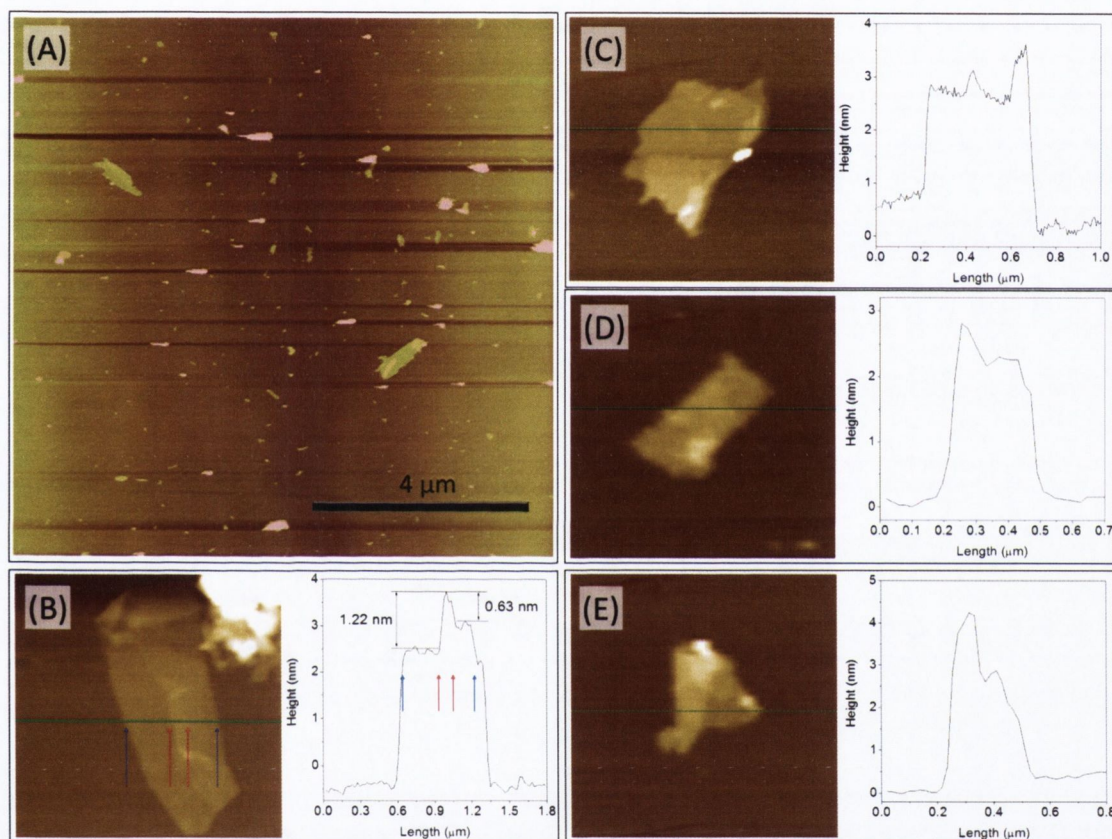


Figure 6.14: AFM images of spray deposited graphene. (A) $10\ \mu\text{m} \times 10\ \mu\text{m}$ scan showing large numbers of deposited flakes. (B) Individual flake, with cross section taken across green line, showing apparent folding. (C), (D) and (E) Magnified images of individual flakes with cross sections along green lines.

6.3.6 *Deposition on Surfaces - AFM Characterisation*

The work on surfactant-based graphene dispersions presented so far in this chapter has focused on characterising the dispersions and examining flake quality using vacuum filtered films. Depositing individual graphene flakes onto flat solid surfaces is important for characterisation by scanning probe analysis and for other studies that require isolated graphene. Such deposition can be problematic for graphene exfoliated in amide solvents as the solvent's high boiling point leads to slow evaporation, allowing sufficient time for extensive re-aggregation to occur [10]. While the aqueous system considered here allows for facile solvent removal, the problem of residual surfactant remains. In an extensive study, carried out jointly by myself and Paul J. King, several methods were explored to deposit a standard graphene/SDBS dispersion. Three different substrates were considered: SiO₂/Si, SiO₂/Si functionalised with 3-aminopropyl-triethoxysilane (ATPS) and mica. These substrates are commonly used for scanning probe characterisation of CNT dispersions [25, 27, 35, 36, 38, 39, 158, 221, 222]. The standard dispersion was applied to these substrates by a number of methods including drop-casting, dip-coating, spin-coating and spraying. In most cases, the results either showed lack of adhesion of graphene to the substrate or excessive coverage with SDBS. This is not surprising given that, per unit volume of dispersion, the surfactant typically had two orders of magnitude higher mass than the graphene flakes. Thus, it was necessary in this study to remove the excess surfactant after deposition. The optimum procedure involved spray casting the dispersion onto freshly cleaved mica, followed by gentle rinsing with water. We speculate that the mica substrate worked well due to the residual surface charge after cleavage [221]. It is likely that improvements in the concentration of dispersed graphene relative to the surfactant will make future deposition easier, facilitating the use of some of the other techniques mentioned above.

A sample of the AFM images obtained is shown in Figure 6.14. Large numbers of flakes can be seen in the 10 μm \times 10 μm AFM image. In addition, a small number of aggregates with heights $>$ 12 nm were observed. The largest flakes were similar in

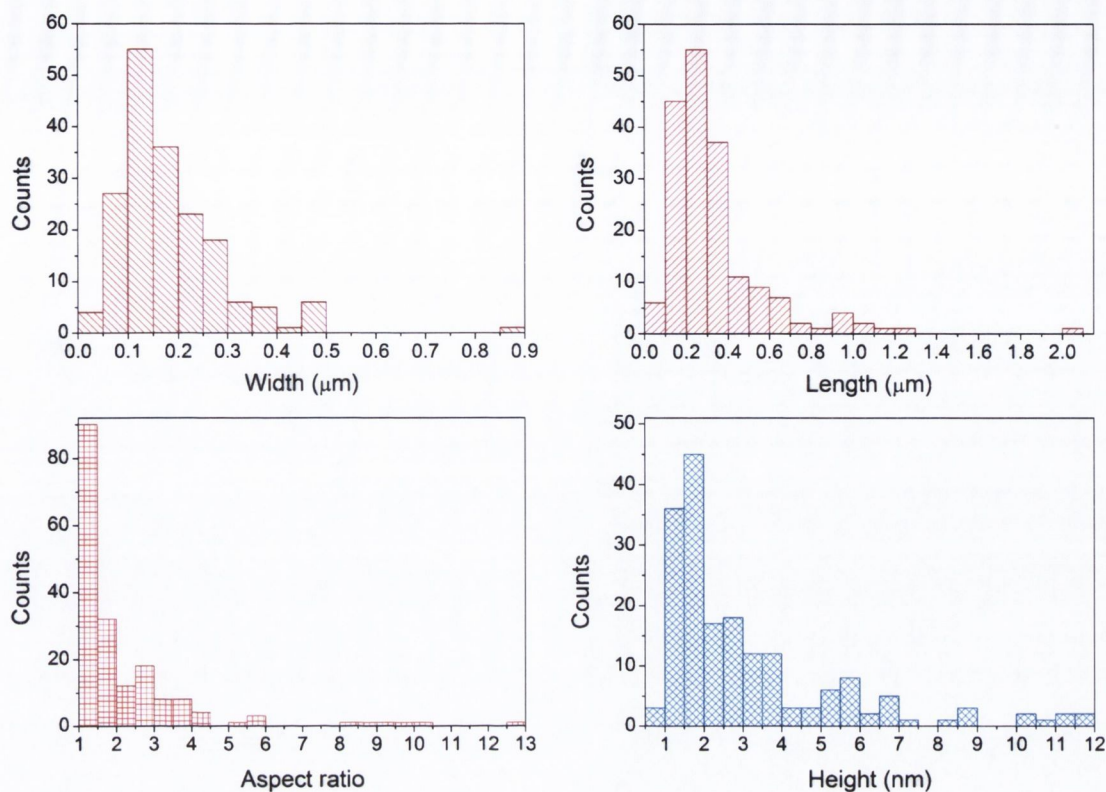


Figure 6.15: Statistics derived from AFM analysis of 182 graphene flakes deposited on mica.

lateral size to those observed in TEM, a typical example is shown in Figure 6.14B with some debris in the top right corner of the image. This flake shows interesting step height features across what appear to be flake folds similar to those observed in TEM imaging (Figure 6.3D), the red arrows marks steps of 1.22 nm and 0.63 nm. These features are consistent with bilayer and monolayer step heights, as literature sources report monolayer graphene having heights ~ 1 nm [77, 223, 224]. Figures 6.14C, D and E show small flakes with cross sections for each. It is worth noting that although monolayer graphene has thickness around 0.4 nm, substrate-tip interactions, residual material (in this case surfactant), humidity and different tip oscillation settings in tapping mode AFM can result in shifts of observed monolayer graphene heights of around 1 nm [225].

This AFM analysis was extended by examining images of a large number of flakes (182), ignoring aggregates with height > 12 nm, to yield a distribution of flake dimensions (height, length and width). This data is presented in Figure 6.15. The lateral dimensions of length and width were corrected for tip distortion by subtracting 50 nm.

The data shows that $\sim 10\%$ of flakes had thickness ~ 1 nm, consistent with monolayer graphene. The length and width data indicate peaks of ~ 250 nm and ~ 150 nm, these are significantly different to the TEM data where the majority of thin flakes were ~ 1 μm wide. It is possible that this discrepancy is due to small flakes being washed through the holes in the TEM carbon mesh, thereby biasing the TEM results. Alternatively, it is possible that the larger flakes were more unstable towards the water rinsing process and were preferentially removed. The aspect ratio data show most flakes had length/width ratios up to 2, though some ribbons were observed with aspect ratios approaching 13.

As mentioned above, some aggregated material with height > 12 nm was observed, with some of these objects having lateral dimensions ranging from 300 nm to ~ 2 μm . As some of these objects have relatively small lateral dimensions they cannot be associated with the large flakes seen in TEM or observed to be embedded in deposited graphene films. It is proposed that these are clusters of small exfoliated graphene flakes that re-aggregated during the AFM deposition process. Spraying the surfactant-based dispersion onto the heated mica substrate yielded significant quantities of exfoliated graphene but also an extensive coating of SDBS. The subsequent rinsing was necessary to remove this SDBS residue. It can be speculated that this washing not only removed SDBS from the mica surface but also from the deposited graphene. At the very least, some of the graphene flakes were likely to be mobile during the rinsing process; if these flakes were mobile and deficient in surfactant coating then aggregation was likely. These aggregates would then be left behind on the substrate. This assessment is supported by the strong dependence of the aggregation observed on the deposition processes used and the details of the washing/drying process. The data presented here relates to the optimum deposition process that was found for this system. Despite the presence of some aggregates, thin exfoliated graphene material can be easily observed, opening the way for further characterisation of individual deposited flakes.

6.4 CONCLUSIONS

This work was the first of its kind, demonstrating a method to produce graphene in surfactant/water solutions with the aid of ultrasound. The method is simple, cheap, safe and scalable, requiring only graphite, water and surfactant without the need for aggressive chemical treatments. The process yields large quantities of few-layer graphene with < 5 layers, with smaller quantities of monolayer material. TEM analysis shows these flakes are of high quality. The exfoliated graphene flakes are reasonably stable with larger flakes sedimenting out time-scales of ~ 6 weeks. The system is well described by colloidal theory and is shown to be stabilised against re-aggregation by a potential barrier that derives from the electrostatic repulsion between surfactant-coated flakes. The liquid-phase dispersions readily permit the formation of thin and thick films of randomly oriented graphene via vacuum filtration. The dispersions can also be spray cast to give isolated individual flakes for further study, with the potential to scale up the spraying process to give very thin networks of flakes. AFM analysis of small deposited graphene flakes shows heights consistent with monolayer material. Characterisation of ensembles of these flakes in film form, by Raman, FTIR and XPS analyses, confirms the quality of the material with only low levels of defects or oxides on the graphene basal plane. The films can be made semitransparent and are reasonably conductive, making them suitable for a range of potential future applications. This work enhances the field of liquid-phase graphene processing, with improvements to the dispersion processing and film formation anticipated. Some of these improvements were pursued as part of this thesis and are dealt with in the next chapter.

HIGH-CONCENTRATION SURFACTANT STABILISED GRAPHENE DISPERSIONS

7.1 INTRODUCTION

The work presented in the Chapter 6 showed that graphene can be successfully produced via mild sonication of graphite in surfactant/water systems. It was shown that the chosen processing conditions yielded dispersions of pristine, largely few-layer graphene with final concentrations < 0.01 mg/ml. The simple method used boasts significant advantages including negligible cost, scalability and high safety. However, with such low graphene concentrations, the dispersions shown up till now are completely impractical for many applications. Graphene oxide, by comparison, can be prepared with concentrations around 1 mg/ml in organic solvents [76, 84, 86, 226] and in water at concentrations up to 7 mg/ml [217]. In order to gain full advantage from dispersions of pristine graphene using surfactant/water systems, the dispersion concentration needs to be greatly improved whilst maintaining high graphene quality. The goal of the work shown in this chapter is to prepare aqueous surfactant-stabilised dispersions of graphene at high concentrations, building on earlier results that used mild sonication of graphite followed by centrifugation. This was attempted by optimising various experimental parameters and employing long bath sonication times (up to 430 hours).

7.2 EXPERIMENTAL PROCEDURE

Natural flake graphite was used in all experiments (Branwell Graphite Ltd, Grade RFL 99.5, cost $\sim\text{€}3$ kg⁻¹) and used as provided. Sodium cholate (SC), purchased from

Sigma Aldrich (SigmaUltra > 99%), was dissolved in Millipore water and made up to various concentrations between 0.01 and 20 mg/ml. Typical graphene dispersions were prepared by adding graphite at initial graphite concentration of $C_{g,i} = 5$ mg/ml using a total sample volume of 400 ml SC solution in 500 ml capped round-bottomed flasks. Ultrasonication was carried out in a low power sonic bath. The nominal power output of the bath was rated at 80 W but the true output was estimated at 16 W, this was done by measuring the temperature increase while sonicating a known mass of water. The sonic bath typically operates at a temperature of around 60 °C. However, due to the long sonication times used in these experiments, continuous re-filling of the sonic bath water by siphoning from a reservoir was needed to maintain sonication efficiency and prevent overheating. Samples extracted from the flasks by pipette were left to stand overnight to allow any large unstable graphite aggregates to form and then centrifuged in 14 – 28 ml glass vials for either 30 or 90 minutes. Centrifugation rates of 500 – 5000 rpm (25 – 2500g) were used. After centrifugation the top two thirds of the dispersions were extracted by pipette and retained for use.

Optical absorption measurements and sedimentation measurements were performed as before. Samples for TEM analysis were prepared as before on holey carbon grids (400 mesh). Bright-field TEM images were taken with a Jeol 2100, operated at 200 kV. Energy filtered TEM (EF-TEM) images were taken with the FEI Titan operating at 80 kV, selecting the carbon energy loss spectrum using a 15 eV plasmon window centred at 25 eV.

Deposited films were prepared by vacuum filtration onto porous mixed cellulose ester membranes (Millipore, 0.025 μm pore size, 47 mm diameter). Thin deposited films were transferred onto glass slides by wetting with isopropanol to remove trapped air between the film and substrate to improve adhesion. The glass slide was then saturated with an acetone vapour and immersed in acetone baths followed by a rinse in a methanol bath to complete the removal of cellulose. Free-standing films were prepared by vacuum filtration onto porous alumina membranes (Millipore, 0.2 μm pore size, 47 mm diameter) and drying in a 70 °C oven. TGA analysis was performed on a Perkin-Elmer Pyris 1 in an oxygen atmosphere.

The dispersion preparation, optimisation of experimental parameters, and film preparation shown in this chapter were carried out jointly with Paul J. King.

7.3 RESULTS AND DISCUSSION

7.3.1 *Production of High-Concentration Graphene Dispersions*

The method chosen in this work for preparing graphene dispersions required the use of sonication followed by centrifugation. Thus, it was expected that optimising the dispersion parameters would enhance the final graphene concentration and dispersion quality. The main parameters considered were the initial graphite concentration ($C_{g,i}$), the surfactant concentration, the CF rate (ω) and the sonication time (t_{sonic}).

The other key component of the system is the chosen surfactant. In Chapter 6 SDBS was selected because it had been proven to be effective in dispersing carbon nanotubes [27]. However, there are many surfactants available. A brief study of a selection of seven different surfactants was carried out, using fixed initial graphite concentrations, fixed sonication times and fixed CF rates at a variety of surfactant concentrations. The surfactants tested were SDBS, sodium dodecyl sulfate (SDS), lithium dodecyl sulfate (LDS), sodium decyl sulfate (SDeS), cetyl trimethylammonium bromide (CTAB), household Fairy liquid and sodium cholate (SC). In this initial study, sodium cholate performed the best (molecular sketch given in Figure 2.6), being readily soluble in water up to very high concentrations and giving a high yield of graphene. It was used for all experiments shown in this chapter. The reader is referred to subsequent work led by Ronan Smith for a detailed study of the use of a wide range of ionic and non-ionic surfactants for graphene dispersion [227].

The first part of this study determined the optimum sodium cholate concentration (C_{SC}), using fixed parameters $C_{g,i} = 5 \text{ mg/ml}$, $t_{sonic} = 24 \text{ hrs}$ and CF time 30 min at $\omega = 1000 \text{ rpm}$. The initial sonication time and CF rate were chosen based on work done in our group with graphene/NMP dispersions [228]. The reasonably high initial graphite concentration was chosen as the aim of the study was to maximise the

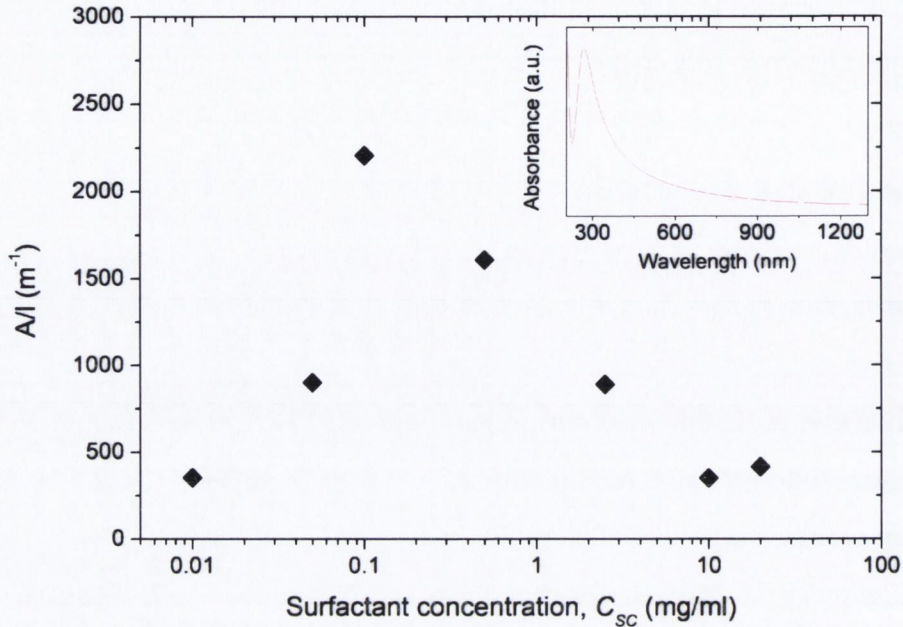


Figure 7.1: Absorbance per unit cell length as a function of sodium cholate concentration.

$$C_{g,i} = 5 \text{ mg/ml}, t_{sonic} = 24 \text{ hrs}, \omega = 1000 \text{ rpm for 30 min.}$$

final dispersed graphene concentration. It is noted that the chosen sonication time was already much longer than that used for the earlier graphene/SDBS systems. The measured absorbance per unit cell length at 660 nm after CF (A/l) was used to measure efficiency as a function of surfactant concentration, this data is shown in Figure 7.1. Also shown in the inset of Figure 7.1 is a typical absorbance spectrum for these dispersions. As expected, and seen before with graphene/SDBS dispersions, the spectrum was mostly flat and featureless. However, for these higher concentration dispersions an inter-band absorption feature around 270 nm characteristic of graphite/graphene was observed [78, 209, 210].

From Figure 7.1, it is clear that the dispersion concentration peaked strongly for $C_{SC} = 0.1 \text{ mg/ml}$. This is somewhat surprising as the optimum value was expected to be closer to the CMC of SC ($\sim 5 \text{ mg/ml}$), as was observed for graphene/SDBS dispersions. The new data indicates that the CMC is not an important parameter for the graphene/sodium cholate system at least. The reason for the observed behaviour is not clear. One can speculate that it may be due to the 2D nature of the graphene flakes, whereby the surfactant cannot encapsulate a given flake (micelle size typical a few

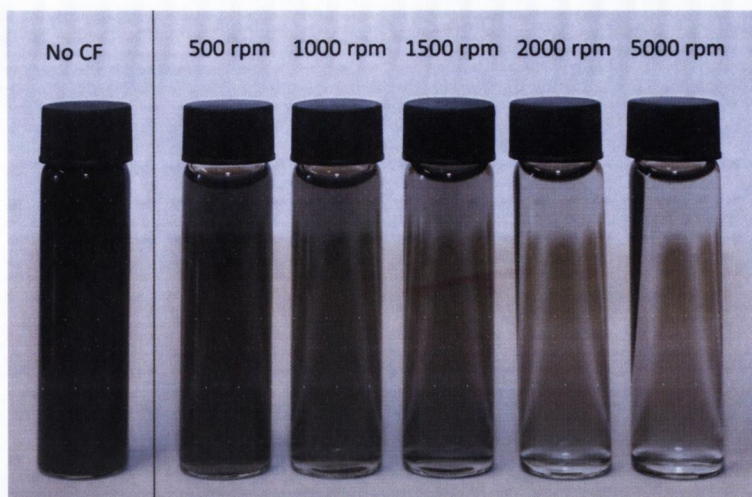


Figure 7.2: Photos of surfactant stabilised dispersions. Left, as-prepared stock dispersion without centrifugation. The centrifuged samples have been diluted by a factor of 10 to highlight the concentration change.

nm, flake sizes > 100 nm) but rather randomly adsorbs onto the flake surface. In this scenario the presence of micelles in the surrounding surfactant solution may not be necessary. If this is the case, the earlier linking of optimum SDBS concentration with CMC may have been incorrect. Another puzzling attribute of Figure 7.1 is the behaviour at higher surfactant concentrations where a fall-off in dispersion concentration is observed. The reason for the observed behaviour remains unknown. Nevertheless, the optimum concentration found here is lower than the $C_{SDBS} = 0.5$ mg/ml used before which should assist residual surfactant removal. Thus all subsequent dispersions, unless stated otherwise, were prepared with $C_{SC} = 0.1$ mg/ml.

The next dispersion parameter studied was the CF rate. A stock graphene dispersion was prepared with $C_{g,i} = 5$ mg/ml and $t_{sonic} = 24$ hrs, with portions centrifuged at different rates from 500 – 5000 rpm (25 – 2500 g) for 90 min. 90 min CF times were chosen for this and all subsequent experiments as it was found to be more effective at removing graphite starting material and aggregates than a 30 min CF. In all cases the dispersions were very dark, even after CF. On dilution, a gradation in concentration was apparent, as shown in Figure 7.2.

In order to properly assess the concentrations of these dispersions, the extinction coefficient, α_g , needed to be determined. This was done by measuring A/l at 660 nm

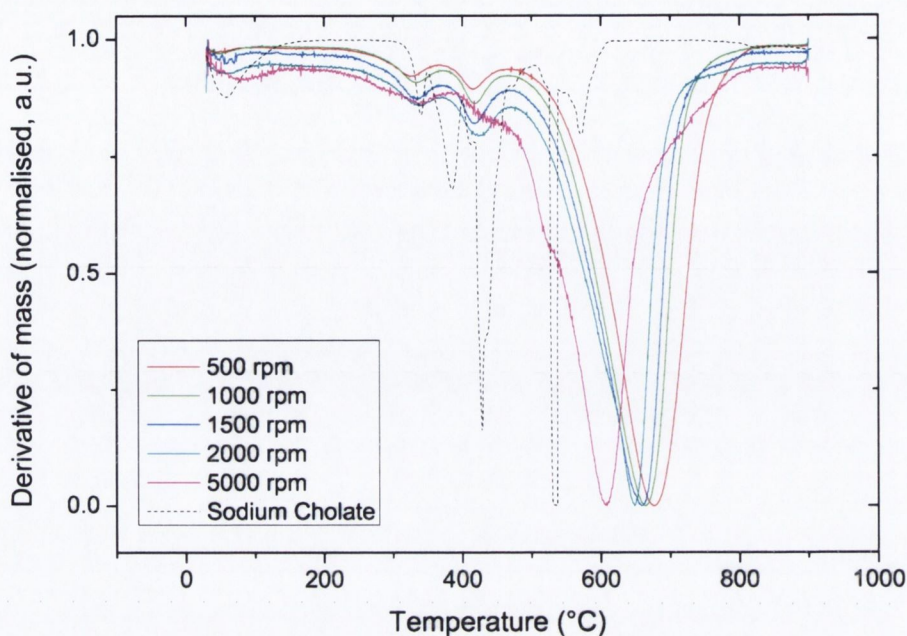


Figure 7.3: Differentiated TGA curves for graphene films made using a range of centrifugation rates. Also shown is reference TGA curve for sodium cholate. These differentiated spectra have been normalised to enable comparisons.

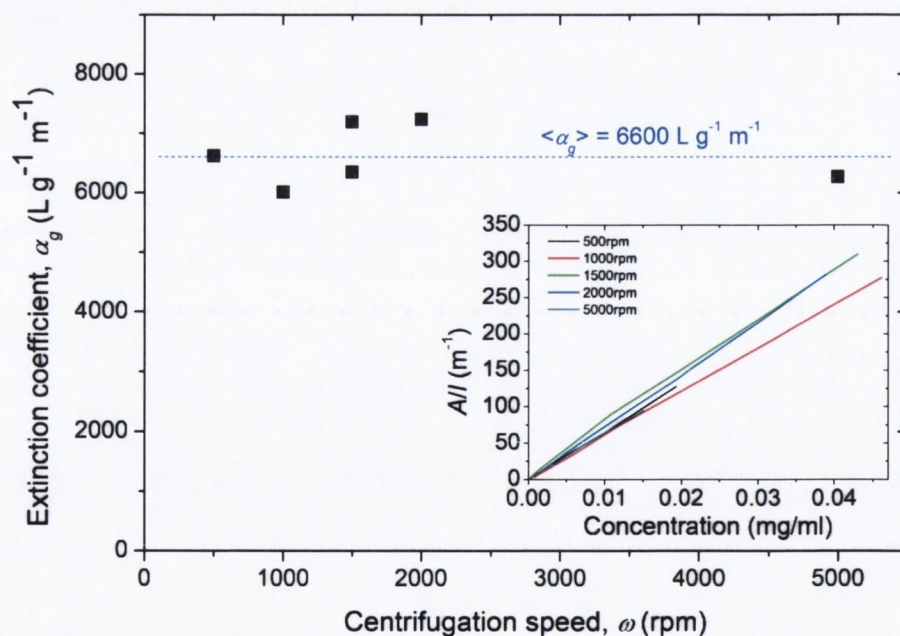


Figure 7.4: Extinction coefficient as a function of centrifugation rate. Inset: absorbance per unit cell length as a function of concentration for various ω .

for large stocks of dispersions across the range of ω shown in Figure 7.2. These dispersions (in excess of 400 ml) were then filtered through pre-weighed porous alumina membranes. After drying under warm vacuum, the films were re-weighed to give the deposited graphitic mass. TGA analysis was performed on material scraped off the alumina membranes, with derivatives of the mass curves shown in Figure 7.3. Integrating these curves across the peaks attributable to sodium cholate allowed the content of graphitic material to be determined for each film. It was found that these unwashed films were largely composed of graphitic material, having 15 – 30% residual surfactant by mass. Plotting A/l versus the dispersion concentration, as shown in the inset of Figure 7.4, gave the extinction coefficient from the line slope via Equation 4.5. As shown in Figure 7.4, the extinction coefficient was largely invariant with ω , with a mean value of $\langle \alpha_g \rangle = 6600 \text{ L g}^{-1} \text{ m}^{-1}$.

This value is significantly higher than the initial estimate of $1390 \text{ L g}^{-1} \text{ m}^{-1}$ for low concentration graphene/SDBS dispersions, and also higher than the value of $2460 \text{ L g}^{-1} \text{ m}^{-1}$ reported for graphene dispersed in amide solvents [10]. As the graphene flakes have been produced using similar processing conditions across all three studies one would expect the extinction coefficient values to match fairly closely. In my view the earlier measurements suffered from experimental errors that were not present in the current work, these may explain the discrepancies. Firstly, in both of the previous measurements, the dispersions were prepared with centrifugation conditions that were not optimised and so contained some nano-graphite particles - these were the large thick flakes of the type shown in Figure 6.3F. The particulates, comprised of the order of perhaps hundreds of graphene layers, would have a mass equivalent to many exfoliated flakes. This may be significant as the equation used to derive the value of α_g was as follows:

$$\alpha_g = \frac{A_{660 \text{ nm}} V}{Ml} \quad (7.1)$$

where $A_{660 \text{ nm}}$ is the absorbance of the dispersion, V is the volume of dispersion filtered, M is the mass of material deposited on the filtration membrane from the dispersion and l is the path length of the measurement cuvette - M/V defines the dispersion concentration C_g . It is reasonable to suggest that the nano-graphite particles could

have a lower light attenuation effect per unit mass than well-exfoliated graphene flakes. This can be justified by crudely considering the light absorption per graphene layer of $\sim 2.3\%$ [51–53], a 40-layer thick nano-graphite particle would block all light incident on it. If another nano-graphite particle had more than 40 layers then the light absorption effect was the same while the mass of the particle was increased. Thus, from Equation 7.1 it can be seen that such thick nano-graphite particles could contribute to a reduced $A_{660\text{ nm}}/M$ ratio and so lead to a lowered α_g value. It will be shown in subsection 7.3.2 that improved processing conditions reduced the population of these nano-graphite residual particles for the work shown in this chapter. In addition, much higher masses of material (~ 100 mg) were deposited in the new measurements in order to derive C_g . Thus, the errors involved in weighing and assessing the graphitic mass through TGA analysis were greatly reduced compared to work on low-concentration graphene/S-DBS dispersions. This also compares favourably with the work on graphene/NMP dispersions where low dispersion concentrations led to very small masses of graphene, of the order of only 2 mg, being assessed to derive C_g [10]. Taking into account the reduced impact of nano-graphite residuals and the greatly reduced errors in dispersion concentration analysis the new value of $\langle \alpha_g \rangle = 6600 \text{ L g}^{-1} \text{ m}^{-1}$ should be much more reliable.

With the value of α_g known, the change of concentration as a function of ω was assessed. The data in Figure 7.5 shows that as ω was increased the dispersion concentration fell from about 0.2 mg/ml to 0.03 mg/ml; an empirical scaling of C_g with ω^{-1} was observed. It was found later during the course of this work that the dispersion concentrations could be increased by raising the initial graphite concentration $C_{g,i}$ whilst maintaining the 50 : 1 ratio of graphite to sodium cholate initially used. One of these stock solutions was prepared using $t_{sonic} = 170$ hrs, with $C_{g,i} = 25$ mg/ml and $C_{SC} = 0.5$ mg/ml. This gave the data shown in the inset of Figure 7.5, demonstrating that graphene concentrations in excess of 1 mg/ml can be achieved through the use of prolonged low power ultrasonication.

The final processing parameter to be explored was the sonication time. Previous work in our group using graphene/NMP dispersions had shown that the final dispersed graphene concentrations could be readily increased by extending the bath sonication

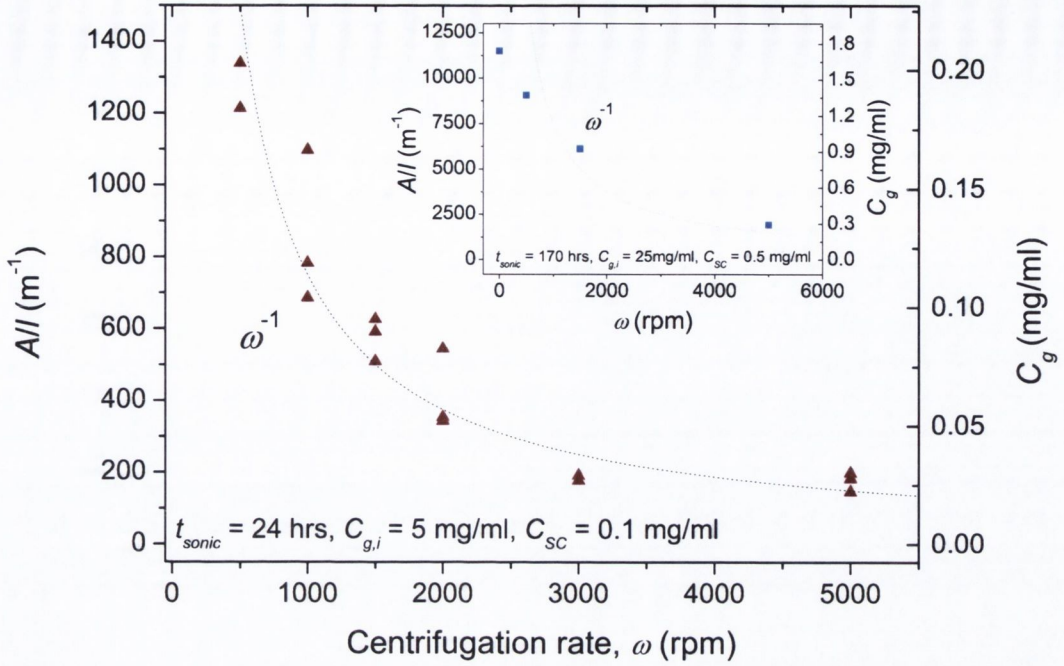


Figure 7.5: Dispersed graphene concentration as a function of centrifugation rate for a fixed sonication time of 24 hrs. Inset: concentration versus ω for samples taken after ~ 7 days sonication using further optimised initial graphite and surfactant concentrations.

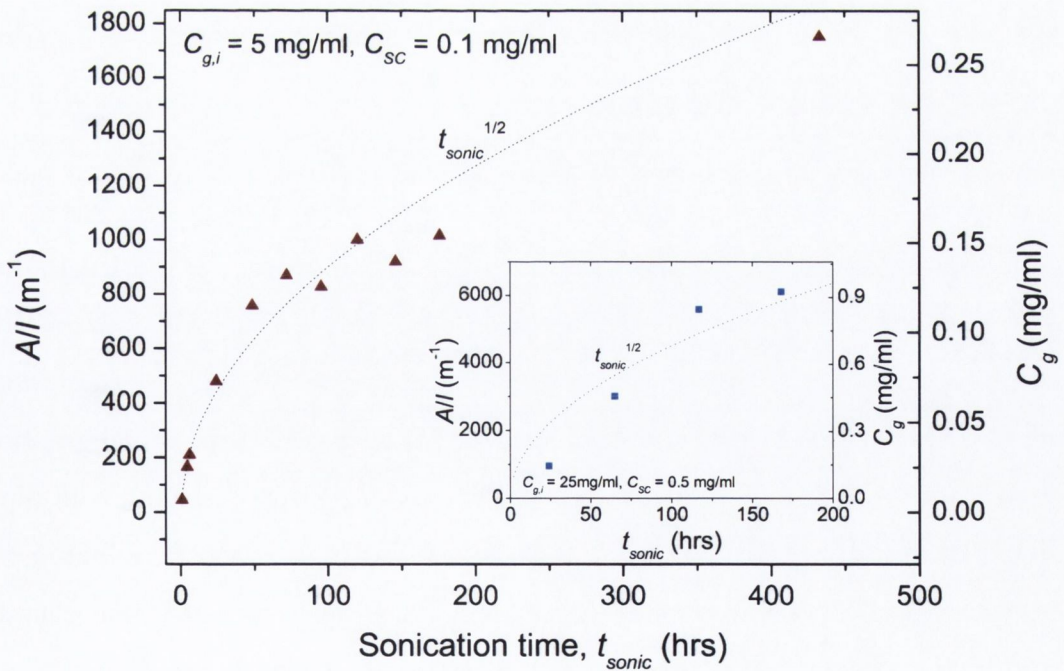


Figure 7.6: Dispersed graphene concentration as a function of sonication time. Inset: concentration versus t_{sonic} for further optimised initial graphite and surfactant concentrations. Dashed lines show scaling of A/l and C_g with $\sqrt{t_{sonic}}$. All samples were centrifuged at $\omega = 1500$ rpm.

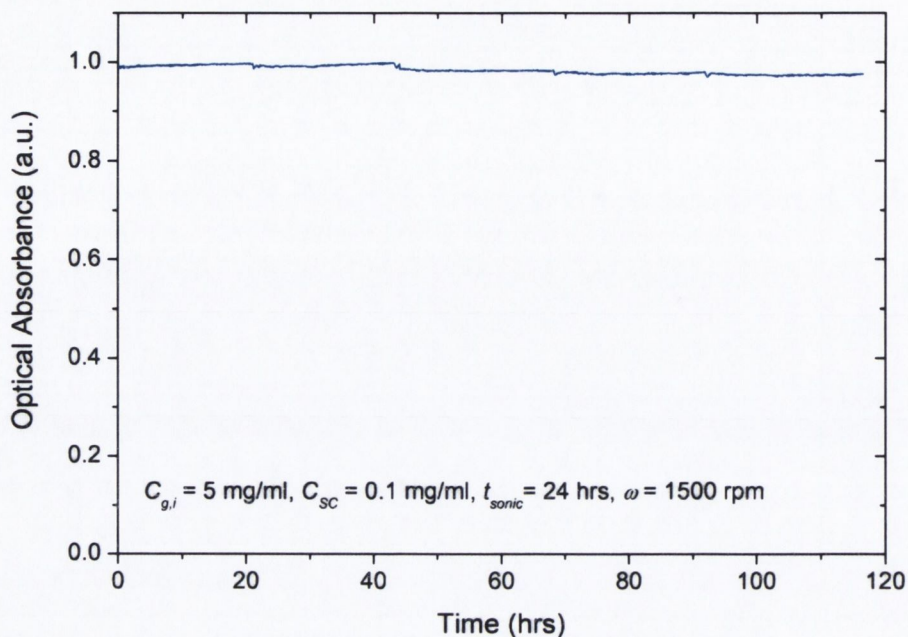


Figure 7.7: Sedimentation behaviour for a typical high concentration graphene dispersion. This dispersion had been diluted by a factor of 2 in 0.1 mg/ml SC solution.

time [228]. To test if such behaviour applied to graphene/surfactant systems, a large 400 ml stock dispersion was prepared in a round-bottomed flask with $C_{g,i} = 5$ mg/ml and $C_{SC} = 0.1$ mg/ml. This flask was sonicated for ~ 430 hrs, with 5 ml aliquots removed during this period and centrifuged at $\omega = 1500$ rpm. The aliquots were centrifuged at $\omega = 1500$ rpm giving the concentration versus t_{sonic} data shown in Figure 7.6. The dispersion concentration showed a sharp increase over the first 100 hrs or so, with a more gradual increase thereafter, ultimately reaching 0.3 mg/ml. The dispersion concentration also shows an empirical scaling with $\sqrt{t_{sonic}}$, similar to that seen in graphene/NMP dispersions [228]. In addition, use of higher initial graphite and sodium cholate concentrations yields a similar concentration scaling with time, giving 0.93 mg/ml concentrations after 170 hrs, as shown in the inset of Figure 7.6. These concentrations are two orders of magnitude higher than those shown in Chapter 6 for typical graphene/SDBS dispersions and represent a major improvement.

The usability of these high concentration dispersions is strongly affected by their temporal stability. This was tested by sedimentation measurements on a typical dispersion ($C_{g,i} = 5$ mg/ml, $C_{SC} = 0.1$ mg/ml, $t_{sonic} = 24$ hrs, $\omega = 1500$ rpm); this dispersion had to be diluted by a factor of 2 with 0.1 mg/ml SC solution to allow sufficient trans-

mitted intensity from the probe lasers. The data shown in Figure 7.7 shows excellent stability. Over 5 days, 97% of the sample remained suspended. This compares very favourably with results discussed in Chapter 6 for low concentration systems where only 60% of material remained over the same time period. In Chapter 6 the initial sedimenting phase (19 wt%) with time constant 24 hrs was attributed to large thick flakes resembling nanographite rather than few layer graphene; these were flakes inadvertently left in the dispersion after decantation. The absence of these large flakes in the current dispersions and improved stability is attributed to the use of a higher CF rate (1500 rpm vs 500 rpm) which has yielded more efficient flake separation.

It is likely that additional optimisation of sonication conditions will further increase the dispersed concentrations. For example, employing high powered point probe or horn tip sonication results in more concentrated energy transfer to the starting material. This combined with adjustments to the starting material concentrations should yield high concentration dispersions in less time than required with low powered sonic baths. Horn tip processing has been employed by Green and Hersam [229] for graphene/SC dispersions, resulting in concentrations around 0.3 mg/ml. In our group we can now routinely prepare high concentration graphene/SC dispersions around 2 mg/ml using pulsed horn tip sonication over time-frames of a few days.

It is noted that work on very high concentration aqueous graphene dispersions (> 0.3 mg/ml) post-dates the main body of work of presented in this chapter. Therefore, the remaining results in this chapter relate to large stock dispersions (400 ml) prepared via mild bath sonication, with $C_{g,i} = 5$ mg/ml and $C_{SC} = 0.1$ mg/ml.

7.3.2 Exfoliation Quality - TEM Analysis

Despite the high yield and good stability shown by these dispersions, the quality of the flakes produced must be evaluated. The flake size and thickness was evaluated with TEM analysis. TEM analysis was chosen due to the ease of sample preparation and the easy measurement of lateral flake dimensions. As before, thickness estimates were possible by careful examination of flake edges. Use of TEM analysis also avoided

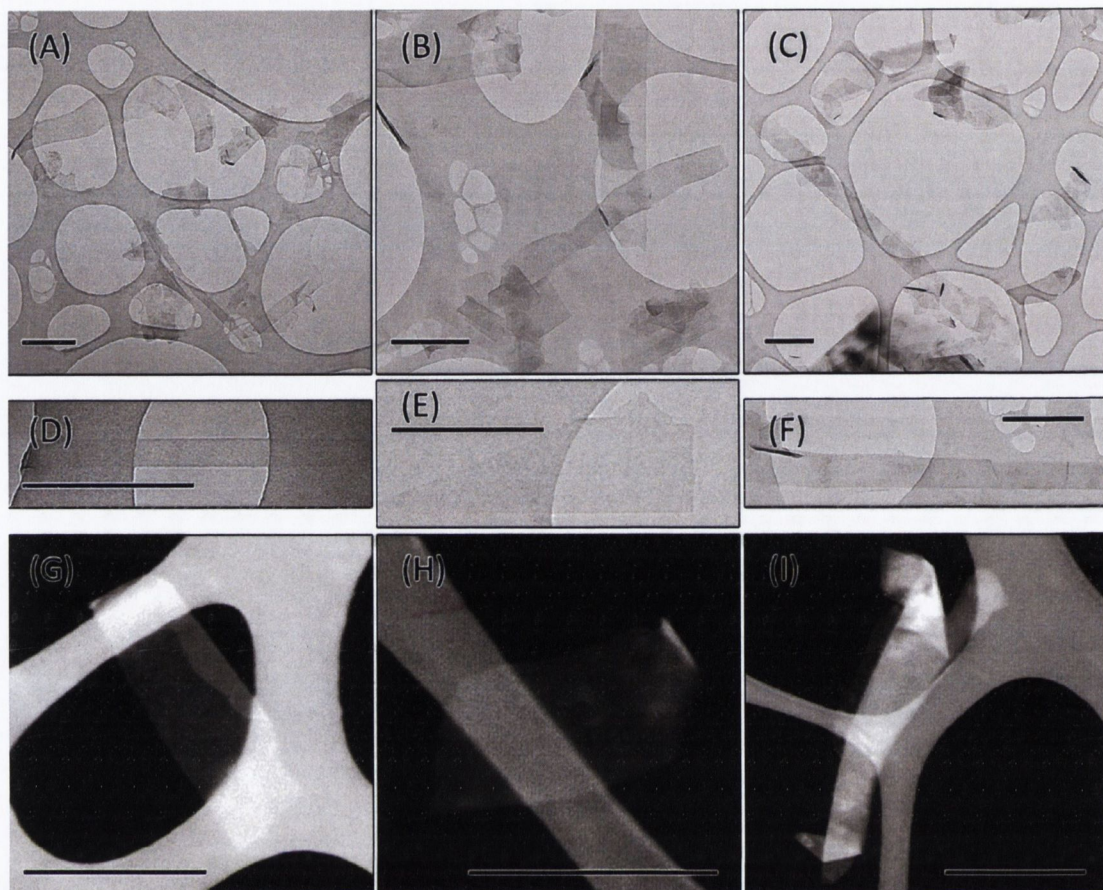


Figure 7.8: Selected TEM images from high concentration aqueous graphene/SC dispersions. Wide area bright field images and isolated flakes at $\omega = 1500$ rpm for different t_{sonic} : (A) 72 hrs, (B) 144 hrs, (C) 433 hrs, (D) 2 hrs, (E) 144 hrs and (F) 144 hrs. (G), (H) and (I) Isolated flakes imaged using energy filtered TEM. Monolayer graphene flakes shown in (D), (E), (G) and (H). All scale bars 500 nm.

the deposition-related problems experienced previously with AFM analysis, though it is possible that lateral flake dimensions may be biased towards larger flakes due to loss of the small flakes through holes in the grid.

TEM analysis was used to characterise a wide range of dispersions, made either under conditions of variable sonication time (t_{sonic} : 6 – 433 hrs) with fixed $\omega = 1500$ rpm or using a variable CF rate (ω : 500 – 5000 rpm) with fixed $t_{sonic} = 24$ hrs. A sample of the images obtained at fixed $\omega = 1500$ rpm, using bright field TEM imaging, are shown in Figures 7.8A-F. Also shown are selected EF-TEM images of flakes produced in this study, displaying enhanced contrast due to removal of the

zero-loss electrons. From all these images, the high quality of the flakes is apparent with well-exfoliated material produced. A few thick objects opaque to the electron beam, with lateral dimensions $4 - 15 \mu\text{m}$, were observed across the entire TEM grid in the sample with lowest CF rate of 500 rpm. These were nanographite particles, but their population was small - by examining several low-magnification TEM images the number fraction of these particles was estimated at less than 2%. At CF rates of 1500 rpm and above no such objects were observed. One of the primary concerns commonly raised by peers in relation to the use of long sonication times was that the graphene would be severely damaged or destroyed. From the images in Figure 7.8, this is clearly not the case with no evidence of large-scale defects or holes in the graphene flakes, even for those exposed to sonication times of over two and a half weeks (433 hrs). It is also interesting to note the high aspect ratios seen in many of the flakes, including monolayer and bilayer ribbons as illustrated in Figures 7.8D and F respectively.

A large set of TEM images was analysed to derive statistical data on the exfoliation state of the graphene. This was done for a grand total of 1000 flakes, with a total of $N_T = 100$ for each CF rate and sonication time chosen. A monolayer number fraction N_1/N_T of $\sim 10\%$ was observed across all sonication times at $\omega = 1500$ rpm. By taking the ratio of the number of monolayers counted to the total number of layers observed across all flakes [10], an estimated monolayer mass fraction of 1.1 wt% was derived. The TEM analysis found that the combined number fraction of monolayer and bilayer flakes was $N_{1-2}/N_T = 50\%$, while the fraction of flakes with less than 5 layers was $N_{1-4}/N_T = 80\%$. These data demonstrate a very high degree of exfoliation in these samples. In addition, the value of N_1/N_T rose to $\sim 20\%$ for the sample having $\omega = 5000$ rpm, made using 24 hrs sonication. The rise in monolayer number fraction with increased CF rate is consistent with subsequent work shown in literature using the surfactant sodium deoxycholate (SDOC, Figure 2.6), a close relative of SC, where a monolayer number fraction of $\sim 26\%$ was found using a CF rate of 10000 rpm [230]. This is important as it shows that enrichment of monolayer graphene in surfactant-stabilised dispersions is possible by simply increasing the centrifugation rate. In addition, density gradient ultracentrifugation has been applied to graphene/SC

systems, showing that these types of dispersions can be further processed to sort the graphene flakes by layer number [229, 231]. While there is a cost to be paid with reduced overall dispersion concentration, this can be offset by making higher concentration stock graphene dispersions as discussed earlier.

The TEM data can be analysed using the plots shown in Figure 7.9. The full data set of the number of layers per flake (N), length (L), width (W) and aspect ratio (L/W) analyses are given as histograms in the Appendix, Figures 10.2 and 10.3 on pages 183 and 184, respectively. From Figures 7.9A-C, the mean number of layers per flake, mean flake length and mean flake width all decrease with increasing CF rate. Over the range 500 – 5000 rpm, $\langle N \rangle$ falls from 5.2 to 3.4, $\langle L \rangle$ falls from 1200 to 500 nm and $\langle W \rangle$ falls from 600 to 300 nm. This shows that increased CF rates preferentially remove larger flakes. In all dispersions some small flakes with lengths as short as 50 nm were observed. These results are as expected and agree with work on high concentration graphene/NMP dispersions [228] and graphene/surfactant systems [229–231].

A surprising result is given by the data in Figures 7.9E-G, where the flake dimensions are observed to hardly vary with sonication time. Over a broad range from 6 – 433 hrs the flake dimensions remain fairly constant with $\langle N \rangle \sim 4$, $\langle L \rangle \sim 800$ nm and $\langle W \rangle \sim 350$ nm. The dispersions display a similar size distribution during prolonged sonication, with increasing concentrations of material produced. As a further experiment, a stock of graphene/SC dispersion sonicated for 48 hrs was settled and transferred to a clean round-bottomed flask, with a further 48 hrs sonication applied. This had the effect of removing the starting graphite material and exposing the already dispersed material to further sonication. TEM analysis of the original and re-sonicated dispersions showed no noticeable change in flake dimensions. A recent study on very high concentration graphene dispersions in NMP also showed an absence of extensive scission under prolonged sonication conditions [232]. The dependence of nanoparticle dimensions on sonication time has been examined in literature in the context of CNT dispersions [233, 234]. It was shown that sonication-induced scission relies on stress transfer caused by motion of the CNTs relative to the surrounding fluid; this motion is due to the collapse of cavitation bubbles in the liquid phase [234]. If the applied tensile stresses in the dispersed material exceeds the maximum tolerable stress then fracture occurs;

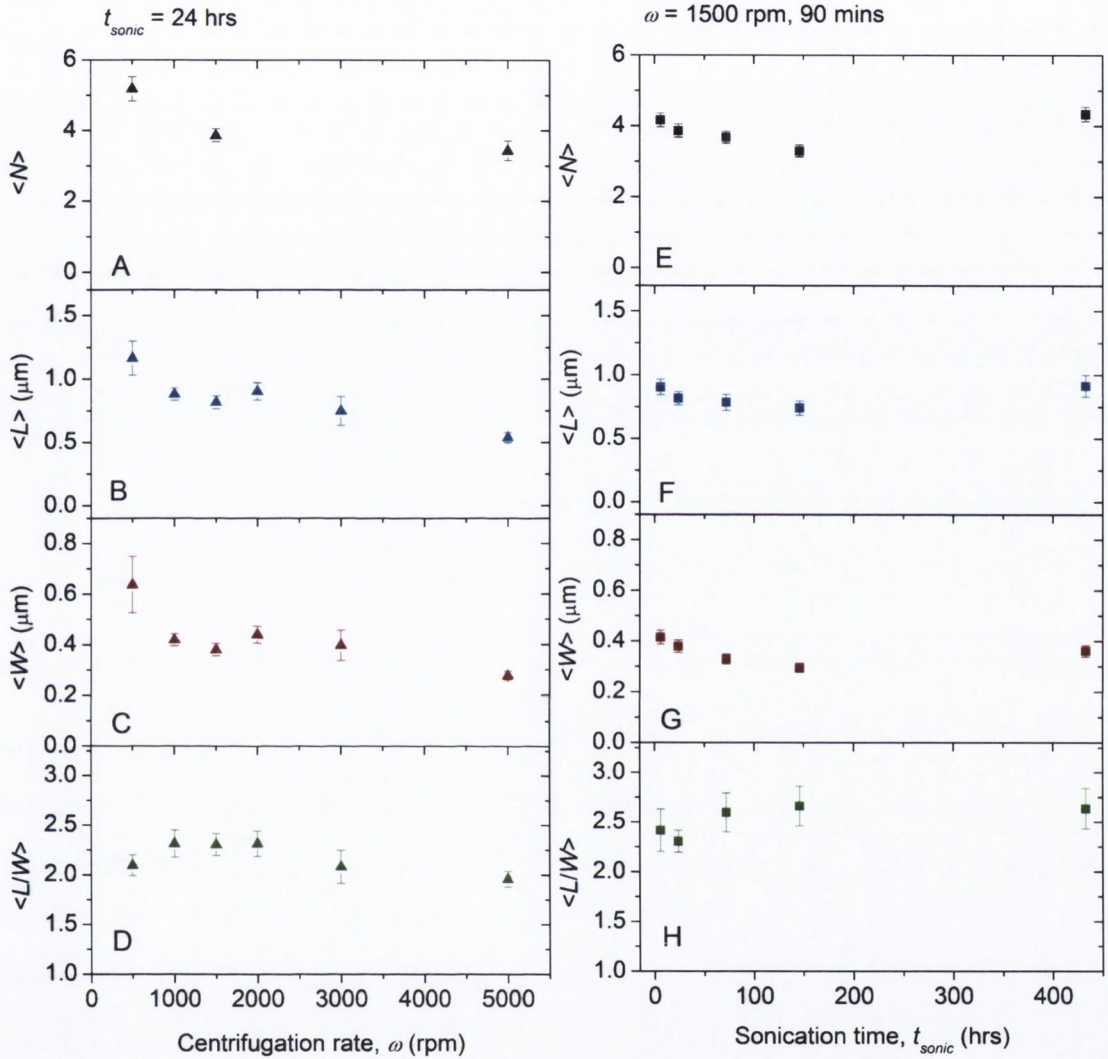


Figure 7.9: Flake size data derived from TEM analysis as a function of centrifugation rate and sonication time. Left panel: (A) mean number of layers per flake $\langle N \rangle$, (B) mean flake length $\langle L \rangle$, (C) mean flake width $\langle W \rangle$ and (D) mean aspect ratio $\langle L/W \rangle$ as a function of centrifugation rate for fixed $t_{sonic} = 24$ hrs. Right panel: (E) $\langle N \rangle$, (F) $\langle L \rangle$, (G) $\langle W \rangle$ and (H) $\langle L/W \rangle$ as a function of sonication time for fixed $\omega = 1500$ rpm. Each data point was derived from analysis of 100 flakes, error bars taken from the standard error of mean values.

in the case of CNTs this happens over time until a critical length is reached [233]. The absence of such behaviour in graphene/surfactant systems may point to a limitation in the stress-transfer in the system. The difference in behaviour may be related to the 2D nature of the graphene flakes compared to the 1D CNTs. It is possible that surfactant slippage at the graphene/surfactant/water double interface may also limit stress transfer.

A final observation from Figures 7.9D and H is the fairly constant mean flake aspect ratio ranging between 2.0 and 2.5. This is in agreement with previous work on graphene/NMP systems [228] and with earlier data from AFM analysis of graphene/SDBS dispersions. This suggests that sonication-induced exfoliation (and scission) favours asymmetric flakes, with the formation of some very high aspect ratio graphene ribbons as shown in Figure 7.8.

7.3.3 Graphene Quality - Raman Analysis

The quality of the graphene dispersions was further analysed by Raman spectroscopy. Thin films were prepared by vacuum filtration from the same sets of dispersions analysed by TEM. These films were then transferred to glass, with Raman spectra taken at a number of points on each film. Representative spectra are given in Figure 7.10. All of the film spectra showed 2D-bands that are indicative of exfoliation and consistent with few-layer material [189, 190, 229]. In all cases, significant D-band intensities were observed, with larger peaks than the starting powder. The observed D and D' bands are due to the introduction of defects during the processing, and are attributable to either flake edges or basal plane defects. The formation of edge defects is inevitable as the sonication process breaks up the starting graphite crystals to form smaller graphene flakes. These flakes have more edges per unit flake area, resulting in a higher edge defect population.

To examine this more closely, the mean D:G band intensity ratios (I_D/I_G) of the thin films were examined as functions of t_{sonic} and ω . From Figure 7.11A, I_D/I_G was surprisingly invariant with sonication time, displaying values around 0.57. This shows

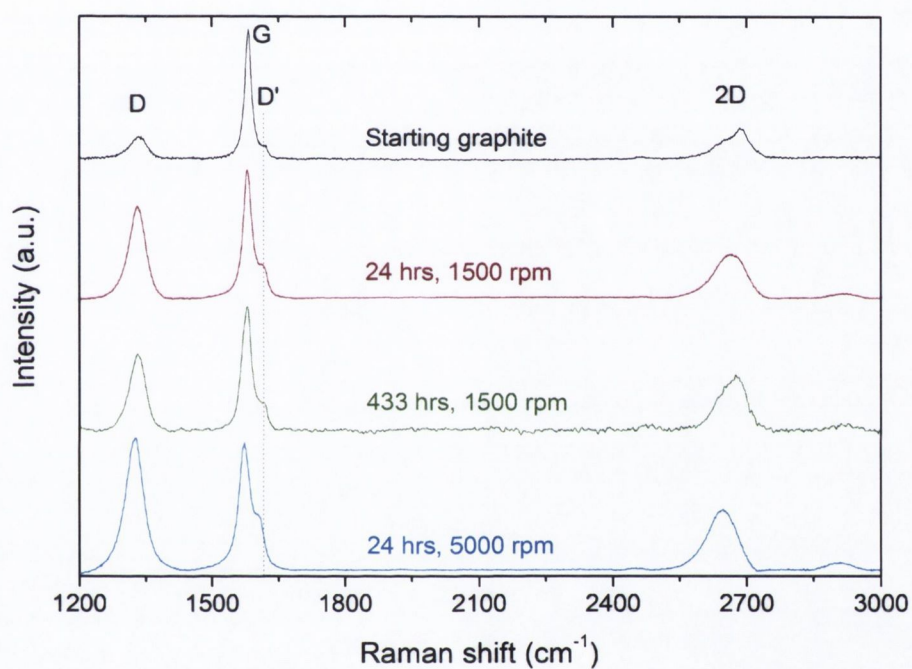


Figure 7.10: Raman spectra for thin films made with high concentration graphene dispersions. Spectra have been normalised to the intensity of the G-band. These films were deposited on glass, with a reference spectrum for the starting graphite powder also shown.

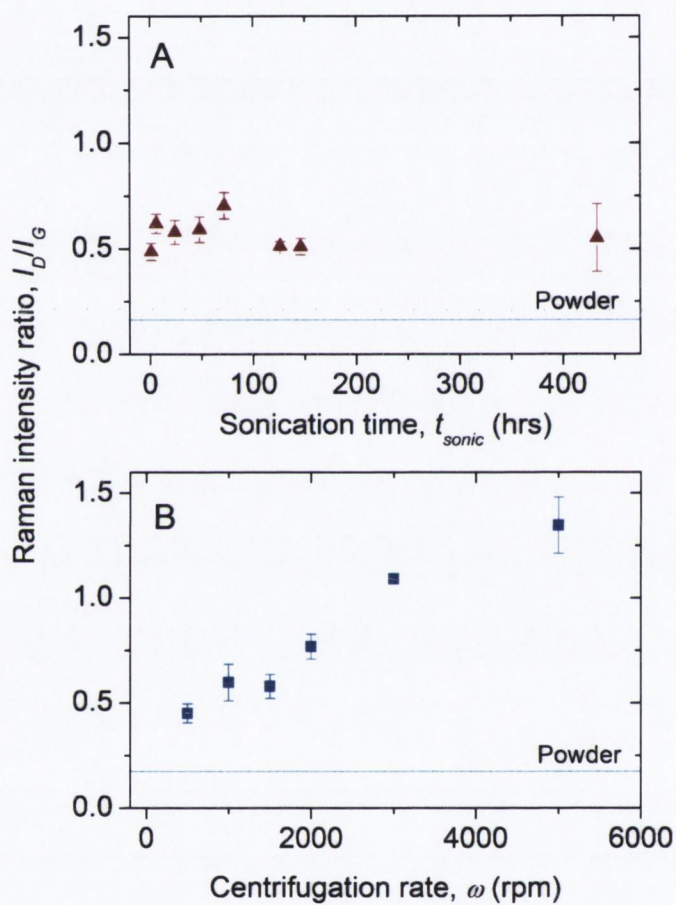


Figure 7.11: Mean Raman D:G band intensity ratios as a function of (A) sonication time and (B) centrifugation rate. Samples in (A) made using fixed CF rate $\omega = 1500$ rpm, (B) using fixed sonication time $t_{sonic} = 24$ hrs.

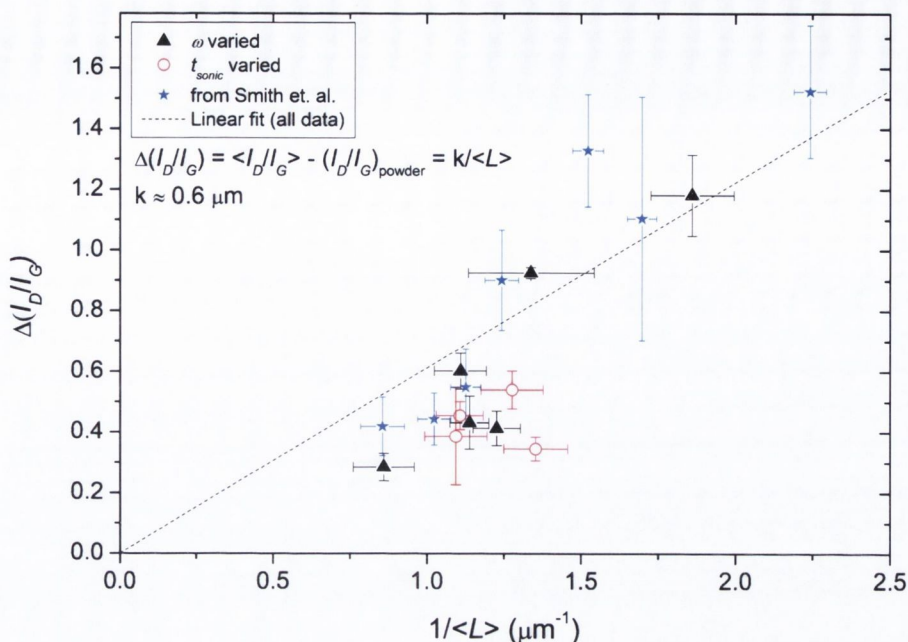


Figure 7.12: Mean Raman D:G band intensity ratio as a function of mean graphene flake length. Blue data points are taken from data on high concentration graphene/SC dispersions that were separated by size-exclusion column chromatography [235]. The dashed line is a linear fit data for samples with varied ω and data from Smith et. al. [235]

that prolonged sonication in aqueous surfactant systems does not introduce new flake edges in the dispersions. This implies that the graphene flakes are not cut to a significant extent during prolonged sonication; this data agrees strongly with the TEM flake size analysis. More importantly, Figure 7.11A indicates that the flakes do not suffer increased basal plane damage as t_{sonic} is increased, even up to extremely long durations.

A different picture is painted by Figure 7.11B, where I_D/I_G increased significantly with CF rate. This indicates that flakes produced at higher rotation rates are either smaller, as suggested by TEM data, and/or possess a higher density of basal plane defects. To correlate the Raman and TEM data, one can consider the relationship between the Raman intensity and lateral flake dimensions. The value of I_D is proportional to the

total flake edge length probed by the laser ($I_D \propto \langle L \rangle + \langle W \rangle$) while I_G is proportional to the flake area ($I_G \propto \langle L \rangle \langle W \rangle$). Modelling the flakes as rectangles means that

$$\frac{I_D}{I_G} \propto \langle W \rangle^{-1} + \langle L \rangle^{-1} \quad (7.2)$$

This proportionality accounts for the change in D:G ratio due to the formation of new edges as graphene flakes are formed from the parent bulk crystal. As the flake aspect ratio is nearly constant across all samples ($\langle L/W \rangle \approx 2.2$), the contribution of edges to the D:G ratio can be written in terms of flake length as

$$\Delta \frac{I_D}{I_G} = a \left(2.2 \langle L \rangle^{-1} + \langle L \rangle^{-1} \right) = k \langle L \rangle^{-1} \quad (7.3)$$

where a and k are constants. In addition, the measured Raman intensity ratio has a contribution from the starting graphite powder, $(I_D/I_G)_{\text{powder}}$. Assuming the D band intensity is dominated by flake edges, one can write

$$\frac{I_D}{I_G} = \left(\frac{I_D}{I_G} \right)_{\text{powder}} + \Delta \frac{I_D}{I_G} \quad (7.4)$$

For the graphite used in this study, $(I_D/I_G)_{\text{powder}} = 0.17$. This allows Equation 7.3 to be plotted as shown in Figure 7.12. The data relating to samples analysed with varied sonication times is marked by the open red circles, as expected this dataset is clustered due to the invariance of flake size with t_{sonic} . The data relating to the samples prepared with varied ω showed nearly linear $\Delta I_D/I_G$ scaling with $\langle L \rangle^{-1}$. The combined set of data roughly scales linearly through the origin as would be expected if edge defects account for the observed D:G ratios [228]. An interesting observation on the observed flake size variation can be made by considering subsequent work in our group by Smith et. al. [235]. A high concentration aqueous graphene dispersion was prepared with sodium cholate using horn tip sonication. The dispersion was centrifuged mildly and passed through a porous gel filtration medium packed into a column. This size exclusion chromatography technique allowed physical separation of the graphene flakes by lateral size (in our case size selection was achieved by tuning the centrifugation speed, as shown by TEM and Raman data). The $\Delta I_D/I_G$ and $\langle L \rangle^{-1}$ data from the various column fractions collected has been added as the blue stars in Figure 7.12. This shows an excellent correlation as the chromatography data closely follows the trend set by

varying ω . This indicates that the two very different processing techniques can yield very similar average graphene flake sizes while the closely matched Raman D:G band ratios indicate flakes of similar quality are formed.

By considering the data from both size-selection routines, a fitting parameter for Equation 7.3 of $k \approx 0.6 \mu\text{m}$ was found; this was somewhat higher than values of ~ 0.3 found in solvent-dispersed graphene systems [228, 232, 236]. The solvent systems were processed using less aggressive centrifugation conditions that could influence flake size statistics and reduce D:G ratios, thus explaining the different fit value. Alternatively the data could indicate a genuine difference in the defect density in graphene/surfactant dispersions. From the limited data available it is not clear whether the observed D:G ratios can be solely explained by edge formation due to sonication-induced scission. It is possible, though unlikely, that a basal-plane defect contribution that increases linearly with $\langle L \rangle^{-1}$ is contributing to the slope of the line fit in Figure 7.12. At best we can state that the linear scaling of Δ^{I_D/I_G} scaling with $\langle L \rangle^{-1}$ is consistent with edge formation.

7.3.4 Film Formation

One of the key strengths of producing aqueous graphene dispersions is their ease of use in a range of applications. While surfactant-stabilised graphene has been assessed for use in transparent conducting film applications [49, 219, 220], many other possibilities are opened by the availability of high concentration dispersions. Dispersions of the type displayed in this chapter are suitable for the formation of composite materials, using water-soluble polymers. In addition, they could be used to form much thicker films than have been shown in the work presented so far.

To demonstrate this, free-standing assemblies of randomly stacked few-layer graphene have been prepared by scaling up the mass deposited on filter membranes via vacuum filtration, images of these films are shown in Figure 7.13. Free-standing films were prepared with thicknesses in the range 50 – 120 μm . The films were matt on top but shiny on the side formed in contact with the filter membrane, an example of the shiny

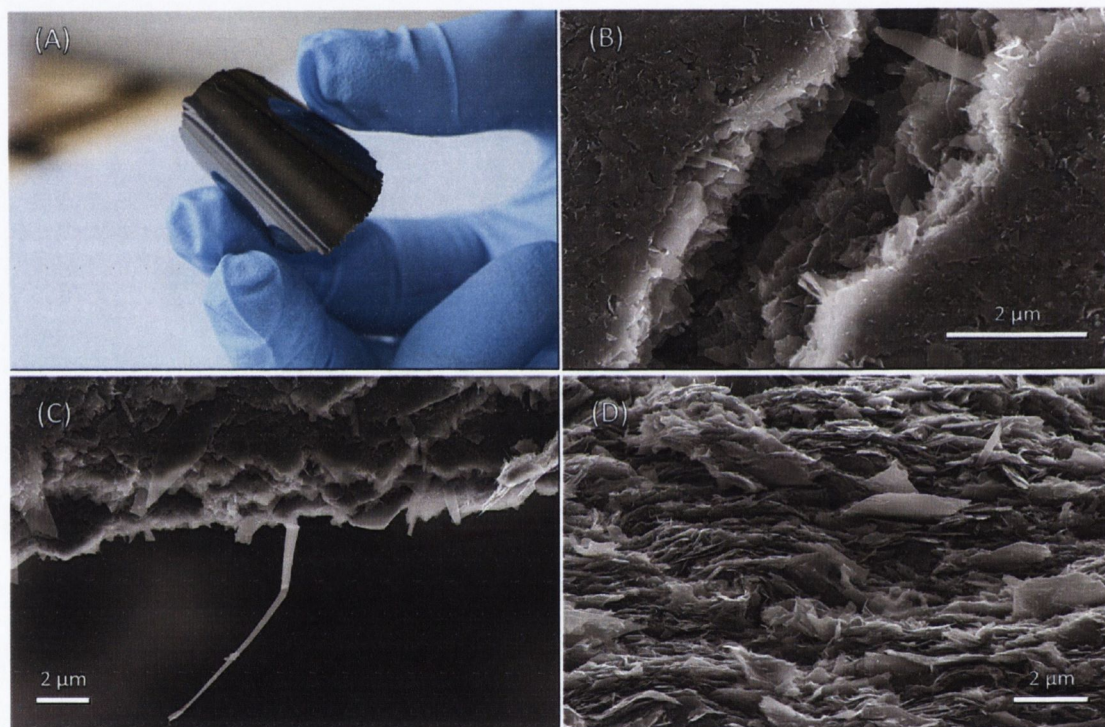


Figure 7.13: Free-standing graphene films from aqueous graphene/SC dispersions. Films made with $C_{g,i} = 5 \text{ mg/ml}$, $C_{SC} = 0.1 \text{ mg/ml}$. (A) Photo of film prepared using 171 hrs sonication. (B) SEM image of crack on the surface of a film. (C) SEM image of a fracture edge showing protruding graphene ribbons. (D) Cross-sectional SEM image of a fracture edge. Films in (B), (C) and (D) prepared using 24 hrs sonication.

face is shown in Figure 7.13A. The SEM images show that the flakes were well aligned in the film plane. From these images the flakes appear to have randomly packed, with many very thin protruding flakes visible including ribbons of the type shown in 7.13C. The 2D bands of the Raman spectra of these films matched those of the thin films, confirming that the flakes remain electronically decoupled and do not stack in an ordered AB arrangement to re-form graphite. A slightly higher averaged I_D/I_G ratio was observed on the shiny sides of the films compared to the matt side, suggesting that the smoother surface was formed by smaller flakes that packed tightly to dominate the initial formation of the film.

The films displayed reasonable mechanical properties (measured by Umar Khan), with Young's moduli (Y) typically in the range 4 – 10 GPa and ultimate tensile strengths (UTS) around 15 – 30 MPa. These values are very similar to those found in films made from graphene/NMP dispersions [228] but fall short of values of reported for films made with GO ($Y \sim 40$ GPa, $UTS \sim 100$ MPa [75]) and reduced GO ($Y \sim 20 - 43$ GPa, $UTS \sim 250$ MPa [78, 237]). The reason these films are mechanically weaker than their GO and reduced GO counterparts likely rests in the absence of oxide functional groups; these oxide groups can significantly improve inter-flake linkages through hydrogen bonding interactions [75]. The presence of residual surfactant may also influence the mechanical properties. The films also displayed promising electrical properties (measured by Sukanta De), displaying mean conductivity values of 1.75×10^4 S/m after annealing at 500 °C for 2 hrs under an argon/hydrogen atmosphere. Again, this agrees very well with values found in free-standing graphene/NMP films and with work on optimised flexible thin films of graphene from aqueous surfactant systems [220].

7.4 CONCLUSIONS

To conclude, the work presented in this chapter has demonstrated that highly concentrated and stable aqueous suspensions of graphene can be produced using surfactant stabilisers. Concentrations exceeding 1 mg/ml can be achieved using a facile, low-

cost, safe and scalable procedure utilising low power ultrasonication. High quality dispersions can be produced, with increased bath sonication times, t_{sonic} , yielding increased concentrations that empirically follow $\sqrt{t_{sonic}}$ dependence. Mild centrifugation at 1500 rpm yields dispersions with $\sim 10\%$ monolayer number fraction and $\sim 80\%$ of graphene flakes composed of fewer than 5 layers. Over a sonication time range of ~ 430 hrs the flake dimensions were largely invariant under mild centrifugation conditions ($\omega = 1500$ rpm) with $\langle N \rangle \sim 4$, $\langle L \rangle \sim 800$ nm and $\langle W \rangle \sim 350$ nm. It was shown that the monolayer number fraction can be increased to $\sim 20\%$ by simply increasing the centrifugation rate to 5000 rpm, suggesting that rotation rate optimisation can be used to form dispersions enriched with monolayer graphene. In addition, increasing the centrifugation rotation rate from 1500 rpm to 5000 rpm reduced the flake dimensions to $\langle N \rangle \sim 3.4$, $\langle L \rangle \sim 500$ nm and $\langle W \rangle \sim 300$ nm; this suggests a degree of flake size sorting is possible by tuning the centrifugation parameters. The scaling of the Raman D-band to G-band intensity ratio, I_D/I_G , with sonication time and TEM imaging shows that prolonged sonication does not measurably damage the graphene flakes or reduce their lateral dimensions through sonication-induced scission. The I_D/I_G scaling with centrifugation rate is largely consistent with new edges being observed due to overall flake size reductions. The flake size and Raman data correlate well with surfactant dispersed graphene flakes physically separated by size using column chromatography [235]. The dispersions can be easily cast into conductive free-standing films with good mechanical and electrical properties. These dispersions, and their resultant films, can facilitate the large-scale production of a range of graphene-based devices and composite materials where aqueous liquid-phase processing is advantageous.

BEYOND GRAPHENE: 2D NANOSHEETS FROM LIQUID-PHASE EXFOLIATION OF INORGANIC LAYERED COMPOUNDS

8.1 INTRODUCTION

Thus far, the work presented in this thesis has focused on the liquid-phase production of graphene. Dispersions of predominantly few-layer graphene have been demonstrated using sonication-induced exfoliation of layered graphite material. While graphene is an important and potentially useful 2D crystal, it is important to note that a myriad of other layered materials exist. These layered materials are a largely untapped resource which, given a simple scalable exfoliation method, could yield a set of nanosheets offering diverse electronic and physical properties coupled with high specific surface areas. In this chapter, the experimental methods and characterisation techniques used previously with graphene, as shown in Chapters 5 to 7, are applied to inorganic layered compounds. Two sets of layered materials are examined, with the aim of producing solvent-based dispersions of well-exfoliated material. The first class of materials discussed are the transition metal dichalcogenides (TMDs), with emphasis on MoS_2 and WS_2 . These materials are combined with graphene and CNT dispersions to form hybrid films. A hybrid MoS_2/CNT material is demonstrated and its potential for use in lithium ion batteries is examined. The second set of materials discussed in this chapter are used in thermoelectric devices, with nano-structuring suggested as a route to improve device performance [112]. The specific materials examined are Bi_2Te_3 , Bi_2Se_3 and Sb_2Se_3 ; a discussion of the preparation and characterisation of solvent-based dispersions of these materials is given.

8.2 EXPERIMENTAL PROCEDURE

Commercially available starting powders of MoS₂ and WS₂ from Sigma Aldrich were used; these powders consisted of platelets with lateral sizes ranging from a few microns to around 20 μm. Bi₂Te₃, Bi₂Se₃ and Sb₂Se₃ chunks (approximately 5 mm pieces) were purchased from Cerac Incorporated (via ABSCO UK). The powders were used as supplied while chunks were cut down into small fragments with a razor blade before use. For MoS₂ and WS₂ the solvents NMP, NVP and CHP were used, while CHP was used for preparing Bi₂Te₃, Bi₂Se₃ and Sb₂Se₃ dispersions. All solvents were purchased from Sigma Aldrich.

MoS₂ and WS₂ dispersions were prepared using either bath, horn or point probe sonication. Bath-sonicated samples were prepared with initial powder concentrations of 5 mg/ml using 400 ml solvent volume in 500 ml round bottom flasks, and sonicated for 48 hrs. Bath-sonicated dispersions were used to determine the extinction coefficients of the dispersions. Point probe sonication was used for samples studied with detailed TEM analysis, these were prepared at initial concentrations of 10 mg/ml in 14 ml vials using 1 hr sonication at a nominal output of 38%. Samples prepared with a horn tip used 10 – 15 mg/ml initial powder concentrations in 100 ml volumes with 3 hr sonication at 75% amplitude. All samples were settled overnight and centrifuged at 1500 rpm for 60 or 90 min.

Point probe sonicated dispersions in NMP were deposited on holey carbon grids for TEM analysis. Dispersions of MoS₂ were also deposited for scanning Raman, SEM and AFM analysis by spray casting. High concentration MoS₂/NMP dispersions at 0.36 mg/ml were diluted by a factor of 100 in IPA. Silicon wafers with 300 nm thermally grown oxide were rinsed with IPA and blow dried prior to use as substrates. The silicon was pre-heated to 90 °C and 2 ml of the diluted was applied using an Evolution Airbrush at a pressure of 1.5 bar. Alignment marks were scored onto the substrate after deposition and the resulting silicon debris gently blown away by compressed air.

The horn-sonicated dispersions were used for the preparation of hybrid films by blending with graphene or SWNT dispersions. Graphene dispersions were prepared

in DMF via 48 hr bath sonication. Iijin SWNTs were dispersed in CHP at 1 mg/ml using 5 min point probe sonication at 20% amplitude followed by 1 hr bath sonication and a further 5 min probe sonication; these dispersions were not centrifuged in order to maintain a high concentration of SWNTs. The MoS₂/WS₂ dispersions were blended with graphene/SWNT dispersions using precise volumes to give controlled mass fractions. Free-standing hybrid films, with mass close to 50 mg, were prepared by vacuum filtration onto alumina membranes.

MoS₂ hybrid films for battery testing were made using concentrated MoS₂ dispersions. These were prepared by taking stock dispersions in CHP centrifuged at 1500 rpm and applying a second centrifugation step at 15000 rpm for 4 hrs at a temperature of 10 °C. This had the effect of forming a highly concentrated dispersion at the bottom of the Eppendorf centrifuge tubes, the relatively clear supernatant was discarded and the concentrate extracted and diluted with IPA. This concentrate was then blended with Iijin SWNT dispersions in CHP and diluted by a factor of approximately 20 with IPA. These diluted blends were then filtered onto nitrocellulose membranes. A reference film made with MoS₂ only was also prepared. The resulting films were transferred, using acetone vapour and baths, to copper foils to be tested as cathodes in coin cell lithium ion batteries. The testing and analysis of these films was performed by collaborators Dr. Jun Chen from the Intelligent Polymer Research Institute at the University of Wollongong and Prof. Andrew Minett from the Laboratory for Sustainable Technology at the University of Sydney. The electrochemical testing of these foils was carried out using 2032 coin cells. The cells were assembled inside an argon-filled glove box using an electrolyte solution of 1M lithium hexafluorophosphate (LiPF₆) in ethylene carbonate/diethyl carbonate (EC/DEC, 1 : 2 v/v ratio) with lithium metal foil as the counter electrode. Charge-discharge tests were performed at a rate of 100 mA g⁻¹ in the range 0.1 – 3.0 V.

Bi₂Te₃, Bi₂Se₃ and Sb₂Se₃ dispersions were largely prepared using horn tip (up to 3 hr) and point probe sonication (up to 90 min), with bath sonication also used for early testing. Centrifugation was typically carried out at a rate of 500 rpm or 1000 rpm for 45 mins. The lower intensity centrifugation compared to the TMDs was found to be sufficient to remove the largest aggregates from the dispersions whilst

maintaining high concentrations, this can be explained by the higher density of these materials compared to graphene or TMDs. For thin film formation on glass or silicon substrates, concentrated Bi_2Te_3 dispersions were prepared using a second centrifugation at 10000 rpm for 3 hrs, diluted with IPA and filtered onto nitrocellulose before being transferred. Raman spectra for Bi_2Te_3 films deposited on alumina membranes were collected with a 532 nm laser and $20\times$ lens with manually reduced laser intensity to reduce sample heating and burning.

8.3 RESULTS AND DISCUSSION: MoS_2 AND WS_2

8.3.1 *Dispersion Preparation and Optical Characterisation*

It was found that powders of bulk MoS_2 and WS_2 could be successfully dispersed using a variety of ultrasonication types, including bath sonication, horn tip and point probe methods. For both materials, homogeneous dark green dispersions, free of visible particles, were produced in a wide range of solvents with NMP, NVP and CHP found to be quite effective [238]. SEM images of the starting materials and photos of typical dispersions are given in Figure 8.1.

The optical absorption spectra of all MoS_2 and WS_2 dispersions prepared were recorded. In all samples, across all solvents, the absorption spectra for both materials showed distinct peaks below 700 nm. The observed features appeared to sit on a background, which was most likely due to scattering. In order to examine this further the spectra were plotted using logarithmic axes. Figure 8.2 gives the absorption spectra for typical MoS_2 and WS_2 dispersions prepared by 48 hr bath sonication in NVP. From this plot, the background appears to be approximately linear in the non-resonant region of the spectrum. This power-law dependence of the absorbance on wavelength ($A \propto \lambda^{-n}$) is characteristic of light scattering [239]. Three types of scattering are possible: (i) Rayleigh scattering by molecules with size much smaller than the wavelength of incident light, (ii) Tyndall scattering that is independent of wavelength and (iii) Mie scattering covering scattering between Rayleigh and Tyndall scattering regimes [239].

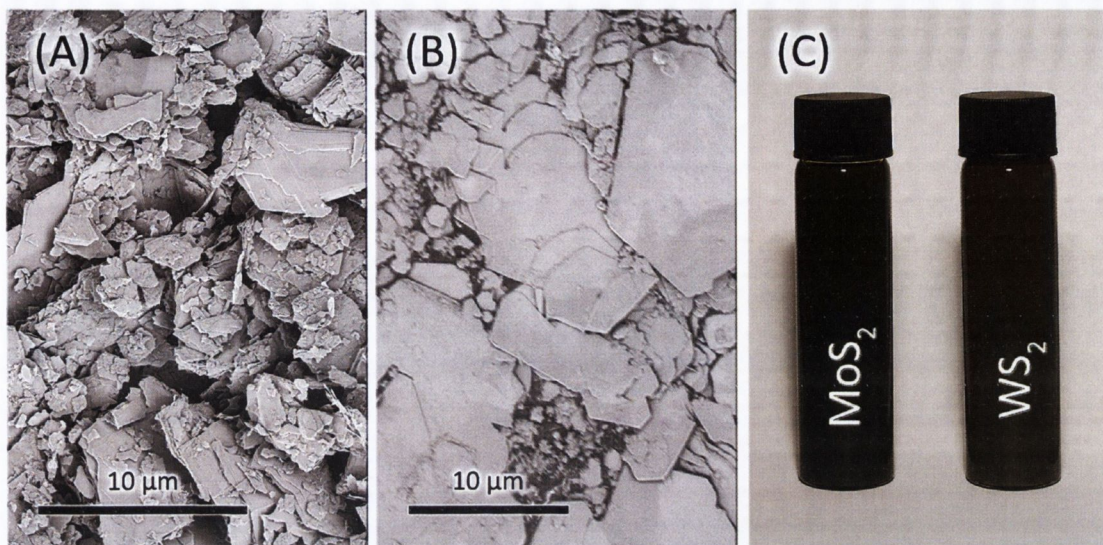


Figure 8.1: Images of starting material and typical MoS_2 and WS_2 liquid phase dispersions. (A) SEM image of MoS_2 bulk starting powder. (B) SEM image of WS_2 bulk starting powder. (C) Dispersions of MoS_2 and WS_2 prepared in NMP using point probe sonication and centrifugation at 1500 rpm.

Mie scattering is described by exponents $-1 < \eta < -4$ [239]; the fitted data in Figure 8.2 is consistent with Mie scattering with $\eta = -3.3$ and -3.9 for MoS_2 and WS_2 respectively. Subtracting the scattering background gives the absorption spectra of the MoS_2 and WS_2 as shown in the inset of Figure 8.2. Absorption peaks at 671 nm and 621 nm are observed in MoS_2 and at 629 nm in WS_2 ; these spectral features agree with literature data relating to micro-mechanically exfoliated and electrochemically deposited MoS_2 [99, 240, 241] and fragmented bulk WS_2 crystals [110].

The next step in characterising these dispersions was to determine the extinction coefficients. This was done in a similar manner to that used for high concentration graphene dispersions in Chapter 7. Large stock dispersions of MoS_2 and WS_2 were prepared by bath sonication, centrifuged and filtered through PVDF membranes ($0.22 \mu\text{m}$) of known mass. Following deposition, the films were dried for 24 hrs at 70°C and re-weighed to derive the deposited mass; TGA analysis confirmed that the NVP solvent had been removed. Green coloured filtrates were observed indicating loss of some of the dispersed particles through the membranes. The value of A/l for the filtrates was compared to that of the initial stock dispersion to correct the

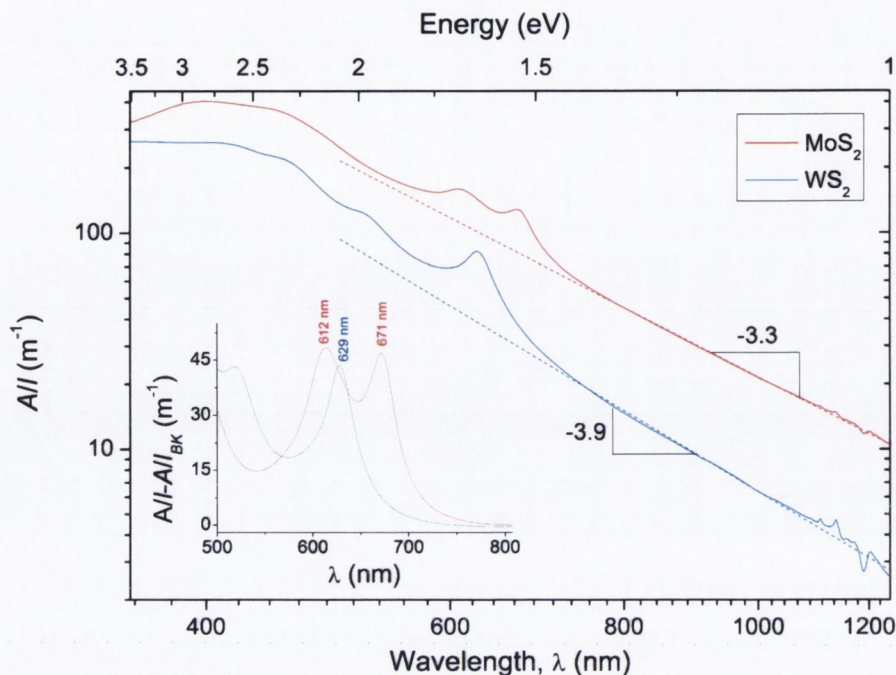


Figure 8.2: Optical absorption spectra for MoS₂ and WS₂ dispersions in NVP. Dashed lines show power-law scattering backgrounds fitted in the non-resonant regions of the spectra. Inset: absorbance per unit cell length with scattering background A/l_{BK} subtracted.

values of deposited mass (12 wt% and 46 wt% of dispersion mass had been retained in the filtrate for MoS₂ and WS₂ respectively). This allowed calculation of extinction coefficient values of $\alpha_{MoS_2} = 1900 \text{ L g}^{-1} \text{ m}^{-1}$ and $\alpha_{WS_2} = 1000 \text{ L g}^{-1} \text{ m}^{-1}$. Dispersions with concentration of the order of 1 mg/ml after 1500 rpm CF were routinely obtained using horn tip or point probe sonication. Such high concentrations can enable the production films, polymer composite materials and hybrid materials; some of these applications will be explored later in this chapter.

The usefulness of these liquid-phase dispersions is strongly influenced by their temporal stability. This was assessed by sedimentation measurements using typical MoS₂ and WS₂ dispersions prepared by bath sonication in NVP. The data in Figure 8.3 shows that the MoS₂ dispersion was very stable, with 94% of material remaining suspended after three weeks. The WS₂ dispersion showed some sedimentation with 70% remaining over the same time period, with a stable phase from the decay fitting of 56%. This level of stability still allows a very good processing window. It is likely that

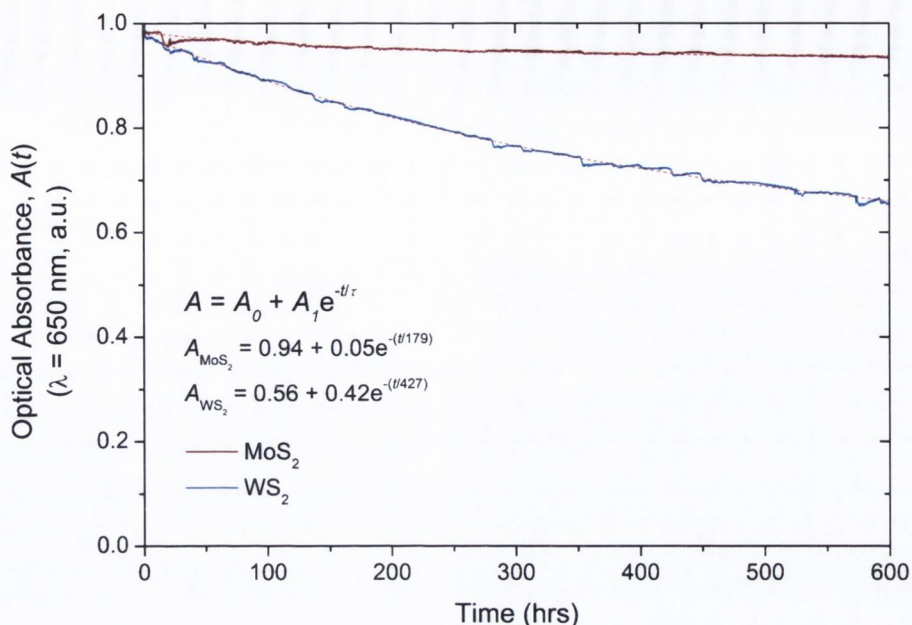


Figure 8.3: Sedimentation behaviour for typical MoS_2 and WS_2 dispersions. The dispersions were prepared using 48 hrs bath sonication in NVP with 90 min centrifugation at 1500 rpm. Fitted exponential decay curves are indicated by red dashed lines.

the use of optimised dispersion parameters (i.e. solvent choice, sonication conditions and CF rotation rate) can improve the observed stability further.

8.3.2 Exfoliation Quality - TEM Analysis

TEM analysis was carried out in order to assess the quality of the dispersed materials. In general, large quantities of thin nanosheets were observed. Figure 8.4 shows a selection of images of these flakes. Flakes of the types shown in Figures 8.4A-D were frequently observed, with many very thin small flakes deposited on the surface of the holey carbon mesh and on the surface of larger flakes (these small flakes are visible in Figure 8.4B and C). A HR-TEM image of a WS_2 flake is shown in Figure 8.4E, with the inset showing a fast Fourier transform of the marked area. The relative intensity of FFT or electron diffraction spots cannot be used to infer the layer number as calculations of the structure factors for MoS_2 and WS_2 showed that electron diffraction intensity ratios were insensitive to the number of stacked layers [238]. From these types of images and their FFTs, it was clear that the hexagonal structure of the original bulk

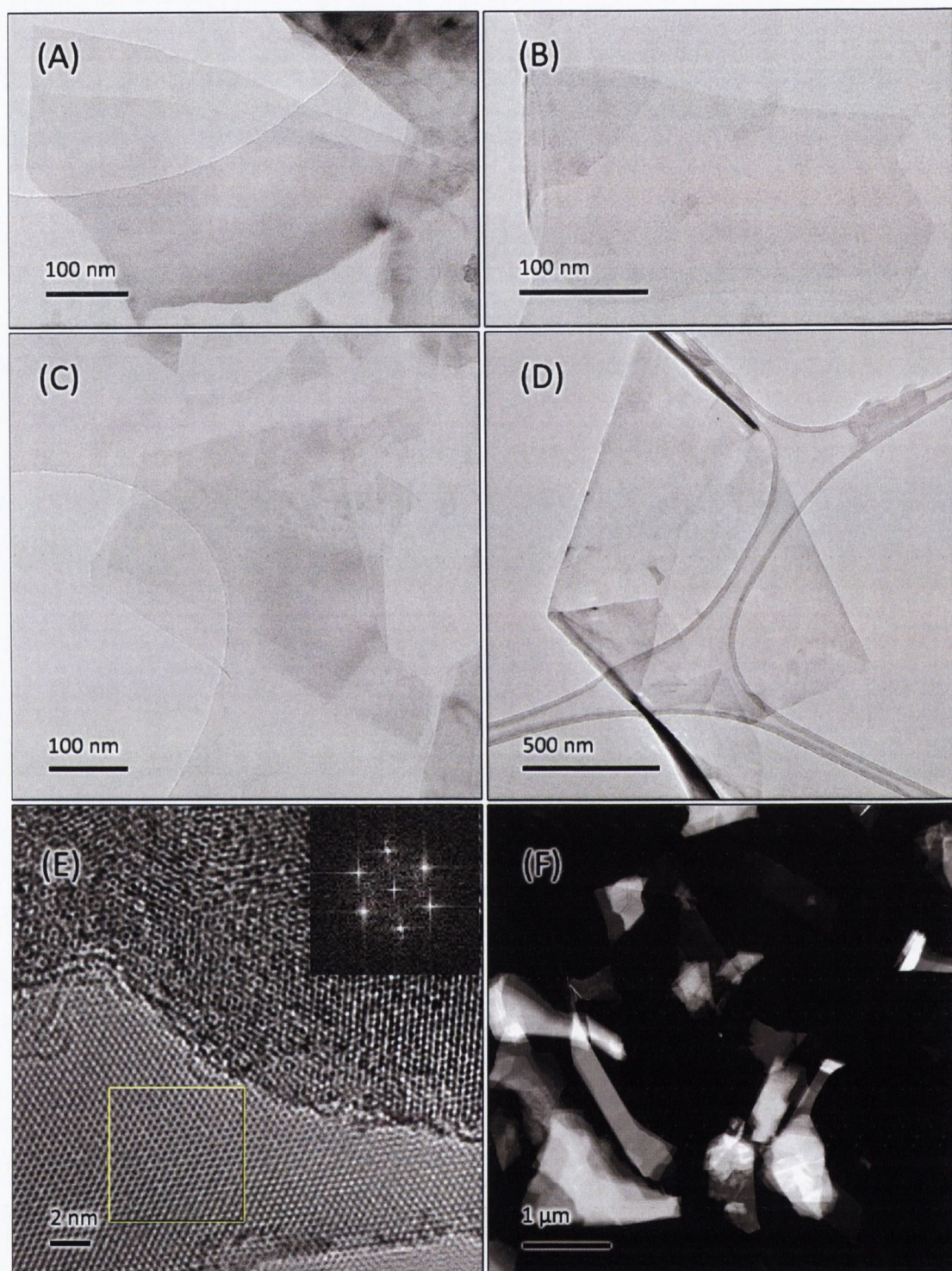


Figure 8.4: TEM and STEM images of MoS₂ and WS₂ from exfoliation in NMP. (A) and (C) TEM images of MoS₂ flakes. (B) and (D) TEM images of WS₂ flakes. (E) HR-TEM image of a thin plane protruding from a multi-layer WS₂ flake, inset FFT of the area marked with the yellow box. (F) High contrast STEM image of a cluster of MoS₂ flakes..

WS_2 had been retained - this was confirmed by the absence of new spots characteristic of a superlattice and spot splitting in the FFTs [242]. This is important as it shows that the processing has not structurally converted the WS_2 atomic configuration from hexagonal 2H to octahedral 1T, this type of atomic re-arrangement has been observed when exfoliating TMDs using lithium ion intercalation [105–108]. Figure 8.4F shows an assortment of MoS_2 flakes imaged using annular dark-field STEM. From this image a range of flake sizes and thicknesses are visible, with very thin layers appearing as the darkest objects. Annular dark-field STEM imaging gives better layer contrast for TMDs than for graphene as the electron energy loss due to Rutherford scattering by atoms is roughly proportional to the square of the atomic number [201]. High resolution STEM imaging combined with EELS analysis was used by our collaborators (Dr Valeria Nicolosi and co-workers, University of Oxford) to show that such thin MoS_2 and WS_2 layers had electron loss spectra distinct from the bulk materials, indicating successful exfoliation [238]. In addition, they confirmed the presence of monolayer material using atomic resolution aberration corrected HR-TEM combined with the simulation of intensity distributions.

The TEM analysis of MoS_2 and WS_2 can be extended by looking at the dimensions of a large number of flakes. This was done by examining low-res TEM images of the type shown in Figures 8.4A-D. For graphene, it has been shown that edge counting is a reasonably reliable way to determine layer number. However, in TMDs the individual layers of the material are three atoms thick. This more complicated structure makes edge counting more difficult. A more accurate way to conduct the study would be to exploit the high contrast of STEM imaging, using fixed microscope conditions and a precisely calibrated annular dark-field detector. This could allow the use of intensity cross sections at flake edges to reliably count layer number. However, such analysis requires special equipment, is time consuming and can be complicated by sample contamination caused by the STEM probe. Thus, the flake thickness analysis was attempted using careful edge-counting, in the same manner as for graphene, noting the approximate outcome of the results. Statistics of lateral flake dimensions were reliable. The data is summarised in Figure 8.5. From Figure 8.5A and E, few-layer flakes made up the majority components of the dispersions. The MoS_2 and WS_2 flakes had lateral

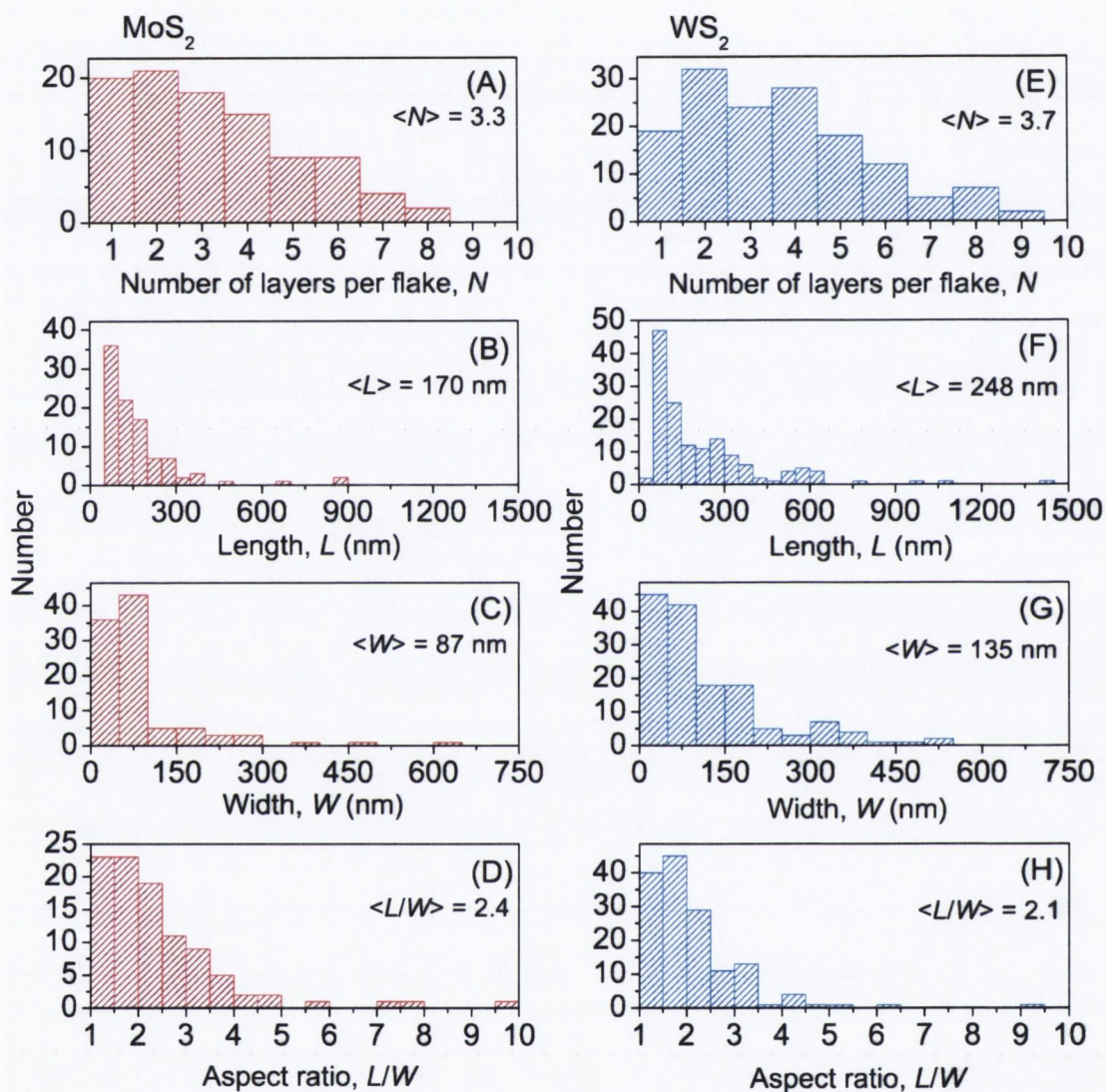


Figure 8.5: Statistical TEM analysis of TMD flake dimensions: number of layers per flake (N), length (L), width (W) and aspect ratio (L/W). Data for 98 MoS_2 (A-D) and 147 WS_2 (E-H) are shown. Samples were prepared using 1 hr point probe sonication in NMP using CF rate of 1500 rpm.

dimensions in the range 50 – 1000 nm. In general, the flakes were smaller than those found previously in graphene with mean lengths of 170 nm and 248 nm observed in MoS_2 and WS_2 respectively. The smaller sizes of these flakes, compared to graphene, is possibly a reflection of the lower tensile strength of the parent crystal, offering lower resistance to sonication induced scission. Alternatively, the higher density of the TMDs may result in a distribution of smaller flake sizes being selected by the centrifugation process [195]. The sonication process produced asymmetric flakes, with aspect ratio distributions for both materials matching each other closely. The mean aspect ratio values were very similar to those shown previously in Chapter 7 for aqueous graphene dispersions.

8.3.3 MoS_2 Deposition on Surfaces - AFM, SEM and Raman

The MoS_2 and WS_2 dispersions shown in this work are highly versatile and nanoflakes of these materials were deposited for further study. It was found that exfoliated flakes could be easily deposited on surfaces by spray casting, this was done for MoS_2 dispersed in NMP by point probe sonication. A $20 \times 20 \mu\text{m}$ region of the substrate was isolated using alignment marks and characterised with non-resonant scanning Raman spectroscopy (using a 488 nm laser), AFM and SEM.

Figures 8.6A and B show AFM and SEM images of a $6.2 \times 6.2 \mu\text{m}$ area containing small flake-like objects, these objects were typical of those observed across the substrate with sizes in the range 50 nm – 1 μm . Shown in Figure 8.6E are close-up SEM and AFM images of the flake highlighted with the yellow box in Figure 8.6B, along with a horizontal AFM cross section.

Raman spectroscopy was used in order to determine whether the observed objects were MoS_2 . The Raman features of bulk MoS_2 are well-known. Under 488 nm laser excitation conditions, as used here, an in-plane vibrational mode (E_{2g}^1) at 383 cm^{-1} and an out-of-plane vibration (A_{1g}) at 408 cm^{-1} are observed in bulk 2H- MoS_2 [103, 105, 107, 243–245]. Raman spectra of the spray deposited material closely resembled 2H- MoS_2 with peaks at 382 cm^{-1} and 406 cm^{-1} , as shown in Figure 8.6C for a typical

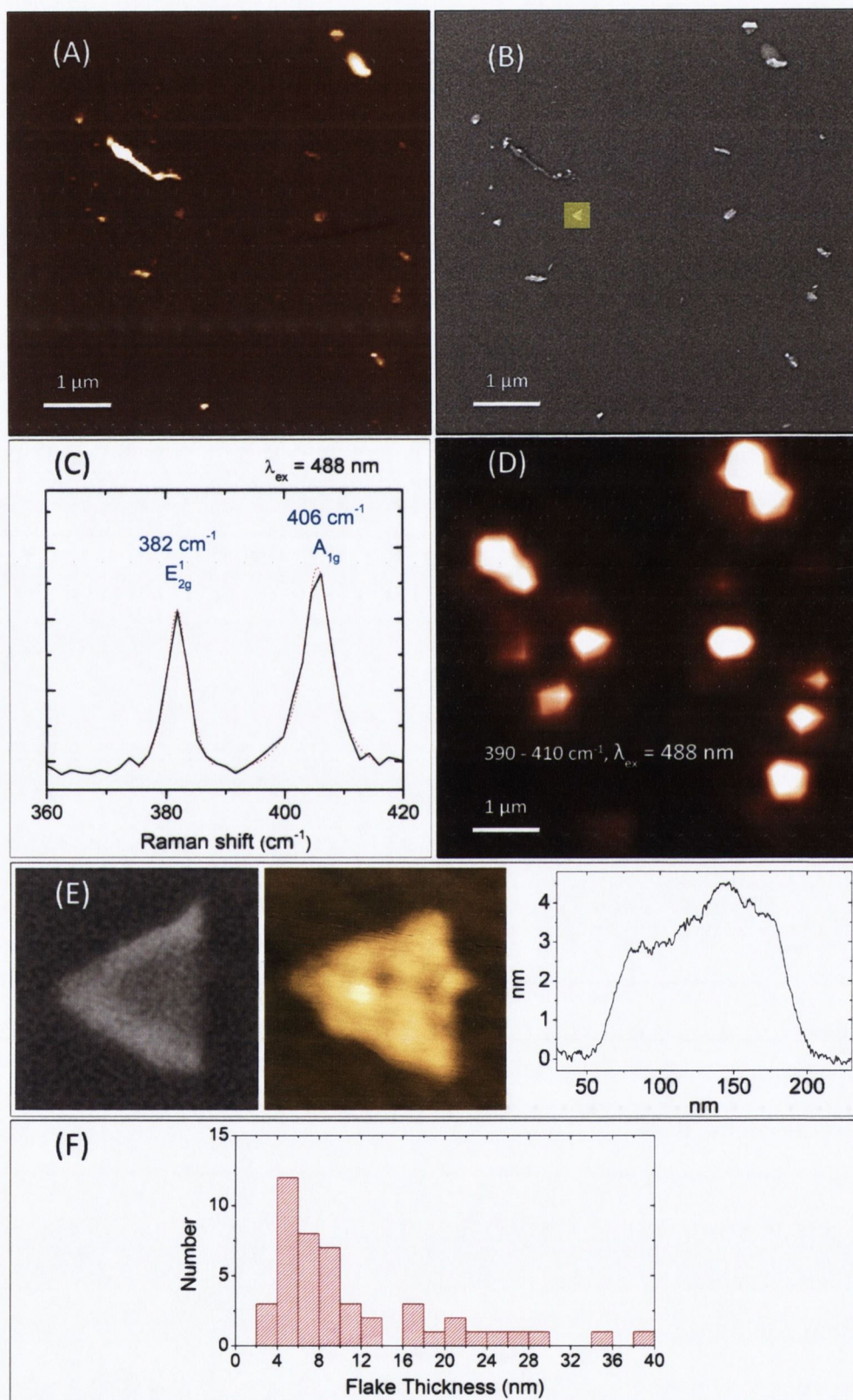


Figure 8.6: MoS₂ flakes deposited on silicon. (A) AFM image, (B) SEM image, (C) Raman spectrum of a typical MoS₂ flake, Lorentzian peak fits as red lines, (D) scanning Raman map of the same $6.2 \times 6.2 \mu\text{m}$ area in A and B. (E) Left - SEM image, Middle - AFM image, Right - horizontal AFM cross section of flake marked by yellow box in (B). (F) AFM flake thickness statistics for 100 MoS₂ flakes.

object. The higher energy A_{1g} mode can be described by a single Lorentzian fit centred at 405.5 cm⁻¹ with a FWHM of 5.8 cm⁻¹, these values agree with literature data for mechanically exfoliated bi-layer MoS₂ sheets analysed with a 514 nm excitation source [245]. The lower energy E_{2g}¹ mode also follows a single Lorentzian profile with a peak at 381.9 cm⁻¹ and FWHM of 4.5 cm⁻¹; the peak position is in line with the 382 – 384 cm⁻¹ range for few layer mechanically exfoliated flakes though the spectral line width is slightly broader than the ~ 2 cm⁻¹ reported in literature [245].

The key point to note is that while spectra such as the one shown in Figure 8.6C indicate the presence of thin flakes, they confirm that the MoS₂ flakes produced are of the 2H polytype. Flakes produced by lithium ion intercalation of MoS₂ have been shown to undergo an intercalation-induced phase transformation to 1T-MoS₂ bearing an octahedral atomic configuration [105, 108, 246]. In 1T-MoS₂ the E_{2g}¹ mode is inactive [105, 107]. Additional distortion due to the intercalation process has also been shown to result in the activation of new Raman modes [107]. The flakes produced in this work bear Raman signatures exclusive to 2H-MoS₂ and are consistent with pristine samples of mechanically exfoliated MoS₂ crystals [245]. This is significant as it confirms that solvent assisted exfoliation yields undistorted 2H-MoS₂ and that no structural transformations occur due to the processing.

Raman mapping centred around the A_{1g} mode (scanning grid size 300 nm, Figure 8.6D) allowed identification of MoS₂ flakes. MoS₂ flakes made up the majority of the objects seen in AFM and SEM imaging, though some of the smallest objects observed did not have the required Raman signature - these contaminants were probably particles of silicon debris from the substrate marking process. Across a sample of 50 MoS₂ flakes, the E_{2g}¹ peak centres fell within the range 376 – 384 cm⁻¹ while the A_{1g} peak centres were in the range 400 – 406 cm⁻¹. Such shifts and peak broadening have been observed in the Raman spectra of chemically synthesised few-layer MoS₂ and in fullerene-like MoS₂ [244]. In order to test if the shifts were due to size effects, the AFM heights and Raman spectral features were compared for the 50 MoS₂ flakes studied. No obvious trend with flake thickness was observable. The data is plotted in Appendix Figure 10.4 on page 185. It is quite possible that the use of an unfiltered maximum intensity Raman excitation laser caused variable sample heating, resulting in the peak

shifts - the maximum intensity laser source was required to produce an adequate Raman signal for mapping and MoS₂ flake identification. In addition, literature data does not examine lateral size effects, leaving open the possibility that variations in flake lateral dimensions, thickness and shape affect the Raman signal.

As part of this analysis, a set of MoS₂ flake heights were obtained. The height data for 50 flakes is summarised in Figure 8.6F. It was found that larger objects with lateral dimensions 500 – 1000 nm tended to be thicker than smaller flakes, sometimes with heights in the tens of nanometres as shown to the right of the distribution. The SEM images indicated some aggregation was present which would skew the data towards larger heights. The smaller flakes below ~ 500 nm in size were much thinner in general with heights in the range 3 – 7 nm. A few steps in the range 0.9 – 1.2 nm were observed consistent with MoS₂ monolayers, meaning the small flakes were likely 3 – 7 layers thick. These small flakes dominate the distribution in Figure 10.4F. No unambiguous monolayer material was observed with AFM and this was likely due to aggregation effects. It is noted that the AFM analysis was somewhat limited by the available equipment, use of a higher resolution instrument with larger scan areas and > 512 samples per line and > 512 lines per image would facilitate the search for monolayer and bi-layer material and yield more accurate step height information. Contact mode AFM could also be considered to yield better topographic information.

8.3.4 TMD Films and Hybrid Materials

The MoS₂ and WS₂ dispersions were easily prepared in large volumes at high concentrations (0.5 – 1 mg/ml) using bath or horn tip processing. This enabled the formation of free-standing films. These liquid-phase systems are highly versatile, allowing the facile formation of hybrid films by simply blending with dispersions of other nanomaterials. Figure 8.7A shows photos of free-standing films prepared with pure MoS₂ and WS₂ dispersions, along with a graphene film and hybrid films. The SEM images in Figure 8.7B and C show that the MoS₂ and WS₂ flakes roughly aligned themselves in the plane of the film. These films showed no evidence of impurities and had surface

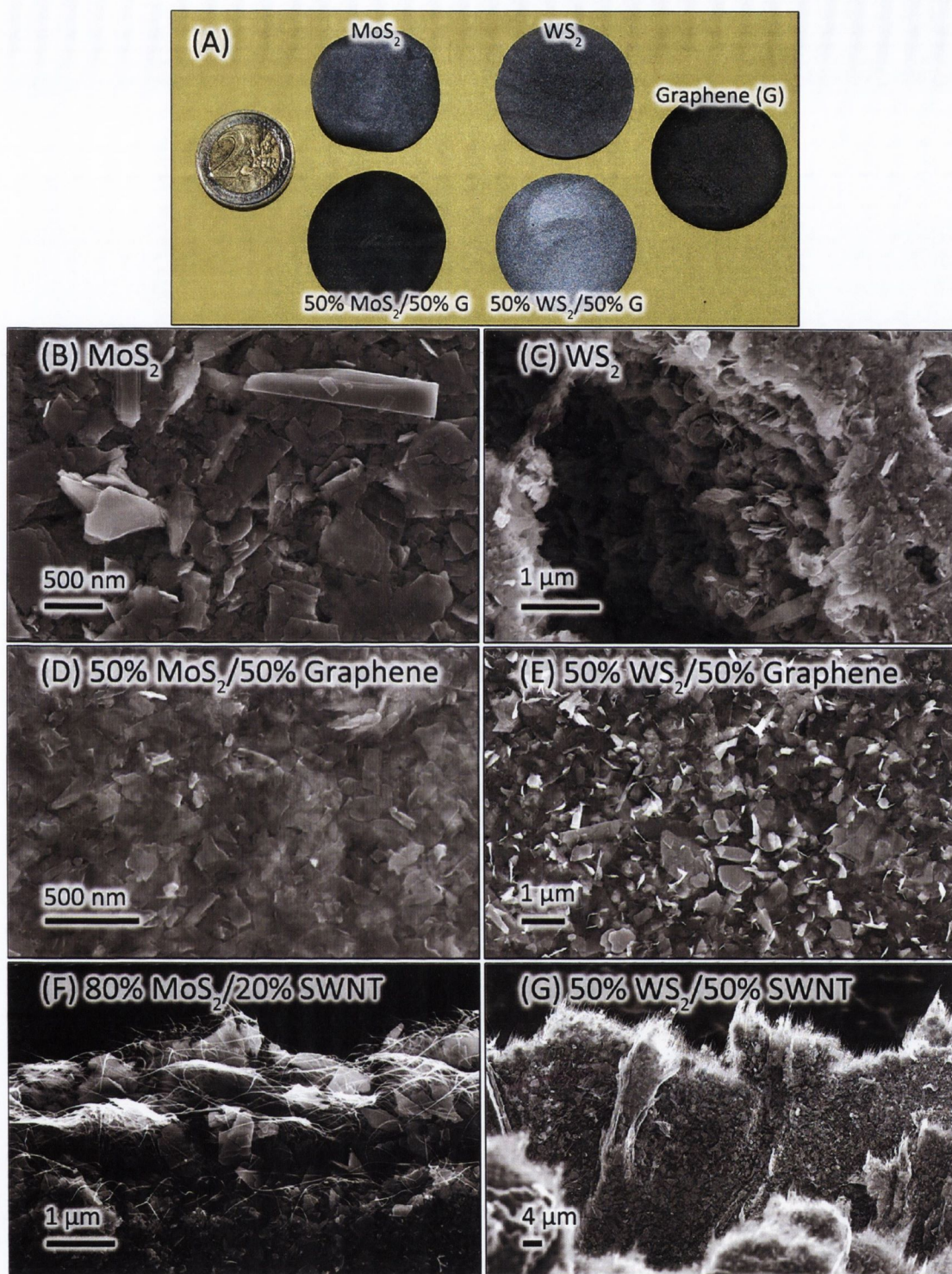


Figure 8.7: Images of MoS_2 and WS_2 nanosheet films and hybrid materials. (A) Photos of free-standing MoS_2 , WS_2 and graphene films along with hybrid films made of 50 : 50 mass ratio blends. (B) and (C) SEM images of the surfaces of pure MoS_2 and WS_2 nanosheet films. (D) and (E) SEM images of the surfaces of free-standing $\text{MoS}_2(\text{WS}_2)$ /graphene hybrid films at 50 : 50 mass ratios. (F) and (G) SEM images of fractured edges of hybrid $\text{MoS}_2(\text{WS}_2)$ /SWNT films.

morphology that closely resembled the graphene films shown in Chapter 7. Indeed, in the SEM images of the hybrid films shown in Figure 8.7D and E it is impossible to distinguish MoS₂ and WS₂ from graphene. The addition of graphene in making the 50% mass fraction hybrids improved the mechanical properties of MoS₂ and WS₂. The pure graphene film had Young's modulus of ~ 1 GPa. Comparing pure TMD and hybrid films, the Young's modulus rose from ~ 0.4 GPa to ~ 1.8 GPa for MoS₂ and from ~ 1.8 GPa to ~ 3.2 GPa for WS₂ (these measurements were performed by Umar Khan).

In a similar fashion, TMDs can be blended with SWNTs. In this case, the MoS₂ and WS₂ flakes were blended with Iijin SWNTs nanotubes that had been originally dispersed in CHP. As shown in Figure 8.7F and G, the MoS₂ and WS₂ flakes were embedded in a network of long SWNTs. It was found that filtering the total blended dispersion volume of up to 20 ml onto a filter membrane at once produced an inhomogeneous film, with a higher concentration of MoS₂ or WS₂ on the film side in contact with the membrane and a rougher top surface rich in SWNTs. To overcome this, a layered deposition process was used, with small aliquots of 2 – 5 ml of dispersion filtered at a time and allowing each aliquot to dry and compact before applying the next aliquot. This produced more robust and homogeneous hybrid films.

A set of MoS₂/SWNT hybrid films were prepared from concentrated MoS₂ dispersions on nitrocellulose and transferred to metal foils. To illustrate the potential utility of hybrid TMD films these samples were tested as cathodes in lithium ion batteries. The battery cell operated by reversibly exchanging Li⁺ ions with the working material via the electrolyte; for an MoS₂ electrode this exchange process can be written as $x\text{Li} + \text{MoS}_2 \leftrightarrow \text{Li}_x\text{MoS}_2$. The lithium intercalates into the layered structure of MoS₂, resulting in a conversion from 2H to 1T structure [247]. Initial testing of the hybrid films indicated a marked improvement in performance over MoS₂ films prepared by solvent-assisted exfoliation. Figure 8.8 shows data for a pure MoS₂ film and a 80% MoS₂-20% SWNT hybrid film. The MoS₂ film shows a rapid degradation in capacity over the first 10 cycles, with 86% of capacity lost by the 40th cycle. The hybrid film performed better over the same number of cycles with 75% of the initial capacity retained. This data compares well with literature for other MoS₂-based nano-structured and com-

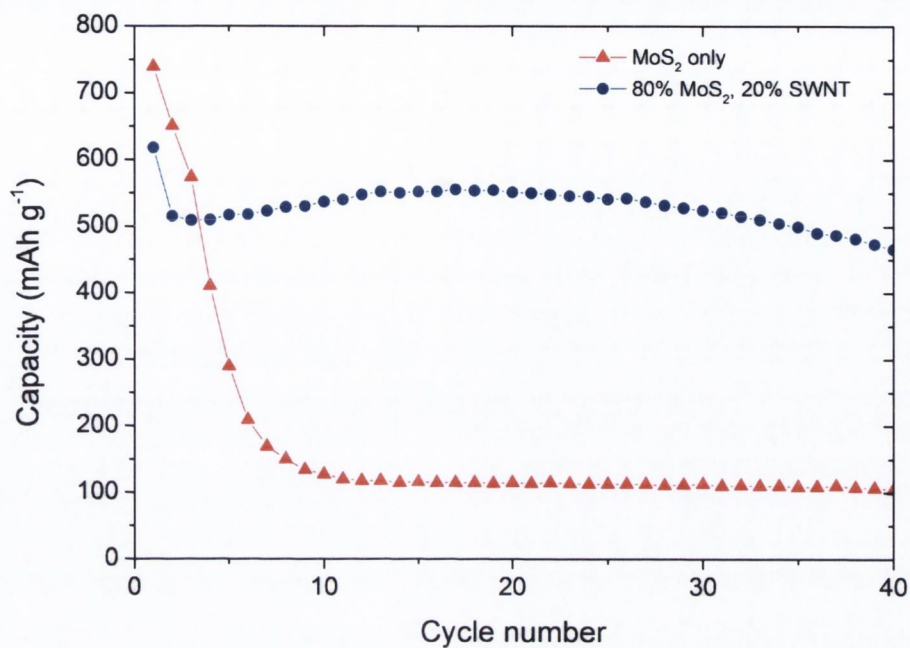


Figure 8.8: Comparison of battery capacity for MoS_2 and MoS_2/SWNT cathode materials

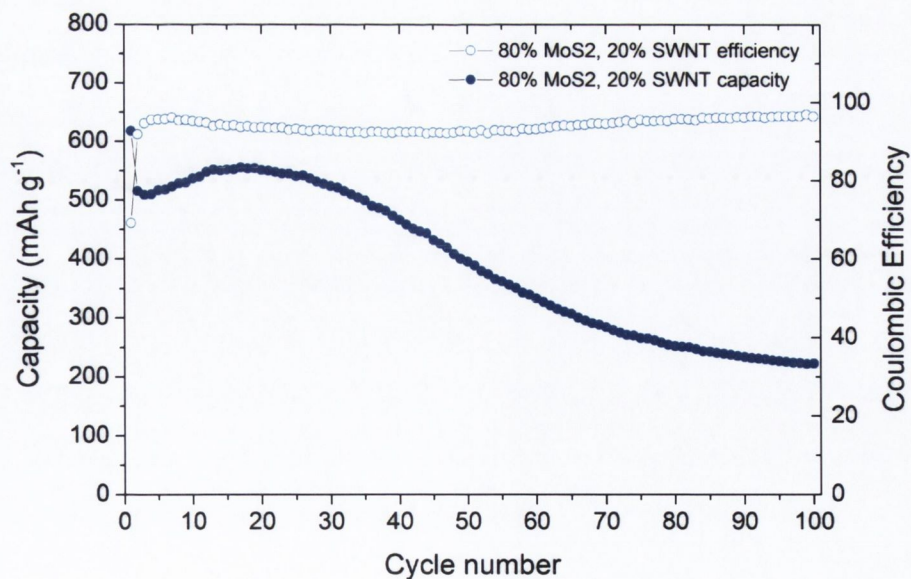


Figure 8.9: Extended battery capacity and efficiency testing of MoS_2/SWNT cathode material

posite materials tested in lithium batteries over similar numbers of charge/discharge cycles [247–251]. The rapid fall-off in MoS₂ electrode capacity has been attributed in literature to aggregation and degradation of active particles during charge/discharge cycling [252]. In the MoS₂/SWNT nanocomposite, the MoS₂ flakes are distributed in a mechanically robust CNT network with restricted mobility, this should help limit aggregation. In addition, the highly electrically conducting CNT network facilitates electron transfer during lithiation and de-lithiation processes. Figure 8.9 shows the results of extending the testing of the hybrid cell to 100 cycles. Also shown is the Coulombic efficiency, this metric relates charge input and output through the cell. The Coulombic efficiency was high at above 95% for all measurements and indicated low energy losses over the charge/discharge cycles. The extended testing revealed a gradual degradation in charge capacity. The final capacity of 222 mAh g⁻¹ is very close to that observed in a similar MoS₂/SWNT hybrid film prepared using MoS₂ and SWNTs exfoliated in aqueous surfactant systems [253]. The reason for the observed degradation with charge cycling is unclear and further tests are under way to study this; several factors including the CNT mass fraction, current density used, electrolyte degradation and CNT purity may be significant.

As the data presented here is limited primarily to charge capacity as a function of cycle number, a full comparison with other battery systems is not possible. With future work performance metrics such as power density, self-discharge levels, temperature performance and specific production costs can be derived for MoS₂/CNT hybrid electrodes of the type discussed above - this will enable a full assessment of the true value of the current work and allow for the setting of targeted performance improvements. One limiting factor in the overall performance of Li-ion batteries is long charge/discharge times, which are largely due to the limited diffusion rate of Li⁺ ions to the interior of the electrode material. Thus, it would be advantageous to increase the porosity of the electrode material. One could envisage exploiting the relatively porous structure of CNT networks in a hybrid system to increase ion flow capacity. In addition, the use of exfoliated 2D materials could improve charge/discharge rates if they could be assembled in such a way as to form a porous electrode that retains a high specific surface area. While charge/discharge data for the system above is not yet available, it is

instructive to compare the final capacity at 100 cycles to other battery cathode materials. Most Li-ion cells operate with natural graphite cathodes with a theoretical maximum capacity of around 370 mAh g^{-1} [254]. Current state-of-the-art cells being examined for use in all-electric vehicle applications use cathode materials based on cobalt oxides, or compounds containing various ratios of cobalt/nickel/manganese/aluminium [255]. These cathode materials typically have capacity of the order of $340 - 680 \text{ mAh g}^{-1}$ [255]. Thus, on capacity alone the hybrid material demonstrated here needs significant improvement to begin rivalling state of the art systems. These improvements could come from the use of improved CNTs with better electrochemical performance and the use of more stable exfoliated layered compounds. Nevertheless, the battery measurements shown here illustrate a key application for liquid-phase exfoliated nanomaterials. The processing enables the simple formation of hybrid materials with properties that surpass the original material. It is hoped work in progress will shed further light on the behaviour of these battery systems and lead to further improvements.

8.4 RESULTS AND DISCUSSION: Bi_2Te_3 AND RELATED COMPOUNDS

The general method of sonication-assisted exfoliation in liquid-phase systems can be extended to other layered materials. In this section, the exfoliation of Bi_2Te_3 , Bi_2Se_3 and Sb_2Se_3 is explored; sonication of these materials resulted in dark grey/black dispersions. As for MoS_2 and WS_2 , a selection of good graphene solvents including CHP, NMP and NVP were found to be effective dispersal media for these materials. Figure 8.10 gives typical optical absorption spectra for these materials dispersed in CHP using 10 min point probe sonication in CHP. The band gaps for these materials are typically $\sim 0.3 \text{ eV}$ (4000 nm) [135, 138, 256] which was beyond the range of available spectrometers. Optical transitions are visible at 272 nm , 268 nm and 264 nm (in Bi_2Te_3 , Bi_2Se_3 and Sb_2Se_3 respectively).

The stability of these types of dispersions was assessed by sedimentation analysis, this data is shown in Figure 8.11. Fitted exponential decay curves are also shown. It is clear that the Sb_2Se_3 dispersion was less stable than the others with fitting indicating a

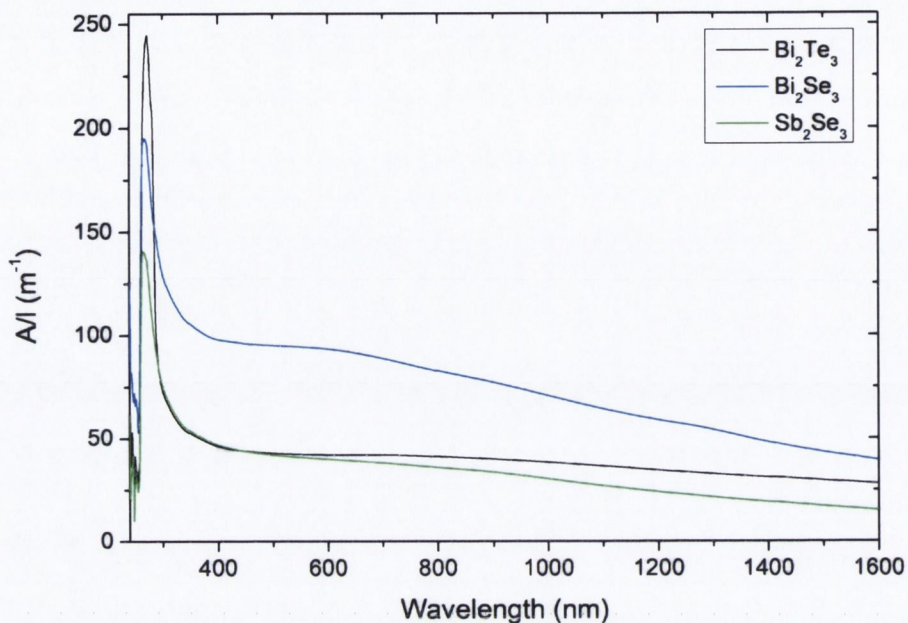


Figure 8.10: Optical absorption spectra for Bi_2Te_3 , Bi_2Se_3 and Sb_2Se_3 dispersed in CHP by 10 min point probe sonication and 1000 rpm centrifugation.

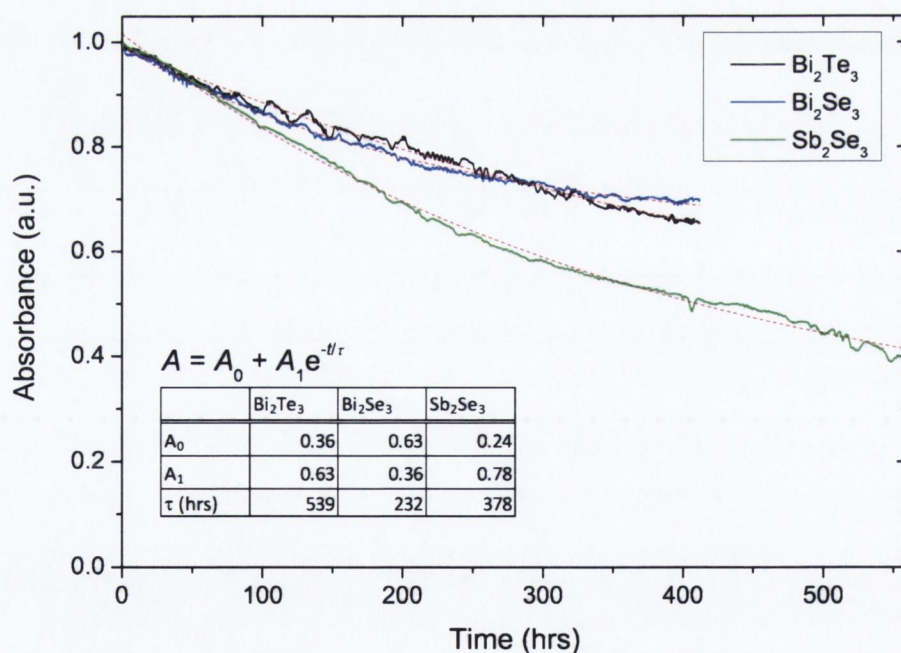


Figure 8.11: Sedimentation behaviour of Bi_2Te_3 , Bi_2Se_3 and Sb_2Se_3 dispersions in CHP. Samples at initial concentration $C_i = 5 \text{ mg/ml}$ were point probe sonicated for 10 min and centrifuged at 1000 rpm. Fitted exponential decay curves are indicated by red dashed lines.

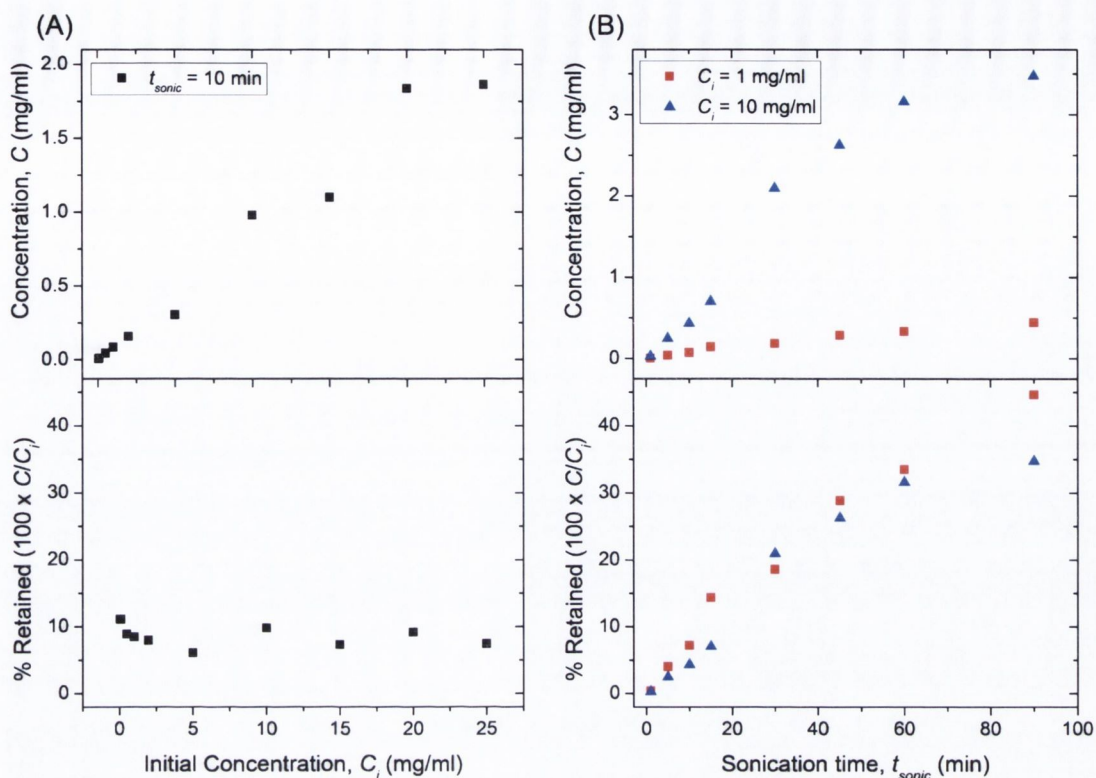


Figure 8.12: Final Bi_2Te_3 dispersion concentration and percentage of starting material retained as a function of (A) initial concentration and (B) sonication time.

stable phase of only 24%. Comparing the fits for Bi_2Te_3 and Bi_2Se_3 shows very different fitting constants despite the similarity of the curves, this appears to be an artefact of the fitting process that could be addressed by recording the data over a longer time period. Nevertheless, after 24 hrs over 96% of material remained dispersed for all three systems, with over 89% remaining after three days in all cases. After three weeks, $\sim 55\%$ of Sb_2Se_3 and $\sim 70\%$ of the Bi_2Te_3 and Bi_2Se_3 remained dispersed. This data suggests reasonable stability of the dispersions and allows a good processing window. Further refinements in solvent selection and centrifugation parameters will help improve the stability further.

The preparation conditions of Bi_2Te_3 dispersions were studied in further detail. The first parameter assessed was the extinction coefficient. The dispersions were found to follow Beer-Lambert behaviour upon dilution. As done previously for MoS_2 , the mass contained in a known volume of stock dispersion was determined by filtration onto a pre-weighed membrane. This allowed calculation of an extinction coefficient

of $\alpha_{\text{Bi}_2\text{Te}_3} = 800 \text{ L g}^{-1} \text{ m}^{-1}$, at an arbitrary wavelength of 740 nm. Following this, the effect of sonication time, t_{sonic} , and the initial concentration of starting material, C_i , was investigated. Figure 8.12A shows a marked increase in final concentration as C_i is scaled up before saturating at the highest values of C_i , with constant yields of around 9% for all initial concentrations studied. A scaling of concentration with sonication time was also observed, as displayed in Figure 8.12B. Unlike the high concentration graphene systems discussed in Chapter 7, the trend did not quite follow $\sqrt{t_{\text{sonic}}}$ behaviour. However, as seen before, increasing the sonication time improved the final concentration of dispersed material. The use of higher initial concentrations can improve yields further, allowing up to 45% of the initial material to be dispersed.

Samples of these dispersions were analysed by TEM. Figures 8.13A and C show examples of ribbon-like Bi_2Te_3 structures. In general these flakes, and others like them, were quite opaque to the electron beam when compared to the materials discussed up till now, i.e. graphene, MoS_2 and WS_2 . This was partly due to the material being more dense and having constituent atoms with higher atomic masses relative graphene and the TMDs imaged previously; this resulted in enhanced scattering of incident electrons yielding higher contrast [201]. Another factor was that the exfoliation was not as complete as before, with most of the flakes composed of more than a few layers. In addition, the lack of clear edge contrast in these types of flakes prohibited the use of quantitative thickness analysis by edge counting.

Nevertheless, in nearly all cases thin protruding regions were observed. A close up of a typical edge is shown in Figure 8.13B. In the inset, a fast Fourier transform of the image displays a hexagonal pattern indicating a hexagonal parent crystal structure. In addition, direct measurement of the observed hexagonal lattice fringes shows a lattice spacing of 0.219 nm, this is in perfect agreement with literature data on chemically synthesised Bi_2Te_3 nanoparticles [139, 257], and with simple direct calculations based on the known lattice constant of $a_H = 0.4384 \text{ nm}$ [130, 131]. Figure 8.13D also shows a Bi_2Se_3 flake imaged with annular dark-field STEM. The close-up of the marked yellow square shown in Figure 8.13E clearly illustrates that the layered structure of the parent bulk crystal has been retained, with exposed single QLs visible. The enhanced surface area of these flakes and the presence of thinned edges, with exposed QLs, may affect

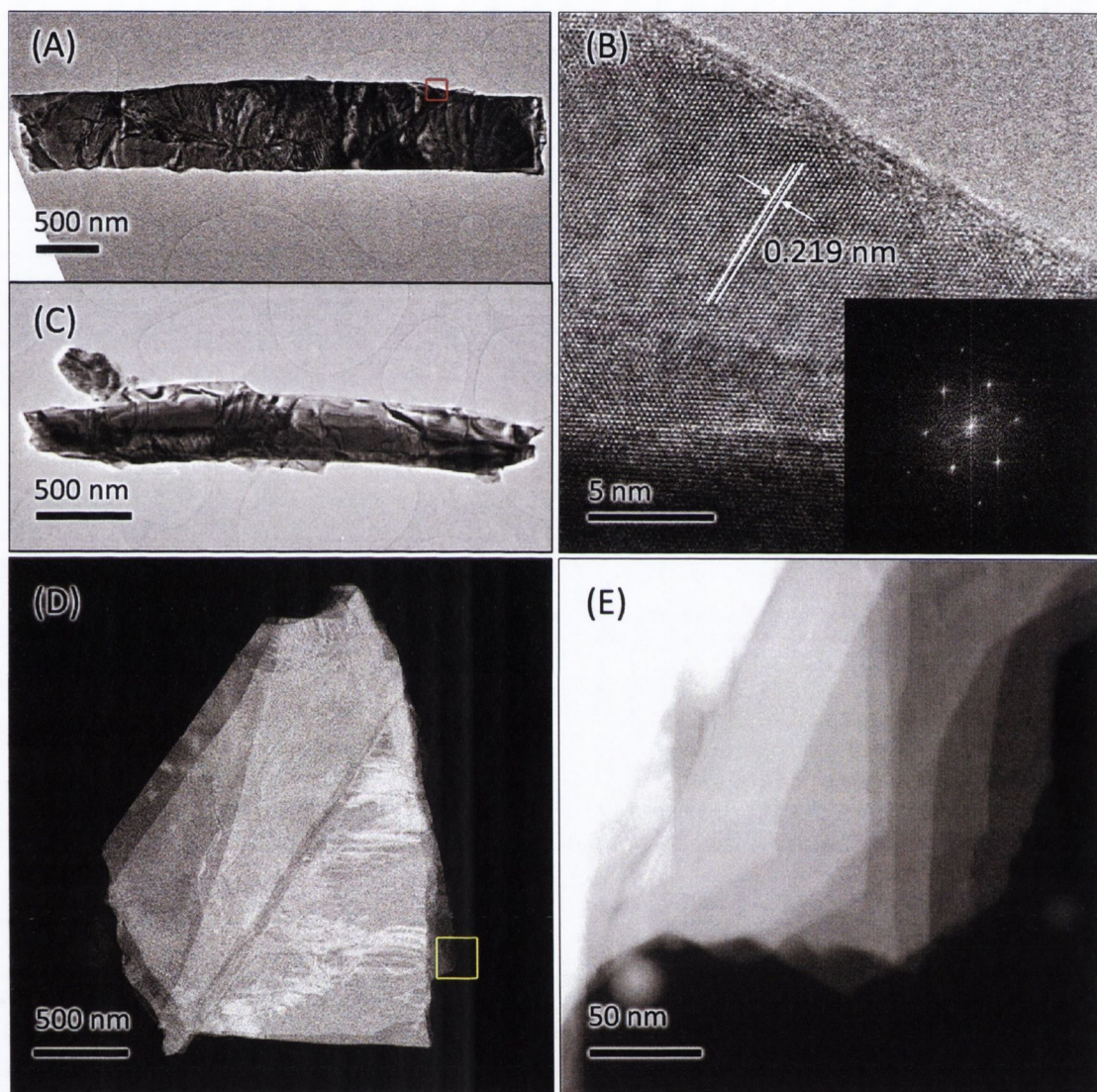


Figure 8.13: TEM and STEM images of material found in Bi_2Te_3 and Bi_2Se_3 dispersions prepared in CHP. (A) and (C) Ribbons of Bi_2Te_3 . (B) High resolution image of the region marked by the red square in (A) with spacing of lattice fringes marked, inset showing FFT of the image. (D) STEM image of a Bi_2Se_3 flake with close-up of the area marked by the yellow square shown in (E).

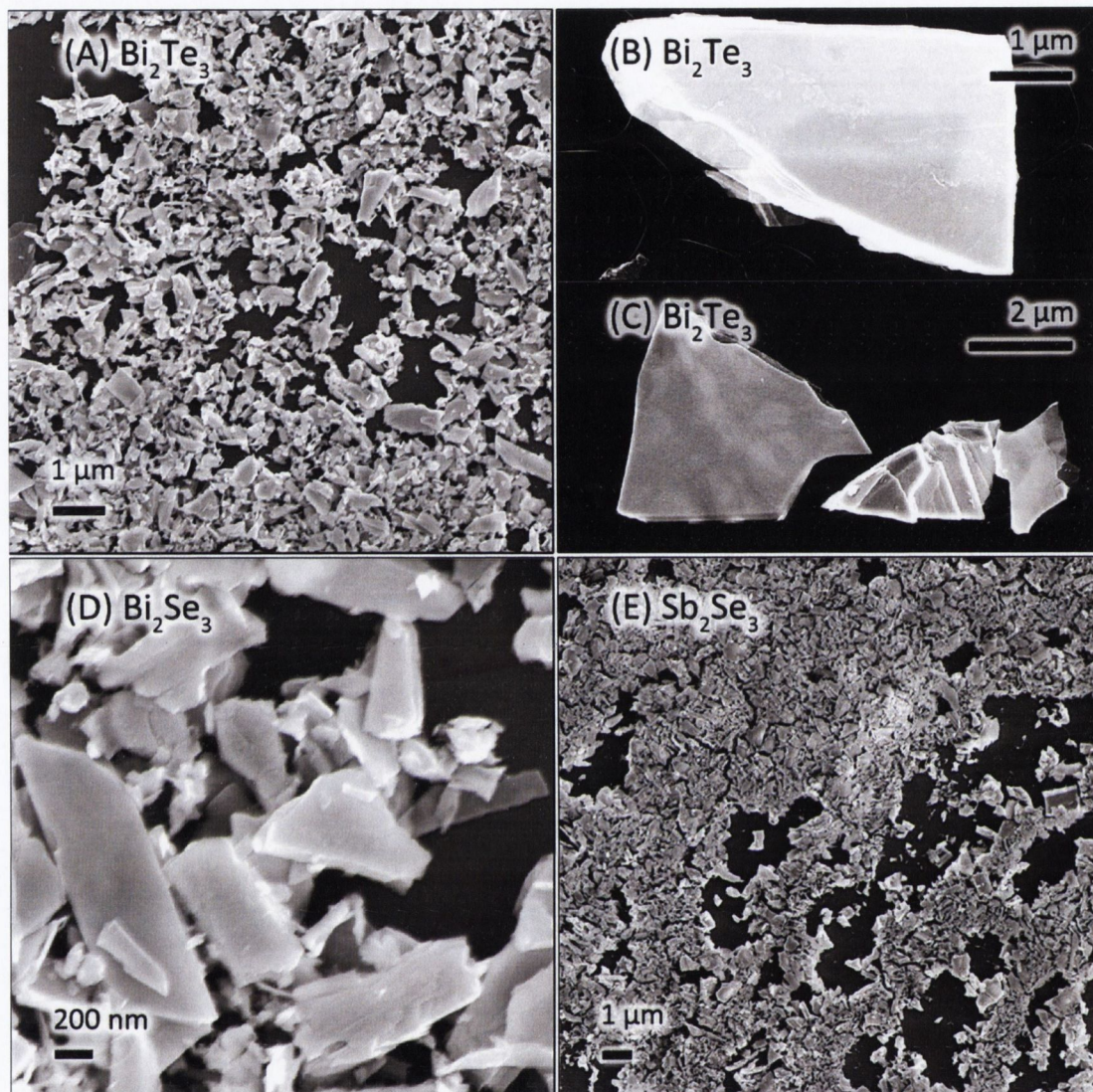


Figure 8.14: SEM images of (A-C) Bi₂Te₃, (D) Bi₂Se₃ and (E) Sb₂Se₃ flakes and thin films. The large flake in (B) and the cluster of flakes in (C) were suspended on a TEM grid.

electrical and thermal characteristics; this may prove useful in future thermoelectric device applications and in the making of nano-structured composites.

To further characterise these materials, films were prepared and transferred to silicon substrates. SEM images of flakes and thin films prepared from Bi₂Te₃, Bi₂Se₃ and Sb₂Se₃ are shown in Figure 8.14. For all materials, the films were composed of a disordered array of platelets of various sizes ranging from about 20 nm to several μm. The films were not mechanically robust and were easily rubbed off glass or silicon substrates, with bare patches and cracks visible in SEM imaging of thin films.

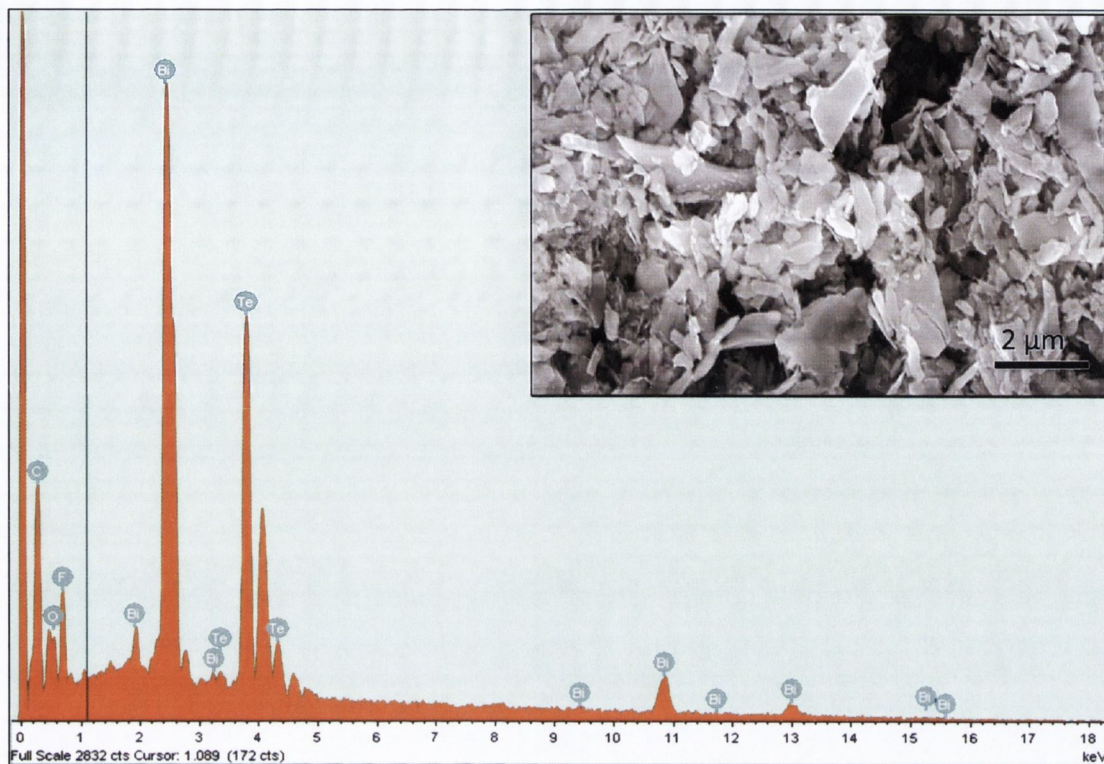
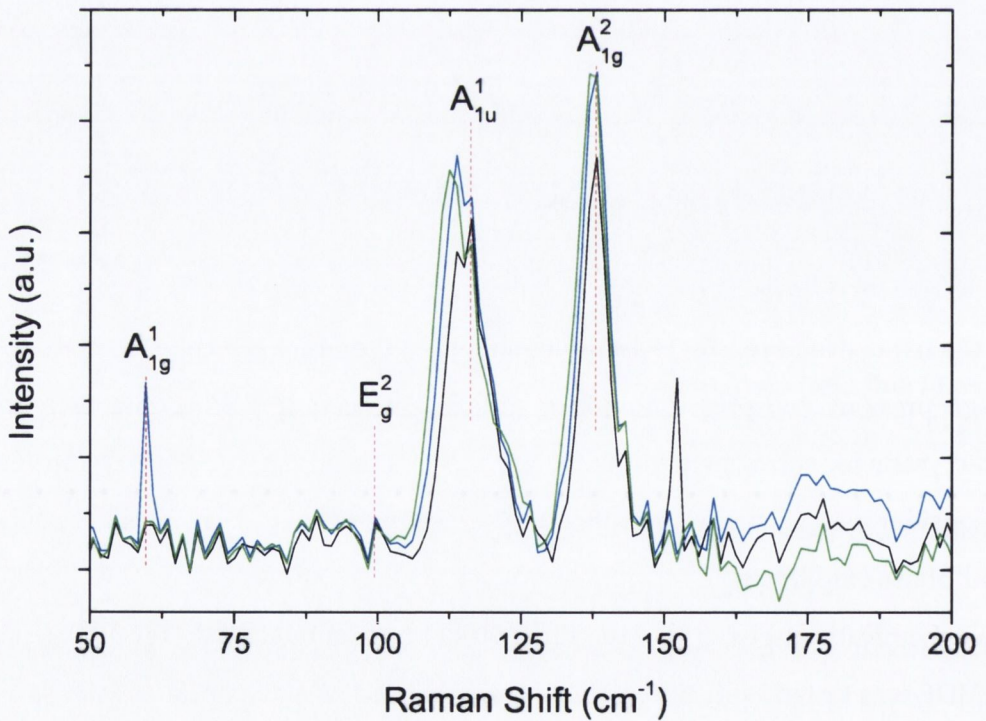


Figure 8.15: SEM/EDX analysis of Bi_2Te_3 film deposited on a PVDF membrane. EDX spectrum acquired using 20 kV electron beam. Inset: SEM image of the sampled area.

The poor packing of the flakes made electrical measurements on the films difficult. Typical electrical conductivity values of between 10^{-3} and 10^{-4} S/m were measured for Bi_2Te_3 films, far below typical literature values in excess of 10^3 S/m. It is noted that the nano-structured Bi_2Te_3 samples shown in literature typically used some form of high pressure compression and/or sintering process to form dense pellets from nano-crystals for subsequent electrical and thermal testing [120, 258–264], future work can consider using a similar densification/annealing process on material produced by liquid phase exfoliation.

The chemical composition of the films was also examined. A Bi_2Te_3 film deposited on PVDF was tested with EDX. Silicon was not used as a substrate as intense silicon X-ray features dominated the spectra and were found to corrupt the elemental analysis. The EDX spectrum is shown in Figure 8.15, with an SEM image of the area sampled in the inset. The bismuth M line and tellurium L line are the dominant peaks in the spectrum. Some oxygen, carbon and fluorine were also detected. The detection of

Element	Emission line	Weight %	Atomic %
C	K	14.6	49.2
O	K	2.5	6.2
F	K	12.8	27.1
Bi	M	37.0	7.1
Te	L	33.1	10.4

Table 8.1: EDX elemental analysis for exfoliated Bi_2Te_3 deposited on a PVDF membraneFigure 8.16: Raman spectra at three points along a film of Bi_2Te_3 flakes deposited on an alumina membrane. Spectra were collected with low laser power and 10 min acquisition times, averaged over two accumulations.

carbon and fluorine can be attributed to the penetration of the high tension electron beam into the underlying PVDF membrane with molecular formula $-(\text{C}_2\text{H}_2\text{F}_2)_n-$. The oxygen detected was also probably due to functional groups attached to the PVDF during manufacturing to render it hydrophilic. The results of the elemental analysis by the SEM/EDX software are shown Table 8.1. This shows a Te:Bi ratio of 1.46, within 4% of the expected stoichiometric ratio of 1.5; the difference may be due to a slight Te deficiency caused by sonication-induced damage or maybe be attributed to uncertainty in the the EDX analysis. Significantly, the data shows that the processing has not introduced large-scale contamination or dramatically altered the chemical composition of the Bi_2Te_3 flakes.

In addition, Raman spectra were collected from a Bi_2Te_3 film deposited on an alumina membrane. Due to the low thermal conductivity of Bi_2Te_3 , pronounced heating effects and visible sample burning made the acquisition of a large number of spectra difficult. Low laser intensities and long accumulation times were required. Figure 8.16 shows spectra collected from three points on a typical film. A series of peaks are visible from each spot, two peaks are common to all three spectra. The peak labelled A_{1g}^2 at 138.1 cm^{-1} is an IR and Raman active out-of-plane (c -axis) vibration commonly observed in Bi_2Te_3 while one of the spectra also featured a related A_{1g}^1 out-of-plane vibration [130, 132, 133, 257, 265]. The peak at 116.3 cm^{-1} , labelled A_{1u}^1 , corresponds to an IR active out-of-plane vibration. This mode is normally Raman inactive in bulk Bi_2Te_3 but has been observed in mechanically exfoliated and chemically synthesised Bi_2Te_3 nanoflakes [130, 132, 133, 257]. The activation of this peak has been attributed to the loss of crystal periodicity normally found in bulk Bi_2Te_3 as flakes are thinned and new inter-layer interfaces are formed [133]. Another feature typical of Bi_2Te_3 is normally found around 100 cm^{-1} and is denoted E_g^2 and corresponds to an in-plane lattice vibration, this feature was not observed within the limits set by the noise of the spectra of Figure 8.16. This feature has been shown to be largely absent in 2D Bi_2Te_3 synthesised by chemical vapour transport [257]. In mechanically exfoliated flakes, the E_g^2 peak also showed a drop in intensity relative the A_{1u}^1 peak with decreasing flake thickness [133]. The dominance of the A_{1u}^1 peak over the E_g^2 in liquid-phase exfoliated flakes may indicate the loss of bulk crystalline properties as surface-to-volume ratios

are increased. The shoulders of the $A_{1\mu}^1$ peak at 112.5 cm^{-1} and 113.8 cm^{-1} and the peak at 152 cm^{-1} in one of the spectra are unknown features.

Finally, dispersed Bi_2Te_3 flakes were spray-cast onto silicon and analysed by AFM. Figure 8.17A and B show samples of two regions analysed. The SEM images show a random scattering of flakes, similar to the thin films in Figure 8.14 but with a lower areal density. On close examination, widespread clustering of flakes and aggregation is present. Figure 8.17C gives statistics for heights measured across 100 objects - these measurements were taken from higher magnification AFM scans within the areas shown in Figure 8.14. Only 6% of objects could be classed as very thin with height $< 10\text{ nm}$ (corresponding to about 10 QLs or three unit cells), the majority were much thicker with a mean value of 37 nm. The high values are partly due to aggregation, though with reference to the TEM images it appears that incomplete exfoliation has occurred. This may be due to a lower tensile strength of Bi_2Te_3 and perhaps stronger inter-layer van der Waals interactions relative to materials like graphite; this may result in more facile tearing of the flakes under the tensile stresses applied to the bulk material during sonication [228, 238]. Nonetheless, these flakes show enhanced surface to volume ratios that could increase surface electronic effects. Furthermore, literature data shows a marked reduction in the in-plane and cross-plane thermal conductivity (κ) of mechanically exfoliated $\sim 50\text{ nm}$ thick Bi_2Te_3 stacks, with in-plane κ reduced by factor ~ 2.4 and cross plane κ reduced by factor ~ 3.5 from bulk values [132]. By analogy, similar thermal conductivity effects can be expected from the liquid-phase exfoliated material shown here. In addition, the dispersions can be easily processed and mixed with other nanomaterials such as graphene, CNTs, TMDs or others for the formation of hybrid materials, as illustrated for MoS_2 and WS_2 earlier. Future studies on the formation of these hybrids could potentially yield novel cost-effective thermoelectric materials with high electrical conductivity and high Seebeck coefficients.

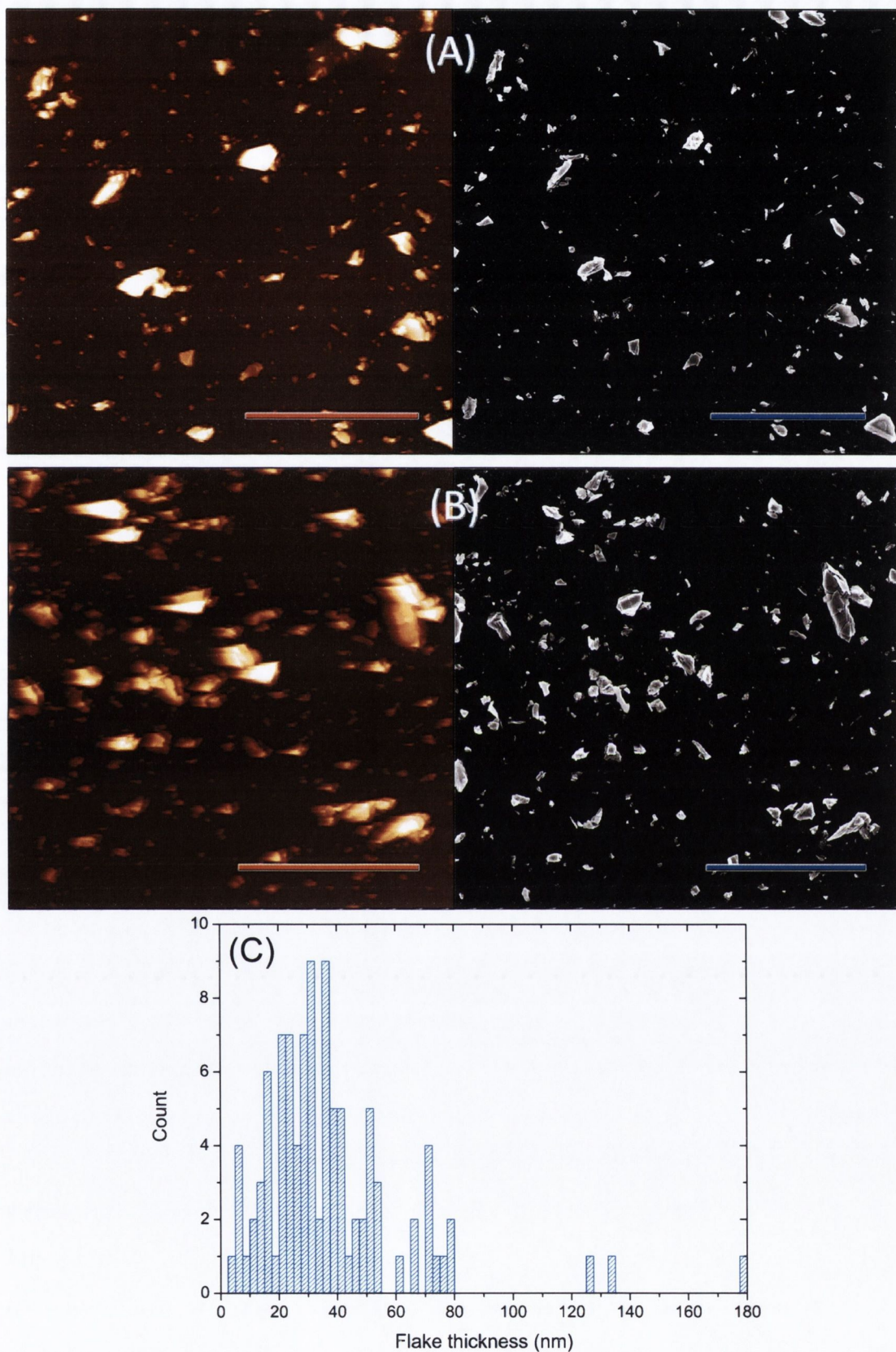


Figure 8.17: AFM/SEM analysis of Bi_2Te_3 flakes deposited on silicon by spray casting. (A) and (B) show AFM (left, orange) and SEM (right, grayscale) images of two different $14\ \mu\text{m}$ areas analysed. (C) Histogram of Bi_2Te_3 flake thickness. All scale bars are $4\ \mu\text{m}$ in length.

8.5 CONCLUSIONS

The work presented in this chapter has demonstrated that the sonication-assisted liquid-phase processing techniques previously used to produce graphene can be extended to form a wide range of other layered nanomaterials. Very stable dispersions of two transition metal dichalcogenides, MoS₂ and WS₂, have been prepared in common amide solvents. TEM analysis shows the flakes are of high quality and provides evidence of large-scale exfoliation to yield flakes that closely resemble graphene and few-layer graphene in shape and appearance. Further studies of deposited MoS₂ flakes by scanning Raman spectroscopy showed features characteristic of 2H-MoS₂. This confirmed that the preparation procedure did not chemically modify the crystalline structure to yield a 1T octahedral geometry and distinguishes the chosen method from traditional Li-ion intercalation exfoliation routines. In addition, the Raman data allowed positive identification of MoS₂ flakes to allow characterisation by SEM and AFM. The AFM data showed the presence of small few-layer flakes consistent with the TEM results, though a correlation between flake height and Raman peak shifts was not found.

Hybrid materials consisting of MoS₂ and WS₂ blended with graphene and SWNTs were successfully prepared. Testing of MoS₂/SWNT films for Li-ion battery applications showed improved cycling stability and storage capacity compared to pure MoS₂ films. Some degradation was observed over large numbers of charge/discharge cycles with further work required to improve performance. The MoS₂/SWNT hybrid system provides proof-of-concept. The range of hybrid materials that could be formed in this manner is extensive, with the ability to utilise not just graphene and CNTs but also a broad collection of polymers and other exfoliated TMDs.

Finally, the exfoliation of a class of materials with known thermoelectric properties and topological insulator qualities was examined. Dispersions of Bi₂Te₃, Bi₂Se₃ and Sb₂Se₃ were prepared in CHP. TEM and SEM analysis showed nanoflakes had been produced which retained the layered structure of the bulk materials. Raman spectra showed peaks characteristic of Bi₂Te₃ with possible spectral evidence of surface effects.

EDX analysis confirmed that the production process did not yield chemically modified Bi_2Te_3 flakes. AFM and SEM analysis of deposited Bi_2Te_3 flakes showed some evidence of aggregation and confirmed TEM evidence suggesting limited exfoliation in these materials. Nonetheless, the enhanced surface to volume ratio of these nanomaterials warrants further study and may lead to the observation of novel electrical characteristics. In addition, the facile production of hybrids of these materials through liquid-phase processing will facilitate future studies in thermoelectric devices.

CONCLUSIONS AND FUTURE WORK

9.1 CONCLUSIONS

The aim of this thesis was to study the ultrasound-assisted exfoliation and dispersion of layered nanosheets in liquid phases. Across all systems studied, the processing method offered a scalable route to produce high quality material without the need for aggressive chemical treatments. To begin, this study examined the exfoliation of graphite to produce graphene across a broad range of solvents. It was shown that graphene could be successfully produced in over 40 solvents, 28 of which were new graphene solvents. It is noted that significant populations of monolayer and bilayer graphene were observed, even in solvents showing poor dispersibility. TEM analysis of graphene produced across all six solvents showed $> 63\%$ of flakes were composed of 1 – 5 graphene layers. This is important as many of the new solvents have advantages over those previously studied such as NMP, including low boiling points and compatibility with polymers to facilitate composite formation. The energetics of graphene-solvent interactions have been examined. It was confirmed that good graphene solvents have surface tensions close to 40 mJ/m^2 and Hildebrand parameter $\sim 23 \text{ MPa}^{1/2}$. Studying the dispersions in terms of Hansen solubility parameters showed that dispersive interactions alone do not specify good solvents and that a degree of solvent polarity is required to disperse graphene well. In addition the Hansen solubility parameters of graphene itself have been estimated as $\langle \delta_D \rangle = 18.0 \text{ MPa}^{1/2}$, $\langle \delta_P \rangle = 9.3 \text{ MPa}^{1/2}$ and $\langle \delta_H \rangle = 7.6 \text{ MPa}^{1/2}$. This has allowed the Flory-Huggins parameter to be calculated for each solvent to show that the energetic cost of graphene exfoliation strongly influences the ability of a solvent to disperse graphene.

Graphene production in aqueous systems using surfactant stabilisers was demonstrated for the first time. It was shown that large quantities of few-layer graphene

could be readily produced ($\sim 43\% < 5$ layers), including significant quantities of monolayer material as proven with reference to electron diffraction data. The flakes were shown to be of high quality with no evidence of large-scale structural defects. This showed that oxidative chemical treatments or other functionalisation routines are not required to produce graphene in water-based systems. The dispersions were shown to be reasonably stable over a time frame of ~ 6 weeks. Zeta potential measurements and the application of DLVO theory probed the stabilisation mechanism, proving the dispersions were stabilised against re-aggregation by electrostatic repulsions between surfactant coated graphene flakes. The graphene flakes were deposited to form films and shown to be composed of few-layer material by Raman spectroscopy, in agreement with TEM data. FTIR and XPS analyses confirmed the quality of the material with evidence of only very low levels of oxidation. AFM analysis demonstrated that spray casting allows small flakes to be easily deposited, revealing a significant population of flakes with thickness consistent with monolayer material.

High concentration surfactant-stabilised graphene dispersions were also prepared. Graphene concentrations exceeding 1 mg/ml were made using low power sonication for long times and optimised starting concentrations of graphite and surfactant. The dispersion concentration followed $\sqrt{t_{sonic}}$ behaviour. Mild centrifugation at $\omega = 1500$ rpm yielded very stable dispersions having an estimated 10% number fraction of graphene monolayers with $\sim 80\%$ of flakes composed of < 5 layers. Higher centrifugation rates were shown to increase the monolayer yield. Raman and TEM analyses showed that prolonged sonication up to ~ 430 hours did not reduce overall flake dimensions ($\langle L \rangle \sim 800$ nm, $\langle W \rangle \sim 350$ nm) or increase the density of basal plane defects. The concentration of the high concentration dispersions scaled with ω^{-1} , with increased rotation rates shown to decrease the overall graphene flake size. The ratio between the Raman D-band and G-band intensities was shown to scale linearly with the flake dimensions, with an observed trend in defect density that was consistent with the formation of new flake edges. The Raman and flake size data compared well to that obtained from studies on graphene-surfactant dispersions physically size selected using column chromatography. Free-standing films composed of predominantly few-layer graphene flakes were prepared with mechanical and electrical properties that

compared well to similar films shown in literature prepared from reduced graphene oxide.

Finally, other materials composed of layered atomic planes were studied. Very stable high concentration dispersions of exfoliated MoS₂ and WS₂ were prepared in solvent-based systems. These dispersions showed optical features characteristic of the parent crystals. TEM analysis confirmed that large-scale exfoliation occurred, revealing flakes similar in appearance to graphene. Raman spectra of MoS₂ flakes showed that the original bulk 2H crystal structure had been retained, this distinguished the chosen method from alternative methods using lithium ion intercalation where transformations to a 1T structure are observed. Scanning Raman measurements confirmed the nature of MoS₂ flakes deposited on silicon by spray casting and enabled AFM analysis to reveal small flakes with heights consistent with 3 – 7 layer thickness. Hybrid materials were prepared by blending MoS₂ and WS₂ dispersions with graphene and single-walled carbon nanotubes. MoS₂/carbon nanotube films were tested as cathode materials in lithium ion batteries. The hybrid film showed enhanced capacity and cycling stability compared to the exfoliated MoS₂. Dispersions of thermoelectric materials Bi₂Te₃, Bi₂Se₃ and Sb₂Se₃ were also prepared by sonication in solvent systems and shown to have moderate temporal stability. TEM and AFM studies of Bi₂Te₃ flakes showed that partial exfoliation had occurred, although protrusions of thin quintuple layers were frequently observed. TEM and SEM/EDX analysis confirmed that the core crystal structure and stoichiometry of Bi₂Te₃ was retained during processing. Raman spectra from Bi₂Te₃ flakes showed features characteristic of the bulk material whilst displaying peak intensity ratios that suggest enhanced surface effects.

Overall, I strongly feel this thesis contributes to the understanding and development of diverse liquid-phase dispersions of exfoliated layered materials and that this work will promote future advances in nanomaterials research.

9.2 FUTURE WORK

The methods and results shown in this thesis enhance the availability of layered materials to researchers. It is hoped the knowledge gained in relation to solvent performance and Hansen solubility parameters for graphene will facilitate the formulation of high performance solvent blends and polymer composite materials. A similar study is under way in our group to determine the Hansen solubility parameters of a selection of transition metal dichalcogenides, this will further advance the study of solvent-based exfoliation routines. The work on surfactant-assisted graphene exfoliation in water offers an alternative liquid-phase processing route with a number of benefits including minimal cost, high safety and compatibility with aqueous reagents. These dispersions are suitable for a wide range of applications with work in progress examining their use in gas sensors and electrodes in energy storage devices. The successful liquid-phase exfoliation of layered inorganic materials such as MoS_2 and WS_2 offers an exciting opportunity to exploit layered structures with a wide range of useful attributes. As part of this future work we are currently investigating ways to improve the performance of lithium ion batteries using blends of various liquid-phase dispersed low dimensional nanomaterials. Furthermore, the availability of liquid-dispersed layered compounds offers a route to form nanostructured hybrid materials which may have advantageous thermoelectric performance for energy conversion applications.

Some aspects of this future work can be specified more precisely as targeted projects for future PhD candidates. These are now given for the study of the effects of ultrasound in the liquid-phase processing of layered materials and for the development of high performance thermoelectric materials based on 2D nanostructures.

9.2.1 *Investigation of the mechanics/kinetics of ultrasound-assisted liquid-phase exfoliation of 2D materials*

It has been shown that liquid-phase dispersions of exfoliated layered materials such as graphene or MoS_2 can be formed in suitable media by applying ultrasonic energy to

bulk parent materials [9, 10, 162, 238]. However, there is only a limited understanding of the role of ultrasound and the role of the starting material.

The first part of this study would aim to examine the influence of modified sonication parameters on a model system, e.g. graphite exfoliated to graphene. Different sonication frequencies could be tested and results compared to literature where fixed 20 kHz frequency generators were used. By examining the size and defect densities of the graphene flakes with TEM and Raman spectroscopy, improved production procedures can be derived.

Following this the variation of yield with other parameters that influence sonication such as solvent viscosity and temperature would be tested. In particular the study of solvent viscosity could be related directly to the sonic wave propagation within the liquid medium.

To further knowledge of the effects of sonication on the quality of material produced, tip-enhanced Raman spectroscopy could be used to examine the basal plane and edge defect densities of the flakes. Observed trends could be related to the sonication frequency. In addition, tip enhanced Raman could be used in the determination of the defect densities of different starting materials (e.g. HOPG, Kish graphite, various mined graphites). In addition, FTIR and XPS spectroscopies can be used to assess the extent of chemical functional groups in the starting material. This analysis of the starting material could be related back to the quality of the graphene flakes produced. The data could also potentially be fitted to simulations based on the fracture of defective graphene/graphite crystals with a view to understanding the influence of defects in the shear of graphite crystals during sonication and the factors influencing the sizes of graphene flakes produced.

9.2.2 *Investigation of the improvement of thermoelectric devices using liquid-exfoliated 2D nanomaterials*

Thermoelectric materials have promise for use in energy conversion but improvements in the thermoelectric figure of merit ZT are needed to make their widespread usage vi-

able. In particular, the availability of 2D thermoelectric materials like bismuth telluride opens the prospect of using nano-structuring to improve devices [112].

One of the challenges with current work on thin film thermoelectrics lies with determination of ZT . Whilst electrical conductivity (σ), Seebeck coefficient (S) and carrier concentrations can be determined easily, say using deposited contacts, the thermal conductivity (κ) is not easy to measure. Most work to date on thin-film thermoelectric devices has relied on using bulk values for thermal conductivity or on cross-plane measurements. Work is now under way to measure all the relevant thermoelectric parameters for thin films systems using a van der Pauw testing method. Thus, the first part of this project would be to adapt this van der Pauw technique to characterise thin films of thermoelectric materials produced in different ways (e.g. assembly of flakes deposited from liquid phases, co-sputtering and electrodeposition). This work would develop a much-needed characterisation protocol for thin-film thermoelectric materials and lead into the next phase of the project.

2D thermoelectric materials could be used to fabricate thin film hybrids with anisotropic thermal and electrical conductivities. The components of these hybrids could be judiciously selected to maximise ZT . As one case, CNT fillers (high σ) could be coupled with exfoliated Bi_2Te_3 (high S). By forming films the 1D CNT network will be aligned in the film plane, with in-plane alignment of the 2D material also possible. One would then expect that the values of in-plane and cross-plane S , σ and κ should differ considerably. What is not known is if these properties would vary in a correlated fashion or if the use of a thermally and electrically conductive component would benefit the overall ZT . By using the previously developed ZT measurement technique, together with existing methods for cross-plane measurements, the anisotropy in ZT could be determined. Percolation behaviour across S , σ and κ as a function of the composition of these systems could also be studied. This knowledge would lead a wide range of hybrid systems being developed for further study.

These optimum systems could then be applied to produce a test device. One can visualise one simple geometry where stacks of thin film thermoelectric hybrids could be fabricated. Potentially by electrically insulating the stacks from the other using a dielectric a bulk thermoelectric block could be fabricated. Within this block each

layer could act as its own independent thermoelectric device, which may give may have advantages in some device applications. Indeed, the formation of novel device architectures from thin-film thermoelectric hybrid materials could itself warrant a further study.

APPENDIX

10.1 GRAPHENE DISPERSIBILITY IN SOLVENTS

Table 10.1: Graphene dispersibilities, Hansen solubility parameters and Hildebrand parameters for all 40 solvents studied. Hansen and Hildebrand parameters were taken from HSPiP software. Most of this data can also be found in Hansen Solubility Parameters - A User's Handbook [165].

Solvent	δ_D MPa ^{1/2}	δ_P MPa ^{1/2}	δ_H MPa ^{1/2}	δ_T MPa ^{1/2}	C_g $\mu\text{g/ml}$	ΔC_g $\mu\text{g/ml}$
1. Cyclopentanone (CPO)	17.9	11.9	5.2	22.1	8.5	1.2
2. Cyclohexanone	17.8	8.4	5.1	20.3	7.3	1.3
3. <i>N</i> -formyl piperidine (NFP)	18.7	10.6	7.8	22.9	7.2	1.0
4. <i>N</i> -vinyl pyrrolidone (NVP)	16.4	9.3	5.9	19.8	5.5	1.5
5. 1,3-Dimethyl-2-imidazolidinone (DMEU)	18.0	10.5	9.7	23.0	5.4	1.3
6. Bromobenzene	19.2	5.5	4.1	20.4	5.1	–
7. Benzonitrile	18.8	12.0	3.3	22.5	4.8	0.6
8. Benzyl benzoate	20.0	5.1	5.2	21.3	4.7	1.9
9. <i>N</i> -methyl-pyrrolidone (NMP)	18.0	12.3	7.2	23.0	4.7	1.9

Solvent	δ_D MPa ^{1/2}	δ_P MPa ^{1/2}	δ_H MPa ^{1/2}	δ_T MPa ^{1/2}	C_g $\mu\text{g/ml}$	ΔC_g $\mu\text{g/ml}$
10. <i>N,N</i> -Dimethylpropylene urea (DMPU)	17.8	9.5	9.3	22.2	4.6	1.3
11. γ -Butyrolactone (GBL)	18.0	16.6	7.4	25.6	4.1	1.1
12. Dimethylformamide (DMF)	17.4	13.7	11.3	24.9	4.1	1.4
13. <i>N</i> -ethyl-pyrrolidone (NEP)	18.0	12.0	7.0	22.7	4.0	0.7
14. Dimethylacetamide (DMA)	16.8	11.5	9.4	22.4	3.9	1.5
15. Cyclohexylpyrrolidone (CHP)	18.2	6.8	6.5	20.5	3.7	1.0
16. Dimethyl sulfoxide (DMSO)	18.4	16.4	10.2	26.7	3.7	1.5
17. Dibenzyl ether	19.6	3.4	5.2	20.6	3.5	0.6
18. Chloroform	17.8	3.1	5.7	18.9	3.4	0.7
19. Isopropanol (IPA)	15.8	6.1	16.4	23.6	3.1	1.0
20. Chlorobenzene	19.0	4.3	2.0	19.6	2.9	0.5
21. 1-octyl-2-pyrrolidone (N8P)	17.4	6.2	4.8	19.1	2.8	1.0
22. 1-3 dioxolane	18.1	6.6	9.3	21.4	2.8	1.4
23. Ethyl acetate	15.8	5.3	7.2	18.2	2.6	1.2
24. Quinoline	20.5	5.6	5.7	22.0	2.6	0.6
25. Benzaldehyde	19.4	7.4	5.3	21.4	2.5	1.5
26. Ethanolamine	17.5	6.8	18.0	26.0	2.5	0.4
27. Diethyl phthalate	17.6	9.6	4.5	20.5	2.2	1.9

Solvent	δ_D MPa ^{1/2}	δ_P MPa ^{1/2}	δ_H MPa ^{1/2}	δ_T MPa ^{1/2}	C_g $\mu\text{g/ml}$	ΔC_g $\mu\text{g/ml}$
28. <i>N</i> -dodecyl-2-pyrrolidone (N ₁₂ P)	17.5	4.1	3.2	18.3	2.1	1.1
29. Pyridine	19.0	8.8	5.9	21.8	2.0	1.7
30. Dimethyl phthalate	18.6	10.8	4.9	22.1	1.8	0.4
31. Formamide	17.2	26.2	19.0	36.7	1.7	–
32. Ethanol	15.8	8.8	19.4	26.5	1.6	0.7
33. Vinyl acetate	16.0	7.2	5.9	18.5	1.5	0.7
34. Acetone	15.5	10.4	7.0	19.9	1.2	0.4
35. Water	15.5	16.0	42.3	47.8	1.1	0.4
36. Ethylene glycol	17.0	11.0	26.0	33.0	1.0	0.8
37. Toluene	18.0	1.4	2.0	18.2	0.8	0.4
38. Heptane	15.3	0.0	0.0	15.3	0.3	0.4
39. Hexane	14.9	0.0	0.0	14.9	0.2	0.1
40. Pentane	14.5	0.0	0.0	14.5	0.16	0.05

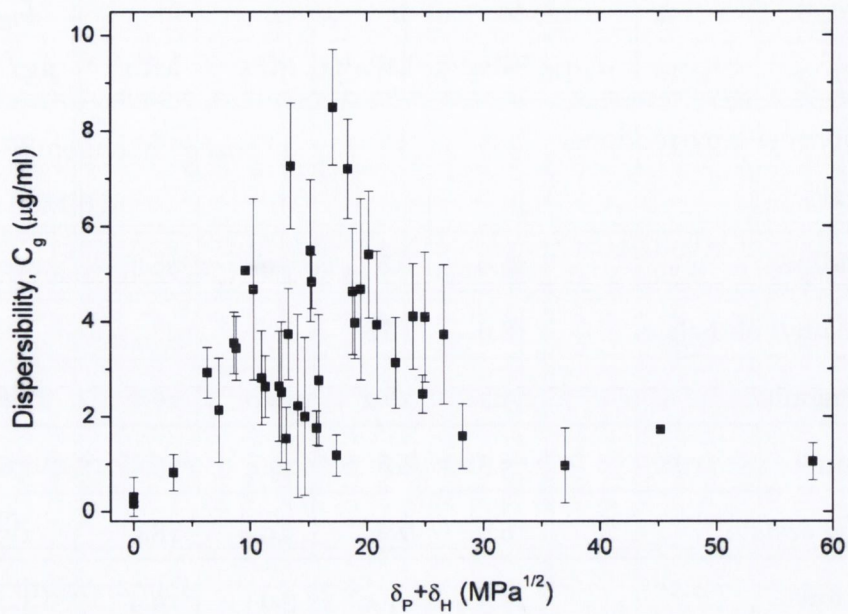


Figure 10.1: Graphene dispersibility, C_g , as a function of the sum of polar and hydrogen bonding HSPs

10.2 HIGH CONCENTRATION GRAPHENE/SC DISPERSIONS - TEM STATISTICS

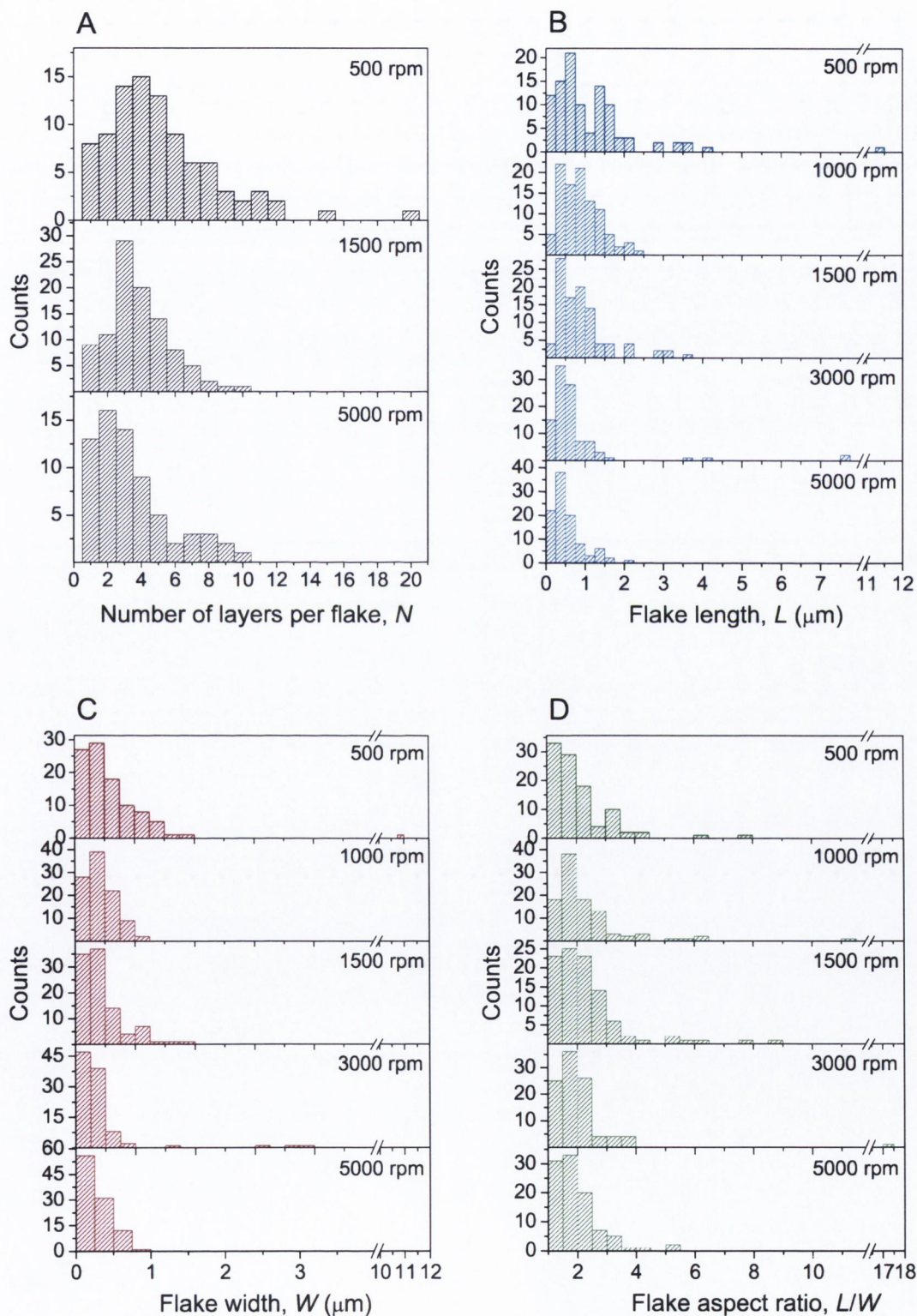


Figure 10.2: Histograms of TEM data as a function of CF rate, ω . All samples prepared using 90 min CF time with $t_{\text{sonic}} = 24$ hrs, $C_{g,i} = 5$ mg/ml, $C_{SC} = 0.1$ mg/ml.

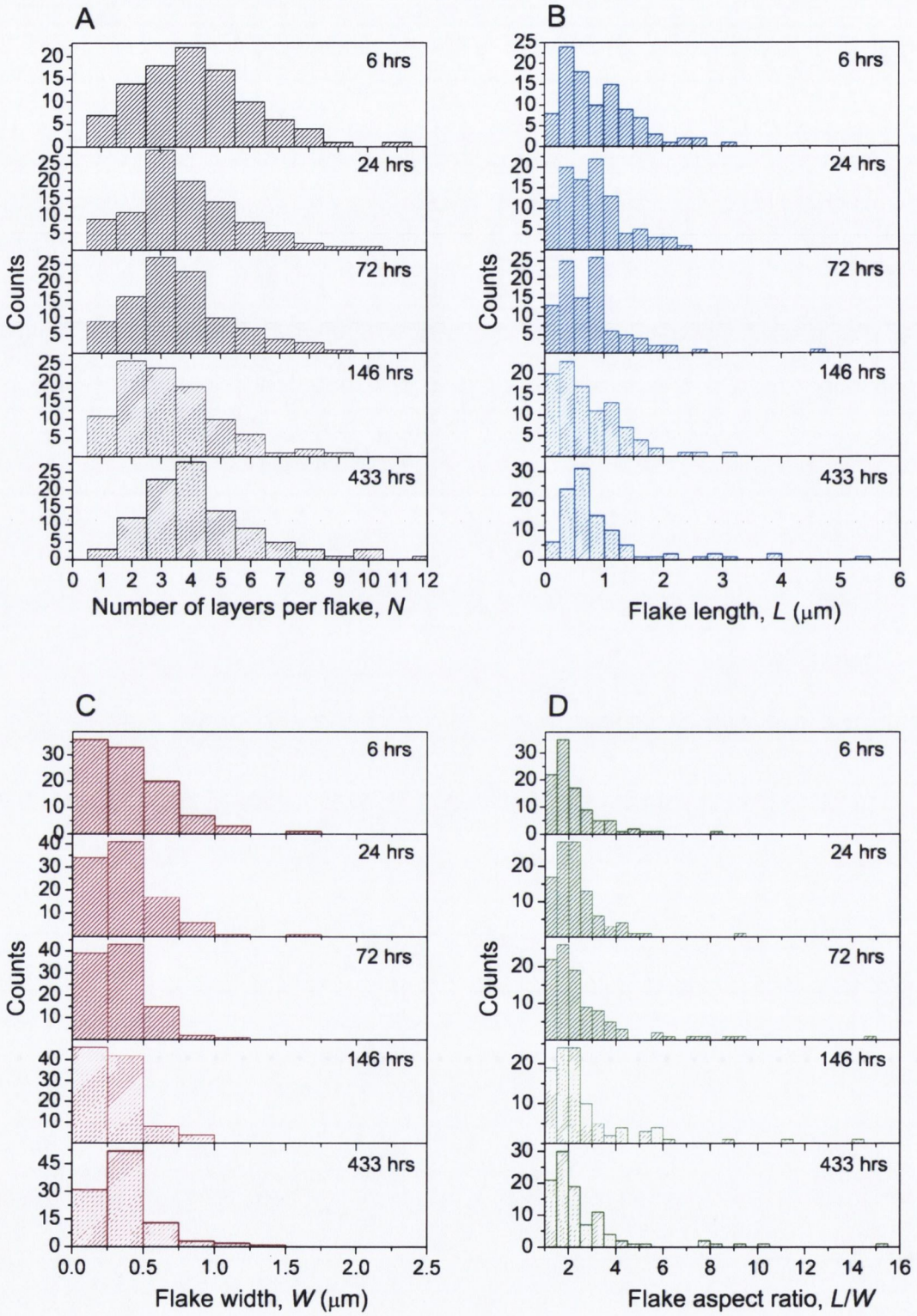


Figure 10.3: Histograms of TEM data as a function of sonication time, t_{sonic} . All samples prepared using 90 min CF time with $\omega = 1500$ rpm, $C_{g,i} = 5$ mg/ml, $C_{SC} = 0.1$ mg/ml.

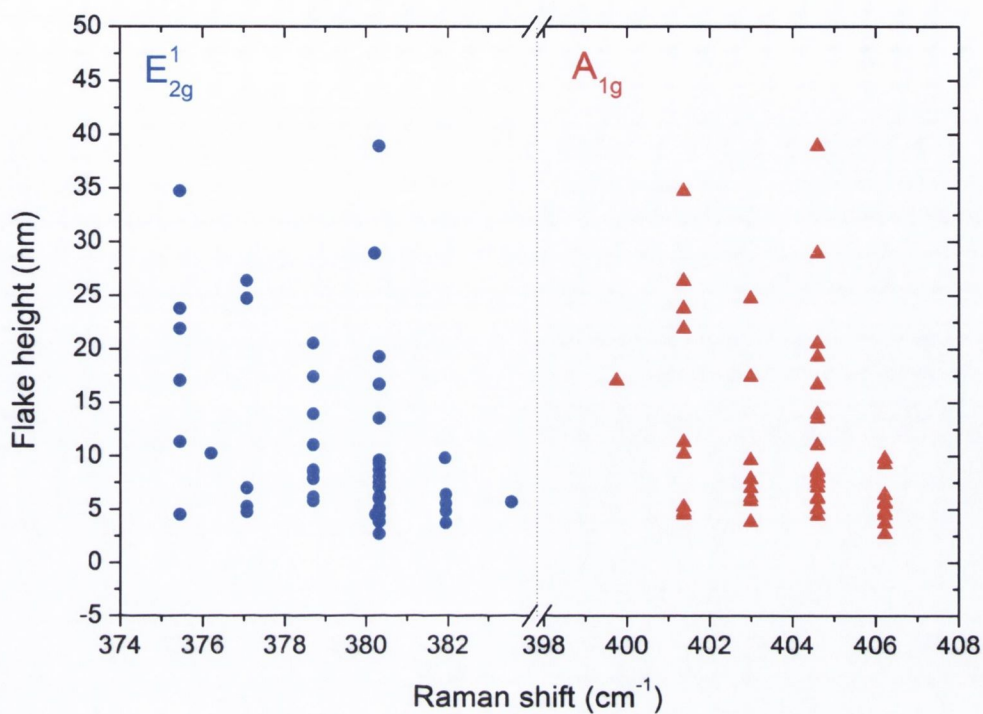
10.3 INORGANIC LAYERED COMPOUNDS - MoS_2 AFM DATA

Figure 10.4: Flake height from AFM analysis vs Raman peak position for solvent exfoliated MoS_2 . Flakes were deposited on silicon by spray casting and analysed with a 488 nm Ar ion laser.

BIBLIOGRAPHY

- [1] Kroto, H. W., Heath, J. R., O'Brien, S. C., Curl, R. F., and Smalley, R. E. (1985) C₆₀: Buckminsterfullerene. *Nature* 318, 162–163.
- [2] Iijima, S. (1991) Helical microtubules of graphitic carbon. *Nature* 354, 56–58.
- [3] Baughman, R. H., Zakhidov, A. A., and de Heer, W. A. (2002) Carbon Nanotubes—the Route Toward Applications. *Science* 297, 787–792.
- [4] Terrones, M. (2004) Carbon nanotubes: synthesis and properties, electronic devices and other emerging applications. *International Materials Reviews* 49, 325–377.
- [5] Coleman, J. N., Khan, U., Blau, W. J., and Gun'ko, Y. K. (2006) Small but strong: A review of the mechanical properties of carbon nanotube-polymer composites. *Carbon* 44, 1624–1652.
- [6] Novoselov, K. S., Geim, A. K., Morozov, S. V., Jiang, D., Zhang, Y., Dubonos, S. V., Grigorieva, I. V., and Firsov, A. A. (2004) Electric Field Effect in Atomically Thin Carbon Films. *Science* 306, 666–669.
- [7] Geim, A. K., and Novoselov, K. S. (2007) The rise of graphene. *Nature Materials* 6, 183–191.
- [8] Nobelprize.org, The Nobel Prize in Physics 2010. 2010; http://www.nobelprize.org/nobel_prizes/physics/laureates/2010/.
- [9] Coleman, J. N. (2009) Liquid-Phase Exfoliation of Nanotubes and Graphene. *Advanced Functional Materials* 19, 3680–3695.
- [10] Hernandez, Y. et al. (2008) High-yield production of graphene by liquid-phase exfoliation of graphite. *Nature Nanotechnology* 3, 563–568.
- [11] Pierson, H. O. *Handbook of Carbon, Graphite, Diamond and Fullerenes - Properties, Processing and Applications*; William Andrew Publishing/Noyes, 1993.

- [12] Fradkin, E. (1986) Critical behavior of disordered degenerate semiconductors. II. Spectrum and transport properties in mean-field theory. *Physical Review B* 33, 3263.
- [13] Wei, B. Q., Vajtai, R., and Ajayan, P. M. (2001) Reliability and current carrying capacity of carbon nanotubes. *Applied Physics Letters* 79, 1172–1174.
- [14] Yu, M.-F., Lourie, O., Dyer, M. J., Moloni, K., Kelly, T. F., and Ruoff, R. S. (2000) Strength and Breaking Mechanism of Multiwalled Carbon Nanotubes Under Tensile Load. *Science* 287, 637–640.
- [15] Iijima, S., and Ichihashi, T. (1993) Single-shell carbon nanotubes of 1-nm diameter. *Nature* 363, 603–605.
- [16] Chiang, I. W., Brinson, B. E., Huang, A. Y., Willis, P. A., Bronikowski, M. J., Margrave, J. L., Smalley, R. E., and Hauge, R. H. (2001) Purification and Characterization of Single-Wall Carbon Nanotubes (SWNTs) Obtained from the Gas-Phase Decomposition of CO (HiPco Process). *The Journal of Physical Chemistry B* 105, 8297–8301.
- [17] McDonald, T. J., Engtrakul, C., Jones, M., Rumbles, G., and Heben, M. J. (2006) Kinetics of PL quenching during single-walled carbon nanotube rebundling and diameter-dependent surfactant interactions. *Journal of Physical Chemistry B* 110, 25339–25346.
- [18] Reibold, M., Paufler, P., Levin, A. A., Kochmann, W., Patzke, N., and Meyer, D. C. (2006) Materials: Carbon nanotubes in an ancient Damascus sabre. *Nature* 444, 286–286.
- [19] Nanosensors, <http://www.windsorscientific.co.uk/AFM-Probe-CNT-NCH.html>.
- [20] Nanocyl, <http://www.nanocyl.com/>.
- [21] Bachilo, S. M., Strano, M. S., Kittrell, C., Hauge, R. H., Smalley, R. E., and Weisman, R. B. (2002) Structure-assigned optical spectra of single-walled carbon nanotubes. *Science* 298, 2361–2366.

- [22] O'Connell, M. J., Bachilo, S. M., Huffman, C. B., Moore, V. C., Strano, M. S., Haroz, E. H., Rialon, K. L., Boul, P. J., Noon, W. H., Kittrell, C., Ma, J. P., Hauge, R. H., Weisman, R. B., and Smalley, R. E. (2002) Band gap fluorescence from individual single-walled carbon nanotubes. *Science* 297, 593–596.
- [23] Strano, M. S., Moore, V. C., Miller, M. K., Allen, M. J., Haroz, E. H., Kittrell, C., Hauge, R. H., and Smalley, R. E. (2003) The role of surfactant adsorption during ultrasonication in the dispersion of single-walled carbon nanotubes. *Journal of Nanoscience and Nanotechnology* 3, 81–86.
- [24] Moore, V. C., Strano, M. S., Haroz, E. H., Hauge, R. H., Smalley, R. E., Schmidt, J., and Talmon, Y. (2003) Individually suspended single-walled carbon nanotubes in various surfactants. *Nano Letters* 3, 1379–1382.
- [25] Islam, M. F., Rojas, E., Bergey, D. M., Johnson, A. T., and Yodh, A. G. (2003) High weight fraction surfactant solubilization of single-wall carbon nanotubes in water. *Nano Letters* 3, 269–273.
- [26] Matarredona, O., Rhoads, H., Li, Z. R., Harwell, J. H., Balzano, L., and Resasco, D. E. (2003) Dispersion of single-walled carbon nanotubes in aqueous solutions of the anionic surfactant NaDDBS. *Journal of Physical Chemistry B* 107, 13357–13367.
- [27] Bergin, S. D., Nicolosi, V., Cathcart, H., Lotya, M., Rickard, D., Sun, Z. Y., Blau, W. J., and Coleman, J. N. (2008) Large populations of individual nanotubes in surfactant-based dispersions without the need for ultracentrifugation. *Journal of Physical Chemistry C* 112, 972–977.
- [28] Coleman, J. N., Dalton, A. B., Curran, S., Rubio, A., Davey, A. P., Drury, A., McCarthy, B., Lahr, B., Ajayan, P. M., Roth, S., Barklie, R. C., and Blau, W. J. (2000) Phase separation of carbon nanotubes and turbostratic graphite using a functional organic polymer. *Advanced Materials* 12, 213.

- [29] Cadek, M., Coleman, J. N., Barron, V., Hedicke, K., and Blau, W. J. (2002) Morphological and mechanical properties of carbon-nanotube-reinforced semicrystalline and amorphous polymer composites. *Applied Physics Letters* 81, 5123–5125.
- [30] Coleman, J. N., Cadek, M., Dalton, A. B., Munoz, E., Razal, J., Baughman, R. H., and Blau, W. J. (2003) Mechanical properties of hybrid polymer nanotube systems. *Nanotechnology* 5118, 271–279.
- [31] Martin, C. A., Sandler, J. K. W., Windle, A. H., Schwarz, M. K., Bauhofer, W., Schulte, K., and Shaffer, M. S. P. (2005) Electric field-induced aligned multi-wall carbon nanotube networks in epoxy composites. *Polymer* 46, 877–886.
- [32] Blighe, F. M., Hernandez, Y. R., Blau, W. J., and Coleman, J. N. (2007) Observation of percolation-like scaling - Far from the percolation threshold - In high volume fraction, high conductivity polymer-nanotube composite films. *Advanced Materials* 19, 4443.
- [33] Hasan, T., Scardaci, V., Tan, P. H., Rozhin, A. G., Milne, W. I., and Ferrari, A. C. (2008) Dispersibility and stability improvement of unfunctionalized nanotubes in amide solvents by polymer wrapping. *Physica E-Low-Dimensional Systems & Nanostructures* 40, 2414–2418.
- [34] Zheng, M., Jagota, A., Semke, E. D., Diner, B. A., McLean, R. S., Lustig, S. R., Richardson, R. E., and Tassi, N. G. (2003) DNA-assisted dispersion and separation of carbon nanotubes. *Nature Materials* 2, 338–342.
- [35] Cathcart, H., Quinn, S., Nicolosi, V., Kelly, J. M., Blau, W. J., and Coleman, J. N. (2007) Spontaneous debundling of single-walled carbon nanotubes in DNA-based dispersions. *Journal of Physical Chemistry C* 111, 66–74.
- [36] Bergin, S. D., Giordani, S., Mae Kernan, D., Minett, A., Coleman, J. N., and Blau, W. J. (2005) Characterisation of single-walled carbon nanotube bundle dissociation in amide solvents. *Electronic Properties of Novel Nanostructures* 786, 240–243.

- [37] Giordani, S., Bergin, S. D., Drury, A., Ni Mhuircheartaigh, E., Coleman, J. N., and Blau, W. J. (2005) Effect of solvents and dispersants on the bundle dissociation of single-walled carbon nanotube. *Electronic Properties of Novel Nanostructures* 786, 232–235.
- [38] Giordani, S., Bergin, S. D., Nicolosi, V., Lebedkin, S., Kappes, M. M., Blau, W. J., and Coleman, J. N. (2006) Debundling of single-walled nanotubes by dilution: Observation of large populations of individual nanotubes in amide solvent dispersions. *Journal of Physical Chemistry B* 110, 15708–15718.
- [39] Bergin, S. D., Nicolosi, V., Giordani, S., de Gromard, A., Carpenter, L., Blau, W. J., and Coleman, J. N. (2007) Exfoliation in ecstasy: liquid crystal formation and concentration-dependent debundling observed for single-wall nanotubes dispersed in the liquid drug gamma-butyrolactone. *Nanotechnology* 18.
- [40] Bergin, S. D., Nicolosi, V., Streich, P. V., Giordani, S., Sun, Z. Y., Windle, A. H., Ryan, P., Niraj, N. P. P., Wang, Z. T. T., Carpenter, L., Blau, W. J., Boland, J. J., Hamilton, J. P., and Coleman, J. N. (2008) Towards solutions of single-walled carbon nanotubes in common solvents. *Advanced Materials* 20, 1876.
- [41] Oxford University Press, www.oxforddictionaries.com.
- [42] Boehm, H. P., Setton, R., and Stumpp, E. (1986) Nomenclature and Terminology of Graphite-Intercalation Compounds. *Carbon* 24, 241–245.
- [43] Boehm, H. P., Setton, R., Stumpp, E., Boehm, H.-P., and Stumpp, E. (2007) Citation errors concerning the first report on exfoliated graphite. *Carbon* 45, 1381–1383.
- [44] Schafhaeutl, C. (1840) *Phil. Mag.* 16, 570–590.
- [45] Dreyer, D. R., Ruoff, R. S., and Bielawski, C. W. (2010) From Conception to Realization: An Historical Account of Graphene and Some Perspectives for Its Future. *Angewandte Chemie International Edition* 49, 9336–9344.
- [46] Lu, X. K., Yu, M. F., Huang, H., and Ruoff, R. S. (1999) Tailoring graphite with the goal of achieving single sheets. *Nanotechnology* 10, 269–272.

- [47] Morozov, S. V., Novoselov, K. S., Katsnelson, M. I., Schedin, F., Elias, D. C., Jaszczak, J. A., and Geim, A. K. (2008) Giant Intrinsic Carrier Mobilities in Graphene and Its Bilayer. *Physical Review Letters* 100, 016602.
- [48] Lin, Y.-M., Dimitrakopoulos, C., Jenkins, K. A., Farmer, D. B., Chiu, H.-Y., Grill, A., and Avouris, P. (2010) 100-GHz Transistors from Wafer-Scale Epitaxial Graphene. *Science* 327, 662.
- [49] De, S., King, P. J., Lyons, P. E., Khan, U., and Coleman, J. N. (2010) Size Effects and the Problem with Percolation in Nanostructured Transparent Conductors. *Acs Nano* 4, 7064–7072.
- [50] Bonaccorso, F., Sun, Z., Hasan, T., and Ferrari, A. C. (2010) Graphene photonics and optoelectronics. *Nat Photon* 4, 611–622.
- [51] Blake, P., Hill, E. W., Neto, A. H. C., Novoselov, K. S., Jiang, D., Yang, R., Booth, T. J., and Geim, A. K. (2007) Making graphene visible. *Applied Physics Letters* 91.
- [52] Nair, R. R., Blake, P., Grigorenko, A. N., Novoselov, K. S., Booth, T. J., Stauber, T., Peres, N. M. R., and Geim, A. K. (2008) Fine structure constant defines visual transparency of graphene. *Science* 320, 1308–1308.
- [53] Blake, P., Brimicombe, P. D., Nair, R. R., Booth, T. J., Jiang, D., Schedin, F., Ponomarenko, L. A., Morozov, S. V., Gleeson, H. F., Hill, E. W., Geim, A. K., and Novoselov, K. S. (2008) Graphene-based liquid crystal device. *Nano Letters* 8, 1704–1708.
- [54] Lee, C., Wei, X. D., Kysar, J. W., and Hone, J. (2008) Measurement of the elastic properties and intrinsic strength of monolayer graphene. *Science* 321, 385–388.
- [55] Peigney, A., Laurent, C., Flahaut, E., Bacsá, R. R., and Rousset, A. (2001) Specific surface area of carbon nanotubes and bundles of carbon nanotubes. *Carbon* 39, 507–514.
- [56] Berger, C., Song, Z. M., Li, X. B., Wu, X. S., Brown, N., Naud, C., Mayou, D., Li, T. B., Hass, J., Marchenkov, A. N., Conrad, E. H., First, P. N., and de Heer, W. A.

- (2006) Electronic confinement and coherence in patterned epitaxial graphene. *Science* 312, 1191–1196.
- [57] Ohta, T., El Gabaly, F., Bostwick, A., McChesney, J. L., Emtsev, K. V., Schmid, A. K., Seyller, T., Horn, K., and Rotenberg, E. (2008) Morphology of graphene thin film growth on SiC(0001). *New Journal of Physics* 10.
- [58] Aristov, V. Y., Urbanik, G., Kummer, K., Vyalikh, D. V., Molodtsova, O. V., Preobrajenski, A. B., Zakharov, A. A., Hess, C., Hanke, T., Buchner, B., Vobornik, I., Fujii, J., Panaccione, G., Ossipyan, Y. A., and Knupfer, M. (2010) Graphene Synthesis on Cubic SiC/Si Wafers. Perspectives for Mass Production of Graphene-Based Electronic Devices. *Nano Letters* 10, 992–995.
- [59] Hass, J., Heer, W. A. d., and Conrad, E. H. (2008) The growth and morphology of epitaxial multilayer graphene. *Journal of Physics: Condensed Matter* 20, 323202.
- [60] Soldano, C., Mahmood, A., and Dujardin, E. (2010) Production, properties and potential of graphene. *Carbon* 48, 2127–2150.
- [61] Kim, K. S., Zhao, Y., Jang, H., Lee, S. Y., Kim, J. M., Ahn, J. H., Kim, P., Choi, J. Y., and Hong, B. H. (2009) Large-scale pattern growth of graphene films for stretchable transparent electrodes. *Nature* 457, 706–710.
- [62] Reina, A., Jia, X. T., Ho, J., Nezich, D., Son, H. B., Bulovic, V., Dresselhaus, M. S., and Kong, J. (2009) Large Area, Few-Layer Graphene Films on Arbitrary Substrates by Chemical Vapor Deposition. *Nano Letters* 9, 30–35.
- [63] Bae, S. et al. (2010) Roll-to-roll production of 30-inch graphene films for transparent electrodes. *Nat Nano* 5, 574–578.
- [64] Yang, X., Dou, X., Rouhanipour, A., Zhi, L., Rader, H. J., and Mullen, K. (2008) Two-Dimensional Graphene Nanoribbons. *Journal of the American Chemical Society* 130, 4216–4217.
- [65] Viculis, L. M., Mack, J. J., and Kaner, R. B. (2003) A chemical route to carbon nanoscrolls. *Science* 299, 1361–1361.

- [66] Chen, G. H., Weng, W. G., Wu, D. J., Wu, C. L., Lu, J. R., Wang, P. P., and Chen, X. F. (2004) Preparation and characterization of graphite nanosheets from ultrasonic powdering technique. *Carbon* 42, 753–759.
- [67] Brodie, B. C. (1859) On the Atomic Weight of Graphite. *Philosophical Transactions of the Royal Society of London* 149, 249–259.
- [68] Hummers, W. S., and Offeman, R. E. (1958) Preparation of Graphitic Oxide. *J. Am. Chem. Soc.* 80, 1339–1339.
- [69] Hontorialucas, C., Lopezpeinado, A. J., Lopezgonzalez, J. D. D., Rojascervantes, M. L., and Martinaranda, R. M. (1995) Study of oxygen-containing groups in a series of graphite oxides - physical and chemical characterization. *Carbon* 33, 1585–1592.
- [70] Kovtyukhova, N. I., Ollivier, P. J., Martin, B. R., Mallouk, T. E., Chizhik, S. A., Buzaneva, E. V., and Gorchinskiy, A. D. (1999) Layer-by-layer assembly of ultra-thin composite films from micron-sized graphite oxide sheets and polycations. *Chemistry of Materials* 11, 771–778.
- [71] Titelman, G. I., Gelman, V., Bron, S., Khalfin, R. L., Cohen, Y., and Bianco-Peled, H. (2005) Characteristics and microstructure of aqueous colloidal dispersions of graphite oxide. *Carbon* 43, 641–649.
- [72] Stankovich, S., Dikin, D. A., Dommett, G. H. B., Kohlhaas, K. M., Zimney, E. J., Stach, E. A., Piner, R. D., Nguyen, S. T., and Ruoff, R. S. (2006) Graphene-based composite materials. *Nature* 442, 282–286.
- [73] Schniepp, H. C., Li, J. L., McAllister, M. J., Sai, H., Herrera-Alonso, M., Adamson, D. H., Prud'homme, R. K., Car, R., Saville, D. A., and Aksay, I. A. (2006) Functionalized single graphene sheets derived from splitting graphite oxide. *Journal of Physical Chemistry B* 110, 8535–8539.
- [74] Li, X., Zhang, G., Bai, X., Sun, X., Wang, X., Wang, E., and Dai, H. (2008) Highly conducting graphene sheets and Langmuir-Blodgett films. *Nature Nanotechnology* 3, 538–542.

- [75] Dikin, D. A., Stankovich, S., Zimney, E. J., Piner, R. D., Dommett, G. H. B., Evmenenko, G., Nguyen, S. T., and Ruoff, R. S. (2007) Preparation and characterization of graphene oxide paper. *Nature* 448, 457–460.
- [76] Stankovich, S., Dikin, D. A., Piner, R. D., Kohlhaas, K. A., Kleinhammes, A., Jia, Y., Wu, Y., Nguyen, S. T., and Ruoff, R. S. (2007) Synthesis of graphene-based nanosheets via chemical reduction of exfoliated graphite oxide. *Carbon* 45, 1558–1565.
- [77] Gilje, S., Han, S., Wang, M., Wang, K. L., and Kaner, R. B. (2007) A chemical route to graphene for device applications. *Nano Letters* 7, 3394–3398.
- [78] Li, D., Muller, M. B., Gilje, S., Kaner, R. B., and Wallace, G. G. (2008) Processable aqueous dispersions of graphene nanosheets. *Nature Nanotechnology* 3, 101–105.
- [79] Eda, G., Fanchini, G., and Chhowalla, M. (2008) Large-area ultrathin films of reduced graphene oxide as a transparent and flexible electronic material. *Nature Nanotechnology* 3, 270–274.
- [80] Lomeda, J. R., Doyle, C. D., Kosynkin, D. V., Hwang, W.-F., and Tour, J. M. (2008) Diazonium Functionalization of Surfactant-Wrapped Chemically Converted Graphene Sheets. *Journal of the American Chemical Society* 130, 16201–16206.
- [81] Si, Y., and Samulski, E. T. (2008) Synthesis of water soluble graphene. *Nano Letters* 8, 1679–1682.
- [82] Valles, C., Drummond, C., Saadaoui, H., Furtado, C. A., He, M., Roubeau, O., Ortolani, L., Monthieux, M., and Penicaud, A. (2008) Solutions of Negatively Charged Graphene Sheets and Ribbons. *Journal of the American Chemical Society* 130, 15802.
- [83] Eda, G., and Chhowalla, M. (2009) Graphene-based Composite Thin Films for Electronics. *Nano Letters* 9, 814–818.
- [84] Park, S., An, J. H., Jung, I. W., Piner, R. D., An, S. J., Li, X. S., Velamakanni, A., and Ruoff, R. S. (2009) Colloidal Suspensions of Highly Reduced Graphene Oxide in a Wide Variety of Organic Solvents. *Nano Letters* 9, 1593–1597.

- [85] Choucair, M., Thordarson, P., and Stride, J. A. (2009) Gram-scale production of graphene based on solvothermal synthesis and sonication. *Nat Nano* 4, 30–33.
- [86] Tung, V. C., Allen, M. J., Yang, Y., and Kaner, R. B. (2009) High-throughput solution processing of large-scale graphene. *Nat Nano* 4, 25–29.
- [87] Gomez-Navarro, C., Weitz, R. T., Bittner, A. M., Scolari, M., Mews, A., Burghard, M., and Kern, K. (2007) Electronic Transport Properties of Individual Chemically Reduced Graphene Oxide Sheets. *Nano Letters* 7, 3499–3503.
- [88] Ramanathan, T., Abdala, A. A., Stankovich, S., Dikin, D. A., Herrera-Alonso, M., Piner, R. D., Adamson, D. H., Schniepp, H. C., Chen, X., Ruoff, R. S., Nguyen, S. T., Aksay, I. A., Prud'homme, R. K., and Brinson, L. C. (2008) Functionalized graphene sheets for polymer nanocomposites. *Nature Nanotechnology* 3, 327–331.
- [89] Wu, Z.-S., Ren, W., Gao, L., Liu, B., Jiang, C., and Cheng, H.-M. (2009) Synthesis of high-quality graphene with a pre-determined number of layers. *Carbon* 47, 493–499.
- [90] Yang, D., Velamakanni, A., Bozoklu, G., Park, S., Stoller, M., Piner, R. D., Stankovich, S., Jung, I., Field, D. A., Ventrice Jr, C. A., and Ruoff, R. S. (2009) Chemical analysis of graphene oxide films after heat and chemical treatments by X-ray photoelectron and Micro-Raman spectroscopy. *Carbon* 47, 145–152.
- [91] Wilson, J. A., and Yoffe, A. D. (1969) Transition Metal Dichalcogenides Discussion and Interpretation of Observed Optical, Electrical and Structural Properties. *Advances in Physics* 18, 193.
- [92] Ayari, A., Cobas, E., Ogundadegbe, O., and Fuhrer, M. S. (2007) Realization and electrical characterization of ultrathin crystals of layered transition-metal dichalcogenides. *Journal of Applied Physics* 101, 014507.
- [93] Tenne, R., Margulis, L., Genut, M., and Hodes, G. (1992) Polyhedral and Cylindrical Structures of Tungsten Disulfide. *Nature* 360, 444–446.
- [94] Margulis, L., Salitra, G., Tenne, R., and Talianker, M. (1993) Nested Fullerene-like Structures. *Nature* 365, 113–114.

- [95] Tenne, R., and Redlich, M. (2010) Recent progress in the research of inorganic fullerene-like nanoparticles and inorganic nanotubes. *Chemical Society Reviews* 39, 1423–1434.
- [96] Rosentsveig, R., Margolin, A., Gorodnev, A., Popovitz-Biro, R., Feldman, Y., Rapoport, L., Novema, Y., Naveh, G., and Tenne, R. (2009) Synthesis of fullerene-like MoS₂ nanoparticles and their tribological behavior. *Journal of Materials Chemistry* 19, 4368–4374.
- [97] Rothschild, A., Sloan, J., and Tenne, R. (2000) Growth of WS₂ nanotubes phases. *Journal of the American Chemical Society* 122, 5169–5179.
- [98] Nath, M., and Rao, C. N. R. (2002) Nanotubes of the disulfides of groups 4 and 5 metals. *Pure and Applied Chemistry* 74, 1545–1552.
- [99] Frindt, R. F. (1965) Optical Absorption of a Few Unit-Cell Layers of MoS₂. *Physical Review* 140, A536.
- [100] Novoselov, K. S., Jiang, D., Schedin, F., Booth, T. J., Khotkevich, V. V., Morozov, S. V., and Geim, A. K. (2005) Two-dimensional atomic crystals. *Proceedings of the National Academy of Sciences of the United States of America* 102, 10451–10453.
- [101] Radisavljevic, B., Radenovic, A., Brivio, J., Giacometti, V., and Kis, A. (2011) Single-layer MoS₂ transistors. 6, 147–150.
- [102] Rao, C. N. R., and Nag, A. (2010) Inorganic Analogues of Graphene. *European Journal of Inorganic Chemistry* 4244–4250.
- [103] Matte, H., Gomathi, A., Manna, A. K., Late, D. J., Datta, R., Pati, S. K., and Rao, C. N. R. (2010) MoS₂ and WS₂ Analogues of Graphene. *Angewandte Chemie-International Edition* 49, 4059–4062.
- [104] Joensen, P., Frindt, R. F., and Morrison, S. R. (1986) Single-layer MoS₂. *Materials Research Bulletin* 21, 457–461.

- [105] Yang, D., Sandoval, S. J., Divigalpitiya, W. M. R., Irwin, J. C., and Frindt, R. F. (1991) Structure of Single Molecular Layer MoS₂. *Physical Review B* 43, 12053–12056.
- [106] Joensen, P., Crozier, E. D., Alberding, N., and Frindt, R. F. (1987) A study of single-layer and restacked MoS₂ by x-ray-diffraction and x-ray absorption-spectroscopy. *Journal of Physics C-Solid State Physics* 20, 4043–4053.
- [107] Jimenez Sandoval, S., Yang, D., Frindt, R. F., and Irwin, J. C. (1991) Raman study and lattice dynamics of single molecular layers of MoS₂. *Physical Review B* 44, 3955.
- [108] Gordon, R. A., Yang, D., Crozier, E. D., Jiang, D. T., and Frindt, R. F. (2002) Structures of exfoliated single layers of WS₂, MoS₂, and MoSe₂ in aqueous suspension. *Physical Review B* 65, 125407.
- [109] Wypych, F., and Schollhorn, R. (1992) 1T-MoS₂, a new metallic modification of molybdenum disulfide. *Journal of the Chemical Society, Chemical Communications* 1386–1388.
- [110] Yang, D., and Frindt, R. F. (1995) Li-intercalation and exfoliation of WS₂. *Journal of Physics and Chemistry of Solids* 57, 1113–1116.
- [111] Rowe, D. (1999) Thermoelectrics, an environmentally-friendly source of electrical power. *Renewable Energy* 16, 1251–1256.
- [112] Dresselhaus, M., Chen, G., Tang, M. Y., Yang, R. G., Lee, H., Wang, D., Ren, Z., Fleurial, J.-P., and Gogna, P. (2007) New Directions for Low-Dimensional Thermoelectric Materials. *Advanced Materials* 19, 1043–1053.
- [113] Bell, L. E. (2008) Cooling, Heating, Generating Power, and Recovering Waste Heat with Thermoelectric Systems. *Science* 321, 1457–1461.
- [114] Snyder, G. J., and Toberer, E. S. (2008) Complex thermoelectric materials. *Nat Mater* 7, 105–114.

- [115] Poudel, B., Hao, Q., Ma, Y., Lan, Y., Minnich, A., Yu, B., Yan, X., Wang, D., Muto, A., Vashaee, D., Chen, X., Liu, J., Dresselhaus, M. S., Chen, G., and Ren, Z. (2008) High-Thermoelectric Performance of Nanostructured Bismuth Antimony Telluride Bulk Alloys. *Science* 320, 634–638.
- [116] Kanatzidis, M. G. (2010) Nanostructured Thermoelectrics: The New Paradigm? *Chemistry of Materials* 22, 648–659.
- [117] Rowe, D., and Bhandari, C. *Modern thermoelectrics*; Holt, Rinehart and Winston, 1983.
- [118] Minnich, A. J., Dresselhaus, M. S., Ren, Z. F., and Chen, G. (2009) Bulk nanostructured thermoelectric materials: current research and future prospects. *Energy & Environmental Science* 2, 466–479.
- [119] Vineis, C. J., Shakouri, A., Majumdar, A., and Kanatzidis, M. G. (2010) Nanostructured Thermoelectrics: Big Efficiency Gains from Small Features. *Advanced Materials* 22, 3970–3980.
- [120] Zhao, L. D., Zhang, B. P., Li, J. F., Zhang, H. L., and Liu, W. S. (2008) Enhanced thermoelectric and mechanical properties in textured n-type Bi₂Te₃ prepared by spark plasma sintering. *Solid State Sciences* 10, 651–658.
- [121] Golia, S., Arora, M., Sharma, R. K., and Rastogi, A. C. (2003) Electrochemically deposited bismuth telluride thin films. *Current Applied Physics* 3, 195–197.
- [122] Zhou, W., and Wang, Z. L. *Scanning Microscopy for Nanotechnology - Techniques and Applications*; Springer - Verlag, 2006.
- [123] Li, X. L., Cai, K. F., Li, H., Wang, L., and Zhou, C. W. (2010) Electrodeposition and characterization of thermoelectric Bi₂Se₃ thin films. *International Journal of Minerals Metallurgy and Materials* 17, 104–107.
- [124] Chen, C. L., Chen, Y. Y., Lin, S. J., Ho, J. C., Lee, P. C., Chen, C. D., and Harutyunyan, S. R. (2010) Fabrication and Characterization of Electrodeposited Bismuth Telluride Films and Nanowires. *Journal of Physical Chemistry C* 114, 3385–3389.

- [125] Kim, M. Y., and Oh, T. S. (2010) Crystallization Behavior and Thermoelectric Characteristics of the Electrodeposited Sb_2Te_3 Thin Films. *Thin Solid Films* 518, 6550–6553.
- [126] Jeon, S.-j., Oh, M., Jeon, H., Hyun, S., and Lee, H.-j. (2011) Effects of post-annealing on thermoelectric properties of bismuth-tellurium thin films deposited by co-sputtering. *Microelectronic Engineering* 88, 541–544.
- [127] Kim, D.-H., and Lee, G.-H. (2006) Effect of rapid thermal annealing on thermoelectric properties of bismuth telluride films grown by co-sputtering. *Materials Science and Engineering: B* 131, 106–110.
- [128] Wang, R. Y., Feser, J. P., Gu, X., Yu, K. M., Segalman, R. A., Majumdar, A., Milliron, D. J., and Urban, J. J. (2010) Universal and Solution-Processable Precursor to Bismuth Chalcogenide Thermoelectrics. *Chemistry of Materials* 22, 1943–1945.
- [129] Mehta, R. J., Karthik, C., Singh, B., Teki, R., Borca-Tasciuc, T., and Ramanath, G. (2010) Seebeck Tuning in Chalcogenide Nanoplate Assemblies by Nanoscale Heterostructuring. *ACS Nano* 4, 5055–5060.
- [130] Teweldebrhan, D., Goyal, V., and Balandin, A. A. (2010) Exfoliation and Characterization of Bismuth Telluride Atomic Quintuples and Quasi-Two-Dimensional Crystals. *Nano Letters* 10, 1209–1218.
- [131] Seizo, N. (1963) The crystal structure of $\text{Bi}_2\text{Te}_{3-x}\text{Se}_x$. *Journal of Physics and Chemistry of Solids* 24, 479–485.
- [132] Goyal, V., Teweldebrhan, D., and Balandin, A. A. (2010) Mechanically-exfoliated stacks of thin films of Bi_2Te_3 topological insulators with enhanced thermoelectric performance. *Applied Physics Letters* 97.
- [133] Shahil, K. M. F., Hossain, M. Z., Teweldebrhan, D., and Balandin, A. A. (2010) Crystal symmetry breaking in few-quintuple Bi_2Te_3 films: Applications in nanometrology of topological insulators. *Applied Physics Letters* 96, 153103–3.

- [134] Teweldebrhan, D., Goyal, V., Rahman, M., and Balandin, A. A. (2010) Atomically-thin crystalline films and ribbons of bismuth telluride. *Applied Physics Letters* 96.
- [135] Hong, S. S., Kundhikanjana, W., Cha, J. J., Lai, K. J., Kong, D. S., Meister, S., Kelly, M. A., Shen, Z. X., and Cui, Y. (2010) Ultrathin Topological Insulator Bi_2Se_3 Nanoribbons Exfoliated by Atomic Force Microscopy. *Nano Letters* 10, 3118–3122.
- [136] Ding, Z., Bux, S. K., King, D. J., Chang, F. L., Chen, T.-H., Huang, S.-C., and Kaner, R. B. (2009) Lithium intercalation and exfoliation of layered bismuth selenide and bismuth telluride. *Journal of Materials Chemistry* 19, 2588–2592.
- [137] Zhang, H. J., Liu, C. X., Qi, X. L., Dai, X., Fang, Z., and Zhang, S. C. (2009) Topological insulators in Bi_2Se_3 , Bi_2Te_3 and Sb_2Te_3 with a single Dirac cone on the surface. *Nature Physics* 5, 438–442.
- [138] Hasan, M. Z., and Kane, C. L. (2010) Colloquium: Topological insulators. *Reviews of Modern Physics* 82, 3045–3067.
- [139] Kong, D., Dang, W., Cha, J. J., Li, H., Meister, S., Peng, H., Liu, Z., and Cui, Y. (2010) Few-Layer Nanoplates of Bi_2Se_3 and Bi_2Te_3 with Highly Tunable Chemical Potential. *Nano Letters* 10, 2245–2250.
- [140] Liu, J., Casavant, M. J., Cox, M., Walters, D. A., Boul, P., Lu, W., Rimberg, A. J., Smith, K. A., Colbert, D. T., and Smalley, R. E. (1999) Controlled deposition of individual single-walled carbon nanotubes on chemically functionalized templates. *Chemical Physics Letters* 303, 125–129.
- [141] Ausman, K. D., Piner, R., Lourie, O., Ruoff, R. S., and Korobov, M. (2000) Organic Solvent Dispersions of Single-Walled Carbon Nanotubes: Toward Solutions of Pristine Nanotubes. *The Journal of Physical Chemistry B* 104, 8911–8915.
- [142] Furtado, C. A., Kim, U. J., Gutierrez, H. R., Pan, L., Dickey, E. C., and Eklund, P. C. (2004) Debundling and dissolution of single-walled carbon nanotubes in amide solvents. *Journal of the American Chemical Society* 126, 6095–6105.

- [143] Landi, B. J., Ruf, H. J., Worman, J. J., and Raffaele, R. P. (2004) Effects of alkyl amide solvents on the dispersion of single-wall carbon nanotubes. *Journal of Physical Chemistry B* 108, 17089–17095.
- [144] Maeda, Y., Kimura, S., Hirashima, Y., Kanda, M., Lian, Y. F., Wakahara, T., Akasaka, T., Hasegawa, T., Tokumoto, H., Shimizu, T., Kataura, H., Miyauchi, Y., Maruyama, S., Kobayashi, K., and Nagase, S. (2004) Dispersion of single-walled carbon nanotube bundles in nonaqueous solution. *Journal of Physical Chemistry B* 108, 18395–18397.
- [145] Tan, Y. Q., and Resasco, D. E. (2005) Dispersion of single-walled carbon nanotubes of narrow diameter distribution. *Journal of Physical Chemistry B* 109, 14454–14460.
- [146] Bergin, S. D., Sun, Z., Rickard, D., Streich, P. V., Hamilton, J. P., and Coleman, J. N. (2009) Multicomponent Solubility Parameters for Single-Walled Carbon Nanotube-Solvent Mixtures. *Acs Nano* 3, 2340–2350.
- [147] Ham, H. T., Choi, Y. S., and Chung, I. J. (2005) An explanation of dispersion states of single-walled carbon nanotubes in solvents and aqueous surfactant solutions using solubility parameters. *Journal of Colloid and Interface Science* 286, 216–223.
- [148] Detriche, S., Zorzini, G., Colomer, J. F., Fonseca, A., and Nagy, J. B. (2007) Application of the Hansen Solubility Parameters Theory to Carbon Nanotubes. *Journal of Nanoscience and Nanotechnology* 8, 6082–6092.
- [149] Cheng, Q. H., Debnath, S., Gregan, E., and Byrne, H. J. (2008) Effect of Solvent Solubility Parameters on the Dispersion of Single-Walled Carbon Nanotubes. *Journal of Physical Chemistry C* 112, 20154–20158.
- [150] Geim, A. K., and MacDonald, A. H. (2007) Graphene: Exploring Carbon Flatland. *Physics Today* 60, 35–41.
- [151] Hunter, R. *Introduction to modern colloid science*; Oxford University Press New York, 1993; Vol. 7.

- [152] Bonard, J.-M., Stora, T., Salvétat, J.-P., Maier, F., Stockli, T., Duschl, C., Forro, L., de Heer, W. A., and Chatelain, A. (1997) Purification and size-selection of carbon nanotubes. *Advanced Materials* 9, 827–831.
- [153] Bandow, S., Rao, A. M., Williams, K. A., Thess, A., Smalley, R. E., and Eklund, P. C. (1997) Purification of Single-Wall Carbon Nanotubes by Microfiltration. *The Journal of Physical Chemistry B* 101, 8839–8842.
- [154] Duesberg, G. S., Burghard, M., Muster, J., Philipp, G., and Roth, S. (1998) Separation of carbon nanotubes by size exclusion chromatography. *Chemical Communications* 435–436.
- [155] Duesberg, G. S., Muster, J., Krstic, V., Burghard, M., and Roth, S. (1998) Chromatographic size separation of single-wall carbon nanotubes. *Applied Physics A: Materials Science & Processing* 67, 117–119.
- [156] Weisman, R. B., Bachilo, S. M., and Tsyboulski, D. (2004) Fluorescence spectroscopy of single-walled carbon nanotubes in aqueous suspension. *Applied Physics a-Materials Science & Processing* 78, 1111–1116.
- [157] Vaisman, L., Wagner, H. D., and Marom, G. (2006) The role of surfactants in dispersion of carbon nanotubes. *Advances in Colloid and Interface Science* 128, 37–46.
- [158] Sun, Z., Nicolosi, V., Rickard, D., Bergin, S. D., Aherne, D., and Coleman, J. N. (2008) Quantitative evaluation of surfactant-stabilized single-walled carbon nanotubes: Dispersion quality and its correlation with zeta potential. *Journal of Physical Chemistry C* 112, 10692–10699.
- [159] Grossiord, N., van der Schoot, P., Meuldijk, J., and Koning, C. E. (2007) Determination of the surface coverage of exfoliated carbon nanotubes by surfactant molecules in aqueous solution. *Langmuir* 23, 3646–3653.
- [160] Rastogi, R., Kaushal, R., Tripathi, S. K., Sharma, A. L., Kaur, I., and Bharadwaj, L. M. (2008) Comparative study of carbon nanotube dispersion using surfactants. *Journal of Colloid and Interface Science* 328, 421–428.

- [161] Haggemueller, R., Rahatekar, S. S., Fagan, J. A., Chun, J. H., Becker, M. L., Naik, R. R., Krauss, T., Carlson, L., Kadla, J. F., Trulove, P. C., Fox, D. F., DeLong, H. C., Fang, Z. C., Kelley, S. O., and Gilman, J. W. (2008) Comparison of the quality of aqueous dispersions of single wall carbon nanotubes using surfactants and biomolecules. *Langmuir* 24, 5070–5078.
- [162] Lotya, M., Hernandez, Y., King, P. J., Smith, R. J., Nicolosi, V., Karlsson, L. S., Blighe, F. M., De, S., Wang, Z., McGovern, I. T., Duesberg, G. S., and Coleman, J. N. (2009) Liquid Phase Production of Graphene by Exfoliation of Graphite in Surfactant/Water Solutions. *Journal of the American Chemical Society* 131, 3611–3620.
- [163] Lotya, M., King, P. J., Khan, U., De, S., and Coleman, J. N. (2010) High-Concentration, Surfactant-Stabilized Graphene Dispersions. *Acs Nano* 4, 3155–3162.
- [164] Gnanou, Y., Fontanille, M., and Corporation, E. *Organic and physical chemistry of polymers*; Wiley Online Library, 2008.
- [165] Hansen, C. *Hansen solubility parameters: a user's handbook*; CRC, 2007.
- [166] Callister Jr, W. *Materials science and engineering: an introduction*; John Wiley & Sons. Inc. New York, USA, 2007.
- [167] Lyklema, J. (1999) The surface tension of pure liquids: Thermodynamic components and corresponding states. *Colloids and Surfaces A: Physicochemical and Engineering Aspects* 156, 413–421.
- [168] Rubinstein, M., and Colby, R. *Polymer physics*; Oxford University Press, USA, 2003.
- [169] Rosen, M. *Surfactants and interfacial phenomena*; Wiley-Interscience, 2004.
- [170] Atkins, P., and Paula, J. *Physical Chemistry*; W.H. Freeman, 2006.
- [171] Malvern-Instruments, Zetasizer Nano Series User Manual. 2004.
- [172] Jones, R. *Soft condensed matter*; Oxford University Press, 2002.

- [173] Israelachvili, J. *Intermolecular And Surface Forces*; Academic Press, 2010.
- [174] Overbeek, J. T. G. (1977) Recent developments in the understanding of colloid stability. *Journal of Colloid and Interface Science* 58, 408–422.
- [175] Ohshima, H. In *Theory of Colloid and Interfacial Electric Phenomena*, 1st ed.; Hubbard, A., Ed.; INTERFACE SCIENCE AND TECHNOLOGY; 2006; Vol. 12; p 474.
- [176] London, F. (1937) The general theory of molecular forces. *Transactions of the Faraday Society* 33, 8b–26.
- [177] Margenau, H. (1939) Van der waals forces. *Reviews of Modern Physics* 11, 1.
- [178] Clark, T. R. M., B.J.; Frost, Ed. *Techniques in Visible and Ultraviolet Spectrometry*; Chapman & Hall, 1993; Vol. 4.
- [179] Wang, J., Hernandez, Y., Lotya, M., Coleman, J. N., and Blau, W. J. (2009) Broad-band Nonlinear Optical Response of Graphene Dispersions. *Advanced Materials* 21, 2430–2435.
- [180] Varian Cary 50 and 4000, 5000, 6000i UV-VIS Specifications. Varian.
- [181] ATR-FTIR Perkin-Elmer Technical Note.
- [182] Long, D. A. *Raman Spectroscopy*; McGraw-Hill, 1977.
- [183] Lewis, I., and Edwards, H. *Handbook of Raman spectroscopy: from the research laboratory to the process line*; Marcel Dekker, 2001.
- [184] McCreery, R. *Raman spectroscopy for chemical analysis*; John Wiley & Sons, 2000.
- [185] Smith, E., and Dent, G. *Modern Raman spectroscopy: a practical approach*; J. Wiley, 2005.
- [186] Ferrari, A. C., Meyer, J. C., Scardaci, V., Casiraghi, C., Lazzeri, M., Mauri, F., Piscanec, S., Jiang, D., Novoselov, K. S., Roth, S., and Geim, A. K. (2006) Raman spectrum of graphene and graphene layers. *Physical Review Letters* 97.

- [187] Dresselhaus, M. S., Jorio, A., Hofmann, M., Dresselhaus, G., and Saito, R. (2010) Perspectives on Carbon Nanotubes and Graphene Raman Spectroscopy. *Nano Letters* 10, 751–758.
- [188] Graf, D., Molitor, F., Ensslin, K., Stampfer, C., Jungen, A., Hierold, C., and Wirtz, L. (2007) Raman imaging of graphene. *Solid State Communications* 143, 44–46.
- [189] Malard, L. M., Pimenta, M. A., Dresselhaus, G., and Dresselhaus, M. S. (2009) Raman spectroscopy in graphene. *Physics Reports-Review Section of Physics Letters* 473, 51–87.
- [190] Ferrari, A. C. (2007) Raman spectroscopy of graphene and graphite: Disorder, electron-phonon coupling, doping and nonadiabatic effects. *Solid State Communications* 143, 47–57.
- [191] Vidano, R. P., Fischbach, D. B., Willis, L. J., and Loehr, T. M. (1981) Observation of Raman Band Shifting with Excitation Wavelength for Carbons and Graphites. *Solid State Communications* 39, 341–344.
- [192] Koh, Y. K., Bae, M. H., Cahill, D. G., and Pop, E. (2011) Reliably Counting Atomic Planes of Few-Layer Graphene ($n > 4$). *Acs Nano* 5, 269–274.
- [193] Casiraghi, C., Hartschuh, A., Qian, H., Piscanec, S., Georgi, C., Fasoli, A., Novoselov, K. S., Basko, D. M., and Ferrari, A. C. (2009) Raman Spectroscopy of Graphene Edges. *Nano Letters* 9, 1433–1441.
- [194] Mason, T., and Lorimer, J. *Sonochemistry: theory, applications and uses of ultrasound in chemistry*; Ellis Horwood, 1988.
- [195] Nicolosi, V., Vrbancic, D., Mrzel, A., McCauley, J., O’Flaherty, S., McGuinness, C., Compagnini, G., Mihailovic, D., Blau, W. J., and Coleman, J. N. (2005) Solubility of Mo₆S₄.₅I₄.₅ nanowires in common solvents: A sedimentation study. *Journal of Physical Chemistry B* 109, 7124–7133.
- [196] Michov, B. M. (1988) Radically simplifying the Henry function. *Electrophoresis* 9, 199–200.

- [197] Binnig, G., Quate, C. F., and Gerber, C. (1986) Atomic Force Microscope. *Physical Review Letters* 56, 930.
- [198] The Atomic Force Microscope Resource Library, <http://www.afmuniversity.org/blog/2007/06/21/what-is-an-atomic-force-microscope/>.
- [199] Wiesendanger, R. *Scanning probe microscopy and spectroscopy: methods and applications*; Cambridge University Press, 1994.
- [200] Bhushan, B. *Handbook of nanotechnology*; Springer, 2007.
- [201] Williams, D., and Carter, C. *Transmission electron microscopy: a textbook for materials science. Basics*; Springer, 2009.
- [202] Meyer, J. C., Geim, A. K., Katsnelson, M. I., Novoselov, K. S., Booth, T. J., and Roth, S. (2007) The structure of suspended graphene sheets. *Nature* 446, 60–63.
- [203] Thornton, P. *Scanning electron microscopy: applications to materials and device science*; Chapman & Hall, 1968.
- [204] Manual for the SUPRA and ULTRA Scanning Electron Microscopes V5.00. Zeiss, 2005.
- [205] Garratt-Reed, A., and Bell, D. *Energy-dispersive X-ray analysis in the electron microscope*; BIOS, 2003.
- [206] Bergin, S. D., Sun, Z., Streich, P., Hamilton, J., and Coleman, J. N. (2009) New Solvents for Nanotubes: Approaching the Dispersibility of Surfactants. *The Journal of Physical Chemistry C* 114, 231–237.
- [207] Ruoff, R. S., Tse, D. S., Malhotra, R., and Lorents, D. C. (1993) Solubility of fullerene (C₆₀) in a variety of solvents. *The Journal of Physical Chemistry* 97, 3379–3383.
- [208] Abergel, D. S. L., and Fal'ko, V. I. (2007) Optical and magneto-optical far-infrared properties of bilayer graphene. *Physical Review B* 75, 155430.

- [209] Taft, E. A., and Philipp, H. R. (1965) Optical Properties of Graphite. *Physical Review* 138, A197.
- [210] Ahuja, R., Auluck, S., Wills, J. M., Alouani, M., Johansson, B., and Eriksson, O. (1997) Optical properties of graphite from first-principles calculations. *Physical Review B* 55, 4999.
- [211] Lockwood, N. A., de Pablo, J. J., and Abbott, N. L. (2005) Influence of surfactant tail branching and organization on the orientation of liquid crystals at aqueous-liquid crystal interfaces. *Langmuir* 21, 6805–6814.
- [212] White, B., Banerjee, S., O'Brien, S., Turro, N. J., and Herman, I. P. (2007) Zeta-potential measurements of surfactant-wrapped individual single-walled carbon nanotubes. *Journal of Physical Chemistry C* 111, 13684–13690.
- [213] Weirich, T., Labar, J., and Zou, X. *Electron crystallography: novel approaches for structure determination of nanosized materials*; Springer, 2006.
- [214] Tkachev, S. V., Buslaeva, E. Y., and Gubin, S. P. (2011) Graphene: A Novel Carbon Nanomaterial. *Inorganic Materials* 47, 1–10.
- [215] Yang, Q., Pan, X. J., Huang, F., and Li, K. C. (2010) Fabrication of High-Concentration and Stable Aqueous Suspensions of Graphene Nanosheets by Noncovalent Functionalization with Lignin and Cellulose Derivatives. *Journal of Physical Chemistry C* 114, 3811–3816.
- [216] Vegh, J. (2006) The Shirley background revised. *Journal of Electron Spectroscopy and Related Phenomena* 151, 159–164.
- [217] Park, S., An, J., Piner, R. D., Jung, I., Yang, D., Velamakanni, A., Nguyen, S. T., and Ruoff, R. S. (2008) Aqueous Suspension and Characterization of Chemically Modified Graphene Sheets. *Chemistry of Materials* 20, 6592–6594.
- [218] Becerril, H. A., Mao, J., Liu, Z., Stoltenberg, R. M., Bao, Z., and Chen, Y. (2008) Evaluation of Solution-Processed Reduced Graphene Oxide Films as Transparent Conductors. 2, 463–470.

- [219] De, S., and Coleman, J. N. (2010) Are There Fundamental Limitations on the Sheet Resistance and Transmittance of Thin Graphene Films? *Acs Nano* 4, 2713–2720.
- [220] De, S., King, P. J., Lotya, M., O'Neill, A., Doherty, E. M., Hernandez, Y., Duesberg, G. S., and Coleman, J. N. (2010) Flexible, Transparent, Conducting Films of Randomly Stacked Graphene from Surfactant-Stabilized, Oxide-Free Graphene Dispersions. *SMALL* 6, 458–464.
- [221] Maslova, M. V., Gerasimova, L. G., and Forsling, W. (2004) Surface properties of cleaved mica. *Colloid Journal* 66, 322–328.
- [222] Liu, T., Luo, S. D., Xiao, Z. W., Zhang, C., and Wang, B. (2008) Preparative Ultracentrifuge Method for Characterization of Carbon Nanotube Dispersions. *Journal of Physical Chemistry C* 112, 19193–19202.
- [223] Weng, L. S., Zhang, L. Y., Chen, Y. P., and Rokhinson, L. P. (2008) Atomic force microscope local oxidation nanolithography of graphene. *Applied Physics Letters* 93.
- [224] Sidorov, A. N., Yazdanpanah, M. M., Jalilian, R., Ouseph, P. J., Cohn, R. W., and Sumanasekera, G. U. (2007) Electrostatic deposition of graphene. *Nanotechnology* 18.
- [225] Nemes-Incze, P., Osvath, Z., Kamaras, K., and Biro, L. P. (2008) Anomalies in thickness measurements of graphene and few layer graphite crystals by tapping mode atomic force microscopy. *Carbon* 46, 1435–1442.
- [226] Paredes, J. I., Villar-Rodil, S., Martinez-Alonso, A., and Tascon, J. M. D. (2008) Graphene oxide dispersions in organic solvents. *Langmuir* 24, 10560–10564.
- [227] Smith, R. J., Lotya, M., and Coleman, J. N. (2010) The importance of repulsive potential barriers for the dispersion of graphene using surfactants. *New Journal of Physics* 12.
- [228] Khan, U., O'Neill, A., Lotya, M., De, S., and Coleman, J. N. (2010) High-Concentration Solvent Exfoliation of Graphene. *SMALL* 6, 864–871.

- [229] Green, A. A., and Hersam, M. C. (2009) Solution Phase Production of Graphene with Controlled Thickness via Density Differentiation. *Nano Letters* 9, 4031–4036.
- [230] Hasan, T., Torrisi, F., Sun, Z., Popa, D., Nicolosi, V., Privitera, G., Bonaccorso, F., and Ferrari, A. C. (2010) Solution-phase exfoliation of graphite for ultrafast photonics. *Physica Status Solidi B-Basic Solid State Physics* 247, 2953–2957.
- [231] Green, A. A., and Hersam, M. C. (2010) Emerging Methods for Producing Monodisperse Graphene Dispersions. *Journal of Physical Chemistry Letters* 1, 544–549.
- [232] Khan, U., Porwal, H., O'Neill, A., Nawaz, K., May, P., and Coleman, J. N. (2011) Solvent-Exfoliated Graphene at Extremely High Concentration. *Langmuir* 27, 9077–9082.
- [233] Hennrich, F., Krupke, R., Arnold, K., Rojas Stutz, J. A., Lebedkin, S., Koch, T., Schimmel, T., and Kappes, M. M. (2007) The Mechanism of Cavitation-Induced Scission of Single-Walled Carbon Nanotubes. *The Journal of Physical Chemistry B* 111, 1932–1937.
- [234] Lucas, A., Zakri, C., Maugey, M., Pasquali, M., Schoot, P. v. d., and Poulin, P. (2009) Kinetics of Nanotube and Microfiber Scission under Sonication. *The Journal of Physical Chemistry C* 113, 20599–20605.
- [235] Smith, R. J., King, P. J., Wirtz, C., Duesberg, G., and Coleman, J. N. Lateral Size Selection of Aqueous Graphene-Surfactant Dispersions using Size Exclusion Chromatography. *Submitted, under review*
- [236] O'Neill, A., Khan, U., Nirmalraj, P. N., Boland, J., and Coleman, J. N. (2011) Graphene Dispersion and Exfoliation in Low Boiling Point Solvents. *The Journal of Physical Chemistry C* 115, 5422–5428.
- [237] Chen, H., Muller, M. B., Gilmore, K. J., Wallace, G. G., and Li, D. (2008) Mechanically strong, electrically conductive, and biocompatible graphene paper. *Advanced Materials* 20, 3557.

- [238] Coleman, J. N. et al. (2011) Two-Dimensional Nanosheets Produced by Liquid Exfoliation of Layered Materials. *Science* 331, 568–571.
- [239] He, G. S., Qin, H.-Y., and Zheng, Q. (2009) Rayleigh, Mie, and Tyndall scatterings of polystyrene microspheres in water: Wavelength, size, and angle dependences. *Optics* 105, 023110.
- [240] Ponomarev, E. A., Neumann-Spallart, M., Hodes, G., and Levy-Clement, C. (1996) Electrochemical deposition of MoS₂ thin films by reduction of tetrathiomolybdate. *Thin Solid Films* 280, 86–89.
- [241] Splendiani, A., Sun, L., Zhang, Y. B., Li, T. S., Kim, J., Chim, C. Y., Galli, G., and Wang, F. (2010) Emerging Photoluminescence in Monolayer MoS₂. *Nano Letters* 10, 1271–1275.
- [242] Chrissafis, K., Zamani, M., Kambas, K., Stoemenos, J., Economou, N. A., Samaras, I., and Julien, C. (1989) Structural studies of MoS₂ intercalated by lithium. *Materials Science and Engineering: B* 3, 145–151.
- [243] McDevitt, N. T., Zabinski, J. S., and Donley, M. S. (1994) The Use of Raman-Scattering to Study Disorder in Pulsed-Laser Deposited MoS₂ Films. *Thin Solid Films* 240, 76–81.
- [244] Frey, G. L., Tenne, R., Matthews, M. J., Dresselhaus, M. S., and Dresselhaus, G. (1999) Raman and resonance Raman investigation of MoS₂ nanoparticles. *Physical Review B* 60, 2883–2892.
- [245] Lee, C., Yan, H., Brus, L. E., Heinz, T. F., Hone, J., and Ryu, S. (2010) Anomalous Lattice Vibrations of Single- and Few-Layer MoS₂. *ACS Nano* 4, 2695–2700.
- [246] Frey, G. L., Reynolds, K. J., Friend, R. H., Cohen, H., and Feldman, Y. (2003) Solution-Processed Anodes from Layer-Structure Materials for High-Efficiency Polymer Light-Emitting Diodes. *Journal of the American Chemical Society* 125, 5998–6007.

- [247] Du, G., Guo, Z., Wang, S., Zeng, R., Chen, Z., and Liu, H. (2010) Superior stability and high capacity of restacked molybdenum disulfide as anode material for lithium ion batteries. *Chemical Communications* 46, 1106–1108.
- [248] Guo, G., Hong, J., Cong, C., Zhou, X., and Zhang, K. (2005) Molybdenum disulfide synthesized by hydrothermal method as anode for lithium rechargeable batteries. *Journal of Materials Science* 40, 2557–2559.
- [249] Wang, Q., and Li, J. (2007) Facilitated Lithium Storage in MoS₂ Overlayers Supported on Coaxial Carbon Nanotubes. *The Journal of Physical Chemistry C* 111, 1675–1682.
- [250] Feng, C., Ma, J., Li, H., Zeng, R., Guo, Z., and Liu, H. (2009) Synthesis of molybdenum disulfide (MoS₂) for lithium ion battery applications. *Materials Research Bulletin* 44, 1811–1815.
- [251] Xiao, J., Choi, D. W., Cosimbescu, L., Koech, P., Liu, J., and Lemmon, J. P. (2010) Exfoliated MoS₂ Nanocomposite as an Anode Material for Lithium Ion Batteries. *Chemistry of Materials* 22, 4522–4524.
- [252] Li, H., Ma, L., Chen, W.-x., and Wang, J.-m. (2009) Synthesis of MoS₂/C nanocomposites by hydrothermal route used as Li-ion intercalation electrode materials. *Materials Letters* 63, 1363–1365.
- [253] Smith, R. J., King, P. J., Lotya, M., Wirtz, C., Khan, U., De, S., O'Neill, A., Duesberg, G. S., Grunlan, J. C., Moriarty, G., Chen, J., Wang, J., Minett, A. I., Nicolosi, V., and Coleman, J. N. (2011) Large-Scale Exfoliation of Inorganic Layered Compounds in Aqueous Surfactant Solutions. *Advanced Materials* 23, 3944–3948.
- [254] Marom, R., Amalraj, S. F., Leifer, N., Jacob, D., and Aurbach, D. (2011) A review of advanced and practical lithium battery materials. *J. Mater. Chem.* 21, 9938–9954.
- [255] Vayrynen, A., and Salminen, J. (2012) Lithium ion battery production. *The Journal of Chemical Thermodynamics* 46, 80 – 85.

- [256] Greenaway, D. L., and Harbeke, G. (1965) Band structure of bismuth telluride, bismuth selenide and their respective alloys. *Journal of Physics and Chemistry of Solids* 26, 1585–1604.
- [257] Zhao, Y., Hughes, R. W., Su, Z., Zhou, W., and Gregory, D. H. (2011) One-Step Synthesis of Bismuth Telluride Nanosheets of a Few Quintuple Layers in Thickness. *Angewandte Chemie International Edition*
- [258] Fan, X. A., and et al., (2006) Characterization and thermoelectric properties of p-type 25activated sintering. *Journal of Physics D: Applied Physics* 39, 740.
- [259] Zhao, Y., Dyck, J. S., Hernandez, B. M., and Burda, C. (2010) Improving Thermoelectric Properties of Chemically Synthesized Bi₂Te₃-Based Nanocrystals by Annealing. *The Journal of Physical Chemistry C* 114, 11607–11613.
- [260] Duan, X. K., Jiang, Y. Z., Zheng, Z. H., Fan, P., Liang, G. X., Zhang, D. P., Cai, X. M., and Chen, T. B. (2010) Annealing temperature influence on electrical properties of ion beam sputtered Bi₂Te₃ thin films. *Journal of Physics and Chemistry of Solids* 71, 1713–1716.
- [261] Fan, S. F., Zhao, J. N., Yan, Q. Y., Ma, J., and Hng, H. H. (2011) Influence of Nano-inclusions on Thermoelectric Properties of n-Type Bi₂Te₃ Nanocomposites. *Journal of Electronic Materials* 40, 1018–1023.
- [262] Li, F., Huang, X. Y., Sun, Z. L., Ding, J. A., Jiang, J., Jiang, W., and Chen, L. D. (2011) Enhanced thermoelectric properties of n-type Bi₂Te₃-based nanocomposite fabricated by spark plasma sintering. *Journal of Alloys and Compounds* 509, 4769–4773.
- [263] Madan, D., Chen, A., Wright, P. K., and Evans, J. W. (2011) Dispenser printed composite thermoelectric thick films for thermoelectric generator applications. *Journal of Applied Physics* 109.
- [264] Navone, C., Soulier, M., Testard, J., Simon, J., and Caroff, T. (2011) Optimization and Fabrication of a Thick Printed Thermoelectric Device. *Journal of Electronic Materials* 40, 789–793.

- [265] Goncalves, L. M., Couto, C., Alpuim, P., Rolo, A. G., Volklein, F., and Correia, J. H. (2010) Optimization of thermoelectric properties on Bi₂Te₃ thin films deposited by thermal co-evaporation. *Thin Solid Films* 518, 2816–2821.